5-2023

On the Impact of Inclination-Dependent Attenuation on the Derived Star Formation Histories of Disk Galaxies

Keith Doore
University of Arkansas-Fayetteville

On the Impact of Inclination-Dependent Attenuation on the Derived Star Formation Histories of Disk Galaxies

A dissertation submitted in partial fulfillment
of the requirements for the degree of
Doctor of Philosophy in Space and Planetary Sciences

by

Keith Doore
University of Northern Iowa
Bachelor of Science in Physics, 2017
Bachelor of Arts in Earth Science, 2017

May 2023
University of Arkansas

This dissertation is approved for recommendation to the Graduate Council.

Bret Lehmer, Ph.D.
Dissertation Director

Julia Kennefick, Ph.D.
Committee Member

Giovanni Petris, Ph.D.
Committee Member

Larry Roe, Ph.D.
Committee Member

Abstract

The physical properties of a galaxy (e.g., its star-formation history and dust content) regulate the distribution of light that is emitted by stars and attenuated by the interstellar gas and dust. This attenuation by dust can have a significant impact on the observed spectral energy distribution (SED) of a disk galaxy, especially when taking into account its viewing angle (i.e., inclination). For example, as the inclination angle of a galactic disk changes from face-on to edge-on (i.e., $i = 0^\circ$ to $i = 90^\circ$), the proportion of light that is attenuated along the line of sight increases, due to an increasing column density of dust. Therefore, additional care must be taken when modeling the SED of a disk galaxy to account for any inclination dependence.

In this work, we develop and implement an inclination-dependent attenuation prescription into our SED fitting code, `Lightning`, to more accurately derive the physical properties of disk galaxies. First, we present the details of our SED fitting code, `Lightning`, as it is the cornerstone of our inclination-dependent analyses. We discuss all of the models in `Lightning`, which can include contributions from a variety of sources, along with the available algorithms to fit the models to observations. Then, to show the future potential of `Lightning`, we present several examples using a variety of observational data.

Next, to better understand how inclination affects the physical properties of disk galaxies, we apply our prescription on two respective galactic samples to (1) study the impact of inclination-dependent attenuation on derived stellar properties and (2) examine and quantify how commonly used star formation rate (SFR) estimators depend on inclination. For the first application, we compare our inclination-dependent attenuation prescription with a more traditional inclination-independent attenuation prescription. Our results indicate stark statistical differences in the derived

optical attenuation and stellar masses, with the traditional attenuation prescription resulting in these properties being underestimated compared to the inclination-dependent attenuation prescription at high inclinations. Therefore, the results from this application suggest that SED fitting assuming inclination-independent attenuation potentially underestimates these properties in highly inclined disk galaxies.

For the second application, We find that two commonly used SFR estimators (the hybrid UV+IR and $A_{\rm FUV}$-β relations) present clear dependencies on inclination. To quantify these dependencies, we expand the parametric form of the estimators to include an inclination-dependence. We then compare both of these new inclination-dependent estimators to similar inclination-independent relations found in the literature. From this comparison, we find that our inclination-dependent relations result in a reduction in the residual scatter of the derived SFRs of our sample by approximately a factor of two. Therefore, this second application demonstrates that inclination must be considered in SFR estimators to produce more accurate SFR estimates in disk galaxies.

Overall, this work provides the crucial steps towards understanding and incorporating the impact of inclination-dependence on the derived star-formation histories of disk galaxies. It additionally presents a novel tool (`Lightning`) which can be used in future studies to more accurately account for this inclination-dependence.

Acknowledgements

I would like to acknowledge my adviser Bret Lehmer for helping guide me during my research and encouraging me to pursue the research projects I found most interesting. I would also like to acknowledge Rafael T. Eufrasio who mentored me throughout my graduate studies, while not officially being listed as an adviser. The contents of the thesis would not have been possible without their continued support and guidance. In terms of research, I would finally like to acknowledge Erik B. Monson, who collaborated with me to refactor and update our spectral energy distribution fitting code `Lightning`.

Outside of my research, I would like to acknowledge and thank my family and friends for their support throughout graduate school. I want to specifically thank my wife, Liz, for all of her encouragement and advise. Without her, reaching the end of my graduate studies would not have been possible.

Finally, I want to acknowledge that this work was primarily supported by NASA Astrophysics Data Analysis Program (ADAP) grant 80NSSC20K0444.

Contents

List of Figures

List of Tables

List of Published Papers

Chapter 2 of this dissertation will appear in press as:

Doore, K., Eufrasio, R. T., Lehmer, B. D., Monson, E. B., Garofali, K., & Basu-Zych, A. 2023, "Lightning: An X-ray to Submillimeter Galaxy SED Fitting Code With Physically-Motivated Stellar, Dust, and AGN Models", ApJ, In review

Chapters 3 of this dissertation has appeared in press as:

Doore, K., Eufrasio, R. T., Lehmer, B. D., Monson, E. B., Basu-Zych, A., Garofali, K., & Ptak, A. 2021, "On the Impact of Inclination-dependent Attenuation on Derived Star Formation Histories: Results from Disk Galaxies in the Great Observatories Origins Deep Survey Fields", ApJ, 923, 26

Chapters 4 of this dissertation has appeared in press as:

Doore, K., Eufrasio, R. T., Lehmer, B. D., Monson, E. B., Basu-Zych, A., & Garofali, K. 2022, "The Impact of Inclination-dependent Attenuation on Ultraviolet Star Formation Rate Tracers", ApJ, 931, 53

Chapter 1

Introduction

One of the big questions currently in astrophysics is: how did the galaxies observed throughout the universe form and evolve? To help answer this big question, we first need tools for measuring how individual galaxies formed and evolved. Then, once we apply these tools to several individual galaxies, we can better understand the evolutionary trends of the broader galaxy population. The work in this dissertation presents a physically motivated and novel method for more accurately modeling the evolution and properties of individual disk galaxies by including one of their most overlooked aspects, their inclination[1].

1.1 Emission and Modeled Properties of Galaxies

Until approximately ten years ago with the advent of gravitational wave and neutrino detectors, all observations in astronomy were limited to detecting and measuring electromagnetic radiation. Since we are unable to send probes to take direct measurements of the physical properties of a galaxy, we are forced to make estimations of these properties, such as the mass and star formation rate, using the observed light that a galaxy emits. To estimate these properties, we can compare observations with models that use a set of physical conditions to determine the expected light that the galaxy would generate. Once this model is adjusted to be consistent with the observations, we can infer the physical properties of a galaxy from the model.

To understand how inclination affects the modeled properties of a disk galaxy, a discussion of the basic components of a galaxy that emit the observable light is needed. As a whole, galaxies are

[1] Inclination of a disk galaxy is defined as the angle between the plane of the galactic disk and the plane of the sky.

massive, gravitationally bound objects that can have light emitted by any combination stars, gas, dust, and/or active galactic nuclei (AGNs). In a normal galaxy, which are the focus of this work, these components are limited to stars, gas, and dust, as normal galaxies by definition do not contain an AGN. In terms of these components, stars are the dominant source of light from the ultraviolet (UV) to near-infrared (NIR) wavelengths (i.e., $\approx$0.0912–3 μm) with gas and dust dominating in the infrared (IR) to submillimeter (i.e., $\approx$5–1000 μm).

1.1.1 Stellar Population

Stars in a galaxy are formed when gas in the interstellar medium (ISM) gravitationally collapses to the point where the nuclear fusion of hydrogen into helium begins and the resulting radiation pressure prevents further collapse. At this point, a star begins its life in a state known as the main-sequence (MS), where it will spend most of its lifetime, before progressing on the remainder of its evolutionary track. On the MS, the physical properties of a star are well established by theory and depend primarily on the initial mass and chemical composition[2] of the star (McKee & Ostriker, 2007). In Table 1.1, a list of stellar parameters for MS stars of a variety of masses and solar chemical composition is given using the values presented in Zombeck (1990). From these values, it can be seen that more massive stars are expected to have higher luminosities and temperatures, lower peak emission wavelengths, and shorter lifetimes on the MS compared to less massive stars. This variation in properties with mass influences the total observed light from galaxies when considering the whole stellar population, since stars are born at different points in time with a distribution of masses.

The rates at which populations of stars formed over time in a galaxy is known as the star

[2]The chemical composition of a star is generally referred to as its metallicity, given in terms of Z, which is defined as the mass fraction of all elements heavier hydrogen and helium.

Table 1.1: Summary of the Main-Sequence Stellar Parameters.

Stellar Class	Mass [$M_\odot$]	Luminosity [$L_\odot$]	Temperature [K]	$\lambda_{\rm peak}$[a] [μm]	$\tau_{\rm MS}$[b] [Myr]
O2	100	8×10^5	50000	0.058	0.1
O6	35	1.8×10^5	38000	0.076	1.4
B0	18	2×10^4	30000	0.096	7.3
B5	6.5	800	16400	0.18	92
A0	3.2	80	10800	0.27	550
F0	1.7	6	7240	0.40	2.7×10^3
G2[c]	1	1	5780	0.50	10^4
K5	0.69	0.16	4410	0.65	2.5×10^4
M5	0.15	2.7×10^{-3}	3120	0.92	1.1×10^6
M8	0.08	4×10^{-4}	2650	1.1	5.5×10^6

[a]Peak wavelength of the emission calculated using Wien's displacement law:
$\lambda_{\rm peak} = \frac{2.8978 \times 10^3 \ \mu{\rm m\ K}}{T}$.
[b]The main-sequence lifetime of the star given by the approximate relation:
$\tau_{\rm MS} \approx 10^{10}$ yr $\left(\frac{M}{M_\odot}\right)^{-2.5}$.
[c]Stellar class of the Sun.

formation history (SFH), a key property to understanding the evolution of normal galaxies. To model the SFH of a galaxy, a distribution of initial masses for the formed stellar population needs to be assumed. Typically, these distributions are empirically derived and called an initial mass function (IMF; Salpeter, 1955; Kroupa, 2001; Chabrier, 2003). In Figure 1.1 panel (*a*), we show some common IMFs from the literature. By combining an IMF with the theoretical evolutionary tracks of stars (i.e., isochrones and stellar spectra, examples of which are shown in panels (*b*) and (*c*) of Figure 1.1, respectively) and assuming the stellar population was created instantaneously, a simple stellar population (SSP) model can be generated that gives the emission of a population at any moment in time. Examples of SSPs at different points in time after formation are shown in panel (*e*) of Figure 1.1. Integrating this SSP with a given model SFH (examples of which are shown in panel (*d.1*) of Figure 1.1), a model for the stellar emission can be created, which can then be compared to the observed galactic emission to determine the SFH of the galaxy. An example of

this model stellar emission is shown as the blue line in panel (*g*) of Figure 1.1.

1.1.2 Gas and Dust

The UV-to-NIR emission that we observe from a galaxy does not contain all of the emission that was produced by its stars. Gas and dust distributed in the ISM can attenuate (which is a combination absorption and scattering) a fraction of the intrinsic UV-to-NIR emission produced by the stellar population, thereby preventing this fraction of light from escaping the galaxy. The fraction of attenuated stellar light depends upon inherent properties of the ISM, such as the distribution of dust grain size and shape, its chemical composition, and its distribution throughout the galaxy. Additionally, attenuation is more efficient at shorter wavelengths (strongest in the UV) compared to longer wavelengths (negligible beyond 5 μm), and therefore, it is commonly represented in terms of the wavelength dependent optical depth. Examples of attenuation curves that gives this wavelength dependent optical depth can be seen in panel (*f.1*) of Figure 1.1.

As the attenuated light is absorbed by the ISM, it causes the dust grains in the ISM to heat. To satisfy the first and second laws of thermodynamics (energy conservation and entropy increase), the dust grains must re-emit the absorbed energy. This emission, referred to as dust emission, is radiated as thermal emission at IR and submillimeter wavelengths. Besides the thermal component, emission from molecular transitions of complex molecules can generate wide emission features in the mid-IR (i.e., $\approx$3–10 μm), with some of the most prominent features being generated by polycyclic aromatic hydrocarbons (PAHs). An example of a dust emission model can be seen in panel (*f.2*) of Figure 1.1.

When modeling attenuation and emission by dust in galaxies, the dust grain size, shapes, and chemical composition are commonly assumed to be like that in the Milky Way and other nearby

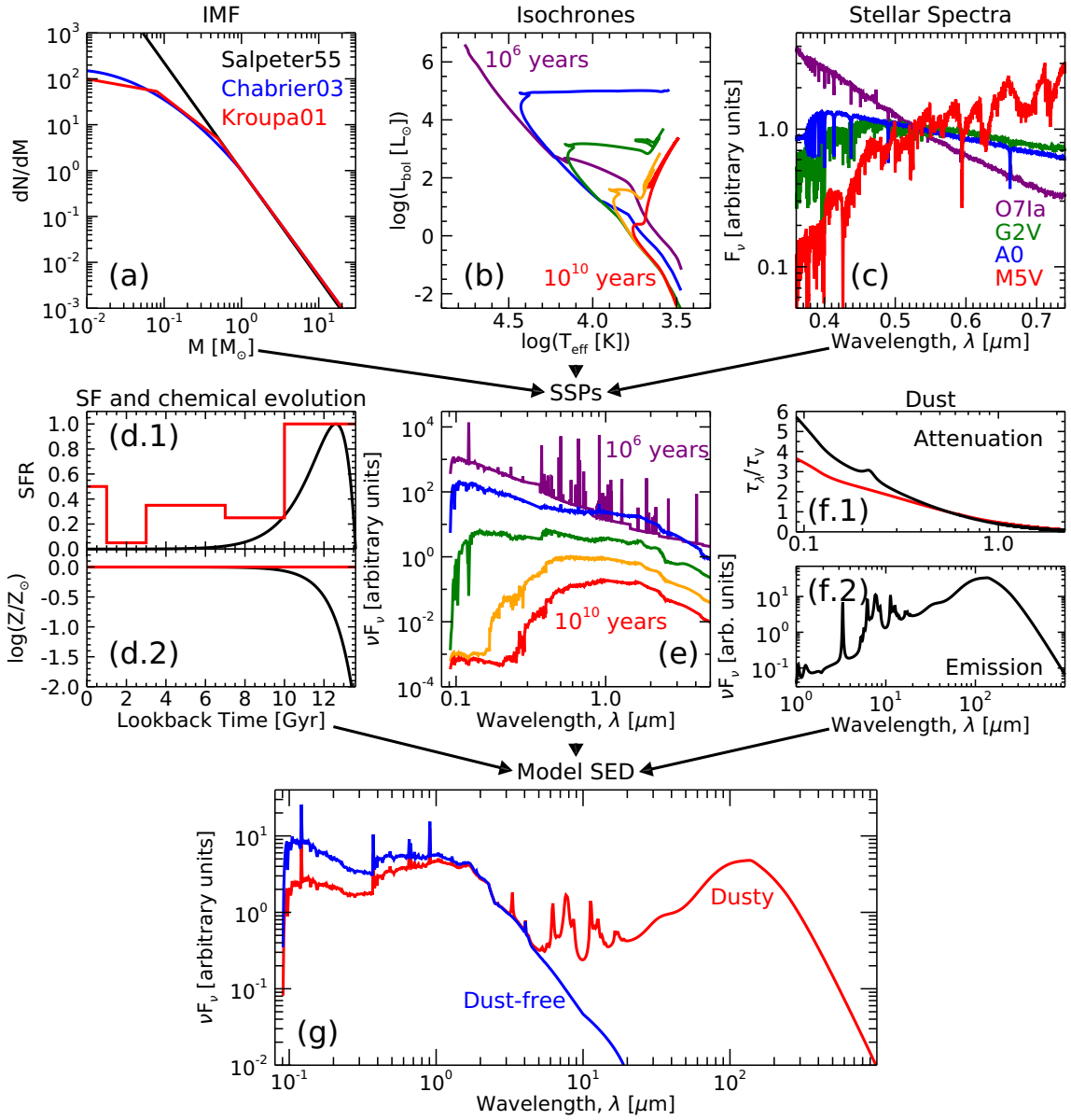

Figure 1.1: Examples of the components of a model spectral energy distribution (SED) and how they combine together to form the full model SED. (*a*) Examples of commonly used IMFs (Salpeter, 1955; Kroupa, 2001; Chabrier, 2003). (*b*) Example isochrones from `MIST` (Dotter, 2016; Choi et al., 2016). (*c*) Example stellar spectra for different stellar types from the `MILES` stellar library (Falcón-Barroso et al., 2011). (*d.1*) Examples of a non-parametric SFH in red and delayed exponential parametric SFH in black. (*d.2*). Examples of metallicity/chemical evolution, with red showing the commonly assumed constant metallicity and black showing a build up to solar metallicity. (*e*) SSPs at different points in time after formation from the `PÈGASE` models (Fioc & Rocca-Volmerange, 1997). (*f.1*) Example Calzetti (2001) dust attenuation curves. (*f.2*) Example Draine & Li (2007) dust emission model. (*g*) A full model SED including contributions from attenuated stellar emission and subsequent dust emission in red. The blue line shows the intrinsic stellar emission if excluding the dust attenuation and emission components in panel (*f*).

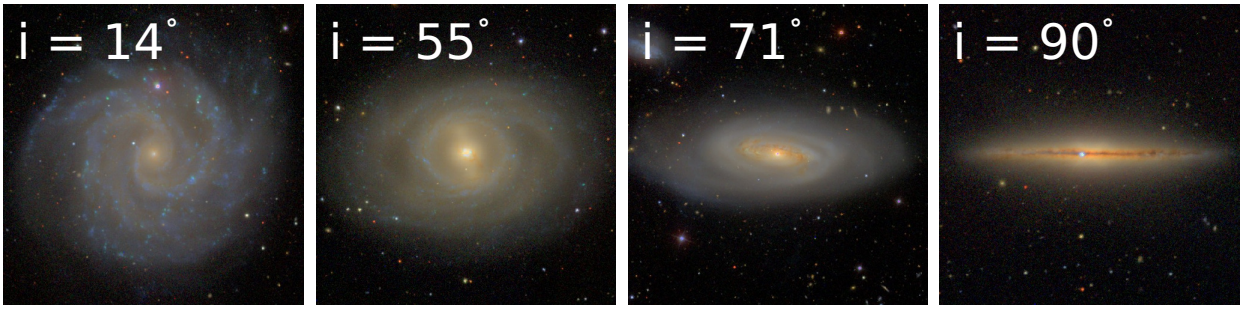

Figure 1.2: Composite SDSS *g*, *r*, *i* postage stamp images of disk galaxies at a variety of inclinations. The galaxies from left to right are NGC 3184, NGC 3351, NGC 4569, and NGC 4013, respectively. An estimated inclination is given for each galaxy in the upper left corner of the respective image. Images have been rotated to align the longest line-of-sight dimension with horizontal. As the inclination increases from face-on ($i \approx 0^\circ$) to edge-on ($i \approx 90^\circ$) for the example galaxies, the column density of dust along the line-of-sight can be seen to increase as well, which results in increased attenuation of the emitted light for the edge-on view compared to the face-on view.

galaxies (Draine & Li, 2007; Galliano et al., 2018). As for the distribution of dust throughout the galaxy, it is expected from basic visual inspections of galaxy images that the dust would be non-uniformly distributed throughout the galaxy, especially in spiral galaxies, which tend to have dust concentrated within the spiral arms. However, during modeling, this non-uniform distribution results in complex model requirements. Therefore, the spatial distribution of dust is generally simplified and assumed to be a uniform, spherical distribution, such that the line-of-sight optical depth is constant for any viewing angle (e.g., Calzetti, 2001; Noll et al., 2009).

While this can be a reasonable assumption for elliptical galaxies, which tend to be more spherical in shape, it is a vast over simplification for spiral galaxies, which contain a substantial fraction of their baryonic mass in a disk (van der Kruit & Freeman, 2011). Since both the stars and dust are contained within the galactic disk, assuming a simple uniform, spherical distribution of dust will lead to incorrect modeling of attenuation and dust emission of disk galaxies at different inclinations due to the line-of-sight variation in optical depth with inclination (e.g., Giovanelli et al., 1994; Driver et al., 2007; Wild et al., 2011; Salim et al., 2018). In Figure 1.2, we show some

examples of disk galaxies at different inclinations to the line of sight to help visualize how inclination would affect attenuation. To clarify the cause of this attenuation bias, if a disk galaxy, whose stars and dust are uniformly distributed in a thin disk[3], could be viewed from multiple inclinations, the column density of UV obscuring dust between the observer and emitting stellar populations would increase with increasing inclination. This would result in an increased optical depth and subsequently lower observed emission for the edge-on view (i.e., $i = 90°$) compared to face-on view (i.e., $i = 0°$). Therefore, by assuming a uniform, spherical distribution of dust rather than a disk-like distribution, the inferred physical properties of a disk galaxy would vary based on the inclination at which it was observed. To properly account for this viewing angle dependence, and derive more accurate SFHs and other galactic properties from modeling, an inclination-dependent attenuation model needs to be applied when modeling disk galaxies.

1.2 Spectral Energy Distribution Modeling

To compare and fit stellar emission, dust attenuation, and dust emission models simultaneously to observational data of a galaxy, a method known as spectral energy distribution (SED; i.e., the distribution of light as a function of wavelength) fitting is utilized (see Conroy 2013 for a review). By fitting these models to the observed SED of a galaxy[4] using a statistical inferencing method (e.g., maximim likelihood estimation or Bayesian sampling), an estimate of the galactic properties, such as the SFH, total stellar mass, and recent star formation rate (SFR), can be made. These properties can then be used to better understand and answer how galaxies have formed and evolved over cosmic time.

[3] A thin disk is one where $h \ll r$, with h and r being the height and radius of the disk, respectively.

[4] The observed SED of a galaxy can consist of a compilation of photometric and/or spectroscopic observations at different wavelengths.

However, to get accurate estimates of these properties, appropriate models must be used. As stated above, the inclination of a disk galaxy can play a significant role in the attenuation of stellar light, and any inclination dependence of the attenuation is commonly ignored in SED fitting. Most works utilize the inclination-independent attenuation model of Calzetti (2001) or its modified version by Noll et al. (2009). While the modified attenuation model by Noll et al. (2009) provides extra flexibility when fitting SEDs, it lacks a direct physically motivated link to disk inclination. Therefore, the work in this dissertation strives to address this by implementing the physically-motivated, inclination-dependent attenuation curves from Tuffs et al. (2004) as updated by Popescu et al. (2011) to evaluate the effects of incorporating inclination dependence in SED fitting and the resulting inferred galactic properties.

1.3 Outline of this Dissertation

Chapters 2–4 of this dissertation consist of a compilation of articles published in or submitted for publication in The Astrophysical Journal. The first of these articles (Chapter 2) introduces our SED fitting code, `Lightning`, which implements the physically-motivated, inclination-dependent attenuation curves discussed above. The next two articles (Chapters 3 and 4) apply `Lightning` and the inclination-dependent attenuation curves to address the problem of how inclination-dependent attenuation affects the derived physical properties of disk galaxies using a base and expanded galactic sample.

In Chapter 2, we present the details of our SED fitting code, `Lightning`. While this chapter contains our most recently submitted article, it is presented first, since understanding the details of how `Lightning` derives the stellar properties of galaxies will help guide its implementation

in the following chapters. When detailing `Lightning`, we discuss all of the models it contains, which can include contributions from stellar populations, dust attenuation and emission, and AGN. Additionally, we describe the currently available algorithms that can be used to fit the models to observations. Then, we present several example applications using a variety of observational data to show the future potential of `Lightning` beyond this dissertation.

In Chapter 3, we apply `Lightning` and the inclination-dependent attenuation curves on our base sample of galaxies to study the impact of inclination-dependent attenuation on derived stellar properties. To understand this impact, we compare our inclination-dependent attenuation results with results using a traditional inclination-independent attenuation curve. Our comparison indicates stark statistical differences in the derived optical attenuation and stellar masses, with the fits using the traditional attenuation curve resulting in these properties being underestimated compared to the inclination-dependent results at high inclinations ($i \gtrsim 80°$).

Since SED fitting is not always possible when observational data is limited, we examine and quantify how commonly used recent SFR estimators (which only require 1–2 photometric observations) depend on inclination in Chapter 4 using our expanded galaxy sample. To perform this analysis, we fit the expanded sample with `Lightning` using the inclination-dependent attenuation curves to derive inclination-dependent SFRs. We then calibrate two commonly used SFR estimators (the hybrid UV+IR and A_{FUV}-β relations) with these derived SFRs and find that the estimators present clear dependencies on inclination. To quantify these dependencies, we expand the parametric form of the estimators to include an inclination-dependence.

Finally, in Chapter 5, we summarize the results from Chapters 2, 3, and 4 and explain how they provide the crucial steps towards understanding and incorporating the impact of inclination-dependence on the derived star-formation histories of disk galaxies.

References

Calzetti, D. 2001, PASP, 113, 1449

Chabrier, G. 2003, PASP, 115, 763

Choi, J., Dotter, A., Conroy, C., et al. 2016, ApJ, 823, 102

Conroy, C. 2013, ARA&A, 51, 393

Dotter, A. 2016, ApJS, 222, 8

Draine, B. T., & Li, A. 2007, ApJ, 657, 810

Driver, S. P., Popescu, C. C., Tuffs, R. J., et al. 2007, MNRAS, 379, 1022

Falcón-Barroso, J., Sánchez-Blázquez, P., Vazdekis, A., et al. 2011, A&A, 532, A95

Fioc, M., & Rocca-Volmerange, B. 1997, A&A, 326, 950

Galliano, F., Galametz, M., & Jones, A. P. 2018, ARA&A, 56, 673

Giovanelli, R., Haynes, M. P., Salzer, J. J., et al. 1994, AJ, 107, 2036

Kroupa, P. 2001, MNRAS, 322, 231

McKee, C. F., & Ostriker, E. C. 2007, ARA&A, 45, 565

Noll, S., Burgarella, D., Giovannoli, E., et al. 2009, A&A, 507, 1793

Popescu, C. C., Tuffs, R. J., Dopita, M. A., et al. 2011, A&A, 527, A109

Salim, S., Boquien, M., & Lee, J. C. 2018, ApJ, 859, 11

Salpeter, E. E. 1955, ApJ, 121, 161

Tuffs, R. J., Popescu, C. C., Völk, H. J., Kylafis, N. D., & Dopita, M. A. 2004, A&A, 419, 821

van der Kruit, P. C., & Freeman, K. C. 2011, ARA&A, 49, 301

Wild, V., Charlot, S., Brinchmann, J., et al. 2011, MNRAS, 417, 1760

Zombeck, M. V. 1990, Handbook of space astronomy and astrophysics

Chapter 2

Lightning: An X-ray to Submillimeter Galaxy SED Fitting Code With Physically-Motivated Stellar, Dust, and AGN Models

Keith Doore, Erik B. Monson, Rafael T. Eufrasio, Bret D. Lehmer, Kristen Garofali, and Antara Basu-Zych

The following chapter was has been submitted to be published in The Astrophysical Journal Supplemental Series with the same title.

Abstract

We present an updated version of `Lightning`, a galaxy spectral energy distribution (SED) fitting code that can model X-ray to submillimeter observations. The models in `Lightning` include the options to contain contributions from stellar populations, dust attenuation and emission, and active galactic nuclei (AGN). X-ray emission, when utilized, can be modeled as originating from stellar compact binary populations with the option to include emission from AGN. We have also included a variety of algorithms to fit the models to observations and sample parameter posteriors; these include an adaptive Markov-Chain Monte-Carlo (MCMC), affine-invariant MCMC, and Levenberg-Marquardt gradient decent (`MPFIT`) algorithms. To demonstrate some of the capabilities of `Lightning`, we present several examples using a variety of observational data. These examples include (1) deriving the spatially resolved stellar properties of the nearby galaxy M81, (2) demonstrating how X-ray emission can better constrain the degeneracies of AGN parameters in a distant AGN, (3) exploring how to rectify the attenuation effects of inclination on the derived the star formation rate of the edge-on galaxy NGC 4631, and (4) comparing the performance of

Lightning to similar SED fitting codes when the deriving physical properties of the star-forming galaxy NGC 628. In performing these tasks, Lightning is estimated to be approximately an order of magnitude faster computationally than other similar SED fitting codes. Lightning is an open-source application developed in the Interactive Data Language (IDL) and is available at https://github.com/rafaeleufrasio/lightning.

2.1 Introduction

The light emitted from a galaxy contains a plethora of information about many physical properties of the system, ranging from its star-formation history (SFH) and dust content to the presence of an active galactic nucleus (AGN) and the properties of its supermassive black hole (SMBH). These properties are key to our current understanding of how galaxies and SMBHs formed and evolved, and, thus, the methods for deriving them from spectral energy distributions (SEDs) have been the focus of substantial work (e.g., Silva et al., 1998; Devriendt et al., 1999; Dale et al., 2005; Groves et al., 2008; Noll et al., 2009; Ciesla et al., 2015; Iyer & Gawiser, 2017; Leja et al., 2018; Shanks et al., 2021). The overarching process of deriving the physical properties from an SED is known as SED fitting (see Walcher et al. 2011 and Conroy 2013 for recent reviews). At its core, this process consists of fitting a model (e.g, stellar population synthesis with dust attenuation) to the observed SED. Once a best-fit model is determined using the chosen statistical inferencing method, it can be used to infer the physical properties of the observations.

Numerous SED fitting codes currently exist today for the modeling and inferencing of galaxy properties from their SEDs. Some of the more widely cited codes include CIGALE (Burgarella et al., 2005; Boquien et al., 2019), Prospector (Johnson et al., 2021), MAGPHYS (da Cunha et al.,

2008), BAGPIPES (Carnall et al., 2018), and FAST (Kriek et al., 2009); also see Pacifici et al. (2022) for a more comprehensive list. Each code was designed to help solve unanswered problems unique to their developers. Therefore, each code is unique and comes with its own set of advantages and disadvantages.

Initially, SED fitting codes were developed to use maximum-likelihood statistical inferencing methods (e.g., linear and non-linear optimization) to estimate galactic properties from optical to infrared (IR) observations (e.g., SEDfit, Sawicki & Yee 1998; Sawicki 2012; STARLIGHT, Cid Fernandes et al. 2005; VESPA, Tojeiro et al. 2007). These codes typically model the observations using simple stellar population (SSP) models (e.g., Fioc & Rocca-Volmerange, 1997; Bruzual & Charlot, 2003; Conroy et al., 2009; Eldridge et al., 2017) with simple parametric SFHs (e.g., exponentially declining) and attenuation. The advantage of these codes is that they are fast, simple to use, and return reliable best-fit models. However, the major drawback is that they can have difficulties computing accurate uncertainties on the physical parameters, since these parameters can be highly correlated and usually have non-Gaussian likelihoods. This difficulty is compounded as additional model components are included to account for more complex physical processes within galaxies: for example, non-parametric SFHs (see Carnall et al. 2019 and Leja et al. 2019 for overviews on the differences between parametric and non-parametric SFHs), dust emission (e.g., Draine & Li, 2007; da Cunha et al., 2008; Casey, 2012; Dale et al., 2014), dusty torus emission from an AGN (e.g., Fritz et al., 2006; Nenkova et al., 2008; Stalevski et al., 2012,0), and nebular emission (e.g., Ferland et al., 1998, 2013).

To estimate more accurate uncertainties, the next generation of SED fitting codes were developed to use a gridded Bayesian statistical inferencing method (e.g., CIGALE, Burgarella et al. 2005; Boquien et al. 2019; FAST, Kriek et al. 2009; MAGPHYS, da Cunha et al. 2008). This method

estimates galactic properties and their uncertainties by gridding parameter space, fitting the corresponding gridded models to the observations, and then weighting the models by their goodness-of-fit. The advantage of this method is that it can account for parameter degeneracies and non-Gaussian likelihoods, while still being computationally fast. However, this computational speed excludes the time to create the grid of models, which increases exponentially with the number of parameters. Therefore, sampling of the full posterior distribution becomes intractable in a reasonable amount of time for complex models with many parameters unless parameter space is sparsely sampled.

In order to better sample the parameter space of complex models, new SED fitting codes were developed to use Bayesian sampling statistical inferencing methods which utilize Markov Chain Monte Carlo (MCMC) and/or nested sampling algorithms (Skilling, 2004). This approach (e.g., `BAGPIPES`, Carnall et al. 2018; `BayeSED`, Han & Han 2012,0,0; `BEAGLE`, Chevallard & Charlot 2016; `Prospector`, Johnson et al. 2021) has the advantage of efficiently sampling parameter space of complex models to generate posterior distributions of parameters, while taking into account any prior information on the parameters. Additionally, models can be changed without any computational cost unlike the gridded Bayesian methods, which require the entire grid of models to be recomputed. However, the disadvantage of the Bayesian sampling approach is that sampling the posterior distribution can take significantly longer computational times on a per SED basis.

Some next generation SED fitting codes are trying to bridge the gap between parameter estimation and computational speed using machine learning. For these codes (e.g., Lovell et al. 2019; `mirkwood`, Gilda et al. 2021), machine learning models are trained to learn the relationship between input observations and inferred properties using synthetic galaxy SEDs generated by cosmological simulations. The major advantage of these codes is that, once trained, fitting a new

input SED is incredibly fast and derived parameters can be more accurate than the fully Bayesian approach (Gilda et al., 2021). However, in their current state of development, machine learning SED fitting codes come with a few serious drawbacks. The first is that they have an over-reliance on theoretical models to explain how real galaxies should appear. Since they typically utilize a variety of cosmological simulations, it can be difficult to create a complete training set that is truly representative of all observed galaxies (Genel et al., 2014; Schaye et al., 2015; Somerville & Davé, 2015). Additionally, over-training (which can lead to over-fitting) can occur when an appropriate test set or cross-validation set is not utilized. This can lead to galaxy property estimates that have high precision, which is a direct result of over-fitting rather than a correct uncertainty estimate. Finally, these codes cannot handle missing observations that are commonly present in typical SEDs without retraining. This comes at a significant computational cost if the sample that is to be fit has a variety of observations.

Motivated to have a computationally fast yet fully Bayesian code, we developed the SED fitting code `Lightning`. Originally developed to derive the SFHs needed to empirically calibrate the X-ray luminosity function (XLF) of X-ray binary (XRB) populations (Eufrasio et al., 2017; Lehmer et al., 2017,0,0; Gilbertson et al., 2022), `Lightning` has since been utilized to check for enhanced star formation and AGN activity in protoclusters (Monson et al., 2021), model local analogs to high-redshift galaxies (Motiño Flores et al., 2021), investigate the inclination-dependence of derived SFHs (Doore et al., 2021,0), and provide evidence in favor of density wave theory (Abdeen et al., 2022). Written in the Interactive Data Language (IDL), the newest updates to `Lightning` now allow for modeling of photometric SEDs from the X-rays to submillimeter using efficient MCMC algorithms to fit physical models that account for any combination of stellar, dust, and AGN emission. In Section 2.2, we describe these physical models and their dependencies. The

Table 2.1: References for previously published articles describing the implementation of individual `Lightning` features.

Feature	Reference
Models	
Simple Stellar Populations	Eufrasio et al. (2017)
Non-parametric SFH	Eufrasio et al. (2017)
Stellar X-ray Emission	Monson et al. (2023, submitted)
UV-to-IR AGN Emission	Monson et al. (2023, submitted)
X-ray AGN Emission	Monson et al. (2023, submitted)
Calzetti et al. (2000) Attenuation	Eufrasio et al. (2017)
Inclination-dependent Attenuation	Doore et al. (2021)
X-ray Absorption	Monson et al. (2023, submitted)
Draine & Li (2007) Dust Emission	Doore et al. (2021)
Fitting Algorithms	
Gradient Descent (`MPFIT`)	This work
Adaptive MCMC	Doore et al. (2021)
Affine-Invariant MCMC	Monson et al. (2023, submitted)

statistical inferencing methods that fit these models to input SEDs are described in Section 2.3. In Section 2.4, we demonstrate the capability of `Lightning` by applying it to a variety of examples. Finally, we summarize and discuss future planned additions for `Lightning` in Section 2.5.

`Lightning` is an open-source, well-documented, and publicly available SED fitting code available at https://github.com/rafaeleufrasio/lightning. Since `Lightning` has been in development over the past several years, we include the references to past works that first described each feature (i.e., models and statistical inferencing methods) and the motivation for their implementation in Table 2.1. In Sections 2.2 and 2.3, we reiterate the details from these past works and clarify all assumptions for replicability.

2.2 Physical Models

In this section, we describe the variety of physical models available in `Lightning` to account for any combination of stellar, dust, and AGN emission. To help clarify the free parameters corresponding to each model, we give a description of the parameters, their units, and their allowed

Table 2.2: Summary of possible free parameters for each model SED component in `Lightning`.

Physical Model Component	Parameter	Units[a]	Allowed Range	Description
Stellar Emis.	ψ_j	$M_\odot$ yr^{-1}	$[0,\infty)$	Star formation history coefficients
Calzetti et al. (2000) Atten.	$\tau_{\mathrm{DIFF},V}$	$\cdots$	$[0,\infty)$	V-band optical depth of diffuse dust
	δ	$\cdots$	$(-\infty,\infty)$	Power-law slope deviation
	$\tau_{\mathrm{BC},V}$	$\cdots$	$[0,\infty)$	V-band optical depth of the birth cloud
SKIRTOR UV-to-IR AGN Emis.[b]	$\log_{10} L_{\mathrm{AGN}}$[c]	$\log_{10} L_\odot$	$[0,20]$	UV-to-IR integrated AGN luminosity
	$\tau_{9.7}$	$\cdots$	$[3,11]$	Edge-on optical depth of the AGN torus at 9.7 μm
	$\cos i_{\mathrm{AGN}}$	$\cdots$	$[0,1]$	Cosine of the line-of-sight AGN torus inclination
`qsosed` X-ray AGN Emis.	M_{SMBH}	$M_\odot$	$[10^5, 10^{10}]$	SMBH mass
	$\log_{10} \dot{m}$	$\cdots$	$[-1.5, 0.3]$	SMBH accretion rate, Eddington rate normalized
Inclination-dependent Atten.[b]	$\cos i$	$\cdots$	$[0,1]$	Cosine of the line-of-sight galaxy inclination
	τ_B^f	$\cdots$	$[0,8]$	Central B-band face-on optical depth
	B/D	$\cdots$	$[0,\infty)$	Bulge-to-disk ratio
	F	$\cdots$	$[0, 0.61]$	Clumpiness factor
X-ray Absorption	N_{H}	10^{20} cm^{-2}	$[10^{-4}, 10^5]$	HI column density along the line of sight
Draine & Li (2007) Dust Emis.	α	$\cdots$	$[-10, 4]$	Power law slope of the intensity distribution
	U_{min}	$\cdots$	$[0.1, 25]$	Minimum radiation field intensity
	U_{max}	$\cdots$	$[10^3, 3\times10^5]$	Maximum radiation field intensity
	γ	$\cdots$	$[0,1]$	Dust mass fraction illuminated from U_{min} to U_{max}
	q_{PAH}	$\cdots$	$[0.0047, 0.0458]$	Mass fraction of PAHs in dust mixture
	L_{TIR}[d]	$L_\odot$	$[0,\infty)$	Total integrated IR luminosity

[a]Parameters without units are unitless.
[b]The inclination-dependent attenuation and SKIRTOR AGN models are currently not compatible.
[c]L_{AGN} is only a free parameter if fitting without the `qsosed` X-ray AGN model.
[d]L_{TIR} is only a free parameter if fitting without energy balance.

range in Table 2.2.

2.2.1 Stellar Emission Models

2.2.1.1 Simple Stellar Populations

The intrinsic UV-to-IR stellar emission in `Lightning` is generated using the SSPs from the population synthesis code `PÉGASE` (Fioc & Rocca-Volmerange, 1997). The SSPs, which are generated assuming the Kroupa (2001) initial mass function (IMF), are instantaneous bursts of star formation normalized to a unit star formation rate (SFR) of 1 $M_\odot$ yr^{-1}. We allow for a wide range of metallicity options when generating the stellar populations (0.001, 0.004, 0.008, 0.01, 0.02, 0.05, and 0.1 in terms of Z) along with the option to include the nebular extinction and emission from `PÉGASE` (see Section 2.4 of Fioc & Rocca-Volmerange 1997). While the nebular extinction

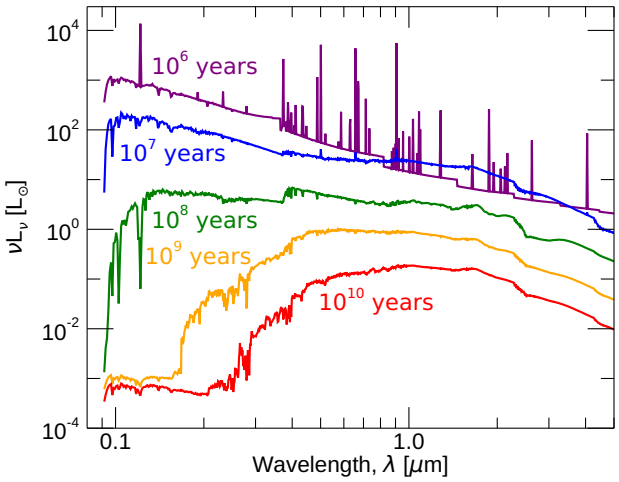

Figure 2.1: The PÉGASE SSP SEDs used in Lightning at various ages after ZAMS for a metallicity of $Z = 0.02$ and initial mass of 1 $M_\odot$. For an age of 1 Myr, nebular emission lines can be clearly seen, while the older displayed ages do not have any lines due to our simplifying assumption. Additionally, as the population ages, the overall bolometric luminosity decreases, and the peak wavelength of the emission shifts from the UV into the NIR.

affects SEDs of all ages, nebular emission is only added to stellar populations with ages < 50 Myr. We make this simplifying assumption since there is minimal ionizing flux, which causes the nebular emission, for populations with ages > 50 Myr (Smith et al., 2002; Byler et al., 2017). In Figure 2.1, we show some example SSPs used in Lightning at different ages for a metallicity of $Z = 0.02$ (i.e., solar metallicity).

2.2.1.2 Star Formation History

To model complex SFHs while remaining computationally fast, Lightning assumes a simple non-parametric SFH. Continuing with the original description in Eufrasio et al. (2017), we define this to be a piece-wise constant SFH, where the free parameters for the SFH are the SFRs (ψ_j) within the user-defined age bins. This is given in analytical form as a function of stellar age t by

$$\psi(t) = \psi_j \qquad \text{for} \qquad t_j < t < t_{j+1}, \tag{2.1}$$

where t_j and t_{j+1} are the respective lower and upper age bin boundaries of the jth bin. The advantage of normalizing by SFR, versus stellar mass like other SED fitting codes, is that any bias toward rising SFHs is prevented, while still allowing for bursty SFHs (Leja et al., 2019).

To compute the intrinsic, rest-frame composite stellar spectrum for the jth age bin, $\tilde{L}^{\star}_{\nu,j}(\nu)$[1], the SSPs are integrated over the age bin after interpolating the SSP evolution to a common time grid using a user-defined time step (e.g., 0.5 Myr). The total composite stellar spectrum for all ages, $\tilde{L}^{\star}_{\nu}(\nu)$, is then given by

$$\tilde{L}^{\star}_{\nu}(\nu) = \sum_{j=1}^{n} \psi_j \tilde{L}^{\star}_{\nu,j}(\nu), \tag{2.2}$$

where $\tilde{L}^{\star}_{\nu,j}(\nu)$ is by construction normalized per unit SFR, specifically 1 $M_{\odot}$ yr^{-1}.

In Figure 2.2, we show composite stellar spectra for a metallicity of $Z = 0.02$ using the default set of age bins in `Lightning` (0–10 Myr, 10–100 Myr, 0.1–1 Gyr, 1–5 Gyr, 5–13.6 Gyr). These age bins were chosen such that the youngest age bin encapsulates the stellar population able to emit the majority of the ionizing flux, while the second bin includes the stellar population which generates the remaining bulk of the UV emission. Finally, the last three age bins were selected to have similar bolometric luminosities as the second bin in the case of a constant SFH.

2.2.1.3 X-ray Binary Model

We include stellar X-ray emission from compact object binaries in `Lightning` with a power-law spectral model given by

$$\tilde{L}_{\nu} \propto \exp\left(h\nu/E_{\rm cut}\right)(h\nu)^{1-\Gamma}, \tag{2.3}$$

[1]When symbolizing intrinsic emission (i.e., no attenuation), we include a tilde over the variable to clarify that it is intrinsic. Emission variables without a tilde signify attenuation/absorption has been applied.

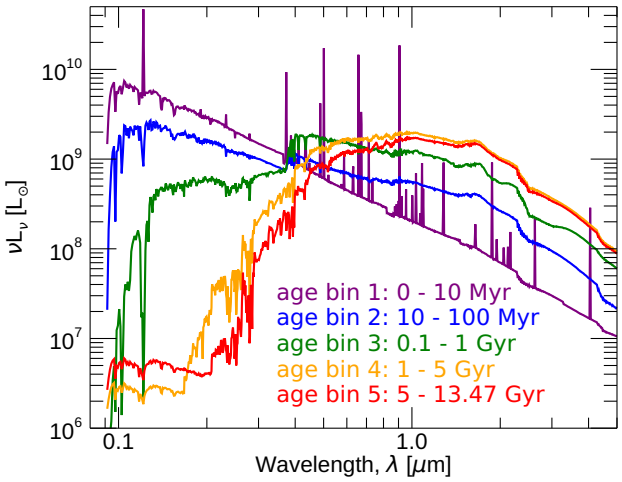

Figure 2.2: Example composite stellar spectrum for a metallicity of $Z = 0.02$ using the default set of age bins in `Lightning`. Similarly to the SSPs in Figure 2.1, the nebular emission lines can be clearly seen in the youngest bin, while the older bins lack any obvious emission features.

where we assume a photon index of $\Gamma = 1.8$ and cutoff energy of $E_{\rm cut} = 100$ keV. We set the normalization of the power-law by its rest-frame 2–10 keV luminosity $\tilde{L}_{\rm X}$, which we model to include contributions from both high-mass XRB (HMXB) emission and low-mass XRB (LMXB) emission:

$$\tilde{L}_{\rm X} = \tilde{L}_{\rm X}^{\rm HMXB} + \tilde{L}_{\rm X}^{\rm LMXB}. \tag{2.4}$$

Our models of $\tilde{L}_{\rm X}^{\rm HMXB}$ and $\tilde{L}_{\rm X}^{\rm LMXB}$ are calculated using the empirical parameterizations with stellar age from Gilbertson et al. (2022):

$$\frac{\tilde{L}_{\rm X}^{\rm HMXB}}{M_\star}(t) = -0.24(\log_{10}(t) - 5.23)^2 + 32.54, \tag{2.5}$$

and

$$\frac{\tilde{L}_{\rm X}^{\rm LMXB}}{M_\star}(t) = -1.21(\log_{10}(t) - 9.32)^2 + 29.09, \tag{2.6}$$

where $\tilde{L}_{\rm X}/M_\star$ has units of erg s^{-1} $M_\odot^{-1}$ and t is the stellar age in yr. While studies have shown that the luminosity of HMXBs depends on metallicity (e.g., Lehmer et al., 2021), we do not currently

implement any metallicity dependence in our X-ray binary model. The age-dependent relationship from Gilbertson et al. (2022) was derived for galaxies with metallicities ranging from 0.40–1.16 $Z_{\odot}$. For larger metallicities, $\tilde{L}_X/M_\star$ may thus be slightly overestimated for $t \lesssim 100$ Myr, while for lower metallicites it may be similarly underestimated.

To calculate the scaling parameter $\tilde{L}_{\rm X}$, we first derive the HMXB and LMXB contribution from each age bin utilizing Equations 2.5 and 2.6. We calculate the stellar mass of each bin ($M_{\star,j}$) as

$$M_{\star,j} = \psi_j M_{\star,j}^{\rm coeff}, \tag{2.7}$$

where $M_{\star,j}^{\rm coeff}$ is the coefficient that converts SFR into stellar mass. We then calculate $\tilde{L}_{\rm X}/M_\star$ at the mean stellar age of each SFH bin, multiply by the stellar mass in the bin, and sum the contributions from each bin to derive the total contributions from the HMXBs and LMXBs, which are then incorporated into Equation 2.4 to determine $\tilde{L}_{\rm X}$ and finally the X-ray luminosity spectrum.

2.2.2 AGN Emission Models

2.2.2.1 AGN UV-to-IR Models

`Lightning` uses the SKIRTOR library of UV-to-IR AGN SED templates (Stalevski et al., 2012,0), which consist of a broken power law accretion disk component and a clumpy two-phase dusty torus that reprocesses light from the accretion disk into the NIR. Our implementation uses

the default accretion disk power law from the SKIRTOR library, where

$$\lambda \tilde{L}_\lambda \propto \begin{cases} \lambda^{1.2} & 0.001\ \mu\text{m} \leq \lambda \leq 0.01\ \mu\text{m} \\ \lambda^{0} & 0.01\ \mu\text{m} < \lambda \leq 0.1\ \mu\text{m} \\ \lambda^{-0.5} & 0.1\ \mu\text{m} < \lambda \leq 5\ \mu\text{m} \\ \lambda^{-3} & 5\ \mu\text{m} < \lambda \leq 50\mu\text{m} \end{cases} . \tag{2.8}$$

The full SKIRTOR templates have 6 free parameters: $\tau_{9.7}$, the edge-on optical depth of the torus at 9.7 μm; p, the power law index for the radial dust density gradient; q, the power law index for the polar dust density gradient; Δ, the opening angle of the dusty cone of the torus; R, the ratio of the torus' inner and outer radii; and i_{AGN}, the inclination angle from the pole to the line of sight. To simplify the SKIRTOR models and allow us to sample the parameter space and interpolate between models, our implementation in `Lightning` only allows for $\tau_{9.7}$ and $\cos i_{\text{AGN}}$ to be free parameters. We fix $p = 1$ and $q = 0$ (i.e., there is no polar dependence of the dust density) as in Stalevski et al. (2016), and fix $\Delta = 40^\circ$ based on their findings of typical covering factors in the range of $0.6 - 0.7$. At the moderate covering factor of $\sin 40^\circ \approx 0.64$ that we assume, R has only a small impact on the luminosity of the torus, so we fix $R = 20$. To implement these simplified models, we linearly interpolate the original gridded models both in $\tau_{9.7}$ and $\cos i_{\text{AGN}}$-space for the desired free parameter value. Then if no X-ray AGN model is used, the UV-to-IR AGN model is scaled using its anisotropic integrated luminosity, L_{AGN}, as another free parameter. Examples of these UV-to-IR AGN emission models for different inclinations are shown in Figure 2.3.

We note that the UV-optical light that escapes the torus is subject to being attenuated by the host galaxy dust (see Section 2.2.3). When energy balance is enabled (as discussed in Section 2.2.4),

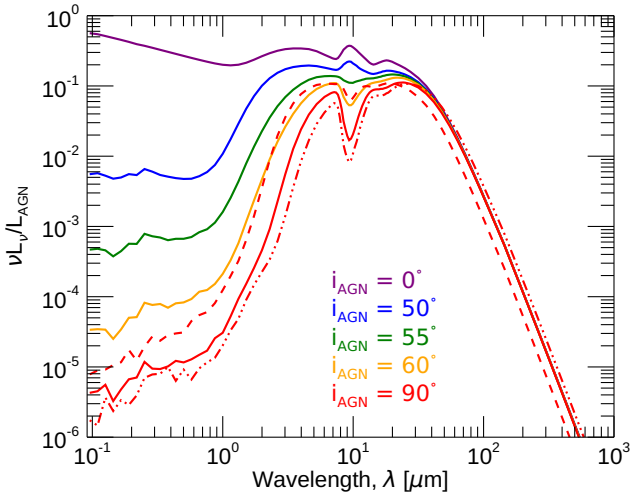

Figure 2.3: Examples of the SKIRTOR AGN emission model generated by `Lightning` for a range of inclinations with $\tau_{9.7} = 7$, normalized by $L_{\rm AGN}$. The dashed and dashed-dotted lines for the $i_{\rm AGN} = 90^\circ$ example are models where $\tau_{9.7} = 3$ and $\tau_{9.7} = 11$, respectively. We only show the variation in $\tau_{9.7}$ for the edge-on example, since $\tau_{9.7}$ is the edge-on optical depth of the torus. Therefore, changing its value for face-on to moderately inclined viewing angles minimally effects the model.

we integrate this attenuated light over all lines of sight[2] and add it to the bolometric luminosity of the attenuated stellar light used to scale the dust model. However, fully energetic self-consistency is not maintained by the AGN model. The ISM is assumed to be opaque to the ionizing Lyman-continuum radiation from the AGN, and the ionizing flux from the AGN does not currently contribute to the nebular emission component, which is built into our `PÉGASE` models.

2.2.2.2 AGN X-ray Models

X-ray observations can place powerful constraints on the bolometric luminosity of AGN, and as such they are very useful in AGN SED modeling. In `Lightning`, we provide two different models to generate the X-ray emission from the AGN component.

[2]For simplicity, `Lightning` currently does not support the simultaneous usage of the SKIRTOR UV-to-IR AGN model and the inclination-dependent attenuation model, due to the fact that the lines of sight of the two models are not required to align (i.e., $\cos i \neq \cos i_{\rm AGN}$), which complicates the energy balance calculation.

Since X-ray spectra of AGN are often empirically described by power-law models, we provide this as the first option in `Lightning`. The equation for the power-law is given in Equation 2.3, where we use a fixed photon index of $\Gamma = 1.8$ and cutoff energy of $E_{\rm cut} = 300$ keV. To connect the X-ray model to the UV-optical AGN component, we use the Lusso & Risaliti (2017) $\tilde{L}_{2\ \rm keV} - \tilde{L}_{2500}$ relationship, which is an empirically calibrated relationship between the intrinsic monochromatic luminosities of luminous AGN at 2 keV and 2500 Å. Therefore, the power-law X-ray and UV-to-IR AGN models are both scaled using $L_{\rm AGN}$ as a free parameter.

Alternatively, we provide an implementation of the physically-motivated `qsosed` X-ray AGN models from Kubota & Done (2018). These models include an accretion disk component and two Comptonizing regions, which produce the X-ray spectrum. Since these models include optical emission from the accretion disk, the relationship between $\tilde{L}_{2500}$ and $\tilde{L}_{2\ \rm keV}$ is encoded in two model parameters: $M_{\rm SMBH}$, the SMBH mass, and $\dot{m}$, the Eddington ratio of the AGN. Kubota & Done (2018) show that their models reproduce the Lusso & Risaliti (2017) relationship, explaining the scatter around the relationship due to variance of $M_{\rm SMBH}$ and $\dot{m}$ among AGN. Thus, when this model is used, we normalize the UV-to-IR AGN model (see Section 2.2.2.1) to the same $\tilde{L}_{2500}$ as the X-ray model and allow the free parameters of $M_{\rm SMBH}$ and $\dot{m}$ to set the normalization of the entire X-ray-to-IR AGN model, thereby replacing $L_{\rm AGN}$ as a free parameter. We note that this model is most appropriate for luminous, high-accretion rate systems ($\log_{10}\dot{m}$ ranges from -1.5 to 0.3) and is not appropriate for low-luminosity AGN and Compton-thick AGN, the latter of which require more careful and complicated X-ray modeling with reflection components.

We show some examples of the connected `qsosed` and SKIRTOR UV-to-IR AGN models in Figure 2.4. While the `qsosed` model extends to optical wavelengths and is used to normalize the UV-to-IR SKIRTOR model, we limit it to $\lambda < 2$ nm rather than directly joining the two models

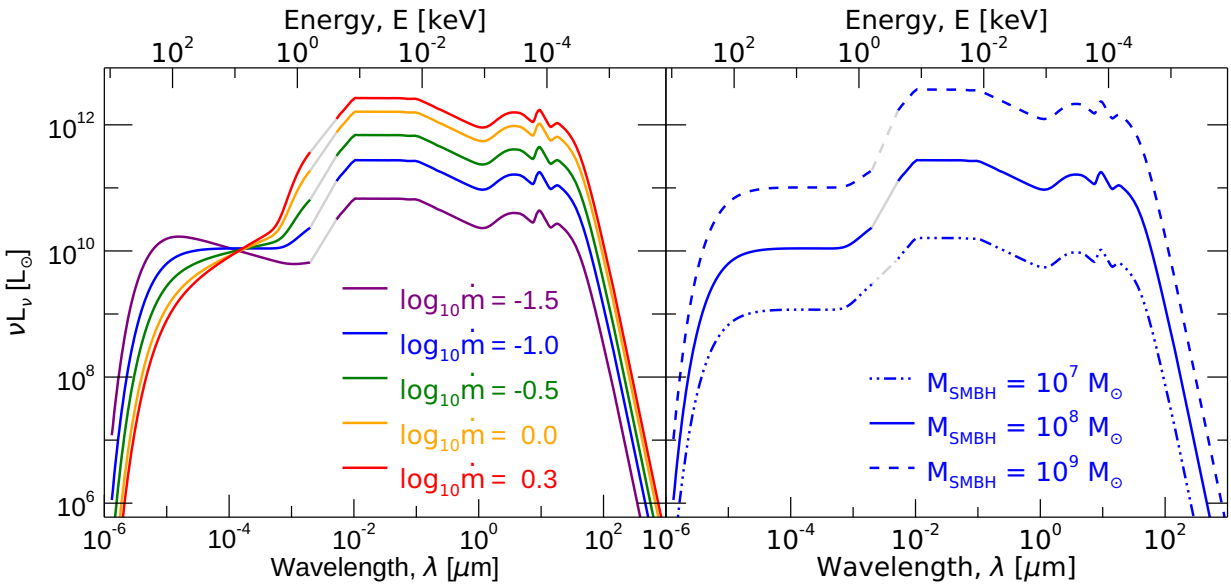

Figure 2.4: Examples of the `qsosed` AGN X-ray emission model connected with the SKIRTOR UV-to-IR model generated by `Lightning`. The SKIRTOR model shape is fixed using $i_{\mathrm{AGN}} = 0°$ and $\tau_{9.7} = 7$ with the normalization being set by the `qsosed` model. The variation in color in the left panel corresponds to a change in $\log_{10}\dot{m}$ with fixed $M_{\mathrm{SMBH}} = 10^8\ M_\odot$, while different line styles in the right panel correspond to variations in M_{SMBH} with fixed $\log_{10}\dot{m} = -1$. The light gray line segments between $\lambda = 2$–5 nm ($E = 0.24$–0.62 keV) show the linear connection of the two models for visualization purposes at the edge of the X-rays. From these examples, it can be seen that $\log_{10}\dot{m}$ affects the shape of the X-ray emission, while M_{SMBH} mainly affects the normalization.

across the extreme-UV wavelength range. Therefore, the light gray line segments in Figure 2.4 show a linear interpolation between the two models for visualization purposes.

This implementation of the connection between the X-ray, optical, and IR AGN emission is a half-step to a fully energetically self-consistent model, in which the X-ray and IR AGN spectra are generated from the same assumed torus model and accretion disk spectrum. For steps toward connecting X-ray and IR spectral models using the same torus, see e.g. Tanimoto et al. (2020).

2.2.3 Dust Attenuation Models

To account for the variety of attenuation laws between and within galaxies, we include several prescriptions for attenuation in `Lightning`. For the UV-to-IR, these include the original and a

variable form of the Calzetti et al. (2000) attenuation curve and the inclination-dependent attenuation curve from Doore et al. (2021). For the X-rays, these include the `tbabs` absorption model (Wilms et al., 2000) and the `Sherpa atten` model from Rumph et al. (1994).[3]

2.2.3.1 Calzetti et al. (2000) Attenuation

We implement the commonly used Calzetti et al. (2000) attenuation curve as the default in `Lightning`. The general details and format of this attenuation curve as implemented in `Lightning` are presented in Section 3.2 of Eufrasio et al. (2017). To briefly summarize these details, we used the Calzetti et al. (2000) curve as linearly extrapolated by Noll et al. (2009) at 1200 Å to extend to the Lyman limit (912 Å). To allow for more flexibility, we include the optional variable slope and 2175 Å bump feature modifications as presented in Noll et al. (2009). Reformatting to use the optical depth, rather than attenuation in magnitudes, this variable diffuse dust attenuation curve is defined as

$$\tau_{\rm DIFF}(\lambda) = \frac{\tau_{\rm DIFF,V}}{4.05}\Big(k'(\lambda) + D(\lambda)\Big)\left(\frac{\lambda}{0.55\ \mu{\rm m}}\right)^{\delta}, \tag{2.9}$$

where $\tau_{\rm DIFF}$ is the optical depth of the diffuse dust at wavelength λ, $\tau_{\rm DIFF,V}$ is the V-band (0.55 μm) normalization, $k'(\lambda)$ is the Calzetti et al. (2000) attenuation curve, $D(\lambda)$ is the functional Drude profile parameterizing the 2175 Å bump feature, and δ is the parameter controlling the variable slope. The Drude profile is defined as

$$D(\lambda) = \frac{E_b(\lambda\ \Delta\lambda)^2}{(\lambda^2 - \lambda_0^2)^2 + (\lambda\ \Delta\lambda)^2}, \tag{2.10}$$

[3] Absorption is the dominant contribution to the attenuation of high energy photons such as X-rays. Therefore, it is conventional to only model absorption rather than attenuation, which includes both absorption and scatter.

where we assume a bump strength of $E_b = 0.85 - 1.9\delta$ following the results of Kriek & Conroy (2013), a bump FWHM of $\Delta\lambda = 350$ Å, and a central bump wavelength of $\lambda_0 = 2175$ Å. Finally, we also include an optional birth-cloud attenuation component given by

$$\tau_{\rm BC}(\lambda) = \tau_{{\rm BC},V}\left(\frac{\lambda}{0.55\ \mu{\rm m}}\right)^{-1}, \tag{2.11}$$

which is only applied to the youngest defined SFH age bin (ψ_1).[4] Combining the diffuse dust and birth-cloud components, the effective optical depth of the attenuation curve for a given age bin j is given by

$$\tau_j(\lambda) = \tau_{\rm DIFF}(\lambda) + \delta_{j1}\tau_{\rm BC}(\lambda), \tag{2.12}$$

where δ_{j1} is the Kronecker delta (not to be confused with the variable slope parameter δ). Therefore, the variable Calzetti et al. (2000) attenuation has up to three free parameters ($\tau_{{\rm DIFF},V}$, δ, and $\tau_{{\rm BC},V}$) that define the shape of the curve.

In Figure 2.5, we show several modified Calzetti et al. (2000) attenuation curves as colored lines to compare with the base Calzetti et al. (2000) attenuation curve (i.e., $\delta = 0$, $\tau_{{\rm BC},V} = 0$, and no UV bump feature), which is shown in black. The variation in color corresponds to a change in δ (left panel), while different line styles correspond to variations in $\tau_{{\rm BC},V}$ (right panel). This comparison clearly shows how the variable slope parameter δ affects the slope of UV attenuation. Additionally, the inclusion of the birth cloud attenuation increases the amount of attenuation at all wavelengths.

[4]We only recommend using birth cloud attenuation when ψ_1 has an upper age bin boundary of 10 Myr or less, as stars older than 10 Myr typically have migrated out of or cleared their birth cloud.

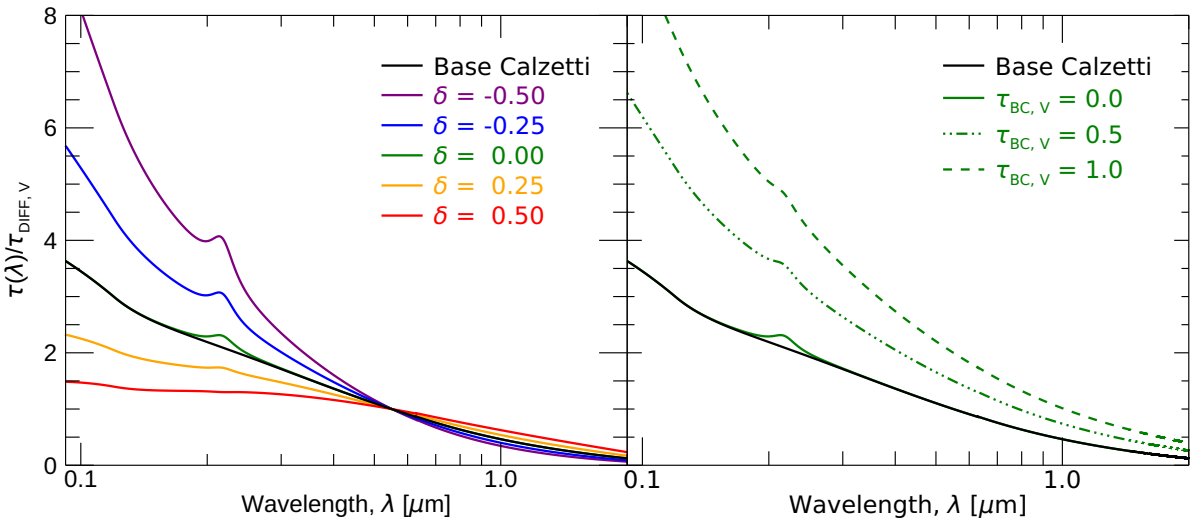

Figure 2.5: Example modified Calzetti et al. (2000) attenuation curves generated by `Lightning`, normalized by $\tau_{\mathrm{DIFF},V}$. The black curve gives the base Calzetti et al. (2000) attenuation curve (i.e., $\delta = 0$, $\tau_{\mathrm{BC},V} = 0$, and no UV bump feature). The variation in color in the left panel corresponds to a change in δ with fixed $\tau_{\mathrm{BC},V} = 0$, while different line styles in the right panel correspond to variations in $\tau_{\mathrm{BC},V}$ with fixed $\delta = 0$.

2.2.3.2 Inclination-dependent Attenuation

To allow for more accurate attenuation in disk galaxies, an inclination-dependent attenuation curve is also included in `Lightning`, the description of which is presented in detail in Section 4.3 of Doore et al. (2021). To give a brief description, the prescription is based on the Tuffs et al. (2004) inclination-dependent attenuation curves, as updated by Popescu et al. (2011), which assume that disk galaxies are comprised of three components, a young thin disk, an old thick disk, and an old dustless bulge. The equation defining the curves in Tuffs et al. (2004) was restructured to depend on the intrinsic properties of these three components rather than their observable properties. This

resulted in the attenuation curve being defined by

$$\Delta m_\lambda = -2.5\log\left(\frac{r^{0,\mathrm{old}}}{1+B/D}\,10^{\frac{\Delta m_\lambda^{\mathrm{disk}}(i,\tau_B^f)}{-2.5}} + (1-r^{0,\mathrm{old}})(1-Ff_\lambda)10^{\frac{\Delta m_\lambda^{\mathrm{tdisk}}(i,\tau_B^f)}{-2.5}} + \left(r^{0,\mathrm{old}} - \frac{r^{0,\mathrm{old}}}{1+B/D}\right)10^{\frac{\Delta m_\lambda^{\mathrm{bulge}}(i,\tau_B^f)}{-2.5}}\right). \quad (2.13)$$

Here, Δm_λ is the attenuation in magnitudes at a given wavelength λ. $r^{0,\mathrm{old}}$ is the fraction of intrinsic flux density from the old stellar components (i.e., thick disk and bulge) compared to the total intrinsic flux density. B/D is the intrinsic bulge-to-thick disk ratio. $\Delta m_\lambda^{\mathrm{disk}}(i,\tau_B^f)$, $\Delta m_\lambda^{\mathrm{tdisk}}(i,\tau_B^f)$, and $\Delta m_\lambda^{\mathrm{bulge}}(i,\tau_B^f)$ are the attenuations from the diffuse dust, parameterized by fifth-order polynomials in Popescu et al. (2011), which are functions of inclination, i, for tabulated values of the B-band face-on optical depth as seen through the center of the galaxy, τ_B^f, and wavelength for the disk, thin disk, and bulge, respectively. Finally, F is the birth cloud clumpiness factor of the thin disk, and f_λ is a tabulated function of wavelength that provides F its wavelength dependence.

The restructuring of the original Tuffs et al. (2004) equation to intrinsic properties was intentional so that the non-parametric SFH in `Lightning` could be used to effectively eliminate $r^{0,\mathrm{old}}$ as a free parameter. This was done by making $r^{0,\mathrm{old}}$ a binary parameter, where each SFH age bin is given its own value for $r^{0,\mathrm{old}}$ based on its age. A value of 0 indicates that the given SFH bin is to be considered part of the young stellar population (e.g., $t < 500$ Myr), while a value of 1 considers it part of the old stellar population (e.g., $t > 500$ Myr). Therefore, with $r^{0,\mathrm{old}}$ tied to the SFH ages, the other four parameters (i, τ_B^f, B/D, and F) are the free parameters defining the shape of the inclination-dependent attenuation curve. Examples of these inclination-dependent attenuation curves can be found in Figures 7 and 8 of Doore et al. (2021).

2.2.3.3 X-ray Absorption

In `Lightning`, the X-ray absorption is modeled using one of two user-selected X-ray absorption models: the `tbabs` model with the default Wilms et al. (2000) abundances or the `Sherpa` `atten` model which combines cross-sections from Morrison & McCammon (1983) and Rumph et al. (1994). The tabulated curves used in `Lightning` were generated with `Sherpa`[5] v4.13, and normalized to a line-of-sight HI column density of $N_{\rm H} = 10^{20}$ cm^{-2}. At energies larger than 10 keV, these models produce negligible absorption; for convenience we set the optical depth to 0 at > 12 keV.

The chosen X-ray absorption is first applied to the SED model in the observed-frame to account for Galactic absorption by the Milky Way, with the Galactic $N_{\rm H}$ being a user input for each galaxy. Further intrinsic absorption is then applied in the rest frame on the stellar binary population and the AGN emission model, if applicable. If there is no X-ray AGN emission, the $N_{\rm H}$ of the stellar population becomes a free parameter in the model. We show some examples of the X-ray stellar model with varying levels of absorption and SFHs in Figure 2.6. The inclusion of X-ray absorption primarily impacts lower energy photons as higher energy X-rays are less likely to be absorbed, with the intensity of the absorption increasing with $N_{\rm H}$.

However, when the model includes an X-ray AGN component, absorption of the stellar X-ray emission is not a free parameter, and is instead linked to the V-band attenuation via

$$N_{\rm H} = (22.4 \times 10^{20}\ {\rm cm}^{-2}) \frac{2.5\ \tau_{{\rm DIFF},V}}{\ln(10)}. \tag{2.14}$$

This scaling was chosen to be the average of observed Milky Way $N_{\rm H} - A_V$ relationships (Predehl & Schmitt, 1995; Nowak et al., 2012). In this case, the $N_{\rm H}$ value of the nuclear region becomes the

[5] https://cxc.cfa.harvard.edu/sherpa/

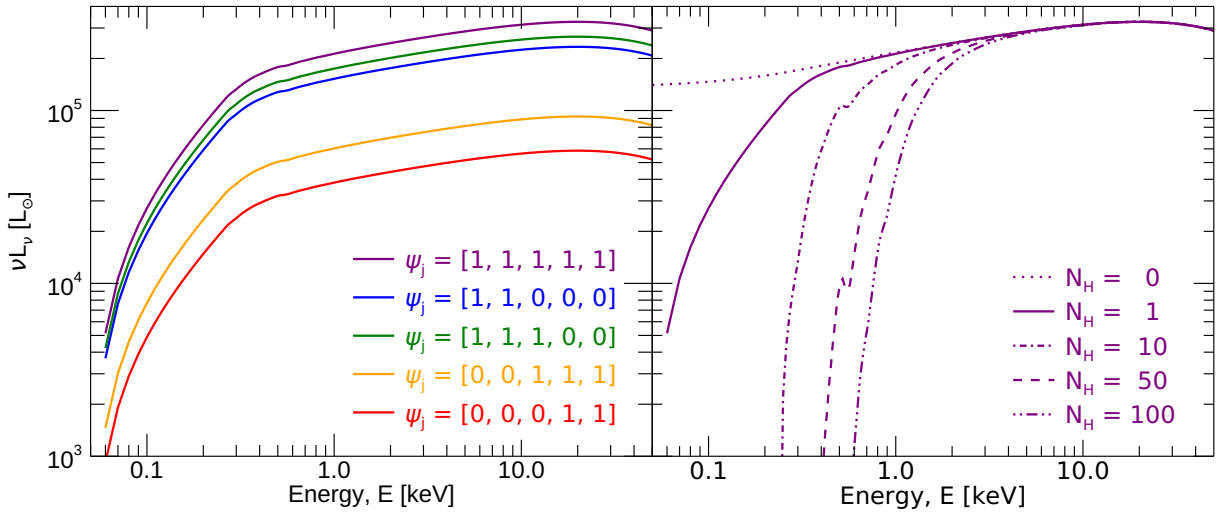

Figure 2.6: Example X-ray stellar spectra with and without X-ray absorption generated by `Lightning`. The used absorption model is the `tbabs` model with Wilms et al. (2000) abundances. The variation in color in the left panel corresponds to a change in the SFH parameters ψ_j with fixed $N_{\rm H} = 1$ ($\times 10^{20}$ cm^{-2}). (The age bins for these ψ_j values are the default set of age bins in `Lightning` as discussed in Section 2.2.1.2.) The variation in lines styles in the right panel correspond to changes in $N_{\rm H}$ with fixed $\psi_j = [1,1,1,1,1]$ $M_\odot$ yr^{-1}. The blue line in the left panel shows an example of a spectrum dominated by young stars (i.e. HMXBs), while the red line shows a spectrum dominated by old stars (i.e., LMXBs).

free parameter in the model, as we expect the X-ray emission from the AGN to be the dominant component of the X-ray spectrum in most cases.

We note here that while $N_{\rm H}$ is allowed to increase above 10^{24} cm^{-2} in our implementation, our X-ray emission models are not currently appropriate for Compton-thick sources, which typically require reflection components that are not included in `Lightning`.

2.2.4 Dust Emission Models

We model IR dust emission in `Lightning` using the Draine & Li (2007) model. To briefly summarize, the model details how the dust mass, $M_{\rm dust}$, is exposed to a radiation field intensity, U.

Analytically, this is given by Equation 23 in Draine & Li (2007),

$$\frac{dM_{\rm dust}}{dU} = (1-\gamma)M_{\rm dust}\delta(U-U_{\rm min}) + \gamma M_{\rm dust}\frac{(\alpha-1)}{(U_{\rm min}^{1-\alpha}-U_{\rm max}^{1-\alpha})}U^{-\alpha}, \;\; \alpha \neq 1, \tag{2.15}$$

where the first additive component is a delta function at the minimum radiation field intensity $U_{\rm min}$ and the second component is a power-law of slope α derived between $U_{\rm min}$ and $U_{\rm max}$, the maximum radiation field intensity. The parameter γ in each additive component dictates the fraction of the dust mass exposed to the power-law compared to the delta function. Additionally, the polycyclic aromatic hydrocarbon (PAH) index, $q_{\rm PAH}$, is a hidden parameter in the model and defines the strength of the PAH emission.

Rather than scaling the model with $M_{\rm dust}$, we instead use the total integrated IR (TIR) luminosity $L_{\rm TIR}$ (i.e., the bolometric luminosity of the dust model), which is proportional to $M_{\rm dust}$. The reason we make this substitution is because of the mechanism generating the dust emission. Simply put, some fraction of UV-to-NIR emission in a galaxy is attenuated by dust. This attenuated energy is conserved via radiation from dust particles at longer wavelengths, mainly across the mid-to-far IR. To account for this conservation of energy, it is expected that the bolometric luminosity of the attenuated light should be equal to the TIR luminosity. This energy conservation (often termed "energy balance" in the SED fitting community) is optional when fitting with the dust emission model in `Lightning`. Therefore, when fitting with energy balance, the dust model has five free parameters: α, $U_{\rm min}$, $U_{\rm max}$, γ, and $q_{\rm PAH}$; and when energy balance is not assumed, $L_{\rm TIR}$ becomes an additional free parameter used for normalization.

In Figure 2.7, we show some examples of the Draine & Li (2007) dust emission model for a variety of input parameters. In these examples and as a default in `Lightning`, we fix $U_{\rm max} =$

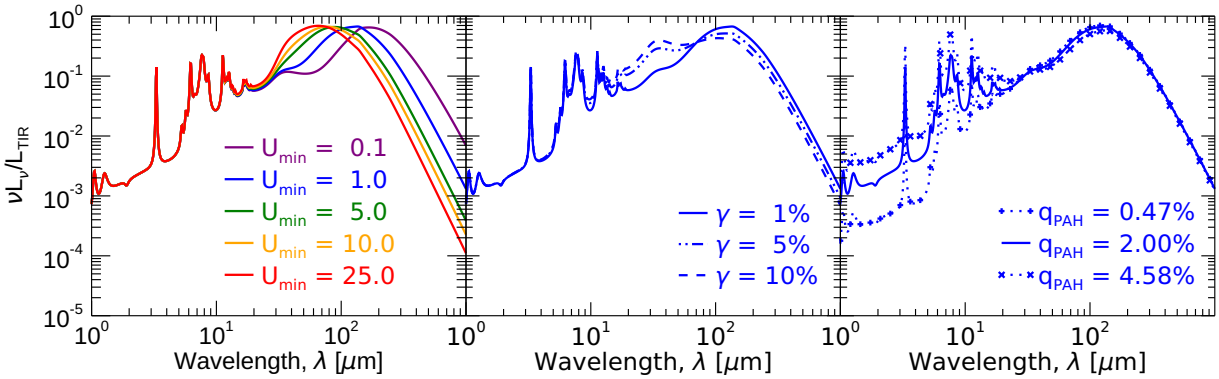

Figure 2.7: Examples of the Draine & Li (2007) dust emission model generated by `Lightning`, normalized by $L_{\rm TIR}$. The parameters $U_{\rm max}$ and α are fixed to 3×10^5 and 2, respectively. The variation in color in the left panel corresponds to a change in $U_{\rm min}$ with fixed $\gamma = 0.01$ and $q_{\rm PAH} = 0.02$. The different lines styles in the middle panel correspond to variations in γ with fixed $U_{\rm min} = 1$ and $q_{\rm PAH} = 0.02$. As for the right panel, the different symbols on the dotted lines correspond to different values of $q_{\rm PAH}$ with fixed $U_{\rm min} = 1$ and $\gamma = 0.01$. Decreasing the value of $U_{\rm min}$ can be seen to shift the peak of the emission to shorter wavelengths, while $q_{\rm PAH}$ independently increases the intensity of the PAH emission features.

3×10^5 and $\alpha = 2$. We make this simplifying assumption as recommended by Draine et al. (2007), since they found that the dust model is not very sensitive to these two parameters and most observed IR SEDs are well reproduced by $U_{\rm max} = 10^6$ and $\alpha = 2$. We note the discrepancy between the fixed value of $U_{\rm min}$ in `Lightning` and that recommended by Draine et al. (2007). The reason for the discrepancy comes from how `Lightning` computes the dust emission model from the publicly available data. To allow for a variable α, the δ-functions of U must be used. However, the largest available δ-function is $U = 3 \times 10^5$. Therefore, $U_{\rm max}$ is limited to this largest available value, since extrapolating to $U = 10^6$ would add unwanted uncertainty to the model.

2.3 Statistical Inferencing of SEDs

2.3.1 Observational Information

To keep `Lightning` computationally fast, we restrict it to modeling only photometric observations, since spectroscopic observations would require additional modeling assumptions. However, any combination of narrow- to broad-band flux densities that have been corrected for Galactic extinction can be used to make up the UV-to-submillimeter input SED. Additionally, any number of uniform sensitivity top-hat energy bands can be used for X-ray observations, whose measurements can be in the form of either net counts or fluxes.

Since the models in `Lightning` are in rest-frame luminosity units, an observed distance indicator is required to convert the SED fluxes to the same luminosity units as the model. The distance indicator can simply be a luminosity distance, or it can be a redshift, where the luminosity distance is calculated from the redshift via the user chosen cosmology. We note that when using a redshift that the assumed age of the Universe, $t_{\rm age}(z)$, will decrease as redshift increases. To account for any effect this will have on the SFH age bins, we have designed `Lightning` to automatically adjust the user-defined age bins such that upper bin boundaries of $t_{j+1} > t_{\rm age}(z)$ will be updated to $t_{j+1} = t_{\rm age}(z)$, and bins with lower bin boundaries of $t_j > t_{\rm age}(z)$ are completely omitted from the SFH.

2.3.2 Loss Function

In order to fit a given model to any data, a loss function, which determines how well the model fits the data, is required. In `Lightning`, we implement a χ^2 loss function given by

$$-\log(\mathscr{L}) \propto \chi^2 = \sum_{f=1}^{n} \frac{(L_{\nu,f}^{\rm obs} - \bar{L}_{\nu,f}^{\rm mod})^2}{\sigma_{{\rm total},f}^2}, \tag{2.16}$$

where $\mathscr{L}$ is the likelihood probability of the model, $L_{\nu,f}^{\rm obs}$ is the observed luminosity in filter f as derived from the input flux, $\bar{L}_{\nu,f}^{\rm mod}$ is the model photometry in filter f, and $\sigma_{{\rm total},f}$ is the total uncertainty associated with filter f. The model photometry is derived by integrating the observed-frame model spectrum through the corresponding filter f using

$$\bar{L}_{\nu,f}^{\rm mod} = \frac{\int T_f(\lambda) L_\nu^{\rm mod}(\lambda)\, d\lambda}{\int T_f(\lambda)\, d\lambda}, \tag{2.17}$$

where $T_f(\lambda)$ is the filter transmission function in units of energy, and $L_\nu^{\rm mod}(\lambda)$ is the model spectrum. The total uncertainty consists of both the observed uncertainty, which is the Gaussian uncertainty of the measurement plus any additional fractional calibration uncertainty, and the model uncertainty added in quadrature or

$$\sigma_{{\rm total},f}^2 = \sigma_{{\rm obs},f}^2 + \sigma_{{\rm mod},f}^2, \tag{2.18}$$

where $\sigma_{{\rm obs},f}$ and $\sigma_{{\rm mod},f}$ are the observed and model uncertainties, respectively. We include a model uncertainty component in `Lightning` to account for any oversimplification of models and potential systematic uncertainties in the models themselves (Charlot et al., 1996; Percival & Salaris, 2009; Conroy et al., 2009,0; Conroy & Gunn, 2010). The model uncertainty is computed simply as a

user-defined fraction of the model photometry that is constant for each filter or

$$\sigma^2_{\mathrm{mod},f} = (\sigma^{\mathrm{frac}}_{\mathrm{mod}} \times \bar{L}^{\mathrm{mod}}_{\nu,f})^2 \tag{2.19}$$

where $\sigma^{\mathrm{frac}}_{\mathrm{mod}}$ is the user-defined fractional model uncertainty. Therefore, by including model uncertainties, our formulation of the χ^2 loss function accounts for both the observational uncertainty and the inherent uncertainty of the models being used.

When fitting X-ray data in terms of counts, we note that Equation 2.16 will not be applicable, since the Poissonian nature of the counts is not compatible with uncertainty formulation. Instead, we calculate the χ^2 contribution of the X-ray counts as

$$\chi^2_{\mathrm{X}} = \sum_{e=1}^{n} \frac{(N^{\mathrm{obs}}_e - N^{\mathrm{mod}}_e)^2}{\sigma^2_{N,e}}, \tag{2.20}$$

where χ^2_{X} is X-ray counts contribution to the total χ^2, N^{obs}_e is the observed net counts (i.e., background subtracted) in energy band e, N^{mod}_e is the model net counts in energy band e, and $\sigma_{N,e}$ is the approximate count uncertainty in energy band e. Since the approximate count uncertainty can be computed in a variety of ways depending on the overall count rate, we allow for the user to either input their own pre-computed count uncertainties or use one of the two built-in methods in `Lightning`. The first method simply sets the count uncertainty equal to the square root of the counts (i.e., $\sigma_{N,e} = \sqrt{N^{\mathrm{obs}}_e}$), since this is the Gaussian approximation in the high count regime. The other uses the upper uncertainty of the Gehrels (1986) approximation given by

$$\sigma_{N,e} = 1 + \sqrt{0.75 + N^{\mathrm{obs}}_e}, \tag{2.21}$$

which is more appropriate for data in the low count regime. User-supplied uncertainties may be used when more flexibility is required, e.g., when the background contributes strongly to the

uncertainty.

2.3.3 Maximum-Likelihood Inferencing

2.3.3.1 MPFIT Algorithm

To allow for the determination of a rapid best-fit solution to an SED without sampling the parameter posteriors, we have added a new maximum-likelihood inferencing method to `Lightning`. The method utilizes the `MPFIT` code (Moré, 1978; Markwardt, 2009), which consists of the gradient-descent LevenbergMarquardt algorithm used to solve non-linear least squares problems. We chose the `MPFIT` implementation since it allows for several necessary constraints in `Lightning`, such as fixing parameters and setting parameter bounds.

When searching for the best solution, one drawback to gradient-decent algorithms like `MPFIT` is that they are prone to getting stuck in local minima in χ^2 space before reaching the global minimum. To mitigate this drawback, we have implemented the algorithm to run a user-defined number of "solvers", where each solver is a fit to the SED using different starting locations in parameter space (see Section 2.3.5). By running multiple solvers from different starting locations, we can compare the solver solutions. If the majority of the solvers have converged to the same solution, then we can be confident that this is likely the best solution and global minimum. More specifically, we require that (1) at least 50% of the solvers have $\chi^2 - 4 \leq \chi^2_{\rm best}$, where $\chi^2_{\rm best}$ is the minimum χ^2 value of all solvers, and (2) all of these solvers satisfying criterion (1) have free parameter values that are within a 1% difference of the best fit.[6] Finally, once convergence to the best solution has been confirmed, the best-fit solver is considered the solution to the SED fit.

[6]The chosen difference in χ^2 of 4 and the 1% difference are arbitrarily chosen from our test fits to well behaved SEDs. We include the χ^2 result and the parameter values for each solver in the output such that a user can further evaluate these cutoffs at their discretion.

2.3.4 Bayesian Inferencing

To allow for a high quality sampling of the posterior to an SED model, we implement two Bayesian inferencing methods in `Lightning`. Both methods utilize MCMC algorithms to sample the posterior distributions of the free parameters, while incorporating prior distributions of these parameters.

2.3.4.1 Prior Distributions

In terms of analytical priors, we only include two basic options in `Lightning`: truncated uniform and normal (Gaussian) priors. We implement by default some truncated priors, since practically all possible free parameters have at least a lower bound. Therefore, limiting the prior range to comply with the physically allowed values is required. Additionally, both analytical priors are implemented in each parameter's sampled space (e.g., a parameter sampled in log space has a uniform or normal prior in log space).

Besides the analytical priors, we include the option for a user to input a prior of any shape in tabulated form. The only restriction for the shape of these priors is that they conform to a parameter's physically allowed range. Otherwise, any shape is allowed, which can be useful for creating complex prior distributions for a given parameter. However, we do note that no free parameters can be linked together via the prior, tabulated or analytical. We exclude user-specified parameter linking in `Lightning`, which is common in other SED fitting codes, to minimize the computational complexity and increase computational speed. Additionally, we automatically link commonly correlated parameters (e.g., $\tau_{\mathrm{DIFF},V}$ and N_{H}), which would potentially be linked by the user.

With the priors specified, the posterior probability is calculated using

$$\log(P_{\rm post}) \propto \log(P_{\rm prior}) + \log(\mathscr{L}), \tag{2.22}$$

where $P_{\rm post}$ is the posterior probability and $P_{\rm prior}$ is the prior probability.[7] Since the goal of the MCMC algorithms is to sample $P_{\rm post}$, the loss function from Section 2.3.2 is updated for these algorithms to include the prior information such that we are minimizing and sampling $-\log(P_{\rm post})$ space rather than χ^2 space.

2.3.4.2 Adaptive MCMC Algorithm

The original MCMC algorithm adopted in `Lightning` was implemented and discussed in Doore et al. (2021). The algorithm is an adaptive version of the standard MetropolisHastings algorithm (Metropolis et al., 1953; Hastings, 1970) created by Andrieu & Thoms (2008). The algorithm simply adjusts the proposal density distribution to achieve an optimal acceptance ratio. Additionally, this adjustment of the proposal density is vanishing, meaning the adaptiveness decreases with each subsequent iteration. Therefore, after many iterations the adaptiveness is insignificant and the algorithm is practically equivalent to the standard MetropolisHastings algorithm.

Similar to the `MPFIT` algorithm, a single chain of the adaptive MCMC algorithm is prone to getting stuck in local minima in $-\log(P_{\rm post})$ space. Once stuck, it can take more than the user-specified number of trials to escape and move towards the global minimum.[8] To confirm if a chain reached the vicinity of the global minimum, we have designed the adaptive MCMC algorithm to run a user-defined number of independent chains in parallel, where each chain is initialized using

[7] The $\mathscr{L}$ here includes the contributions from both χ^2 (UV-to-IR) and $\chi^2_{\rm X}$ (X-ray).

[8] All MCMC algorithms by design will reach and sample the global minimum in $-\log(P_{\rm post})$ space. However, this may take an arbitrarily large number of trials.

different locations in parameters space (see Section 2.3.5). By running parallel chains from different starting locations, we can compare the ending segment of each chain to see if they converged to a single best solution. To test for convergence, we have `Lightning` automatically perform the Gelman-Rubin test (Gelman & Rubin, 1992; Brooks & Gelman, 1998) and its multivariate version from Brooks & Gelman (1998) on the ending segment of the chains, whose length is user-defined. If the ending segments from the parallel chains results in acceptable Gelman-Rubin statistics (i.e., $\sqrt{\hat{R}} \leq 1.2$), then a user can confidently concluded that convergence has been reached and the posterior welll sampled by the algorithm.

Since the ending portion of the full parallel chains, which samples the posterior, is the main interest of a user, `Lightning` automatically post-processes the full chains to create a final post-processed chain portion. For the adaptive MCMC algorithm, this post-processed chain portion is determined as follows. First, each parallel chain has a user-defined number of initial trials discarded as the burn-in phase. Next, these truncated chains are thinned by a user-specified thinning factor (i.e., only every n elements of each chain is kept). Finally, the thinned and truncated chain containing the highest posterior probability is selected, and the ending segment of this highest probability chain, whose length is user-defined, is kept as the sampled posterior.

The reason for selecting the highest posterior probability chain is based on the assumption that convergence may not have been reached. If convergence was reached, then all parallel chains will have very similar distributions, and it does not matter which one is selected for use. However, if convergence was not reached, selecting the chain with the highest probability, guarantees that the chain with the best solution is selected.

2.3.4.3 Affine-Invariant MCMC Algorithm

To more quickly sample the potentially skewed posteriors of the free parameters, we have recently added an affine-invariant MCMC algorithm to `Lightning` (Monson et al. 2023, submitted), which is our default algorithm. This algorithm uses an ensemble of samplers to adjust the proposal density distribution and sample the posterior distribution. The ensemble consists of multiple chains (or walkers) that are run in parallel and allowed to interact with one another so that they can adapt their proposal densities. For our implementation in `Lightning`, we use the affine-invariant "stretch move" method as presented in Goodman & Weare (2010), which was shown to more quickly sample non-Gaussian and skewed posteriors compared to the MetropolisHastings MCMC algorithms.

Unlike the `MPFIT` and adaptive MCMC algorithms, the ensemble nature of the affine-invariant MCMC algorithm typically prevents it from getting stuck in local minima in $-\log(P_{\text{post}})$ space, since each walker is initialized using different locations in parameters space (see Section 2.3.5). However, it is still important to confirm that the ensemble has converged to a stationary solution and to quantify any potential sampling error effects, since each walker in the ensemble is not independent. To test for this convergence, we have `Lightning` automatically perform an autocorrelation analysis on the ensemble (see Goodman & Weare 2010 and Foreman-Mackey et al. 2013 for detailed discussions on autocorrelation analyses). We briefly summarize the idea and methods of the analysis as applied in `Lightning` below.

Autocorrelation, in the context of MCMC algorithms, is how correlated a sample is with previous samples from the same walker or chain. Specifically in `Lightning`, we look at the integrated autocorrelation time, which is a measure of the average number of iterations between independent

samples. If the autocorrelation time is large, then the samples in the ensemble are likely highly correlated and contain few independent samples. To confirm the ensemble has enough independent samples and to quantify the Monte Carlo error, we have designed `Lightning` to calculate the autocorrelation time and check for convergence following the methods of Foreman-Mackey et al. (2013). Their methods recommend that the MCMC algorithm runs for a number of iterations at least $\sim$50 times the integrated autocorrelation time in order for one to trust that the autocorrelation time estimate is accurate and convergence has been reached. A factor fewer than $\sim$50 can cause the autocorrelation time to be underestimated, which could result in a highly correlated sampling with few independent samples. Therefore, we have `Lightning` check if the user-defined number of iterations is large enough to have an accurate autocorrelation time estimate (i.e., autocorrelation time $\geq$ 50) and flag fits that do not.

Similar to the adaptive MCMC, the ensemble is automatically post-processed by `Lightning` to produce a final post-processed chain portion. For the affine-invariant MCMC algorithm, the post-processed chain portion is determined as follows. First, each walker in the ensemble has its burn-in phase discarded, where the burn-in phase is a number of iterations from the beginning of the chain equal to either twice the longest autocorrelation time of any parameter in the ensemble (double the autocorrelation time typically encapsulates the entire burn-in phase) or a user-defined value. Next, the truncated ensemble is then thinned by a thinning factor, which is either half the longest autocorrelation time of any parameter in the ensemble (iterations at half the autocorrelation time typically give fully independent samples) or user-defined. Then, if a walker in the thinned and truncated ensemble is classified as stranded (we explain how we classify walkers as stranded below), they are removed from the ensemble. Finally, the non-stranded ensemble is flattened element-wise into a single chain and the ending segment of this flattened chain, whose length is

user-defined, is kept as the sampled posterior.

We designed `Lightning` to classify walkers as stranded if they have an acceptance fraction less than a user-specified number of standard deviations below the median ensemble acceptance fraction. Due to the boundaries of the free parameters, the affine-invariant MCMC can have trouble accepting moves of walkers separated from the ensemble (typically at higher $-\log(P_{\rm post})$ values) when the ensemble is near a boundary. This results in the walkers becoming stranded and having very low acceptance rates, since they are failing to have any proposal jumps accepted. With enough iterations, these walkers will eventually have a jump that rejoins them with the ensemble. However, only a finite number of iterations are allowed for this to occur. Therefore, once the specified iteration limit has been reached, any stranded walkers that may remain need to be removed, since they would add faulty samples to the final sampled posterior. We have found that the most effective automatic method for correctly selecting stranded walkers is to compare each walker's acceptance fraction with that of the median of the ensemble. Those that are classified as stranded with abnormally low acceptance fractions compared to the rest of the ensemble are consistently considered stranded when using more robust and manual visualization methods.

2.3.5 Algorithm Initialization

All three of the current algorithms in `Lightning` require initial starting values for each free parameter. To select these starting values, `Lightning` randomly samples the user-specified prior distribution of each parameter independently. (For the `MPFIT` algorithm, there are technically no priors, since it is not a Bayesian inferencing method. However, we assume uniform "priors" for all parameters for the purpose of initialization.) Additionally, since a given prior may have a much larger range than what would constitute an appropriate starting range, we allow the user to limit

the initialization to a specified range within the prior range. Therefore, each initialization of the algorithms (i.e., each unique solver, chain, or walker) is initialized randomly from a potentially limited range of the corresponding prior.

2.3.6 Derived Quantities

After fitting an SED with the chosen algorithm, we designed `Lightning` to automatically do additional post-processing to derived typical quantities of interest. In terms of physical properties that are not free parameters in the model, the total and individual model component spectra and photometry with and without attenuation are derived. When using an MCMC algorithm, `Lightning` allows for a user to select and keep the model spectra for a specified fraction of best-fit elements in the final post-processed chain portion. This is useful for deriving and quoting model uncertainties on new simulated photometric data points as well as showing model uncertainties in the spectra when plotting. Additional physical properties are also derived, such as the stellar mass and $L_{\rm TIR}$, if their corresponding model component is included in the total model.

One other important quantity of interest that `Lightning` automatically derives is a p-value from a goodness-of-fit test for each SED fit. Goodness-of-fit tests are often overlooked in SED fitting, but they are important for determining if the chosen model can acceptably model the data and whether the uncertainties are trustworthy. For the `MPFIT` algorithm, we use a χ^2 goodness-of-fit test to derive the p-value using the χ^2 and degrees of freedom as given by the `MPFIT` algorithm. We caution against using this p-value to reject the null hypothesis that the chosen model can acceptably model the given SED. Since the effective number of free parameters is lower than the actual number (due to degeneracies and covariances between parameters), the number of degrees of freedom is likely higher than what is given by `MPFIT`. Therefore, this p-value can be underestimated and can

lead one to falsely conclude that the model is not acceptable for the given SED.

As for the MCMC algorithms, since they are Bayesian methods, `Lightning` performs a posterior predictive check (PPC; Rubin, 1984; Gelman et al., 1996) to derive a p-value for the chosen model. A PPC is a goodness-of-fit test that uses the model itself to estimate the distribution from which the p-value is derived. The model can be considered an accurate description of the data if it can generate simulated (replicated) data that is statistically identical to the actual data. By considering the replicated data as data that could have been measured, the PPC tests whether the model encapsulates all of the variability in the actual data.

In terms of the practical application in `Lightning`, a PPC takes the following steps. First, replicated sets of model photometry are randomly selected from the posterior distribution (i.e., samples are bootstrapped from the post-processed chain portion with the chance of selection being weighted by their posterior probability). Then, the replicated sets of photometry are randomly perturbed by a Gaussian distribution with a variance corresponding to the respective total uncertainty. Next, likelihood probabilities are calculated (see Section 2.3.2) by comparing the actual observations and the perturbed replicated photometry with the unperturbed replicated photometry. Finally, the p-value is computed as the fraction of corresponding likelihood probabilities for the perturbed replicated photometry that are smaller than the likelihood probabilities for the actual observations.[9]

2.4 Example Applications

In this section, we present different example applications of `Lightning` to give interested users ideas of its capabilities. In Figure 2.8, we show composite postage stamp images of the galaxies used in each example, along with a brief description of the example topic. We note that, within

[9] See Section 5.1 of Chevallard & Charlot 2016 for a more detailed description of how PPCs are used in SED fitting.

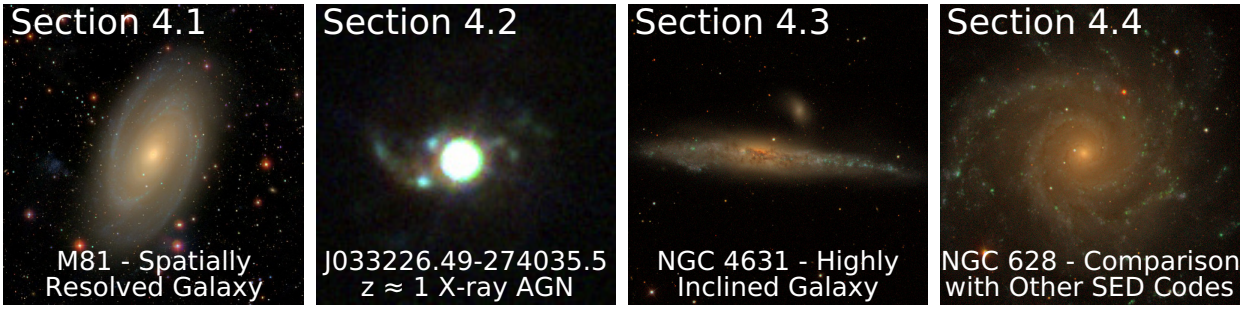

Figure 2.8: Composite SDSS g, r, i (M81, NGC 4631, and NGC 628) and HST F435W, F606W, and F850LP (J033226.49−274035.5) postage stamp images for the galaxies used in the example applications of `Lightning` in Section 2.4.

the "examples" sub-directory of the `Lightning` GitHub repository and online documentation[10], we provide the scripts required to run the examples and generate their presented figures. For interested users, we recommend following along in the online documentation in addition to the below text to get further supplementary details.

For all of these examples, we adopt a cosmology with $H_0 = 70$ km s^{-1} Mpc^{-1}, $\Omega_M = 0.30$, and $\Omega_\Lambda = 0.70$.

2.4.1 Property Maps of M81

To show the power and versatility of `Lightning` when applied to a nearby galaxy, we fit the spatially resolved UV-to-FIR photometry (SED map) of the nearby spiral galaxy, M81 (NGC 3031). To generate the SED map, we gathered 23 publicly-available photometric images ranging in wavelength from GALEX FUV to Herschel 350 μm. We then pre-processed these images for fitting by (1) subtracting foreground stars, (2) convolving each image to a common $25''$ PSF, (3) re-binning them to a common $10''$ pixel scale, (4) estimating the background to update the photometric uncertainties, (5) correcting each bandpass for Galactic extinction, and (6) combining the images into a

[10] https://lightning-sed.readthedocs.io/en/latest/

data cube which contains the pixel-by-pixel SEDs. Since any data pre-processing steps are done external to running `Lightning`, we exclude the intricate details on our image pre-processing methods as the focus of this example is on the application of `Lightning` rather than the creation of SED maps. Interested readers can refer to Section 2 of Eufrasio et al. (2017) for a detailed description of the pre-processing steps involved.

To model the SEDs, we used a stellar population with solar metallicity (i.e, $Z = 0.02$) and SFH age bins of 0–10 Myr, 10–100 Myr, 0.1–1 Gyr, 1–5 Gyr, and 5–13.6 Gyr. The stellar emission was attenuated using the modified Calzetti et al. (2000) curve with the 2175 Å bump feature and excluding any birth cloud attenuation. Finally, the dust attenuation was set to be in energy balance with the Draine & Li (2007) dust emission model, where we fixed $U_{\rm max} = 3 \times 10^5$ and $\alpha = 2$, as recommended by Draine et al. (2007) and discussed in Section 2.2.4. To fit the model to each SED, we utilized the affine-invariant MCMC algorithm, which we ran for 10^4 trials with 75 walkers, assuming 5% model uncertainty. For all free parameters, we implemented uniform priors over either the entire available range or a broad range of values if the available range is infinite. The values defining the priors associated with each free parameter in the model, along with the limited initialization ranges, are listed in Table 2.3.

With the described model and algorithm, we used `Lightning` to fit a subset of the SEDs within the SED map, assuming a luminosity distance to M81 of 3.5 Mpc as given in Dale et al. (2017). The subset included all SEDs that were inside the 25 mag arcsec^{-2} B-band isophotal ellipse as given by HyperLeda[11] (Makarov et al., 2014), which limited our example to the general extent of the optical emission of the galaxy. The fitting process took 65.1 hours total to fit all 6972 SEDs using one 32-core, 2.1 GHz CPU on the Arkansas High Performance Computing Center (i.e., 0.30

[11] http://leda.univ-lyon1.fr

Table 2.3: Summary of parameters used in the M81 example.

Parameter	Prior Function	Initialization Range
ψ_j	$\mathscr{U}(0, 10^3)$	$[0, 1]$
$\tau_{\mathrm{DIFF},V}$	$\mathscr{U}(0, 10)$	$[0, 1]$
δ	$\mathscr{U}(-2.3, 0.4)$	$[-1, 0]$
$\tau_{\mathrm{BC},V}$	Fixed	0
α	Fixed	2
U_{min}	$\mathscr{U}(0.1, 25)$	$[0.1, 5]$
U_{max}	Fixed	3×10^5
γ	$\mathscr{U}(0, 1)$	$[0, 0.1]$
q_{PAH}	$\mathscr{U}(0.0047, 0.0458)$	$[0.0047, 0.0458]$

Notes – $\mathscr{U}(a, b)$ indicates a uniform distribution from a to b. Fixed parameters have their value listed in the initialization range column.

core-hours per SED), with `Lightning` automatically running each SED fit in parallel to maximize CPU usage. To give a general sense of fitting speed, other Bayesian sampling SED fitting codes typically take 1-100 core-hours per SED depending on the complexity of the chosen model, which means `Lightning` fits $\gtrsim 1$ order of magnitude faster than other codes.

Once `Lightning` is finished fitting, it automatically post-processes the fit to each SED as described in Sections 2.3.4.3 and 2.3.6 and combines the results into a single file. When generating the final post-processed chain portion, we manually set the length of the burn-in phase and thinning factor for consistency rather than having `Lightning` automatically determine them for each SED from the autocorrelation times. We chose a burn-in length of 8000 trials and a thinning factor of 250, which is significantly larger than the overall maximum autocorrelation time of 178. Therefore, each element in the final chain portions should be uncorrelated. Finally, we only keep the final 250 elements of each chain so that we can derive reasonable median and 16th and 84th percentile ranges, while minimizing the total memory of the single post-processed file.

With the post-processed results, we first checked that all SEDs converge to stationary solutions as determined by their autocorrelation times derived from the full chain (see Section 2.3.4.3). After

confirming convergence, we then mapped the derived quantities for each SED back to its associated pixel to generate maps of the spatially resolved properties of the galaxy. In Figure 2.9, we show a variety of these derived spatially resolved properties, with the values of each pixel being the median value from the corresponding posterior distribution. The only exception to this is the image of the p-values in panel (f), which only has a single value rather than a distribution. From this image, it can be seen that the vast majority of pixels are well fit by the model, with poor fits mainly being associated with locations where foreground star subtraction occurred. One stand out result from these property maps is that the younger, star-forming population, which is more highly obscured, is concentrated in the spiral arms as seen in the SFR (SFR of the last 100 Myr) and V-band optical depth maps. Additionally, the older, more massive population can clearly been seen to reside in the bulge region, where the stellar mass is high and SFR is low, resulting in a low specific star formation rate (sSFR; $\mathrm{sSFR} = \mathrm{SFR}/M_{\star}$).

To further demonstrate how the spatially resolved results could be used to estimate properties for regions of the galaxy, we separate the galaxy into two parts, the outer and inner region. The outer region being defined as the pixels between the 25 mag arcsec^{-2} B-band isophotal ellipse as given by HyperLeda and one half of the 20 mag arcsec^{-2} K_s-band isophotal ellipse as given by Jarrett et al. (2003), and the inner region comprised of pixels within one half of the 20 mag arcsec^{-2} K_s-band isophotal ellipse. In the left of Figure 2.10, these regions are shown overlaid on the convolved and re-binned SDSS color image as the blue and orange ellipses, respectively. By summing the results of each pixel within each region, a total SED and SFH can be made as shown in the middle and right of Figure 2.10, respectively. These results show, as inferred from the maps in Figure 2.9, that the outer region has comparatively higher UV emission and lower NIR emission, which is distinguished by the fit as an overall younger population compared to the inner region.

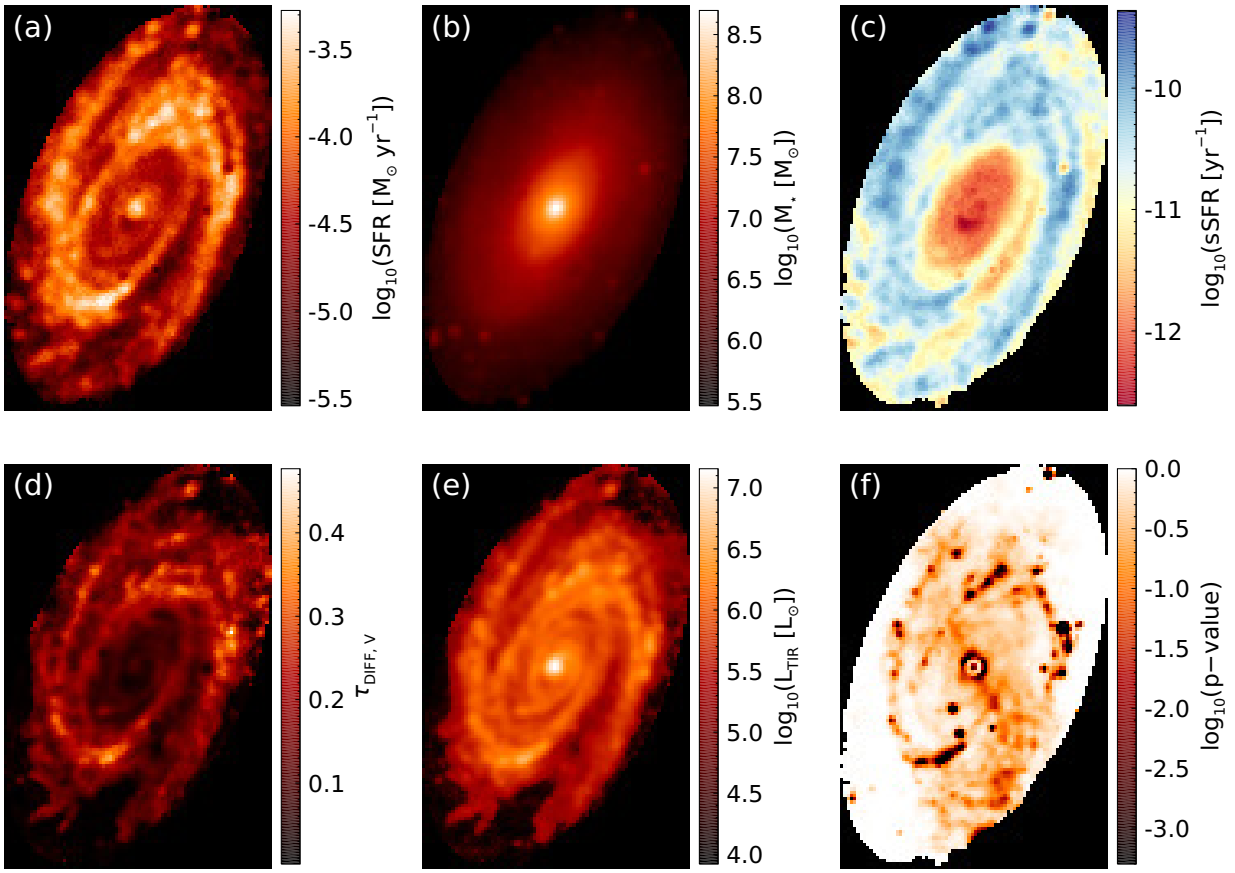

Figure 2.9: Maps of the derived spatially resolved properties of M81. The values of each pixel are the median value from the corresponding posterior distribution (excluding the p-value, which is a single value, in panel (f)). The properties from the upper left to bottom right are (a) the SFR of the last 100 Myr, (b) the stellar mass, (c) the sSFR of the last 100 Myr, (d) the diffuse V-band optical depth, (e) the $L_{\rm TIR}$, and (f) the p-value estimated from the PPC. From these maps, it can be seen that the attenuation and recent star formation is concentrated in the spiral arms, while the stellar mass is concentrated in the bulge. This age stratification is clear in the sSFR map, which uses a different color scheme to highlight younger populations in blue and older populations in red.

Finally, to give a sense of how the maximum likelihood and Bayesian algorithms in `Lightning` compare, we refit the B-band isophote subset of the SED map after swapping the MCMC algorithm with the `MPFIT` algorithm. Using 20 solvers to test for convergence, fitting took 19.1 hours to fit all 6972 SEDs on one of the same 32-core, 2.1 GHz CPUs (i.e., 0.09 core-hours per SED), which is 3.4 times faster than the MCMC algorithm. In Figure 2.11, we show the same property maps as in Figure 2.9, except for the best fit as determined by `MPFIT`. As expected, there are variations

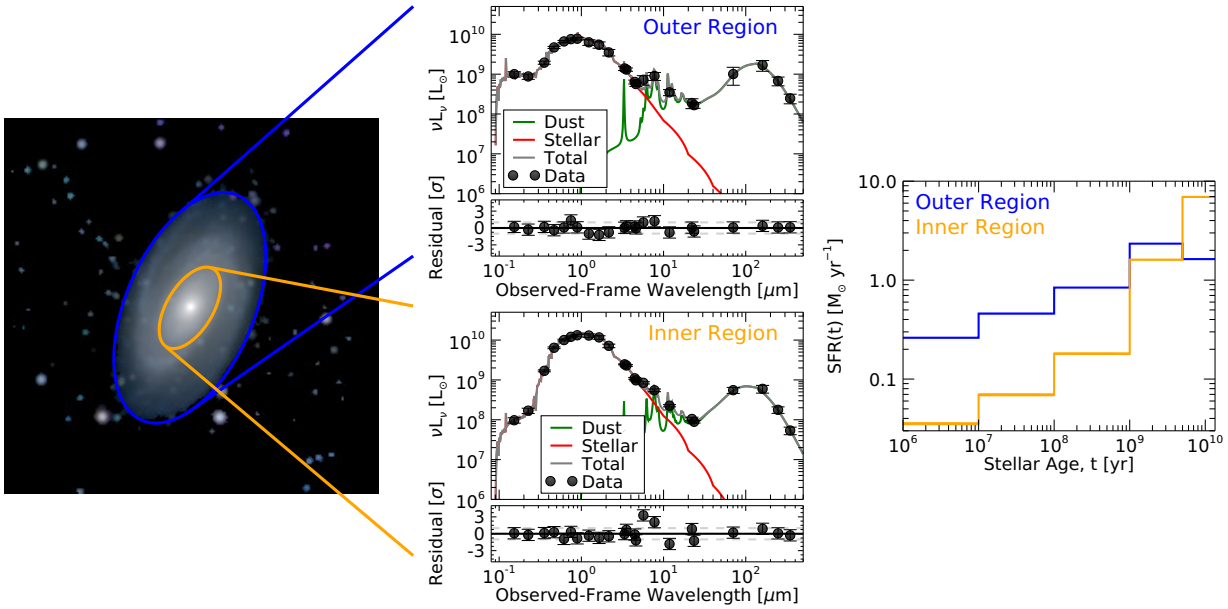

Figure 2.10: (*Left*) Composite SDSS g, r, i color image of M81 after being convolved to a common PSF of 25″ and re-binned to a pixel scale of 10″. Overlain are the 25 mag arcsec^{-2} B-band isophotal ellipse as given by HyperLeda in blue and one half of the 20 mag arcsec^{-2} K_s-band isophotal ellipse as given by Jarrett et al. (2003) in orange. (*Middle*) Total best-fit model spectra and component SEDs of the outer (upper plot) and inner (lower plot) regions of the galaxy derived by summing the individual pixels, where the outer region is all pixels between the B-band ellipse and the half of the K_s-band ellipse (i.e., between blue and orange ellipses) and the inner region is all pixels within the half of the K_s-band ellipse (i.e., inside orange ellipse). (*Right*) Resulting SFH with uncertainty ranges for the outer and inner regions as the blue and orange lines, respectively. From the SEDs and SFHs, it can be seen that the outer region has comparatively higher UV emission and lower NIR emission, which is distinguished by the fit as an overall younger population compared to the inner region.

in the results between algorithms, especially in the smoothness of the SFR and, subsequently, sSFR maps. This loss of smoothness is primarily due to the usage of the best fit rather than medians of the posterior, since the median of the posterior is rarely the same as the best-fit solution. For example, the central region can be seen to have best-fit solutions that are suggesting zero recent star formation (the colorbar is truncated due to the log-scale and to match the colorbar ranges in Figure 2.9). These zero values from `MPFIT` in low SFR regions are not unexpected, since SFR posterior distributions from the MCMC algorithm generally provide upper limits, with the

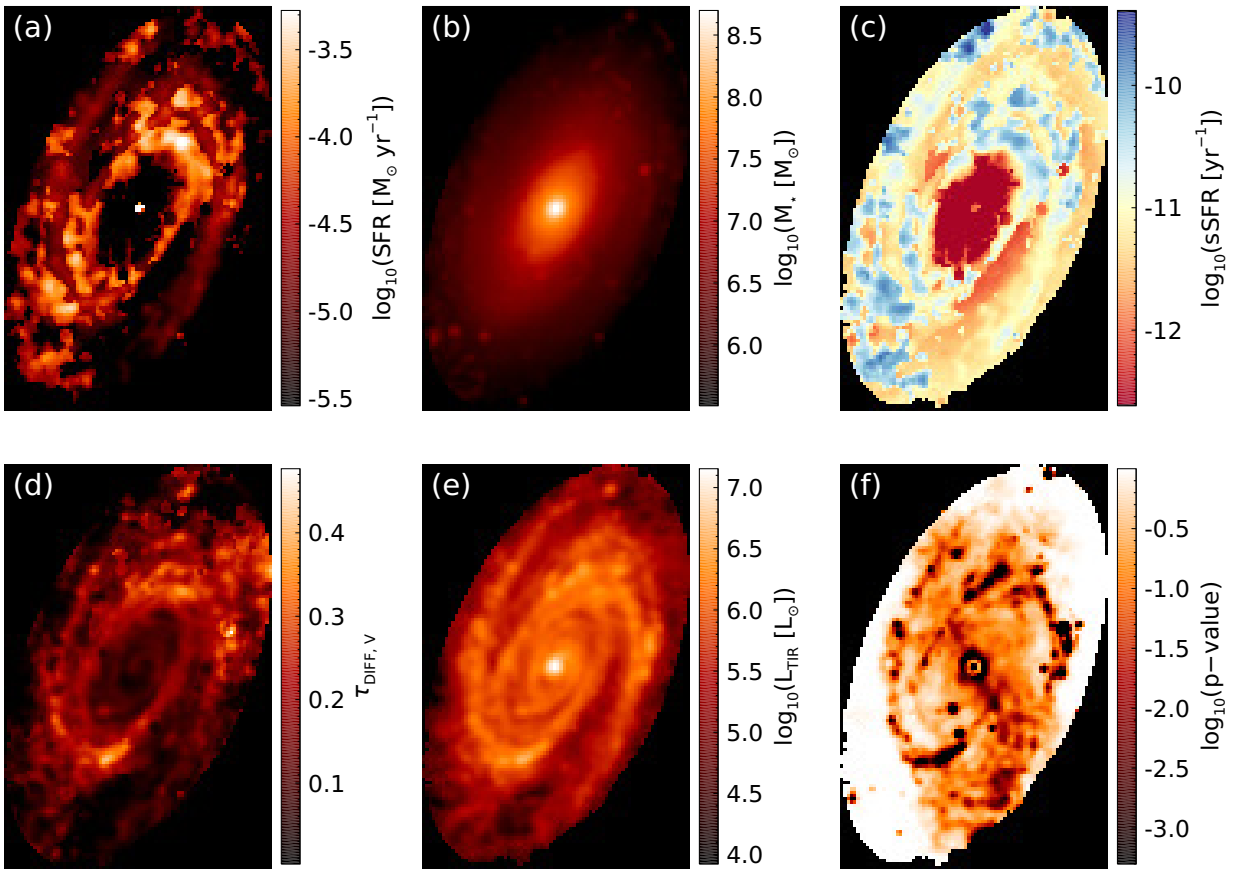

Figure 2.11: Panels (a – e) are the same as Figure 2.9 except the values correspond to the best-fit values derived from the MPFIT algorithm. The p-values in panel (f) are estimated from the a χ^2 goodness-of-fit test. The colorbar minimum and maximum ranges have been truncated to match those in Figure 2.9. Comparing these maps to those in Figure 2.9, it can be seen that some of these maps, particularly the SFR and sSFR, are not nearly as smooth, due to the use of best-fit values rather than the posterior median.

maximum probability coinciding with zero. To show how this variation in best fit and median affects the total SFR of the galaxy, each pixel in the SFR map can be summed to give a total SFR. This results in SFR $= 0.22\ M_\odot\ \mathrm{yr}^{-1}$ and SFR $= 0.44\ M_\odot\ \mathrm{yr}^{-1}$ for the MPFIT and MCMC algorithms, respectively, a difference by a factor of two. In contrast, the stellar mass, in general, is better constrained by SED fits, and the best fit is typically closer in value to the median of the posterior. Summing the pixels for the masses gives $M_\star = 4.05 \times 10^{10}\ M_\odot$ and $M_\star = 4.26 \times 10^{10}\ M_\odot$ for the MPFIT and MCMC algorithms, respectively, a difference of only 5%. Thus, the best-fit mass

map from MPFIT appears nearly identical to the median mass map from the MCMC.

2.4.2 Deep Field AGN

Here, we demonstrate how the AGN module in `Lightning` can be used with and without X-ray data by fitting the SED of J033226.49−274035.5, an X-ray detected AGN in the Chandra Deep Field South at $z = 1.03$. For both fits, the UV-to-NIR photometry were retrieved from the Guo et al. (2013) CANDELS catalog, which covers the U-band to Spitzer IRAC 8.0 μm. We additionally included the FIR data (Spitzer MIPS 24 μm to Herschel SPIRE 350 μm) from Barro et al. (2019). We corrected the CANDELS photometry for Galactic extinction using the Fitzpatrick (1999) curve, with $A_V = 0.025$, as retrieved from the IRSA DUST tool[12]. To construct the X-ray spectrum used for our fits, we queried the Chandra Source Catalog (CSC) by performing a cone search in $1''$ around the source position, finding a unique match, 2CXO J033226.4−274035, within $0.41''$. We stacked the level 3 CSC spectra and responses using the `combine_spectra` contributed script in `CIAO`[13] v4.13 (`ciao_contrib` v4.13.2). To produce the X-ray photometry used for our fits, we subtracted the background and grouped the X-ray counts into 15 log-spaced bins spanning 0.5–8.0 keV using `Sherpa` v4.13.

We modeled the resulting SED for J033226.49−274035.5 both with and without an X-ray model. In both cases, we used a stellar population with solar metallicity (i.e., $Z = 0.02$) and stellar age bins spanning 0–10 Myr, 10–100 Myr, 0.1–1 Gyr, 1–5 Gyr, and 5–5.6 Gyr (the age of the Universe at $z = 1.03$). Both models also included the SKIRTOR UV-to-IR AGN model. Simultaneously constraining the viewing angle and optical depth of the torus is difficult, so we simplified the model by setting $\tau_{9.7} = 7$, the middle of the SKIRTOR model's allowed range, while

[12] https://irsa.ipac.caltech.edu/applications/DUST/
[13] https://cxc.harvard.edu/ciao/

allowing the cosine of the viewing angle to vary freely. For the fit without an X-ray component, we allow the log of the integrated luminosity of the AGN model to vary between 11.0 and 13.0, with a uniform prior. To attenuate the UV-to-NIR emission (both the stellar and AGN emission that escapes the torus; see Section 2.2.2.1), we used the modified Calzetti et al. (2000) curve with the 2175 Å bump feature and excluding any birth cloud attenuation. The dust attenuation was set to be in energy balance with the Draine & Li (2007) dust emission model, with $U_{\rm max} = 3 \times 10^5$, $\alpha = 2$, and $q_{\rm PAH} = 0.0047$. We fix $q_{\rm PAH}$ to the minimum allowed value for this example, since high-redshift galaxies like J033226.49−274035.5 are not expected to have strong PAH emission.

For the X-ray model in this example, `Lightning` automatically includes a stellar component when using an X-ray model, and we additionally use the `qsosed` X-ray model for the AGN X-ray emission component. X-ray absorption was modeled using the `tbabs` model, with Wilms et al. (2000) abundances and a Galactic HI column density fixed at $N_{\rm H} = 9.19 \times 10^{19}$ cm^{-2}, as retrieved using the `prop_colden` tool in `CIAO`. We fit both models using the affine-invariant MCMC sampler, with an ensemble of 75 walkers running for 3×10^4 steps, assuming 10% model uncertainty. We adjusted the proposal distribution width parameter a to 1.8 to achieve acceptance fractions $> 20\%$. The free parameters and associated priors for these fits are summarized in Table 2.4. We set `Lightning` to automatically generate the final chain portion of the posterior distributions from the MCMC chains and keep the last 1000 posterior samples, with the autocorrelation times indicating convergence of the runs.

The photometry and resulting best-fitting models are shown in Figure 2.12. In Figure 2.13, we show a corner plot of the posterior distributions on the AGN parameters. Since the X-ray AGN model directly normalizes the UV-to-IR AGN model, we calculated the equivalent $L_{\rm AGN}$ from its UV-to-IR model to compare with the $L_{\rm AGN}$ estimated from the model without X-ray data. In

Table 2.4: Summary of parameters used in the J033226.49−274035.5 example.

Parameter	Prior Function	Initialization Range
All Models		
ψ_j	$\mathscr{U}(0, 10^3)$	$[10, 20]$
$\tau_{\mathrm{DIFF},V}$	$\mathscr{U}(0, 10)$	$[0, 3]$
δ	$\mathscr{U}(-1.0, 1.0)$	$[-1, 1]$
$\tau_{\mathrm{BC},V}$	Fixed	0
α	Fixed	2
U_{min}	$\mathscr{U}(0.1, 25)$	$[0.1, 5]$
U_{max}	Fixed	3×10^5
γ	$\mathscr{U}(0, 1)$	$[0, 0.1]$
q_{PAH}	Fixed	0.0047
$\tau_{9.7}$	Fixed	7
$\cos i_{\mathrm{AGN}}$	$\mathscr{U}(0, 1)$	$[0, 1]$
AGN Model − No X-ray Component		
$\log L_{AGN}$	$\mathscr{U}(11, 13)$	$[12.0, 12.5]$
AGN Model − With X-ray Component		
N_{H}	$\mathscr{U}(10^{-4}, 10^5)$	$[10^0, 10^2]$
M_{SMBH}	$\mathscr{U}(10^5, 10^{10})$	$[10^6, 10^8]$
$\log \dot{m}$	$\mathscr{U}(-1.5, 0.3)$	$[-1.0, 0.0]$

Notes – $\mathscr{U}(a, b)$ indicates a uniform distribution from a to b. Fixed parameters have their value listed in the initialization range column.

the bottom right corner of the corner plot, it can be seen that the X-ray emission places a strong constraint on the luminosity of the AGN emission. This, along with the independence of our X-ray model from the viewing angle[14], helps reduce the strong covariance of L_{AGN} and $\cos i_{\mathrm{AGN}}$ when using X-ray data.

2.4.3 Stellar X-ray Emission in an Inclined Galaxy

To demonstrate how X-rays emitted from the stellar binary population can be used to help constrain the SFR for an inclined galaxy (since X-rays are less sensitive to dust attenuation), we

[14]Note, however, that a dependence of the X-ray emission on viewing angle is favored by observations and is implemented in, e.g. CIGALE (Yang et al., 2022) and X-ray AGN models incorporating the effects of the torus, e.g. MYTORUS (Murphy & Yaqoob, 2009), XCLUMPY (Tanimoto et al., 2019), and UXCLUMPY (Buchner et al., 2019). We choose not to implement X-ray anisotropy in `Lightning` at this time due to our inclusion of a separate absorption component for the X-ray emission, though we do not rule it out for a future release.

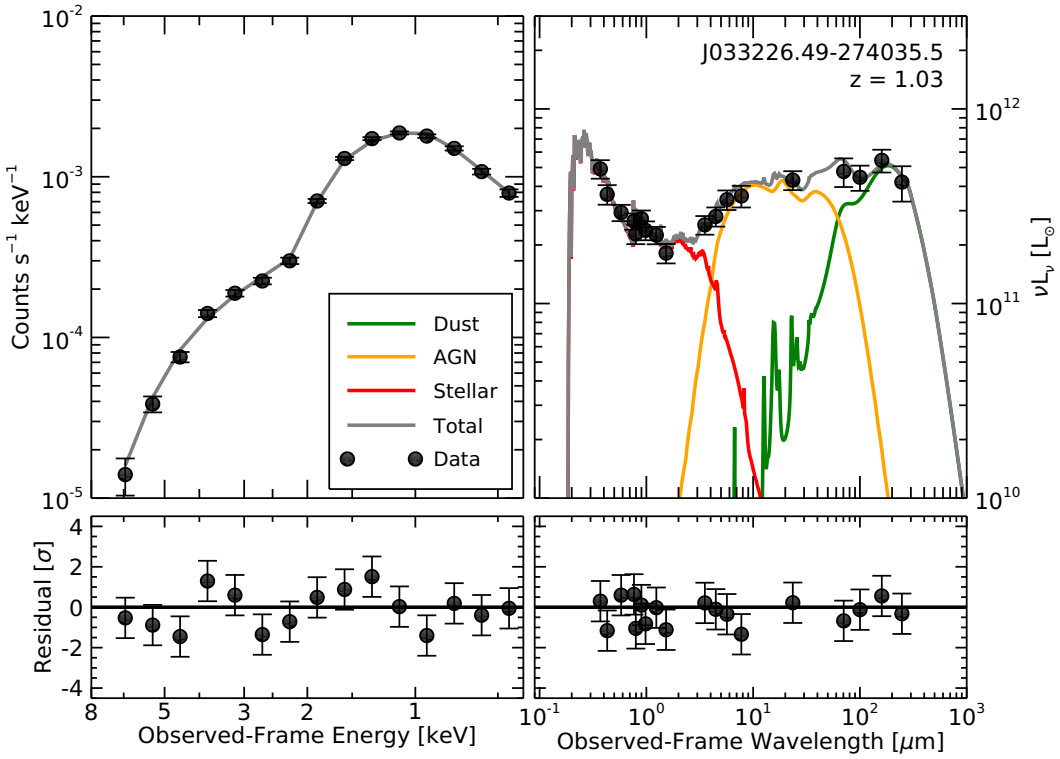

Figure 2.12: The X-ray-to-IR SED fit for J033226.49−274035.5. In the left panels, we show the instrumental X-ray spectrum (in terms of count rate density) with its best-fit model and residuals. In the right panels, we show the observed UV-to-IR SED (in terms of luminosity), its best-fitting model, and residuals. The best-fit model minimizes the total X-ray and UV-to-IR $-\log(P_{\rm post})$. The `Lightning` X-ray model implementation can provide rudimentary X-ray spectral fits, and directly connect them to the UV-to-IR SED fit.

fit the global broadband photometry of the edge-on nearby galaxy, NGC 4631. For the UV-to-submillimeter photometry, we utilized the 30-band SINGS/KINGFISH data presented in Table 2 of Dale et al. (2017). We then corrected the data for Galactic extinction before fitting, using the $E(B-V)$ values in Table 1 and A_V-normalized extinction values in Table 2 of Dale et al. (2017).

For the X-ray photometry, we made use of the Chandra ACIS-I data for a single ≈58 ks observation (ObsID 797). These data were reduced and point-source catalogs were produced following the procedures detailed in Section 3.2 of Lehmer et al. (2019) using `CIAO` v.4.13. To obtain

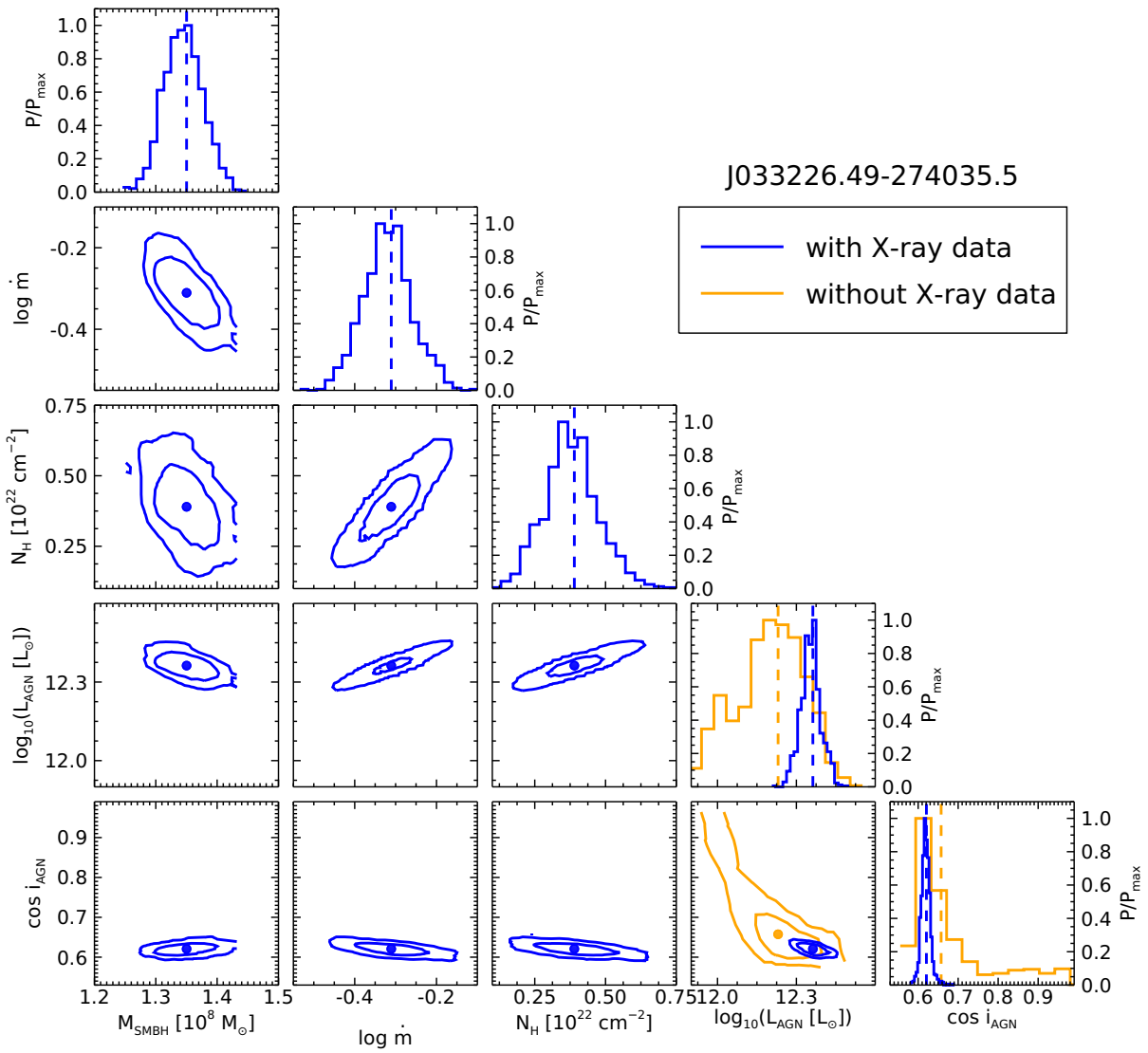

Figure 2.13: A corner plot of the AGN model parameters for J033226.49−274035.5, fit with and without an X-ray component as the blue and orange lines, respectively. The X-ray emission is modeled with the theoretical `qsosed` model, providing indirect estimates of the SMBH mass $M_{\rm SMBH}$ and Eddington ratio $\dot{m} = \dot{M}/\dot{M}_{\rm edd}$. Fitting the X-ray emission also allows us to better constrain the integrated UV-to-IR luminosity of the AGN model ($L_{\rm AGN}$), and reduce the degeneracy of the luminosity with the viewing angle ($\cos i_{\rm AGN}$).

spectral constraints, we utilized the `specextract` routine to extract cumulative point-source and background spectral data. For the point-source spectrum, we chose to utilize circular apertures with radii that were 4 times the 90% encircled energy fraction and centered on the 22 X-ray de-

tected point sources within the K_s-band footprint of the galaxy (see Jarrett et al., 2003, for details on this region). We extracted the background spectrum from four large regions (circles with radii spanning 1–1.5 arcmin) outside the galactic footprint that were chosen to be free of bright X-ray detected point-sources. Using `Sherpa` we fit the background-subtracted point-source spectrum using a model that consisted of both thermal and absorbed power-law components (i.e., `apec + tbabs` $\times$ `pow`) to account for diffuse gas and the X-ray binary emission, respectively. Using the best-fit model, we calculated X-ray fluxes in the energy bands of 0.5–1, 1–2, 2–4, and 4–7 keV, with 10% uncertainty on the fluxes. When fitting this X-ray data with `Lightning`, we accounted for Galactic absorption by assuming a Galactic HI column density of $N_{\rm H} = 1.29 \times 10^{20}$ cm^{-2}, as derived from the `prop_colden` tool in `CIAO`.

To show the effects of including X-rays and inclination-dependence, we modeled and fit the SED using four different permutations that include or exclude X-ray data with either the Calzetti et al. (2000) or inclination-dependent attenuation curves. For all four fits, we used a stellar population with solar metallicity (i.e, $Z = 0.02$) and SFH age bins of 0–10 Myr, 10–100 Myr, 0.1–1 Gyr, 1–5 Gyr, and 5–13.6 Gyr. Additionally, all fits included the Draine & Li (2007) dust emission model with the fixed values of $U_{\rm max} = 3 \times 10^5$ and $\alpha = 2$. As for the dust attenuation, which was set to be in energy balance with the dust emission, the models with the Calzetti et al. (2000) curve utilized the base curve extrapolated to the Lyman limit. For the fits with the inclination-dependent curve, we assumed the galaxy to be disk dominated and have a minimal contribution from the bulge (i.e., $B/D = 0$), a choice motivated by visual inspection. We further assume the youngest three age bins to be part of the young stellar population (i.e., $r^{0,\rm old} = 0$ for 0 – 1 Gyr and $r^{0,\rm old} = 1$ otherwise). Finally, X-ray absorption was included using the `tbabs` model with Wilms et al. (2000) abundances for the fits that included X-rays.

Table 2.5: Summary of parameters used in the NGC 4631 example.

Parameter	Prior Function	Initialization Range
All Models		
ψ_j	$\mathscr{U}(0,10^3)$	$[0,10]$
α	Fixed	2
$U_{\rm min}$	$\mathscr{U}(0.1,25)$	$[0.1,5]$
$U_{\rm max}$	Fixed	3×10^5
γ	$\mathscr{U}(0,1)$	$[0,0.1]$
$q_{\rm PAH}$	$\mathscr{U}(0.0047,0.0458)$	$[0.0047,0.0458]$
Calzetti et al. (2000) Models		
$\tau_{{\rm DIFF},V}$	$\mathscr{U}(0,10)$	$[0,1]$
Inclination-dependent Models		
$\cos i$	Tabulated[a]	$[0,0.2]$
τ_B^f	$\mathscr{U}(0,8)$	$[0,4]$
B/D	Fixed	0
F	$\mathscr{U}(0,0.61)$	$[0,0.61]$
X-ray Models		
$N_{\rm H}$	$\mathscr{U}(10^{-4},10^5)$	$[10^{-1},10^2]$

Notes – $\mathscr{U}(a,b)$ indicates a uniform distribution from a to b. Fixed parameters have their value listed in the initialization range column.
[a]Generated using the Monte Carlo method described in Section 3 of Doore et al. (2022).

To fit the four models to the SED, we utilized the affine-invariant MCMC algorithm with 5% model uncertainty, which we ran with 75 walkers for 10^4 and 5×10^4 trials for the Calzetti et al. (2000) and inclination-dependent models, respectively. The drastic increase in trials for the inclination-dependent models is required to reach convergence (i.e., autocorrelation times ≥ 50) of the $\cos i$ and τ_B^f parameters, since they are generally highly correlated (Doore et al., 2021). For all free parameters, we implemented the priors and limited initialization ranges as listed in Table 2.5. Since we know that NGC 4631 is an edge-on galaxy, we set a tabulated prior on $\cos i$ generated from the Monte Carlo method described in Section 3 of Doore et al. (2021), which converts an axis ratio into a distribution of inclination. The axis ratio and its uncertainty were retrieved from HyperLeda, which provides the axis ratio calclated from the 25 mag arcsec^{-2} B-band isophote.

With the described models and algorithm, we used `Lightning` to fit each model to the SED, assuming a luminosity distance to NGC 4631 of 7.62 Mpc as given in Dale et al. (2017). For each model, we set `Lightning` to automatically generate the final post-processed chain portion from the autocorrelation times and keep the final 2000 posterior samples. After confirming convergence of the fits from the autocorrelation time, we compared how the inclusion of X-rays influenced the derived properties.

In the right panels of Figure 2.14, we show the histograms of the resulting posterior distributions of the recent SFR of the last 100 Myr. From these distributions, each of the four models can be seen to have general agreement. However, the Calzetti et al. (2000) models have a stronger variation when including the X-rays compared to the inclination-dependent models, since the Calzetti et al. (2000) attenuation model, which assumes a uniform, spherical distribution of stars and dust, is too simplistic for edge-on galaxies. Including the inclination dependence allows for a more accurate estimate of the SFR, with the inclusion of the X-rays increasing the precision of the estimate as would be expected when adding additional data. Further, the X-ray data rules out some higher SFR solutions (i.e., SFR $> 8\ M_{\odot}\ \mathrm{yr}^{-1}$), as they become more unlikely with the X-ray data constraint.

2.4.4 Comparison with other SED Fitting Codes

To show how `Lightning` compares with other Bayesian SED fitting codes, we fit the global broadband photometry of the nearby spiral galaxy, NGC 628 using `Lightning`, `Prospector`[15], and `BAGPIPES`[16]. These two comparison codes are by no means a complete sample of the other Bayesian SED fitting codes currently available. However, we have chosen to compare directly

[15] https://github.com/bd-j/prospector
[16] https://github.com/ACCarnall/bagpipes

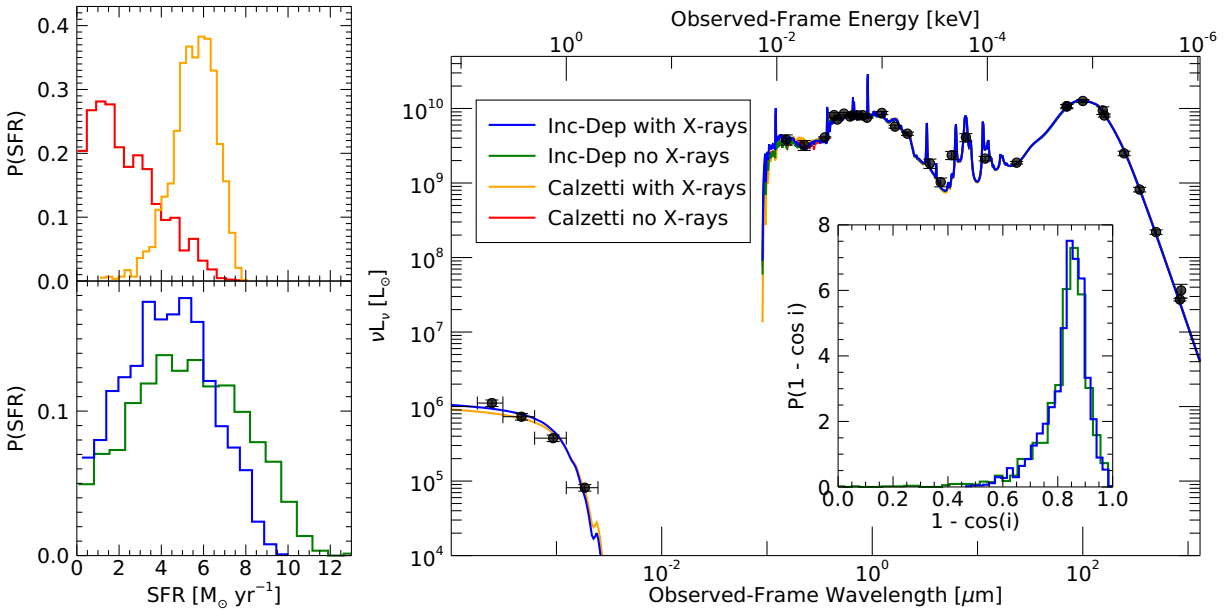

Figure 2.14: (*Left*) Histograms of the posterior distribution functions of the SFR of the last 100 Myr for NGC 4631, which are area normalized. The Calzetti et al. (2000) models are shown in the upper panel and the inclination-dependent models are shown in the lower panel. (*Right*) The total best-fit model spectrum to the observed SED for each of the four models. Inlaid in the SED plot is the posterior distributions of inclination (in terms of $1-\cos i$, where $1-\cos i = 1$ is edge-on) for the inclination-dependent models. This inlay shows that the models are correctly predicting a close to edge-on view. In all plots, the inclination-dependent model with and without X-rays and the Calzetti et al. (2000) model with and without X-rays are shown as the blue, green, orange, and red lines, respectively. While the best-fit model spectra are practically identical for each model, the resulting SFR distributions vary depending on the attenuation model and inclusion of X-ray emission.

with `Prospector` and `BAGPIPES` due to their inclusion of similar models and algorithms (e.g., non-parametric SFHs and Bayesian sampling algorithms) as `Lightning` in the interest of a "fair" comparison.[17] While the codes can be set to have many matching components, there remain some differences between them that will generate differences in their results. We list the components of each code in Table 2.6 for ease in comparison and note that the differences in IMFs are likely to cause the most variation in results (Kennicutt & Evans, 2012; Conroy, 2013).

The UV-to-submillimeter photometry of NGC 628 used for this comparison was taken from the

[17]For a more complete comparison of the most established SED fitting codes, we recommend Pacifici et al. (2022) and note that `Lightning` is not included in their comparison due to its more recent development.

Table 2.6: Summary of the components used when fitting with each SED fitting code.

Code	SSP	IMF	Metal.	SFH	Dust att.	Dust em.	Sampler
`Lightning`	`PÈGASE`	K01	$Z = 0.02$	Non-param.	Calzetti et al. (2000)	Draine & Li (2007)	Affine-in. MCMC
`Prospector`	`MILES+MIST`	K01	$Z = 0.02$	Non-param.	Calzetti et al. (2000)	Draine & Li (2007)	Affine-in. MCMC
`BAGPIPES`	BC03	KB02	$Z = 0.02$	Non-param.	Calzetti et al. (2000)	Draine & Li (2007)	Nested Sampling

Column 1: SED fitting code. Column 2: Stellar population synthesis models (`MILES+MIST` = `MILES` spectral library (Falcón-Barroso et al., 2011) with `MIST` isochones (Dotter, 2016; Choi et al., 2016); BC03 (Bruzual & Charlot, 2003)). Column 3: Initial mass function (K01 (Kroupa, 2001); KB02 (Kroupa & Boily, 2002)). Column 4: Metallicity, set to the specified constant value for all ages of SFH. Column 5: SFH form, all codes used the same age bins of 0 – 10 Myr, 10 – 100 Myr, 0.1 – 1 Gyr, 1 – 5 Gyr, and 5 – 13.4 Gyr. Column 6: Dust attenuation curve, all codes used the base Calzetti et al. (2000) curve extrapolated to the Lyman limit. Column 7: Dust emission model, all codes used the Draine & Li (2007) model with energy balance and fixed $\alpha = 2$. `Prospector` and `BAGPIPES` have $U_{\rm max} = 10^6$, while `Lightning` has $U_{\rm max} = 3 \times 10^5$ (these differences in $U_{\rm max}$ have minimal effects on the models). Column 8: Bayesian sampler, `Lightning` and `Prospector` use the same affine-invariant MCMC algorithm, while `BAGPIPES` uses the `MultiNest` nested sampling algorithm.

30-band SINGS/KINGFISH data presented in Table 2 of Dale et al. (2017), which we corrected for Galactic extinction using the extinction values given in Table 1 and 2 of Dale et al. (2017). Since `Prospector` and `BAGPIPES` do not have a built in model uncertainty method like `Lightning`, we added in quadrature an additional 10% uncertainty to the quoted uncertainties in Dale et al. (2017) to act as model uncertainties in our fits. We note that this is the typically utilized method in SED fitting to account for model uncertainties, and therefore it is a reasonable method for accounting for additional uncertainty not contained within the data.

For the models in each code, we used a stellar population, as given in Table 2.6, with constant solar metallicity (i.e, $Z = 0.02$) and SFH age bins of 0–10 Myr, 10–100 Myr, 0.1–1 Gyr, 1–5 Gyr, and 5–13.4 Gyr. We attenuated the stellar emission in all codes using the original Calzetti et al. (2000) curve extrapolated to the Lyman limit. Finally, the dust attenuation was set to be in energy balance with the Draine & Li (2007) dust emission model, where $\alpha = 2$, $U_{\rm max} = 3 \times 10^5$ for `Lightning`, and $U_{\rm max} = 10^6$ for `Prospector` and `BAGPIPES` (the differences in $U_{\rm max}$ have minimal

effects on the models, see Section 2.2.4).

To fit the SED with each code, we utilized their Bayesian sampling algorithms to generate posterior distributions containing 2000 samples. For `Lightning` and `Prospector`, we ran their affine-invariant MCMC algorithm for 10^4 trials with 75 walkers, which was sufficient for each code to reach convergence using the autocorrelation times. The resulting chains were then post-processed (i.e., burn-in removed and thinned) to the 2000 samples using the longest autocorrelation time of any parameter.[18] For `BAGPIPES`, we used the available `MultiNest` (Feroz et al., 2009,0) nested sampling algorithm, which we ran using 1000 live points. We note that we increased the number of live points from the default of 400 to 1000 after testing showed that we could get significant variation in the posteriors between runs when using fewer than 1000 live points for our chosen model. In Table 2.7, we list the free parameters in each model along with their utilized prior function. We note that we used the same priors across each code, except for the SFH parameters. Unlike `Lightning`, `Prospector` and `BAGPIPES` normalize their SFHs by stellar mass rather than SFR. Therefore, they require different priors to accommodate the change in normalization, which is expected to cause minimal to no effects on the fits due to the utilization of the same SFH bins.

With the results from the fits, we first compared the computational performance of each code. All codes were run sequentially on the author's 2016 MacBook, which contains a 2-core, 1.2 GHz CPU. `Lightning`, `Prospector`, `BAGPIPES` took 1279.7 s, 4864.2 s, and 920.0 s, respectively, to complete their fitting. While `BAGPIPES` can be seen to be almost 1.4 times faster than `Lightning` (which is 3.8 times faster than `Prospector`), it is important to note that this is due to the fewer likelihood evaluations needed by the nested sampling algorithm, which was designed (in part) to

[18] `Prospector` also has a nested sampling algorithm. However, we chose to use the affine-invariant MCMC algorithm to have the closest possible comparison with `Lightning`.

Table 2.7: Summary of parameters used in the NGC 628 example.

Parameter	Prior Function	`Lightning` Init.[a]	`Prospector` Init.[b]	`BAGPIPES` Init.[c]
		All Models		
$\tau_{\mathrm{DIFF},V}$[d]	$\mathscr{U}(0,10)$	$[0,3]$	$[1,0.5]$	$\cdots$
α	Fixed	2	2	2
U_{min}	$\mathscr{U}(0.1,25)$	$[0.1,10]$	$[5,1]$	$\cdots$
U_{max}	Fixed	3×10^5	10^6	10^6
γ	$\mathscr{U}(0,1)$	$[0,0.5]$	$[0.1,0.5]$	$\cdots$
q_{PAH}	$\mathscr{U}(0.0047,0.0458)$	$[0.0047,0.0458]$	$[0.02,0.01]$	$\cdots$
		`Lightning` SFH		
ψ_j	$\mathscr{U}(0,10^3)$	[0, 10]	$\cdots$	$\cdots$
		`Prospector` and `BAGPIPES` SFH		
M_j[e]	$\mathscr{U}(0,10^{12})$	$\cdots$	$[10^7,10^7]$	$\cdots$

Notes – $\mathscr{U}(a,b)$ indicates a uniform distribution from a to b. Fixed parameters have their value listed in the initialization range column.
[a]The initialization range specified for `Lightning`.
[b]The initialization parameters specified for `Prospector`. The first value is the median starting point, and the second is the dispersion scale around that point.
[c]The nested sampling algorithm in `BAGPIPES` does not require initialization. However, we list this column to show the fixed parameter values.
[d]`BAGPIPES` normalizes the Calzetti et al. (2000) curve with A_V, which we convert to τ_V via $\tau_V = 0.4\ln(10)A_V$.
[e]The stellar mass parameter in $M_\odot$. `Prospector` and `BAGPIPES` normalize their SFH bins to unit stellar mass, where `Lightning` normalizes to unit SFR. Therefore, the priors on the parameters are different.

reduce the number of model evaluations required to produce a full sampling of the posterior (see, e.g., Feroz et al., 2009,0). Where `Lightning` and `Prospector` each took 1.125×10^6 likelihood evaluations, `BAGPIPES` only performed an order of magnitude fewer (115,921 evaluations) to fit. Therefore, the difference in algorithms allowed for an overall similar fitting time as `Lightning`. However, in terms of likelihood evaluations per second (which is a better comparison of the practical *speed* of different SED fitting codes), `Lightning` is almost 7 times faster than `BAGPIPES`, which is a result of its designed computational efficiency.

To show how the derived results compare at a base level, we show the observed photometry

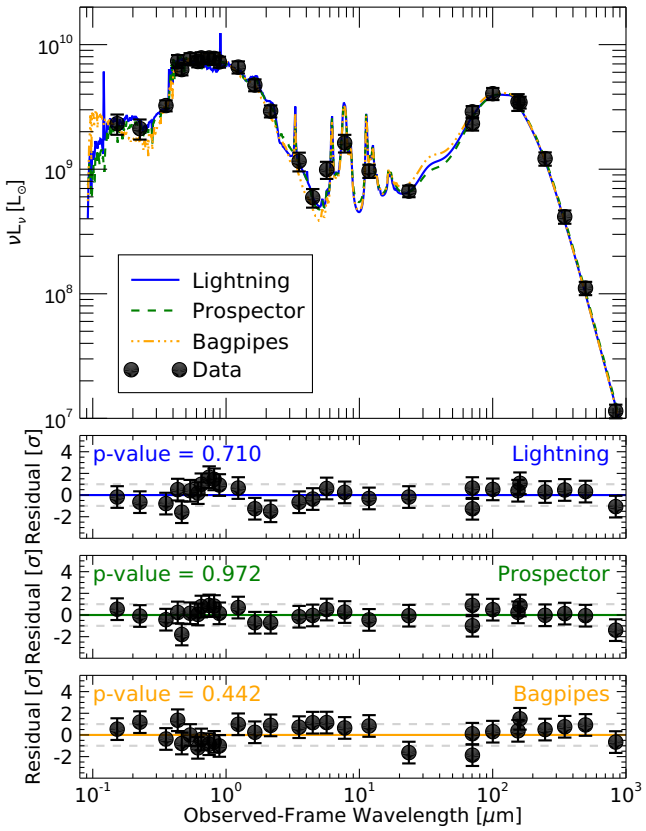

Figure 2.15: The total best-fit model spectra to the observed SED of NGC 628 and the associated residuals as generated by `Lightning`, `Prospector`, and `BAGPIPES` as the blue, green, and orange lines, respectively. For each code, the p-value from a PPC is shown in the upper left of each residual plot. In general, it can be seen that all three codes model the data well, both from the PPC and the residuals.

and best-fitting model spectra in Figure 2.15. In the lower residual panels for each fit, we also show the derived p-value for the fits calculated from a PPC. From the p-values and residuals, it can be seen that all codes appropriately model the data. It is interesting to note that the best-fit model spectra and resulting residuals from the `Lightning` and `Prospector` fits are highly similar, since their models only differ by the SSPs. However, `BAGPIPES` identifies a comparatively unique best-fit spectrum and residuals in the UV-to-NIR. This variation is expected, since the different IMF in `BAGPIPES` can create a substantial variation in the UV-to-NIR stellar emission models.

Finally, in Figure 2.16, we show the derived SFHs and posterior distributions for five commonly

derived parameters from SED fitting: the (surviving) stellar mass ($M_\star$), the SFR of the last 100 Myr, the sSFR of the last 100 Myr, the V-band attenuation (A_V), and $L_{\rm TIR}$ (i.e., the bolometric luminosity from 8–1000 μm). From these distributions in the lower left, it can be seen that all three codes have derived parameters, except stellar mass, that are in excellent agreement. The variation in stellar mass between codes is expected and entirely due to the differences in SSPs and IMFs, which dictate the surviving stellar mass of the populations over time. As for the other parameters and SFHs, `Lightning` and `Prospector` have near identical results, which is a quality indicator given that both codes were run using almost identical models and were independently developed. As for the differences with `BAGPIPES`, these are a combination of the differences in fitting algorithms and IMFs, especially for the SFH. However, overall for both `Lightning` and SED fitting as a whole, it is reassuring that codes with different models and algorithms generally return derived parameters that are in statistical agreement.

2.5 Summary and Planned Additions

In this paper, we have presented the most recent version of the SED fitting code `Lightning`. The new version of `Lightning` contains a variety of models and algorithms that can be used to account for any combination of stellar, dust, and AGN emission in an observed X-ray to submillimeter SED. A brief review of each of these models and algorithms is as follows:

- Stellar emission can be modeled using the SSPs from `PÉGASE` integrated over the age bins given by the user-defined non-parametric SFH. Stellar X-ray emission from the XRBs is linked to the SFH using a power-law spectral model and the empirical parameterizations of $L_X/M_\star$ with stellar age given in Gilbertson et al. (2022).

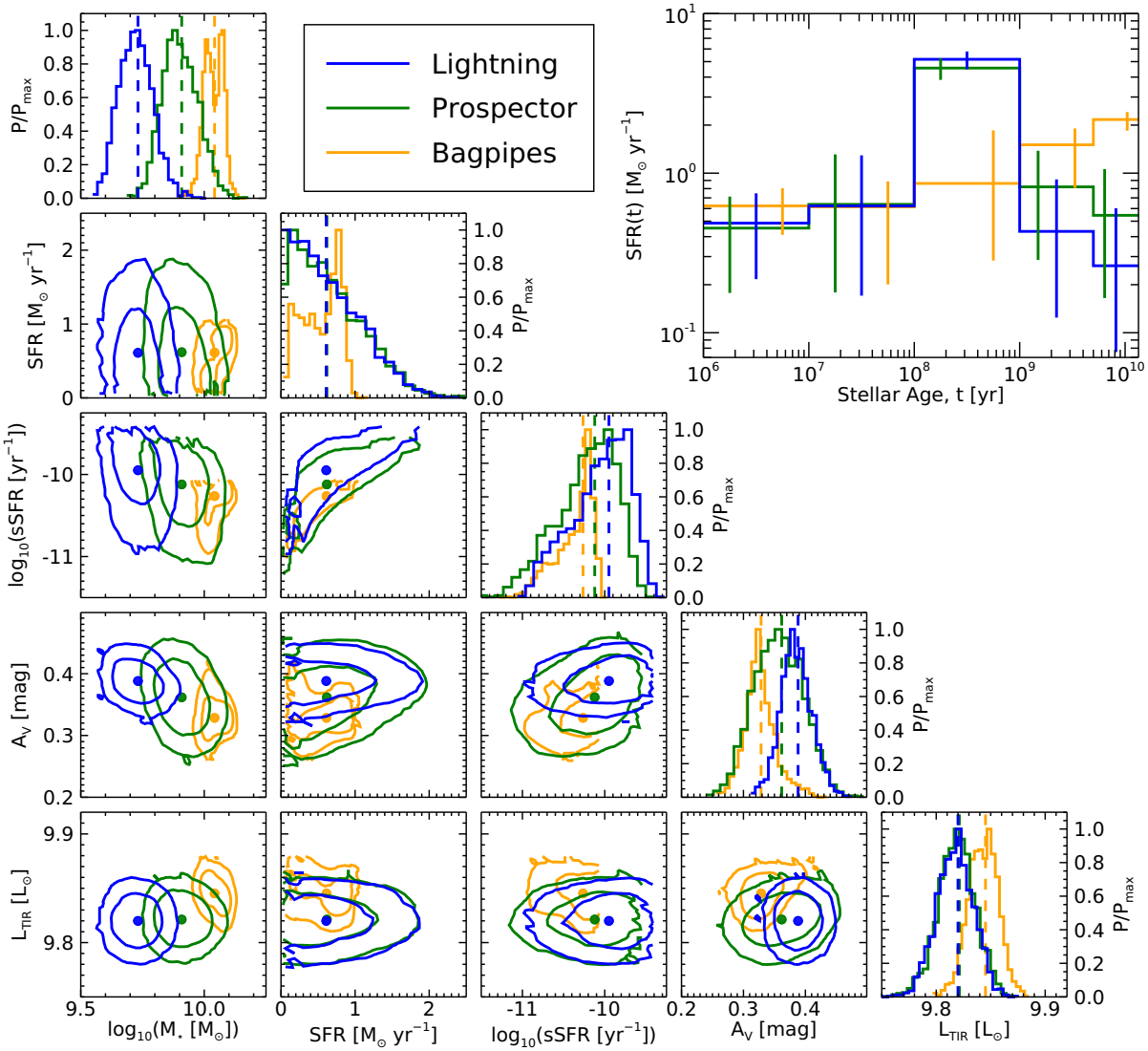

Figure 2.16: (*Lower Left*) A corner plot of the derived parameters for NGC 628. These parameters include the stellar mass ($M_\star$), the recent SFR of the last 100 Myr, the sSFR of the last 100 Myr, the V-band attenuation (A_V), and the $L_{\rm TIR}$ for each SED fitting code. (*Upper Right*) The median SFH with the 16th and 84th percentile uncertainty range given as the offset vertical lines for each SED fitting code. For all plots, the results from `Lightning`, `Prospector`, and `BAGPIPES` are given as the blue, green, and orange lines, respectively. From these plots, it can be seen that the results from `Lightning` and `Prospector` are highly consistent, while the `BAGPIPES` results vary in consistency, especially for the SFH.

- AGN emission can be modeled in the UV-to-IR using a subset of the SKIRTOR models.

  X-ray AGN emission can be modeled as (1) a simple power-law spectra, which is tied to

the UV-to-IR AGN emission using the Lusso & Risaliti (2017) $\tilde{L}_{2\ \mathrm{keV}} - \tilde{L}_{2500}$ relationship or (2) the `qsosed` models from Kubota & Done (2018), which directly scale the UV-to-IR emission as a function of the mass and Eddington ratio of the SMBH.

- Dust attenuation of the UV-to-NIR emission can be modeled using either a modified form of the Calzetti et al. (2000) curve or the inclination-dependent curve described in Doore et al. (2021). Absorption of X-ray emission, when included, is modeled using either the `tbabs` or the `Sherpa atten` models.

- Dust emission can be modeled using the Draine & Li (2007) model. When included, dust emission can be set to be in energy balance with the dust attenuation, which requires the bolometric luminosity of the dust emission to be equal to the bolometric luminosity of the attenuated light.

- Algorithms for fitting the models to the data include both maximum likelihood and Bayesian methods. For the maximum likelihood method, `Lightning` uses the `MPFIT` implementation of the gradient-descent LevenbergMarquardt algorithm. For the Bayesian methods, `Lightning` includes two MCMC algorithms, an adaptive Metropolis-Hastings algorithm from Andrieu & Thoms (2008) and an implementation of the Goodman & Weare (2010) affine-invariant algorithm.

With these models and algorithms, we presented different example applications of `Lightning`. These examples included (1) deriving spatially resolved stellar properties of M81 using an SED map, (2) demonstrating how the covariance between the viewing angle and luminosity of an AGN can be reduced by including X-ray emission, (3) exploring how X-ray emission and inclination-dependent attenuation can be used to constrain the SFR of an edge-on galaxy, and (4) comparing

the performance of Lightning to similar SED fitting codes (Prospector and BAGPIPES). From these examples, we clearly demonstrate the capabilities of Lightning and some of its potential uses.

In future updates to Lightning, we plan to expand our current PÉGASE stellar models. This will include adding additional IMF choices and allowing for a constant but continuous metallicity, which, like other SED fitting codes, we plan to have as an optional free parameter. Additionally, Lightning is currently restricted to using an exact redshift value if it is used as the distance indicator. We plan to allow for increased flexibility in redshift, where it can have an associated prior distribution when fitting using a Bayesian method. This would allow for better propagation of uncertainty when using photometric redshifts, which can have large associated uncertainties.

Further, since Lightning was originally developed to be used in XRB population studies, we plan to add new SSPs like BPASS[19] (Eldridge et al., 2017; Stanway & Eldridge, 2018) and/or POSYDON[20] (Fragos et al., 2022) that include binary population evolution. This would allow for more accurate stellar emission models, as binary populations can significantly influence the stellar emission (Eldridge & Stanway, 2020). Additionally, binary stars are the progenitors of compact object binaries. Future versions of binary stellar population models may provide predictions for the observed X-ray binary luminosity function and its evolution with age and metallicity, based on the same prescriptions that govern the age and metallicity evolution of the stellar population. By adopting such models, we can self-consistently produce $L_X/M_\star$ with our stellar population models rather than relying on empirical relations.

[19]https://bpass.auckland.ac.nz
[20]https://posydon.org

References

Abdeen, S., Davis, B. L., Eufrasio, R., et al. 2022, MNRAS, 512, 366

Andrieu, C., & Thoms, J. 2008, Statistics and Computing, 18, 30

Barro, G., Pérez-González, P. G., Cava, A., et al. 2019, ApJS, 243, 22

Boquien, M., Burgarella, D., Roehlly, Y., et al. 2019, A&A, 622, A103

Brooks, S. P., & Gelman, A. 1998, Journal of Computational and Graphical Statistics, 7, 434

Bruzual, G., & Charlot, S. 2003, MNRAS, 344, 1000

Buchner, J., Brightman, M., Nandra, K., Nikutta, R., & Bauer, F. E. 2019, A&A, 629, A16

Burgarella, D., Buat, V., & Iglesias-Páramo, J. 2005, MNRAS, 360, 1413

Byler, N., Dalcanton, J. J., Conroy, C., & Johnson, B. D. 2017, ApJ, 840, 44

Calzetti, D., Armus, L., Bohlin, R. C., et al. 2000, ApJ, 533, 682

Carnall, A. C., Leja, J., Johnson, B. D., et al. 2019, ApJ, 873, 44

Carnall, A. C., McLure, R. J., Dunlop, J. S., & Davé, R. 2018, MNRAS, 480, 4379

Casey, C. M. 2012, MNRAS, 425, 3094

Charlot, S., Worthey, G., & Bressan, A. 1996, ApJ, 457, 625

Chevallard, J., & Charlot, S. 2016, MNRAS, 462, 1415

Choi, J., Dotter, A., Conroy, C., et al. 2016, ApJ, 823, 102

Cid Fernandes, R., Mateus, A., Sodré, L., Stasińska, G., & Gomes, J. M. 2005, MNRAS, 358, 363

Ciesla, L., Charmandaris, V., Georgakakis, A., et al. 2015, A&A, 576, A10

Conroy, C. 2013, ARA&A, 51, 393

Conroy, C., & Gunn, J. E. 2010, ApJ, 712, 833

Conroy, C., Gunn, J. E., & White, M. 2009, ApJ, 699, 486

Conroy, C., White, M., & Gunn, J. E. 2010, ApJ, 708, 58

da Cunha, E., Charlot, S., & Elbaz, D. 2008, MNRAS, 388, 1595

Dale, D. A., Helou, G., Magdis, G. E., et al. 2014, ApJ, 784, 83

Dale, D. A., Bendo, G. J., Engelbracht, C. W., et al. 2005, ApJ, 633, 857

Dale, D. A., Cook, D. O., Roussel, H., et al. 2017, ApJ, 837, 90

Devriendt, J. E. G., Guiderdoni, B., & Sadat, R. 1999, A&A, 350, 381

Doore, K., Eufrasio, R. T., Lehmer, B. D., et al. 2022, ApJ, 931, 53

—. 2021, ApJ, 923, 26

Dotter, A. 2016, ApJS, 222, 8

Draine, B. T., & Li, A. 2007, ApJ, 657, 810

Draine, B. T., Dale, D. A., Bendo, G., et al. 2007, ApJ, 663, 866

Eldridge, J. J., & Stanway, E. R. 2020, arXiv e-prints, arXiv:2005.11883

Eldridge, J. J., Stanway, E. R., Xiao, L., et al. 2017, PASA, 34, e058

Eufrasio, R. T., Lehmer, B. D., Zezas, A., et al. 2017, ApJ, 851, 10

Falcón-Barroso, J., Sánchez-Blázquez, P., Vazdekis, A., et al. 2011, A&A, 532, A95

Ferland, G. J., Korista, K. T., Verner, D. A., et al. 1998, PASP, 110, 761

Ferland, G. J., Porter, R. L., van Hoof, P. A. M., et al. 2013, RMxAA, 49, 137

Feroz, F., Hobson, M. P., & Bridges, M. 2009, MNRAS, 398, 1601

Feroz, F., Hobson, M. P., Cameron, E., & Pettitt, A. N. 2019, The Open Journal of Astrophysics, 2, 10

Fioc, M., & Rocca-Volmerange, B. 1997, A&A, 326, 950

Fitzpatrick, E. L. 1999, PASP, 111, 63

Foreman-Mackey, D., Hogg, D. W., Lang, D., & Goodman, J. 2013, PASP, 125, 306

Fragos, T., Andrews, J. J., Bavera, S. S., et al. 2022, arXiv e-prints, arXiv:2202.05892

Fritz, J., Franceschini, A., & Hatziminaoglou, E. 2006, MNRAS, 366, 767

Gehrels, N. 1986, ApJ, 303, 336

Gelman, A., Meng, X.-L., & Stern, H. 1996, Statistica Sinica, 6, 733

Gelman, A., & Rubin, D. B. 1992, Statistical Science, 7, 457

Genel, S., Vogelsberger, M., Springel, V., et al. 2014, MNRAS, 445, 175

Gilbertson, W., Lehmer, B. D., Doore, K., et al. 2022, ApJ, 926, 28

Gilda, S., Lower, S., & Narayanan, D. 2021, ApJ, 916, 43

Goodman, J., & Weare, J. 2010, Communications in Applied Mathematics and Computational Science, 5, 65

Groves, B., Dopita, M. A., Sutherland, R. S., et al. 2008, ApJS, 176, 438

Guo, Y., Ferguson, H. C., Giavalisco, M., et al. 2013, ApJS, 207, 24

Han, Y., & Han, Z. 2012, ApJ, 749, 123

—. 2014, ApJS, 215, 2

—. 2019, ApJS, 240, 3

Hastings, W. K. 1970, Biometrika, 57, 12

Iyer, K., & Gawiser, E. 2017, ApJ, 838, 127

Jarrett, T. H., Chester, T., Cutri, R., Schneider, S. E., & Huchra, J. P. 2003, AJ, 125, 525

Johnson, B. D., Leja, J., Conroy, C., & Speagle, J. S. 2021, ApJS, 254, 22

Kennicutt, R. C., & Evans, N. J. 2012, ARA&A, 50, 531

Kriek, M., & Conroy, C. 2013, ApJ, 775, L16

Kriek, M., van Dokkum, P. G., Labbé, I., et al. 2009, ApJ, 700, 221

Kroupa, P. 2001, MNRAS, 322, 231

Kroupa, P., & Boily, C. M. 2002, MNRAS, 336, 1188

Kubota, A., & Done, C. 2018, MNRAS, 480, 1247

Lehmer, B. D., Eufrasio, R. T., Basu-Zych, A., et al. 2022, ApJ, 930, 135

Lehmer, B. D., Eufrasio, R. T., Markwardt, L., et al. 2017, ApJ, 851, 11

Lehmer, B. D., Eufrasio, R. T., Tzanavaris, P., et al. 2019, ApJS, 243, 3

Lehmer, B. D., Ferrell, A. P., Doore, K., et al. 2020, ApJS, 248, 31

Lehmer, B. D., Eufrasio, R. T., Basu-Zych, A., et al. 2021, ApJ, 907, 17

Leja, J., Carnall, A. C., Johnson, B. D., Conroy, C., & Speagle, J. S. 2019, ApJ, 876, 3

Leja, J., Johnson, B. D., Conroy, C., & van Dokkum, P. 2018, ApJ, 854, 62

Lovell, C. C., Acquaviva, V., Thomas, P. A., et al. 2019, MNRAS, 490, 5503

Lusso, E., & Risaliti, G. 2017, A&A, 602, A79

Makarov, D., Prugniel, P., Terekhova, N., Courtois, H., & Vauglin, I. 2014, A&A, 570, A13

Markwardt, C. B. 2009, in Astronomical Society of the Pacific Conference Series, Vol. 411, Astronomical Data Analysis Software and Systems XVIII, ed. D. A. Bohlender, D. Durand, & P. Dowler, 251

Metropolis, N., Rosenbluth, A. W., Rosenbluth, M. N., Teller, A. H., & Teller, E. 1953, The Journal of Chemical Physics, 21, 1087

Monson, E. B., Lehmer, B. D., Doore, K., et al. 2021, ApJ, 919, 51

Moré, J. J. 1978, in Lecture Notes in Mathematics, Berlin Springer Verlag, Vol. 630, 105–116

Morrison, R., & McCammon, D. 1983, ApJ, 270, 119

Motiño Flores, S. M., Wiklind, T., & Eufrasio, R. T. 2021, ApJ, 921, 130

Murphy, K. D., & Yaqoob, T. 2009, MNRAS, 397, 1549

Nenkova, M., Sirocky, M. M., Ivezić, Ž., & Elitzur, M. 2008, ApJ, 685, 147

Noll, S., Burgarella, D., Giovannoli, E., et al. 2009, A&A, 507, 1793

Nowak, M. A., Neilsen, J., Markoff, S. B., et al. 2012, ApJ, 759, 95

Pacifici, C., Iyer, K. G., Mobasher, B., et al. 2022, arXiv e-prints, arXiv:2212.01915

Percival, S. M., & Salaris, M. 2009, ApJ, 703, 1123

Popescu, C. C., Tuffs, R. J., Dopita, M. A., et al. 2011, A&A, 527, A109

Predehl, P., & Schmitt, J. H. M. M. 1995, A&A, 293, 889

Rubin, D. B. 1984, The Annals of Statistics, 12, 1151

Rumph, T., Bowyer, S., & Vennes, S. 1994, AJ, 107, 2108

Sawicki, M. 2012, PASP, 124, 1208

Sawicki, M., & Yee, H. K. C. 1998, AJ, 115, 1329

Schaye, J., Crain, R. A., Bower, R. G., et al. 2015, MNRAS, 446, 521

Shanks, T., Ansarinejad, B., Bielby, R. M., et al. 2021, MNRAS, 505, 1509

Silva, L., Granato, G. L., Bressan, A., & Danese, L. 1998, ApJ, 509, 103

Skilling, J. 2004, in American Institute of Physics Conference Series, Vol. 735, Bayesian Inference and Maximum Entropy Methods in Science and Engineering: 24th International Workshop on Bayesian Inference and Maximum Entropy Methods in Science and Engineering, ed. R. Fischer, R. Preuss, & U. V. Toussaint, 395–405

Smith, L. J., Norris, R. P. F., & Crowther, P. A. 2002, MNRAS, 337, 1309

Somerville, R. S., & Davé, R. 2015, ARA&A, 53, 51

Stalevski, M., Fritz, J., Baes, M., Nakos, T., & Popović, L. Č. 2012, MNRAS, 420, 2756

Stalevski, M., Ricci, C., Ueda, Y., et al. 2016, MNRAS, 458, 2288

Stanway, E. R., & Eldridge, J. J. 2018, MNRAS, 479, 75

Tanimoto, A., Ueda, Y., Odaka, H., et al. 2019, ApJ, 877, 95

—. 2020, ApJ, 897, 2

Tojeiro, R., Heavens, A. F., Jimenez, R., & Panter, B. 2007, MNRAS, 381, 1252

Tuffs, R. J., Popescu, C. C., Völk, H. J., Kylafis, N. D., & Dopita, M. A. 2004, A&A, 419, 821

Walcher, J., Groves, B., Budavári, T., & Dale, D. 2011, Ap&SS, 331, 1

Wilms, J., Allen, A., & McCray, R. 2000, ApJ, 542, 914

Yang, G., Boquien, M., Brandt, W. N., et al. 2022, ApJ, 927, 192

Chapter 3

Results from Disk Galaxies in the Great Observatories Origins Deep Survey Fields

Keith Doore, Rafael T. Eufrasio, Bret D. Lehmer, Erik B. Monson, Antara Basu-Zych, Kristen Garofali, and Andrew Ptak

The following chapter was originally published in The Astrophysical Journal, Volume 923, Issue 1, as article 26, titled "On the Impact of Inclination-Dependent Attenuation on Derived Star Formation Histories: Results from Disk Galaxies in the Great Observatories Origins Deep Survey Fields".

Abstract

We develop and implement an inclination-dependent attenuation prescription for spectral energy distribution (SED) fitting and study its impact on derived star-formation histories. We apply our prescription within the SED fitting code `Lightning` to a clean sample of 82, $z = 0.21$–1.35 disk-dominated galaxies in the Great Observatories Origins Deep Survey North and South fields. To compare our inclination-dependent attenuation prescription with more traditional fitting prescriptions, we also fit the SEDs with the inclination-independent Calzetti et al. (2000) attenuation curve. From this comparison, we find that fits to a subset of 58, $z < 0.7$ galaxies in our sample, utilizing the Calzetti et al. (2000) prescription, recover similar trends with inclination as the inclination-dependent fits for the far-UV-band attenuation and recent star-formation rates. However, we find a difference between prescriptions in the optical attenuation (A_V) that is strongly correlated with inclination (p-value $< 10^{-11}$). For more face-on galaxies, with $i \lesssim 50^\circ$, (edge-on, $i \approx 90^\circ$), the average derived A_V is 0.31 ± 0.11 magnitudes lower (0.56 ± 0.16 mag-

nitudes higher) for the inclination-dependent model compared to traditional methods. Further, the ratio of stellar masses between prescriptions also has a significant (p-value $< 10^{-2}$) trend with inclination. For $i = 0°$–$65°$, stellar masses are systematically consistent between fits, with $\log_{10}(M_\star^{\rm inc}/M_\star^{\rm Calzetti}) = -0.05 \pm 0.03$ dex and scatter of 0.11 dex. However, for $i \approx 80°$–$90°$, derived stellar masses are lower for the Calzetti et al. (2000) fits by an average factor of 0.17 ± 0.03 dex and scatter of 0.13 dex. Therefore, these results suggest that SED fitting assuming the Calzetti et al. (2000) attenuation law potentially underestimates stellar masses in highly inclined disk-dominated galaxies.

3.1 Introduction

It is well understood that some fraction of the ultraviolet (UV) through near-infrared (NIR) light from stars is absorbed and reprocessed by dust into infrared (IR) and submillimeter emission within the interstellar media of galaxies (Mathis et al., 1983; Draine, 2003). The portion of light that is reprocessed depends upon inherent properties, such as the distribution of dust grain size and shape, chemical composition, and the density of the dust (Zubko et al., 2004; Draine & Li, 2007). Additionally, the portion of reprocessed starlight depends upon the geometric properties of the host galaxy, one of them being the orientation of the disk (i.e., inclination; Gordon et al., 2001; Tuffs et al., 2004; Draine, 2011; Chevallard et al., 2013). For example, as the viewing angle of a galactic disk changes from face-on to edge-on (i.e., $i = 0°$ to $i = 90°$), the proportion of light that is processed along the line of sight increases due to an increasing column density of dust. This effect results in increased attenuation of highly inclined disk galaxies compared to low inclination galaxies (e.g., Giovanelli et al., 1994; Driver et al., 2007; Unterborn & Ryden, 2008; Masters et al.,

2010; Wild et al., 2011; Devour & Bell, 2016; Battisti et al., 2017; Salim et al., 2018).

Accounting for the variation in attenuation due to inclination is crucial when determining the physical properties of galaxies. Both Graham & Worley (2008) and Sargent et al. (2010) independently found that the inclination effects of dust can bias measurements of the galaxy B-band surface brightness to be $\approx$0.5 mag arcsec^{-2} brighter for edge-on galaxies. Measurements of the half light radius have been shown to be increased by up to 110% for edge-on galaxies compared to face-on galaxies (Möllenhoff et al., 2006; Leslie et al., 2018b). UV magnitudes have been shown to be 1–2 magnitudes fainter for edge-on galaxies. This leads to underestimating the recent star-formation rates (SFR) by factors of 2.5–4 when using UV SFR calibrations (Wolf et al., 2018; Wang et al., 2018; Leslie et al., 2018a). Conflicting results have been found for the effect of inclination on measurements of stellar mass. Maller et al. (2009) and Devour & Bell (2017) report stellar mass to be almost independent at all inclinations, whereas Driver et al. (2007) and Wolf et al. (2018) consider it inclination-independent from face-on to $\approx$70°, above which masses can be underestimated by a factor of $\approx$2.

The same inclination-based attenuation applies when modeling the spectral energy distributions (SEDs) of galaxies (see Conroy 2013 for a review). Modeling SEDs allows for the derivation of the star formation histories (SFHs) of galaxies, from which the stellar mass and recent SFR are determined. In order to derive these properties from the observed SED, an attenuation curve is applied to stellar population synthesis models to construct attenuated model SEDs. These model SEDs are then fit to the observed SED to estimate the galaxy's SFH, and subsequently the stellar mass and recent SFR.

When determining the attenuated model SED, many studies utilize the Calzetti et al. (2000) attenuation law (e.g., Santini et al., 2015; Kacharov et al., 2018; Barro et al., 2019) or the Wein-

gartner & Draine (2001) extinction curves for the Milky Way (MW), Large Magellanic Cloud, and Small Magellanic Cloud (e.g. Roebuck et al., 2019). These curves are relatively rigid with the main flexibility in the free parameter used for normalization (i.e., A_V). A more flexible attenuation curve example is that from Noll et al. (2009), which consists of a Calzetti et al. (2000) curve modified to include a UV bump and variable slope. Curves such as these are used to provide extra flexibility when fitting SEDs (e.g. Noll et al., 2009; Boquien et al., 2016; Eufrasio et al., 2017), but they lack a direct physically motivated link to the inclination. High-spatial-resolution imaging surveys can provide constraints on the disk inclination and aid in accounting for the effects of inclination-based attenuation. However, these constraints would need to have a direct physically motivated link in the attenuation curve to properly be utilized.

In this paper, we utilize the inclination-dependent attenuation curves from Tuffs et al. (2004) as updated by Popescu et al. (2011) when fitting SEDs as to evaluate the effects of inclination on the derived SFHs. These physically motivated attenuation curves are based on radiative transfer calculations that use the commonly assumed dust composition of Draine et al. (2007) and geometries for the stellar and dust distributions that were shown to reproduce local observed galaxy SEDs (Tuffs et al., 2004; Popescu et al., 2011). The structure of the paper is as follows. In Section 3.2, we describe the data and sample selection. In Section 3.3, the method for estimating each galaxy's inclination is presented. In Section 3.4, we describe our SED fitting procedure and the Tuffs et al. (2004) inclination-dependent attenuation curve. In Section 3.5, we present the results from the SED fittings. In Section 3.6, we discuss the effects of inclination on the derived SFHs, specifically the recent SFR and stellar mass. Lastly, a summary is provided in Section 3.7.

For this study, we assume a Kroupa (2001) initial mass function with solar metallicity ($Z = Z_{\odot}$) and adopt a cosmology with $H_0 = 70$ km s^{-1} Mpc^{-1}, $\Omega_M = 0.30$, and $\Omega_{\Lambda} = 0.70$.

3.2 Data and Sample Selection

To test the inclination-dependent attenuation prescription and study the resulting effects of inclination on the derived SFHs, we required a sample of galaxies that has high-quality uniform broadband data, spanning from the UV to far-infrared (FIR), and Hubble Space Telescope (HST) imaging data from which disk inclinations can be derived. The Great Observatories Origins Deep Survey (GOODS) North (N) and South (S) fields are excellent extragalactic survey fields for our study as they contain over 70,000 galaxies with deep *HST* coverage and supplemental UV to FIR data (Giavalisco et al., 2004).

3.2.1 Photometry

We utilized the UV to mid-infrared (MIR) photometry[1] from Barro et al. (2019) and Guo et al. (2013) within the Cosmic Assembly Near-infrared Deep Extragalactic Legacy Survey (CANDELS) regions (Grogin et al., 2011; Koekemoer et al., 2011) in the GOODS-N and GOODS-S fields, respectively. Both fields contain observations taken with HST Advanced Camera for Surveys (ACS) F435W F435W, F606W, F775W, F814W, and F850LP; HST Wide Field Camera 3 (WFC3) F105W, F125W, and F160W; and Spitzer Infrared Array Camera (IRAC) channels 1–4. The GOODS-N field also includes HST/WFC3 F140W, and the GOODS-S field includes HST/WFC3 F098M. The UV and NIR are supplemented by Kitt Peak National Observatory (KPNO) 4 m/Mosaic U, Large Binocular Telescope (LBT)/Large Binocular Camera (LBC) U, Subaru Multi-Object InfraRed Camera and Spectrograph (MOIRCS) K_s, and Canada France Hawaii Telescope (CFHT) Wide-field InfraRed Camera (WIRCam) K_s ground-based observations for the GOODS-N; and Cerro Tololo Inter-American Observatory (CTIO) Blanco/Mosaic

[1] Retrieved from the *Rainbow* database: http://rainbowx.fis.ucm.es/Rainbow_navigator_public/

II U, Very Large Telescope (VLT)/ Visible Multi-Object Spectrograph (VIMOS) U, VLT Infrared Spectrometer And Array Camera (ISAAC) K_s, and VLT High Acuity Wide field K-band Imager (HAWK-I) K_s ground-based observations for the GOODS-S. The methods from Barro et al. (2019) and Guo et al. (2013) for producing the photometry are the same and are briefly summarized below. The photometry and its uncertainty were extracted in all HST bands by running `SExtractor` (Bertin & Arnouts, 1996) in dual-image mode after identifying sources in the WFC3/F160W mosaic using a two-step cold plus hot strategy, as described in Galametz et al. (2013) and Guo et al. (2013). Source searching and photometry were performed after smoothing all other bands to the WFC3/F160W point-spread function (PSF). The lower resolution ground-based and Spitzer/IRAC photometry were determined using `TFIT` (Laidler et al., 2007) with the WFC3/F160W mosaic as the template image.

The FIR photometry used in our study was produced by Barro et al. (2019) for both the GOODS-N and GOODS-S fields and contains Spitzer Multiband Imaging Photometer (MIPS) 24 and 70 μm bands; Herschel Photodetector Array Camera and Spectrometer (PACS) 100 and 160 μm bands; and Herschel Spectral and Photometric Imaging Receiver (SPIRE) 250, 350, and 500 μm bands. To briefly summarize their methods, the FIR photometry associated with F160W sources consists of merged FIR photometric catalogs built from the data sets presented in Pérez-González et al. (2005,0,0), PACS Evolutionary Probe (PEP) + GOODS-Herschel (Lutz et al., 2011; Magnelli et al., 2013), and Herschel Multi-tiered Extragalactic Survey (HerMES; Oliver et al., 2012). Due to the relatively low spatial resolution of the IR data, a cross-matching procedure was run from high (F160W) to low (SPIRE 500 μm) resolution bands as to obtain a one-to-one match for each F160W source. The most likely counterpart to a given IR source in the F160W image was chosen based on brightness and proximity to the IR source. A full description of the methods can

be found in Appendix D of Barro et al. (2019). We note that even though there should be minimal confusion of source identification for the PACS and SPIRE counterparts to the F160W sources, photometric issues could potentially arise due to nearby IR-bright sources. We discuss these issues and their potential effects on our final sample in Appendix 3.A.

Next, we corrected the photometry of each filter for Galactic extinction as estimated by the NASA Extragalactic Database extinction law calculator[2], which uses the Schlafly & Finkbeiner (2011) recalibration of the Schlegel et al. (1998) Cosmic Background Explorer (COBE) Diffuse Infrared Back- ground Experiment (DIRBE) and Infrared Astronomical Satellite (IRAS) Sky Survey Atlas (ISSA) dust maps. This recalibration assumes a Fitzpatrick (1999) reddening law with $R_V = 3.1$. Our extinction values were determined for the center of each field, and we do not account for any variations across each of the GOODS fields, since extinction corrections for both fields are small and variation across the fields are minimal. These values, the corresponding filters used in each field, and the mean wavelength of the filters are listed in Table 3.1.

To include unaccounted for sources of uncertainty and systematic variations in the photometry, we added calibration uncertainties to the measured flux uncertainties that were derived by `SExtractor`, as is common when fitting SEDs (e.g., Boquien et al., 2016; Leja et al., 2017; Eufrasio et al., 2017; Leja et al., 2019). These calibration uncertainties are listed for each filter in Table 3.1 as σ_C, which are the calibration uncertainties of 2–15% as described by each instrument's user handbook. Further, we included 10% model uncertainties for each band when fitting the SEDs to account for systematic effects in the models (Chevallard & Charlot, 2016; Han & Han, 2019).

[2]https://ned.ipac.caltech.edu/extinction_calculator

Table 3.1: Multiwavelength Coverage Used in SED Fitting

GOODS-North				**GOODS-South**			
Instrument/Band	$\lambda_{\rm mean}$[a] (μm)	A_λ[b] (mag)	σ_C[c]	Instrument/Band	$\lambda_{\rm mean}$[a] (μm)	A_λ[b] (mag)	σ_C[c]
KPNO 4m/Mosaic U	0.3561	0.052	0.05	Blanco/MOSAIC II U	0.3567	0.034	0.05
LBT/LBC U	0.3576	0.052	0.10	VLT/VIMOS U	0.3709	0.033	0.05
HST/ACS F435W	0.4689	0.041	0.02	HST/ACS F435W	0.4689	0.027	0.02
HST/ACS F606W	0.5804	0.031	0.02	HST/ACS F606W	0.5804	0.020	0.02
HST/ACS F775W	0.7656	0.020	0.02	HST/ACS F775W	0.7656	0.013	0.02
HST/ACS F814W	0.7979	0.019	0.02	HST/ACS F814W	0.7979	0.012	0.02
HST/ACS F850LP	0.8990	0.015	0.02	HST/ACS F850LP	0.8990	0.010	0.02
HST/WFC3 F105W	1.0451	0.012	0.02	HST/WFC3 F098M	0.9829	0.008	0.02
HST/WFC3 F125W	1.2396	0.009	0.02	HST/WFC3 F105W	1.0451	0.008	0.02
HST/WFC3 F140W	1.3784	0.007	0.02	HST/WFC3 F125W	1.2396	0.006	0.02
HST/WFC3 F160W	1.5302	0.006	0.02	HST/WFC3 F160W	1.5302	0.004	0.02
CFHT/WIRCam K_s	2.1413	0.004	0.05	VLT/HAWK-I K_s	2.1403	0.002	0.05
Subaru/MOIRCS K_s	2.1442	0.004	0.05	VLT/ISAAC K_s	2.1541	0.002	0.05
Spitzer/IRAC1 [d]	3.5314	0.002	0.05	Spitzer/IRAC1 [d]	3.5314	0.001	0.05
Spitzer/IRAC2 [d]	4.4690	0.000	0.05	Spitzer/IRAC2 [d]	4.4690	0.000	0.05
Spitzer/IRAC3 [d]	5.6820	0.000	0.05	Spitzer/IRAC3 [d]	5.6820	0.000	0.05
Spitzer/IRAC4 [d]	7.7546	0.000	0.05	Spitzer/IRAC4 [d]	7.7546	0.000	0.05
Spitzer/MIPS 24 μm [e]	23.513	0.000	0.05	Spitzer/MIPS 24 μm [e]	23.513	0.000	0.05
Spitzer/MIPS 70 μm [e]	70.389	0.000	0.10	Spitzer/MIPS 70 μm [e]	70.389	0.000	0.10
Herschel/PACS 100 μm [e]	100.05	0.000	0.05	Herschel/PACS 100 μm [e]	100.05	0.000	0.05
Herschel/PACS 160 μm [e]	159.31	0.000	0.05	Herschel/PACS 160 μm [e]	159.31	0.000	0.05
Herschel/SPIRE 250 μm[e]	247.21	0.000	0.15	Herschel/SPIRE 250 μm[e]	247.21	0.000	0.15

[a]Mean wavelength of the filter calculated as $\lambda_{\rm mean} = \frac{\int \lambda T(\lambda) d\lambda}{\int T(\lambda) d\lambda}$, where $T(\lambda)$ is the filter transmission function.
[b]Galactic extinction for the center of the field.
[c]Calibration uncertainties as given by the corresponding instrument user handbook.
[d]Required band for the dust emission SED.
[e]At least two of these bands are required for the dust emission SED, one of which must be $> 100\mu$m in the rest frame.

3.2.2 Galaxy Sample Selection

Since our goal is to present our inclination-dependent attenuation prescription and study the resulting effects of inclination on derived SFHs, we required a clean sample of disk-dominated galaxies, which our inclination-dependent analysis would apply. This sample was not required to be complete, but was limited to sources with high-quality data and unambiguous morphological types. Therefore, we initially selected, from the $\sim$70,000 galaxies within the GOODS fields,

the 5459 galaxies with reliable spectroscopic redshifts (Szokoly et al., 2004; Wirth et al., 2004; Mignoli et al., 2005; Reddy et al., 2006; Ravikumar et al., 2007; Barger et al., 2008; Vanzella et al., 2008; Popesso et al., 2009; Balestra et al., 2010; Fadda et al., 2010; Teplitz et al., 2011; Cooper et al., 2012; Kriek et al., 2015). Photometric redshifts are available for the galaxies that do not have spectroscopic redshifts (e.g., Dahlen et al., 2013; Guo et al., 2013; Skelton et al., 2014; Barro et al., 2019). However, these photometric redshifts were derived from SED fittings and often have large uncertainties. Therefore, we do not include galaxies with photometric redshifts in our sample as the large uncertainties could have significant effects on our results.

Inclination-dependent studies like ours can suffer from potential selection effects (Devour & Bell, 2016). We checked to see if requiring spectroscopic redshifts introduced any clear bias in our sample by preferentially selecting edge-on galaxies with elevated intrinsic luminosity distributions compared to face-on galaxies. Since spectroscopic redshift surveys are limited by the optical magnitude, often in the *r*-band, edge-on galaxies would need to be intrinsically more luminous compared to face-on galaxies to be above the magnitude limits, due to edge-on galaxies having higher optical/UV attenuation. This bias did not seem to be present in our final sample. For instance, the attenuated *r*-band absolute magnitudes of galaxy subsets in the final sample, binned by redshift, showed that nearly edge-on galaxies were fainter by 1–2 mag compared to face-on galaxies in the same redshift bin. This implies that the intrinsic luminosity distributions of the face-on and edge-on galaxies should be similar once attenuation had been removed, since edge-on galaxies would be more highly attenuated. We confirmed that the nearly edge-on ($1-\cos i > 0.8$) and face-on ($1-\cos i < 0.3$) intrinsic luminosity distributions were similar by performing a two-sided Kolmogorov-Smirnov (KS) test using the derived rest-frame *r*-band intrinsic luminosities and the inclinations from the SED fits, which results in a p-value > 0.3 (see Section 3.5.3).

Next, we further limited our sample to galaxies that have at least six photometric measurements in the mid-to-far IR (3–1,000 μm) to better constrain the shape of the dust emission component of the SED, which we discuss in Section 3.4.2. We required that each galaxy has detections in all Spitzer/IRAC bands and permit the remaining two or more bands to be any combination of the Spitzer/MIPS, Herschel/PACS, or Herschel/SPIRE 250 μm data, one of which must be beyond the 100 μm rest frame to constrain the peak of the dust emission (Draine et al., 2007; Conroy, 2013; Faisst et al., 2020). The fluxes for each band were required to have $F_\nu/\sigma_\nu > 2$, where σ_ν includes the flux calibration uncertainty, which results in an original signal to noise ratio > 3. This strict limitation led to the removal of 4918 galaxies from the 5459 galaxy sample, leaving 541 galaxies.

To check if the IR selection requirement introduced any bias in our sample by preferentially selecting more IR luminous edge-on galaxies compared to face-on galaxies, we plotted the MIPS 24 μm fluxes as a function of the axis ratio in galaxy subsets, binned by redshift, as seen in Figure 3.1. It can be seen that the MIPS 24 μm fluxes are similarly distributed at all axis ratios for each redshift bin. Thus, the lack of obvious differences in the 24 μm flux distributions indicates that the edge-on and face-on galaxies in our sample have similar IR luminosities.

We further limited the sample to purely star-forming galaxies by identifying and removing sources that are flagged as active galactic nuclei (AGNs) from the Chandra X-ray catalogs for the GOODS-N (Xue et al., 2016) and GOODS-S (Luo et al., 2017) fields. Sources from the X-ray catalogs were matched to the CANDELS catalogs' sources with a matching radius of $1''$. We further attempted to limit the potential AGNs in our sample by removing obscured MIR-AGNs using the Donley et al. (2012) IRAC selection criteria and Kirkpatrick et al. (2013) Spitzer/Herschel color-color criteria. A total of 114 potential AGNs were removed, leaving 427 galaxies.

Since our inclination-dependent attenuation prescription only applies to galaxies with disk mor-

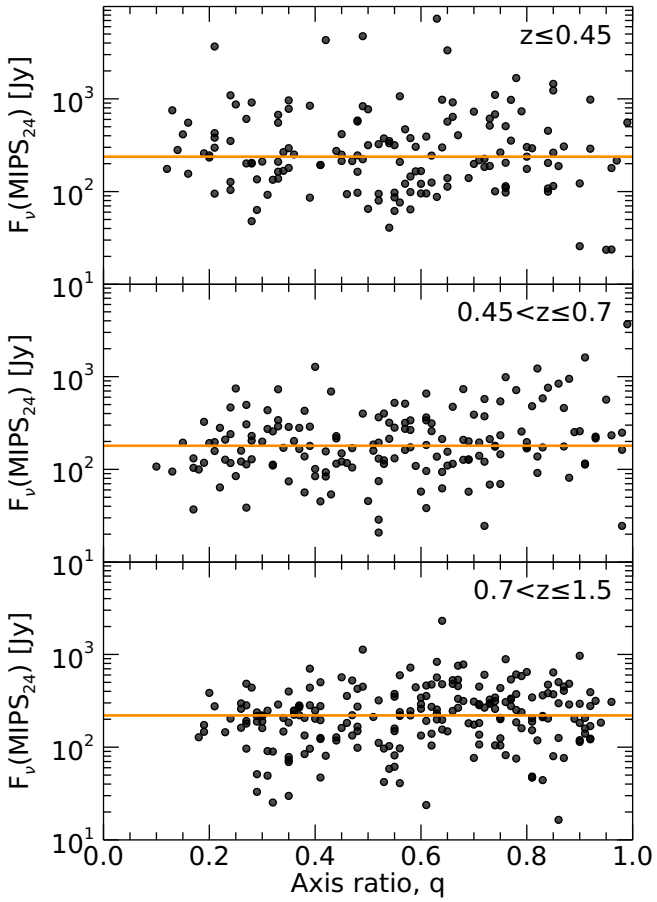

Figure 3.1: Spitzer/MIPS 24 μm fluxes as a function of axis ratio q binned by redshift z. The orange lines in each panel represent the median 24 μm flux for that redshift bin. All three redshift bins can be seen to have no significant trends in the 24 μm fluxes vs. axis ratio, implying that the IR luminosity distributions are similar across inclination. This is expected as the 24 μm is practically attenuation free. So, we would expect no difference between edge-on and face-on galaxies.

phologies, we limited our sample to only galaxies with clear disk morphologies. We selected disk galaxies using their Sérsic index n (Sérsic, 1963), where a galaxy is considered a disk galaxy if $n < 2$. The Sérsic indices for our galaxies were measured by van der Wel et al. (2012) using the `GALFIT` morphological code (Peng et al., 2002) on WFC3/F125W images in both the GOODS-N and GOODS-S fields. From these fits, 49 galaxies of the 427 remaining galaxies were not flagged as having a "good fit" (i.e., flag of 0) and were removed from the sample, leaving 378 galaxies.

Rather than using a Sérsic index cutoff of $n < 2$, we chose to further lower the cutoff to only

include the 154 galaxies with $n < 1.2$ out of the 378 remaining galaxies as to select disk-dominated (i.e., low B/D ratio) galaxies. The choice of the cutoff value of $n < 1.2$ is motivated by the work of Sargent et al. (2007), who showed that disk galaxies in the COSMOS field with purely exponential disks predominantly have $n < 1.2$. The reason for selecting disk-dominated galaxies, rather than disk galaxies in general, is to reduce degeneracies within our SED fittings; we discuss this further in Section 3.5.2.

To confirm the selection of disk-dominated galaxies, we visually inspected the 154 galaxies that met the above criteria to confirm that there was no significant bulge and a clear disk was present. Since we limited our sample to strictly contain disk-dominated galaxies, any galaxy that could potentially be confused with an elliptical or irregular galaxy was removed from the sample. We also identified galaxies that appeared to have companions and may have been undergoing a merger, and removed these from our sample as well. In total, we chose to remove 72 galaxies from the sample that did not pass the visual inspection, and the final sample contains 82 galaxies spanning a redshift range of $z = 0.21$–1.35. In Section 3.5, we derive a mass range of $M_\star = 10^{9.1}$–$10^{11.3} M_\odot$ and a SFR range of SFR $= 0.3$–$170\ M_\odot\ yr^{-1}$ for our sample and show that our galaxies are close to the redshift-dependent galaxy main sequence (e.g., Lee et al., 2015, see Figure 3.10).

Figure 3.2 shows a set of the composite postage stamp images for galaxies that were selected to span the full range of inclination within the final sample. These galaxies will be used for illustrative purposes throughout the rest of the paper. The observed broadband SEDs for these sources are shown in Figure 3.3 normalized to the Subaru/MOIRCS K_s or VLT/ISAAC K_s bands for the GOODS-N and GOODS-S galaxies, respectively. It can been seen that as the axis ratio q decreases (i.e., inclination increases, see Equation 3.1) that the UV-optical emission decreases, due to increased attenuation.

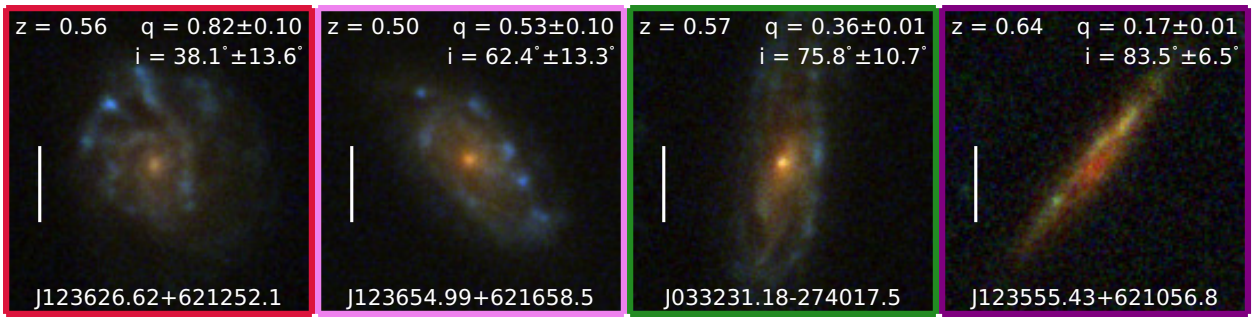

Figure 3.2: Composite HST/ACS F435W, F606W, and F850LP-band postage stamp images for galaxies within the final sample that were selected to span the full range of inclination i and ordered by measured axis ratio q. Each stamp is centered on the source position, and a white $1''$ line is given for reference. NOTE: The outline color of each postage stamp is used to distinguish the respective galaxy in all subsequent figures that use these example galaxies.

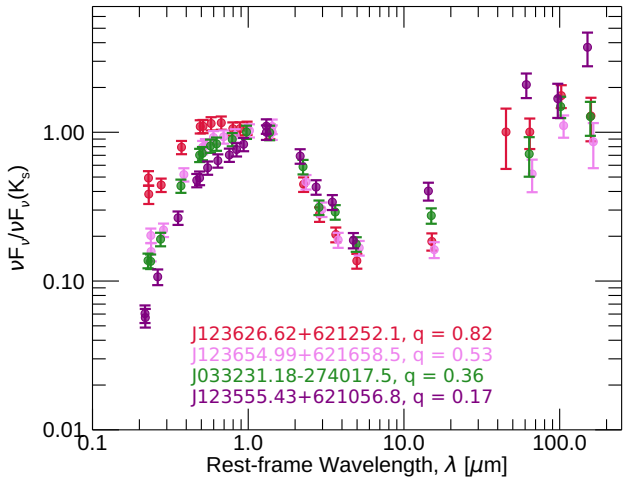

Figure 3.3: Broadband SEDs of the four example galaxies shown in Figure 3.2 using the same color as the outline of the corresponding postage stamp. The SEDs are normalized to the Subaru/MOIRCS K_s or VLT/ISAAC K_s bands for the GOODS-N and GOODS-S galaxies, respectively. These SEDs show that as the axis ratio q decreases that the UV-optical emission decreases, due to increasing attenuation.

3.3 Galaxy Inclinations

The inclination, i, of a disk galaxy is normally defined as the angle between the plane of the galactic disk and the plane of the sky. This means galaxies with $i = 0°$ and $i = 90°$ are considered face-on and edge-on, respectively. Inclination is difficult to measure directly and is normally de-

rived from the axis ratio q measured from an elliptical isophote or Seŕsic profile. If galaxies were smooth, infinitely thin circular disks, then inclination could simply be determined by $\cos i = q$. However, galaxies have an intrinsic thickness (γ) when viewed edge-on, which is generally defined as the ratio between the scale height and scale length. Using the measured axis ratio and intrinsic thickness, inclination can be derived using the formula from Hubble (1926),

$$\cos^2 i = \frac{q^2 - \gamma^2}{1 - \gamma^2}, \tag{3.1}$$

where q is the measured axis ratio, and γ is the intrinsic thickness, which has been found from observations to mainly be within the range of $0.1 < \gamma < 0.4$ (e.g., Padilla & Strauss, 2008; Unterborn & Ryden, 2008; Rodríguez & Padilla, 2013). For our study, we used the axis ratios measured from the fits for the Seŕsic index by van der Wel et al. (2012) on WFC3/F125W images when determining the inclination.

Variation in q with rest-frame wavelength has been observed in galaxies (e.g., Dalcanton & Bernstein, 2002), which means that q has been found to vary at different redshifts for the same observed photometric band. We checked this potential variation by comparing the WFC3/F125W and WFC3/F160W axis ratios from van der Wel et al. (2012) as a function of the redshift. We found that any variation in q at these redshifts was masked by the uncertainties on q, which agrees with the same analysis by van der Wel et al. (2014). Therefore, the WFC3/F125W axis ratios that we used are reliable for our entire sample's redshift range.

Blurring of a galaxy in its image by the PSF can also have a possible influence on the derived value of q. If the angular size of the minor axis is smaller than the angular size of the FWHM of the PSF, an artificial increase in the minor axis could occur, resulting in an overestimated value of q. All of the galaxies in our sample have minor axes that are larger than the PSF FWHM

of the WFC3/F125W filter, such that blurring would not significantly influence our values of q. The minor (major) axis sizes have a range of $0.19''$–$1.53''$ ($0.84''$–$3.70''$), with a median of $0.60''$ ($1.58''$), which is larger than the $0.18''$ PSF FWHM of the WFC3/F125W filter. Therefore, the following method used for determining an inclination from a measured axis ratio is applicable to our galaxies, and we note that the method should only be applied to galaxies that have minor axes larger than the PSF FWHM.

There are two important sources of uncertainty when calculating inclination using Equation 3.1. The first is that the value of γ will vary among galaxies. However, a single value of γ is normally applied when calculating inclinations for a large sample. By using a single value of γ for a whole sample, galaxies can have large deviations between their calculated and true inclinations if their true γ is different from the assumed value. This is a larger source of uncertainty in edge-on galaxies, where the measured axis ratio is small. This effect is shown in Figure 3.4(a), where the colored lines represent different possible values of γ within the observed range. The minimal effect on face-on galaxies is due to the intrinsic thickness of these galaxies not influencing the measured axis ratio as a result of the viewing angle. However, the difference in the intrinsic thickness of inclined galaxies can influence their measured axis ratio and lead to incorrect inclinations up to 23°.

The second source of uncertainty comes from the fact that Equation 3.1 assumes that galaxies are radially symmetric. However, it is apparent that galaxies are not radially symmetric, but instead have at least minor asymmetries due to clumpiness or spiral arms. It has been shown that asymmetries can cause the measured value of q to vary from a radially symmetric value by a factor of $\sim 1/(1-\varepsilon\cos 2\phi)$, where ε is the intrinsic ellipticity (i.e., ellipticity of the disk due to asymmetries when viewed face-on) and ϕ is the azimuthal viewing angle relative to the intrinsic long

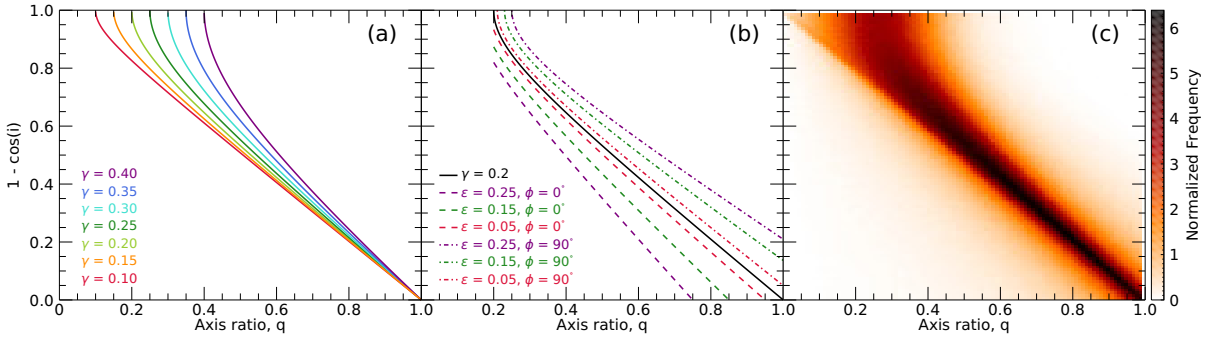

Figure 3.4: Each panel shows inclination $(1-\cos i)$ as a function of axis ratio q. (a) The variation in possible inclinations for the same value of q for different values of γ, a measure of the intrinsic thickness of the disk, within the observed range of disk galaxies represented as different colored lines. (b) The variation in possible inclinations for the same value of q due to asymmetries, where the asymmetries causes q to vary by a factor of $\sim 1/(1-\varepsilon\cos 2\phi)$. The calculated inclinations for symmetric galaxies from Equation 3.1 assuming $\gamma = 0.2$ is represented as the solid black line for reference. (c) The two-dimensional distribution of inclination and q from the Monte Carlo simulation.

axis of the disk (Ryden, 2006; Unterborn & Ryden, 2008). Changing the value of ϕ can be thought of as rotating a galaxy about the axis perpendicular to the plane of the disk such that the intrinsic ellipticity causes the measured axis ratio to vary depending on whether the major or minor axis of the intrinsic ellipticity is aligned to the viewing angle. If ε and ϕ are known, Equation 3.1 could be updated by replacing q with $q/(1-\varepsilon\cos 2\phi)$ to recover the correct inclination. However, ε and ϕ are rarely known for deep-field galaxies and are often ignored when determining the inclination. An example of how this source of uncertainty affects the inclination can be seen in Figure 3.4(b) for the case of $\gamma = 0.2$.

To determine inclinations for the galaxies in our sample in a way that incorporates these sources of uncertainty, we ran a Monte Carlo simulation to determine each galaxy's inclination probability density function (PDF). As stated above, if galaxies were infinitely thin circular disks, then inclination could simply be determined by $\cos i = q$. If they were randomly oriented, we would expect a uniform distribution with respect to $\cos i$ (see below) and therefore q. However, as shown above,

i is dependent upon q as well as γ, ε, and ϕ. This leads to q no longer being a uniform distribution, but rather being a function of the distributions of $\cos i$, γ, ε, and ϕ given by

$$q = \left(\sqrt{\cos^2 i \, (1 - \gamma^2) + \gamma^2} \right) (1 - \varepsilon \cos 2\phi). \tag{3.2}$$

Therefore, the goal of our Monte Carlo simulation is to determine the unknown distribution of q using Equation 3.2 from the known distributions of $\cos i$, γ, ε, and ϕ; from which a distribution of i can be determined for a given value and uncertainty of q.

For the distribution of inclination, $\cos i$ would be uniformly distributed if galaxies were randomly oriented. When observing a galaxy from a random direction, each solid angle element surrounding the galaxy from which to observe it would be equally likely. Comparatively, observing a galaxy at a given inclination could be thought of as viewing it from a solid-angle band (i.e., each inclination is a line of latitude on the surrounding celestial sphere). This band will cover larger areas at $i \approx 90^\circ$ (i.e., equator) compared to $i \approx 0^\circ$ (i.e., the poles). This larger area leads to more external galaxies viewing the galaxy at $i \approx 90^\circ$ compared to $i \approx 0^\circ$. In other words, there are more lines of sight for a nearly edge-on view than for a nearly face-on view of a galaxy. This leads to the probability of observing a galaxy being distributed by a sine function. Via the probability integral transform, this means $1 - \cos i$ is uniformly distributed, and therefore $\cos i$ has a uniform distribution as well.

For ϕ, we assumed a uniform distribution between its possible values of 0 and 2π. As for ε and γ, we used the PDFs for these random variables given in Figure 11 of Rodríguez & Padilla (2013), who derived these distributions from 92,923 spiral galaxies with r-band data from the Sloan Digital Sky Survey (SDSS) Data Release 8 (DR8; Aihara et al., 2011), which had morphologies based on the Galaxy Zoo project (Lintott et al., 2011). The galaxies used in their SDSS DR8 sample were

in the redshift range of $z = 0$–0.15 with a median of $z \approx 0.1$, while our sample galaxies' redshifts are $z = 0.21$–1.35 with a median of $z \approx 0.56$. In the rest frames, the r-band used in their study and the WFC3/F125W band used in our study are $\approx$0.56 μm and $\approx$0.79 μm, respectfully. These rest-frame bands are comparable, and therefore, the error introduced by using these PDFs, which are derived from a different photometric band than our data, is assumed to be negligible. We also tested two additional distributions of γ and ε provided in Figure 11 of Rodríguez & Padilla (2013), which have smaller values of γ, and found negligible differences in the inclination distributions derived from the Monte Carlo simulations. However, we do note that the distributions of γ may be skewed to higher values due to PSF blurring effects from the limited angular resolution of SDSS, especially when compared to the intrinsic thickness of nearby, highly resolved edge-on galaxies.

Further, the inclination-dependent Tuffs et al. (2004) attenuation curves described in Section 3.4.3 assume $\gamma \approx 0.08$ and $\varepsilon = 0$ at the rest-frame wavelength of $\approx$0.56 μm. This leads to an internal inconsistency with our model by using distributions of ε and γ from Rodríguez & Padilla (2013) rather than these fixed values. However, assuming a fixed value for these variables only decreases the uncertainty on the derived inclinations.

We ran the Monte Carlo simulation for 10^7 trials to thoroughly sample the distribution. Each trial consisted of a draw from the distributions of $\cos i$, γ, ε, and ϕ, which resulted in a value of q from Equation 3.2. We discarded $< 6\%$ of the 10^7 trials due to them resulting in $q > 1$, which can occur when the simulated galaxy is nearly face-on ($\cos i \approx 1$) and $\cos 2\phi < 0$. The resulting two-dimensional distribution of inclination and q can be seen in Figure 3.4(c). Having this two-dimensional distribution, we needed to determine each galaxy's inclination PDF from it in a way that incorporated how the uncertainty of the measured value of q is distributed. This was done by generating an additional 10^6 values of q drawn from a Gaussian distribution whose mean

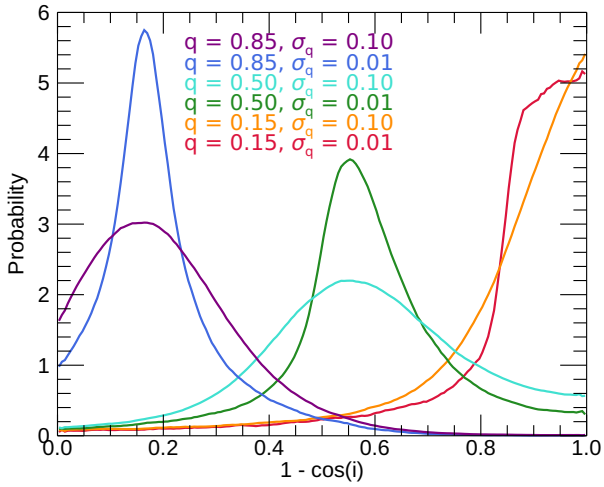

Figure 3.5: Probability distributions of inclination $(1-\cos i)$ from the Monte Carlo simulation for different example distributions of q. The distributions consist of q values of 0.85, 0.5, and 0.15 with σ_q values of 0.1 and 0.01. As σ_q increases for a fixed q, the width of the inclination distribution increases, since an increase in the uncertainty in q expectedly increases the uncertainty in inclination.

and standard deviation were the measured value of q and its uncertainty from van der Wel et al. (2012). After removing any of the additional 10^6 values of q that exceeded the possible values of q, we matched them to their closest q values from the Monte Carlo simulation and recorded the corresponding inclination values. Therefore, each galaxy's inclination PDF consisted of these $\sim 10^6$ corresponding inclination values from the matched values of q.

Figure 3.5 shows example inclination PDFs for $q = 0.85$, 0.5, and 0.15 with standard deviations of $\sigma_q = 0.1$ and 0.01. From these examples, it can be seen that as σ_q increases for a fixed q, the width of the inclination distribution increases. This is expected, since as the uncertainty in q increases, so should the uncertainty in inclination.

Marginalizing the two-dimensional distribution of q and i for q from the Monte Carlo simulation gives the expected distribution if galaxies are randomly oriented (i.e. uniform distribution in $\cos i$), which is shown as a dashed red line in Figure 3.6. The distribution of the measured axis

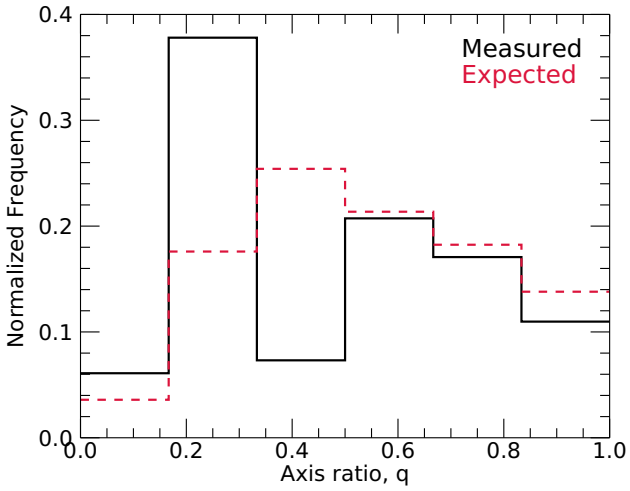

Figure 3.6: Distribution of axis ratio q. The solid black line shows the distribution of our galaxy sample using the measured values from van der Wel et al. (2012), and the dashed red line shows the expected distribution from the Monte Carlo simulation if our sample comprised randomly oriented disk galaxies. The discrepancy between the two distributions is due to various effects in our sample selection. For example, the visual inspection likely leads to more edge-on galaxies, which are easier to visually distinguish as disk galaxies compared to moderately inclined galaxies that were more easily confused for elliptical galaxies.

ratios from van der Wel et al. (2012) for the galaxies in our sample is shown as the black line. The two distributions are statistically distinct (a two-sided KS test gives a p-value $< 10^{-5}$), with our sample showing a deficit of moderately inclined galaxies as well as an excess of edge-on galaxies. However, this is expected, since we did not require a complete sample. For example, during the visual inspection, edge-on galaxies were more likely to be admitted into the sample as they are easier to visually distinguish as disk galaxies compared to moderately inclined galaxies, which were more easily confused for elliptical galaxies.

Finally, we quantified the consequences of not incorporating variation in γ and assuming radial symmetry when determining inclination. We compared the median, 16th, and 84th percentiles of our sample's inclination PDFs to inclinations and uncertainties of our sample calculated using Equation 3.1 assuming radial symmetry and the commonly used fixed values of $\gamma = 0.15$ and

0.2 (e.g., Maller et al., 2009; Sargent et al., 2010; Chevallard et al., 2013; Wang et al., 2018; Leslie et al., 2018b) as well as $\gamma = 0.08$ assumed by Tuffs et al. (2004) in deriving the inclination-dependent attenuation curves. These calculated values for the fixed values of γ are in excellent agreement with the median PDF inclinations for galaxies with $i \gtrsim 30^\circ$. For $i \lesssim 30^\circ$, inclinations are slightly lower (2°–15°) for the calculated values due to not including asymmetries. Comparing the uncertainties, the calculated values uncertainties are underestimated by an average factor of $\approx$7.9 for $\gamma = 0.15$, $\approx$7.5 for $\gamma = 0.2$, and $\approx$8.8 for $\gamma = 0.08$ compared to the PDF uncertainties. Therefore, if the variation in γ is ignored and radial symmetry is assumed, the inclination can be properly recovered from Equation 3.1 if $i \lesssim 30^\circ$, but the uncertainty will be underestimated.

3.4 SED Modeling

3.4.1 SED Fitting Procedure

To fit the SEDs of our galaxies, we used the SED fitting code `Lightning` [3] (Eufrasio et al., 2017). `Lightning` is an SED fitting procedure that models the FUV to NIR stellar emission with `PÉGASE` population synthesis models (Fioc & Rocca-Volmerange, 1997). The modeled stellar emission includes attenuation that can be restricted to be in energy balance with the integrated NIR to FIR (5–1000μm) dust emission. For this paper, we have updated `Lightning` to include a module that models this NIR to FIR dust emission with the dust models from Draine & Li (2007) (see Section 3.4.2).

The SFH model consists of five time steps at 0–10 Myr, 10–100 Myr, 0.1–1 Gyr, 1–5 Gyr, and 5–13.6 Gyr with each period having a constant SFR. The final age bin upper bound for a given

[3] Version 2.0 https://github.com/rafaeleufrasio/lightning

Table 3.2: Adjustable Parameters and Ranges within `Lightning`

Parameter	Possible Range (Min, Max)	Range in This Work (Min, Max)	Prior Distribution
Star Formation History Bins [$M_\odot\ yr^{-1}$]			
ψ_1 (0-10 Myr)	$(0, \infty)$	$(0, \infty)$	Flat
ψ_2 (10-100 Myr)	$(0, \infty)$	$(0, \infty)$	Flat
ψ_3 (0.1-1 Gyr)	$(0, \infty)$	$(0, \infty)$	Flat
ψ_4 (1-5 Gyr)[a]	$(0, \infty)$	$(0, \infty)$	Flat
ψ_5 (5-13.6 Gyr)[a]	$(0, \infty)$	$(0, \infty)$	Flat
Draine & Li (2007) Dust Emission Model			
α	$(-10, 4)$	(2, 2)	Fixed
$U_{\rm min}$	(0.1, 25)	(0.7, 25)	Flat
$U_{\rm max}$	$(10^3, 3\times10^5)$	$(3\times10^5, 3\times10^5)$	Fixed
$\gamma_{\rm dust}$	(0, 1)	(0, 1)	Flat
$q_{\rm PAH}$	(0.0047, 0.0458)	(0.0047, 0.0458)	Flat
Calzetti et al. (2000) Attenuation Law			
$\tau_V^{\rm diff}$ [b]	(0, 3)	(0, 3)	Flat
Inclination-dependent Attenuation Curves			
$\tau_B^{\rm f}$	(0, 8)	(0, 8)	Flat
$r^{\rm 0,old}$ [c]	(0, 1)	(0, 1)[d]	Fixed[d]
B/D	$(0, \infty)$	(0, 0)	Fixed
F	(0, 0.61)	(0, 0.61)	Flat
$\cos i$	(0, 1)	(0, 1)	Flat/Image-based distribution[e]

[a]The age ranges of the oldest two age bins depend upon the redshift.
[b]Proportional to A_V ($\tau_V^{\rm diff} = 0.4 \ln 10 A_V$).
[c]$r^{\rm 0,old}$ is a binary parameter with 0 designating "young' star formation history bins and 1 designating "old' star formation history bins. The star formation history bins that contain ages $\lesssim$ 500 Myr are required to be considered "young' (see Section 3.4.3).
[d]For this work, we define the "young' star formation history bins as those with look-back times $<$ 1 Gyr (i.e., ψ_1, ψ_2, and ψ_3) and the "old' bins as those with look-back times $>$ 1 Gyr (i.e., ψ_4 and ψ_5).
[e]The SEDs were fit twice with the inclination-dependent model. Once with the inclination prior as a flat distribution, and again with the prior as the image-based inclination distributions derived in Section 3.3 (see Section 3.5.3).

galaxy was fixed to the age of the universe at that galaxy's redshift. If the age of the universe for a galaxy was less than 5 Gyr, then the fifth age bin was omitted, and the fourth age bin upper bound was fixed at to the age of the universe at that galaxy's redshift. We list the possible and adopted ranges for the SFR of each bin and the assumed priors used when fitting the SEDs in Table 3.2.

The time steps of the SFH model can be arbitrarily chosen in `Lightning`. However, our time steps were chosen such that the first step, 0–10 Myr, models the stellar population that is able to emit enough hydrogen-ionizing photons to produce noticeable hydrogen recombination lines. The second time step of 10–100 Myr was chosen to model the stellar population that emits the majority of the UV emission when combined with the first step. The combination of the first two time steps provides the average SFR of the past 100 Myr, which is a timescale commonly used by SFR calibrations (e.g., Kennicutt, 1998; Calzetti et al., 2007; Hao et al., 2011). The final three steps were chosen to have comparable bolometric luminosities to that of the second time step for the case of a constant SFR (see Eufrasio et al. 2017 for details).

Due to the relatively large number of free parameters used in this work (all of which are listed in Table 3.2), we added a module to `Lightning` that uses Markov Chain Monte Carlo (MCMC) analysis via the Metropolis-Hastings algorithm (Metropolis et al., 1953; Hastings, 1970) to fit each SED and derive posterior probability densities of the SFH time steps, attenuation parameters, and dust model parameters. Due to the complex nature of our models, manually selecting an optimal covariance matrix for the sampled proposal multivariate normal distribution was challenging. Therefore, we also implemented a vanishing adaptive MCMC algorithm (see Algorithm 4 from Andrieu & Thoms 2008), which adaptively determines the optimal covariance matrix. It does this by modifying the covariance matrix with each step in the chain until an optimal acceptance ratio (Gelman et al., 1996) is reached. This modification of the covariance matrix with previous steps is not a true Markov chain, due to the present being affected by the past. However, the vanishing part of the algorithm causes the amount of modification to the covariance matrix to decrease with each step in the chain. Therefore, with a long enough chain, the modification to the covariance matrix will cease, and the resulting ending segment of the chain will be a true Markov chain.

In Section 3.5, we further discuss the use of the MCMC procedure in estimating the parameter distributions.

The MCMC algorithm was added and utilized over the matrix inversion algorithm in the previous version of `Lightning` (v1.0), since the matrix inversion algorithm required a grid for the dust attenuation and emission parameters. Due to the increase in parameters from the dust emission model (see Section 3.4.2) and inclination-dependent attenuation (see Section 3.4.3), this method was no longer feasible due to very long computational times, whereas the MCMC algorithm run time is less sensitive to an increase in the number of parameters. For example, using the dust emission model and the inclination-dependent attenuation both with all parameters free, the MCMC algorithm with 10^5 iterations takes approximately the same amount of time as the inversion method with a coarse grid of six points per parameter.

3.4.2 Dust Emission Model

Our goal for modeling the dust emission component of the SEDs in this paper is to retrieve the total infrared luminosities. To accomplish this, we use the Draine & Li (2007) dust model, which utilizes a mixture of carbonaceous and silicate grains, whose grain size distributions were made to be compatible with the extinction in the MW (Weingartner & Draine, 2001). The model parameterizes the dust mass exposed to the radiation field intensity U, which ranges from $U_{\rm min}$ to $U_{\rm max}$, as a superposition of a delta function at $U_{\rm min}$ and a power law of slope α between $U_{\rm min}$ and $U_{\rm max}$. This is given by Equation 23 in Draine & Li (2007),

$$\begin{aligned}\frac{dM_{\rm dust}}{dU} =& (1-\gamma_{\rm dust})M_{\rm dust}\delta(U-U_{\rm min}) \\ &+ \gamma_{\rm dust}M_{\rm dust}\frac{(\alpha-1)}{(U_{\rm min}^{1-\alpha}-U_{\rm max}^{1-\alpha})}U^{-\alpha},\ \ \alpha\neq 1,\end{aligned} \tag{3.3}$$

where $M_{\rm dust}$ is the total dust mass, $\gamma_{\rm dust}$ is the fraction of dust mass exposed to the power-law radiation field, and δ is the Dirac δ-function. There is one other relevant parameter in the model, $q_{\rm PAH}$, which is the polycyclic aromatic hydrocarbon (PAH) index. The PAH index is defined to be the fraction of the total grain mass corresponding to PAHs containing less than 1000 carbon atoms.

Excluding the normalization parameter $M_{\rm dust}$, there are five free parameters within the dust model: α, $U_{\rm min}$, $U_{\rm max}$, $\gamma_{\rm dust}$, and $q_{\rm PAH}$. Of these parameters, three most strongly control the shape of the model IR SED: $q_{\rm PAH}$, $\gamma_{\rm dust}$, and $U_{\rm min}$ (Draine et al., 2007; Leja et al., 2017). As for $U_{\rm max}$ and α, Draine et al. (2007) found that dust model fits are not very sensitive to precise values of these two parameters and that the IR SEDs of galaxies in the Spitzer Infrared Nearby Galaxies Survey (Kennicutt et al., 2003) were well reproduced by $U_{\rm max} = 10^6$ and $\alpha = 2$. Therefore, we adopt the fixed values of $U_{\rm max} = 3 \times 10^5$ and $\alpha = 2$ when fitting the SEDs as described in Section 3.5. We note that Draine et al. (2007) used $U_{\rm max} = 10^6$ rather than $U_{\rm max} = 3 \times 10^5$. However, our current set of dust models has a maximum $U_{\rm max}$ of 3×10^5. Therefore, we used this value instead and expect minimal difference in fittings, since $U_{\rm max}$ is insensitive to precise values.[4] The possible and adopted ranges for the dust emission parameters and the assumed priors used when fitting the SEDs can be seen in Table 3.2. We note that $M_{\rm dust}$ is not a free parameter in our models, rather the normalization of the dust emission is dependent upon the total attenuation via energy balance (see Section 3.4.4).

[4] `Lightning` computes the dust emission model using the publicly available δ-functions of U, from which the power-law component can be calculated for any given α. The largest available δ-function of U is $U = 3 \times 10^5$. Therefore, rather than extrapolating to $U = 10^6$, we limit U to the largest available value.

3.4.3 Inclination-dependent Attenuation Curves

The original two FUV to NIR attenuation modules in `Lightning` were the original Calzetti et al. (2000) attenuation law as well as its modified version by Noll et al. (2009), which includes a bump and a variable UV slope. To evaluate the effects of inclination on the derived SFHs, we required an inclination-dependent attenuation model. Therefore, we added another attenuation module that utilizes the inclination-dependent attenuation curves from Tuffs et al. (2004), as updated by Popescu et al. (2011).

To create the inclination-dependent attenuation curves, Tuffs et al. (2004) used the ray-tracing radiative transfer code of Kylafis & Bahcall (1987) to determine the attenuation of the stellar emission from disk galaxies at different inclinations. They used geometries for the stellar and dust distributions that were shown to reproduce observed galaxies' UV to submillimeter SEDs. The model geometry consists of an exponential disk of old stars with associated diffuse dust (disk), a dustless old de Vaucouleurs stellar bulge (bulge), a thin exponential disk of young stars with associated diffuse dust that represents the stars and dust within spiral arms (thin disk), and a clumpy dust component that represents the dense molecular clouds within the star-forming regions of the thin disk (clumpy component). The dust model originally used by Tuffs et al. (2004) was the graphite and silicate dust model of Laor & Draine (1993). However, the dust model was updated by Popescu et al. (2011) to the dust model of Weingartner & Draine (2001) and Draine & Li (2007), which includes PAH molecules in addition to the graphite and silicate particles.

To determine the attenuation from the diffuse dust, Tuffs et al. (2004) superposed the diffuse dust from each disk and derived the attenuation as seen through the combined dust disks for each geometric component (disk, thin disk, and bulge) at various combinations of inclinations, central

face-on optical depths in the B-band (the optical depth of the galaxy in the B-band as seen through the center of the galaxy if it were face-on), τ_B^f, and wavelengths. They then fit the resulting attenuation curves as a function of inclination (i.e., Δm vs. $1-\cos i$) for each component, wavelength, and τ_B^f with fifth order polynomials, whose coefficients were made publicly available[5]. The wavelength range spanned 0.0912 to 2.2 μm, and the sampled values of τ_B^f were 0.1, 0.3, 0.5, 1.0, 2.0, 4.0, and 8.0, which span the range of optically thin to thick.

The attenuation due to the clumpy component in the thin disk was determined analytically rather than with radiative transfer calculations. This was calculated by assuming there was some probability that light from stars would be absorbed by the star's parent molecular cloud. The calculation was represented as a clumpiness factor F, which is defined as the total fraction of UV light that is locally absorbed by the parent cloud. This clumpiness factor is independent of the galaxy inclination, due to it being a local, rather than a global, galactic phenomenon.

The inclination-dependent attenuation for a whole galaxy is calculated by combining each geometric and clumpy component attenuation at a given wavelength and is given by

$$\Delta m_\lambda = -2.5\log\left(r^{0,\mathrm{disk}}10^{\frac{\Delta m_\lambda^{\mathrm{disk}}(i,\tau_B^f)}{-2.5}} + (1-r^{0,\mathrm{disk}}-r^{0,\mathrm{bulge}})(1-Ff_\lambda)10^{\frac{\Delta m_\lambda^{\mathrm{tdisk}}(i,\tau_B^f)}{-2.5}} + r^{0,\mathrm{bulge}}10^{\frac{\Delta m_\lambda^{\mathrm{bulge}}(i,\tau_B^f)}{-2.5}}\right), \quad (3.4)$$

where Δm_λ is the composite attenuation at a given wavelength λ; $r^{0,\mathrm{disk}}$ and $r^{0,\mathrm{bulge}}$ are the fractions of the intrinsic flux densities from the disk and bulge components, respectively, relative to the total intrinsic flux density of the galaxy; $\Delta m_\lambda^{\mathrm{disk}}(i,\tau_B^f)$, $\Delta m_\lambda^{\mathrm{tdisk}}(i,\tau_B^f)$, and $\Delta m_\lambda^{\mathrm{bulge}}(i,\tau_B^f)$ are the

[5]http://cdsarc.u-strasbg.fr/viz-bin/qcat?J/A+A/527/A109

attenuation from the diffuse dust given by the fifth order polynomials that are a function of inclination for a tabulated τ_B^f at the given wavelength for the disk, thin disk, and bulge, respectively; F is the clumpiness factor; and f_λ is a tabulated function of wavelength which gives F its wavelength dependence. Further, the two parameters, $r^{0,\mathrm{disk}}$ and $r^{0,\mathrm{bulge}}$, can be redefined by two, more intuitive parameters, the fraction of intrinsic flux density from the old stellar components compared to the total intrinsic flux density $r^{0,\mathrm{old}}$ and the B/D ratio, which are given by

$$r^{0,\mathrm{old}} = r^{0,\mathrm{disk}} + r^{0,\mathrm{bulge}}, \tag{3.5}$$

$$B/D = r^{0,\mathrm{bulge}}/r^{0,\mathrm{disk}}. \tag{3.6}$$

Therefore, since $\Delta m_\lambda^{\mathrm{disk}}(i, \tau_B^f)$, $\Delta m_\lambda^{\mathrm{tdisk}}(i, \tau_B^f)$, and $\Delta m_\lambda^{\mathrm{bulge}}(i, \tau_B^f)$ are dependent upon the inclination and τ_B^f, the five wavelength-independent free parameters of our attenuation curves are i, τ_B^f, $r^{0,\mathrm{old}}$, B/D, and F.

We note that B/D defined here is the ratio of the intrinsic luminosity of the old stellar bulge to the old stellar disk. Yet, measured values of B/D for galaxies are the observed luminosity ratio of the bulge to the disk. Therefore, since we do not necessarily expect the attenuation in the observed band for each of these components to be the same, the measured B/D could vary from the expected input B/D. Further, the observed emission from the disk will include emission from the young stellar thin disk as well. This inclusion of the thin disk can bias the measured B/D to smaller values than the input B/D parameter should be. However, both of these potential biases can be mitigated if the B/D for a galaxy is measured from a rest-frame NIR band (i.e., J, H, or K), where attenuation and the contribution from the young stellar population should both be minimal.

In the original equation given by Tuffs et al. (2004), $r^{0,\mathrm{disk}}$ and $r^{0,\mathrm{bulge}}$ are observable rather than intrinsic properties (i.e., fraction of observed flux densities from the disk or bulge components

compared to the total observed flux density) and wavelength dependent, with this wavelength dependence being used to vary the weight of each component at a given wavelength. However, by having $r^{0,\mathrm{disk}}$ and $r^{0,\mathrm{bulge}}$ as intrinsic properties and combining them into $r^{0,\mathrm{old}}$ and B/D, we can take advantage of our nonparametric SFH to effectively eliminate the need for a wavelength dependence and $r^{0,\mathrm{old}}$ as a free parameter. This is done by setting $r^{0,\mathrm{old}} = 0$ for all SFH age bins that are considered to be young populations and $r^{0,\mathrm{old}} = 1$ for those that are considered to be old populations. With these criteria, we assume that the young stellar population in the SFH is contained within the thin disk, and the older populations are within the disk and bulge. If $r^{0,\mathrm{old}}$ was allowed to be a free parameter, it would require a wavelength dependence to properly account for how the young and old populations contribute to the total emission at each wavelength. Since this would be computationally expensive, we set $r^{0,\mathrm{old}}$ as a fixed binary parameter in the attenuation curves, leaving four free parameters i, τ_B^f, B/D, and F.

We note that when designating SFH age bins as young and old populations for the binary parameter $r^{0,\mathrm{old}}$, any age bin that contains ages $\lesssim 500$ Myr should be considered part of the young population. This is required due to the assumption by Tuffs et al. (2004) that only the young population in the thin disk emits in the UV, and therefore, the old stellar population attenuation curve components ($\Delta m_\lambda^{\mathrm{disk}}(i, \tau_B^f)$ and $\Delta m_\lambda^{\mathrm{bulge}}(i, \tau_B^f)$) are zero for UV wavelengths ($\lambda \lesssim 4430$ Å). Since stellar models in `Lightning` with ages $\lesssim 500$ Myr can significantly contribute to the unattenuated UV emission, we require any age bin containing ages < 500 Myr to be considered part of the young population as to have this significant UV emission attenuated. Stellar models with ages > 500 Myr have 2–3 orders of magnitude lower unattenuated UV emission than those with ages $\lesssim 500$ Myr at the same SFR and do not significantly contribute to the total UV emission even when unattenuated. However, we strongly emphasize that this will only be the case when there is a prevalent young

population, such as in our galaxy sample. If a galaxy has a highly dominant older population, then the UV emission from this population could dominate the observed UV, and the assumption by Tuffs et al. (2004) that the old stellar population has no UV attenuation would no longer hold.[6]

To compute the total attenuation from Equation 3.4, we first calculated the attenuation from each geometric component $\Delta m_\lambda^{\rm disk}(i,\tau_B^f)$, $\Delta m_\lambda^{\rm tdisk}(i,\tau_B^f)$, and $\Delta m_\lambda^{\rm bulge}(i,\tau_B^f)$ using the tabulated polynomial coefficients from Popescu et al. (2011) for each tabulated wavelength and τ_B^f, for an input inclination. To the tabulated wavelengths and values of τ_B^f, we added the wavelength of 5.0 μm and $\tau_B^f = 0$ for later interpolation smoothness. For these new tabulated values, we set the attenuation of each geometric component to zero. This is because at $\tau_B^f = 0$ there should be no attenuation from the diffuse dust, and we adopted 5.0 μm to be the cutoff wavelength above which there will be no attenuation, because it matched the longest tabulated wavelength of f_λ in Table E.4 of Popescu et al. (2011).

Next, we calculated Δm_λ from Equation 3.4 with the precomputed values of $\Delta m_\lambda^{\rm disk}(i,\tau_B^f)$, $\Delta m_\lambda^{\rm tdisk}(i,\tau_B^f)$, and $\Delta m_\lambda^{\rm bulge}(i,\tau_B^f)$ for an input $r^{0,\rm old}$ and B/D (converted to $r^{0,\rm disk}$ and $r^{0,\rm bulge}$ by rearranging Equations 3.5 and 3.6) and F along with the tabulated values of f_λ. This resulted in Δm_λ as an array of values corresponding to the tabulated values of wavelength and τ_B^f. Finally, we interpolated this array for an input τ_B^f and input wavelengths to determine the total attenuation at the input wavelengths. To assure that there is no erroneous extrapolation beyond our tabulated wavelength range, we set the total attenuation to zero for wavelengths not within the range of $0.0912\ \mu{\rm m} \leq \lambda \leq 5.0\ \mu{\rm m}$. The possible and adopted ranges for each attenuation parameter and the assumed priors used when fitting the SEDs are listed in Table 3.2.

[6]It is possible to extrapolate $\Delta m_\lambda^{\rm disk}(i,\tau_B^f)$ and $\Delta m_\lambda^{\rm bulge}(i,\tau_B^f)$ into the UV, as shown in Chevallard et al. (2013). However, implementing an extrapolation is beyond the scope of this paper, but it will be pursued in future work.

We note that Tuffs et al. (2004) recommends interpolating $\Delta m_{\lambda}^{\rm disk}(i,\tau_B^f)$, $\Delta m_{\lambda}^{\rm tdisk}(i,\tau_B^f)$, and $\Delta m_{\lambda}^{\rm bulge}(i,\tau_B^f)$ for τ_B^f and the wavelength, and interpolating f_λ for wavelength before using Equation 3.4. However, we found that our method is faster computationally by a factor of 2 without any significant differences in the Δm_λ values. Therefore, the inclination-dependent attenuation module in `Lightning` interpolates after using Equation 3.4.

Examples of the young population (i.e., $r^{0,\rm old} = 0$ and $B/D = 0$) attenuation curves for the span of τ_B^f, F, and inclination are shown as the solid curves in Figure 3.7. The increase in τ_B^f with the other parameters fixed gives the expected result of steeper attenuation curves. As inclination increases to edge-on, the attenuation curves again become steeper. However, inclination also has the more influential effect, compared to τ_B^f, of causing attenuation at longer wavelengths. For face-on galaxies, wavelengths beyond 1.0 μm are negligibly attenuated, but edge-on galaxies can be significantly attenuated out to the attenuation curve limit of 5.0 μm. The clumpiness component F can be seen to steepen the attenuation curves in the UV, while leaving the optical attenuation relatively unchanged.

The dotted curves in Figure 3.7 show the original Calzetti et al. (2000) attenuation law for comparison. The normalization of each curve is set to the same A_V (0.55 μm) as the corresponding solid colored line in each panel. The Calzetti et al. (2000) attenuation law has only one free parameter, the diffuse V-band optical depth $\tau_V^{\rm diff}$, which is proportional to A_V. The possible and adopted range for $\tau_V^{\rm diff}$ and its assumed prior used when fitting the SEDs are listed in Table 3.2. We note that $\tau_V^{\rm diff}$ differs in definition from τ_B^f, beyond being in different optical bands. The parameter $\tau_V^{\rm diff}$is defined as the average optical depth over all solid angles, whereas τ_B^f is defined as the optical depth through the center of the galaxy, the location with the maximum dust surface density, when viewed face-on. In Figure 3.7, comparisons between the solid and dotted lines of matching color

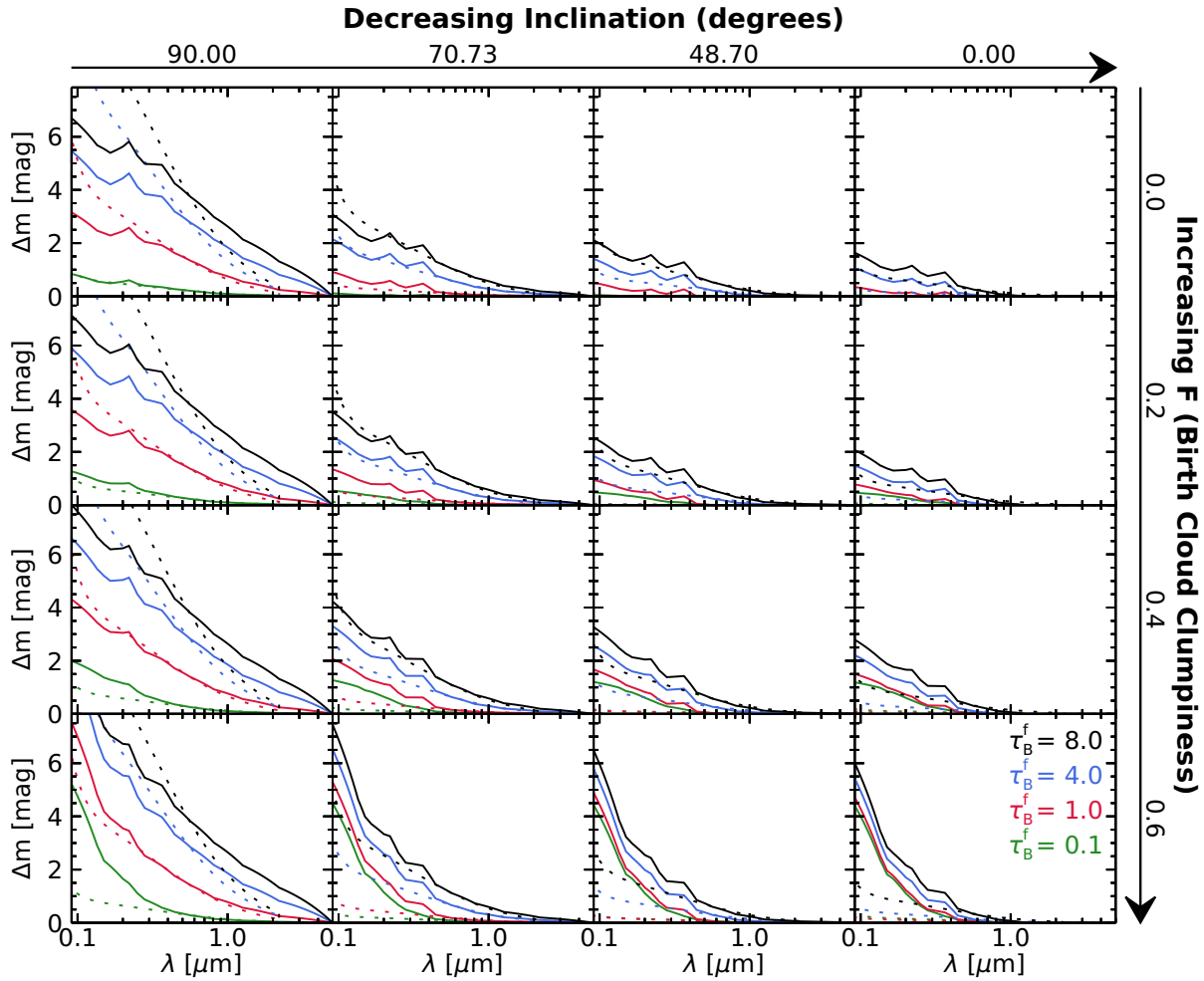

Figure 3.7: Each panel shows the attenuation as a function of the wavelength at four values of τ_B^f, the central face-on optical depth in the B-band (*solid* colored lines). Each curve has $r^{0,\mathrm{old}} = 0$ and $B/D = 0$, which are the fraction of intrinsic flux densities from the old components compared to the total intrinsic flux density of the galaxy and the B/D ratio. The panels from left to right show how the attenuation is affected by decreasing inclination, with the inclination values being equally spaced in $\cos i$ space. The panels from top to bottom show how the birth cloud clumpiness F causes the UV attenuation to become steeper. The *dotted* lines show the Calzetti et al. (2000) attenuation curve normalized to the same A_V (0.55 μm) as the corresponding *solid* colored line for comparison.

show the rigidity of the Calzetti et al. (2000) curve compared to the inclination-dependent curves. Also from the comparison, it can be seen that the Calzetti et al. (2000) curve rarely aligns with the inclination-dependent attenuation curves, especially in cases of edge-on inclinations and high birth cloud clumpiness.

Figure 3.8 shows example attenuation curves of the old population (i.e., $r^{0,\mathrm{old}} = 1$ and $F = 0$) for the span of τ_B^f, B/D, and inclination as the solid curves. The attenuation curves are truncated at wavelengths shortward of 0.443 μm due to the assumption by Tuffs et al. (2004) that the old stellar population does not provide substantial emission at wavelengths shorter than 0.443 μm and therefore does not have attenuation. As with the young population curves, an increase in τ_B^f with the other parameters fixed gives steeper attenuation curves. Increasing inclination to edge-on, the attenuation curves again steepen and attenuation also occurs at longer wavelengths. Increasing the B/D with the other parameters fixed results in steeper attenuation curves similar to increasing τ_B^f. Comparing to the dotted curves, which show the original Calzetti et al. (2000) attenuation law normalized to the same A_V as the corresponding solid colored line in each panel, it can be seen that the Calzetti et al. (2000) attenuation law has a very similar shape as the low inclination curves for all B/D values at optical wavelengths. However, as with the young population curves, the curves diverge as inclination approaches edge-on.

3.4.4 Energy Balance/Conservation

Energy balance in SED fitting is the assumption that the power absorbed by attenuating dust is equal to the radiative power of the dust emission (i.e., the UV through NIR attenuated light is reemitted in the IR and submillimeter; e.g., da Cunha et al., 2008; Leja et al., 2017; Boquien et al., 2019; Buat et al., 2019). However, energy balance is not true energy conservation, due to it considering the line-of-sight intensity as representative of the isotropic power rather than the total 4π steradian anisotropic integrated power. As stated above, the attenuation in disk galaxies is not equivalent at all viewing angles, but depends on the inclination. Therefore, to apply more realistic energy conservation, an inclination-dependent attenuation curve can be used to account

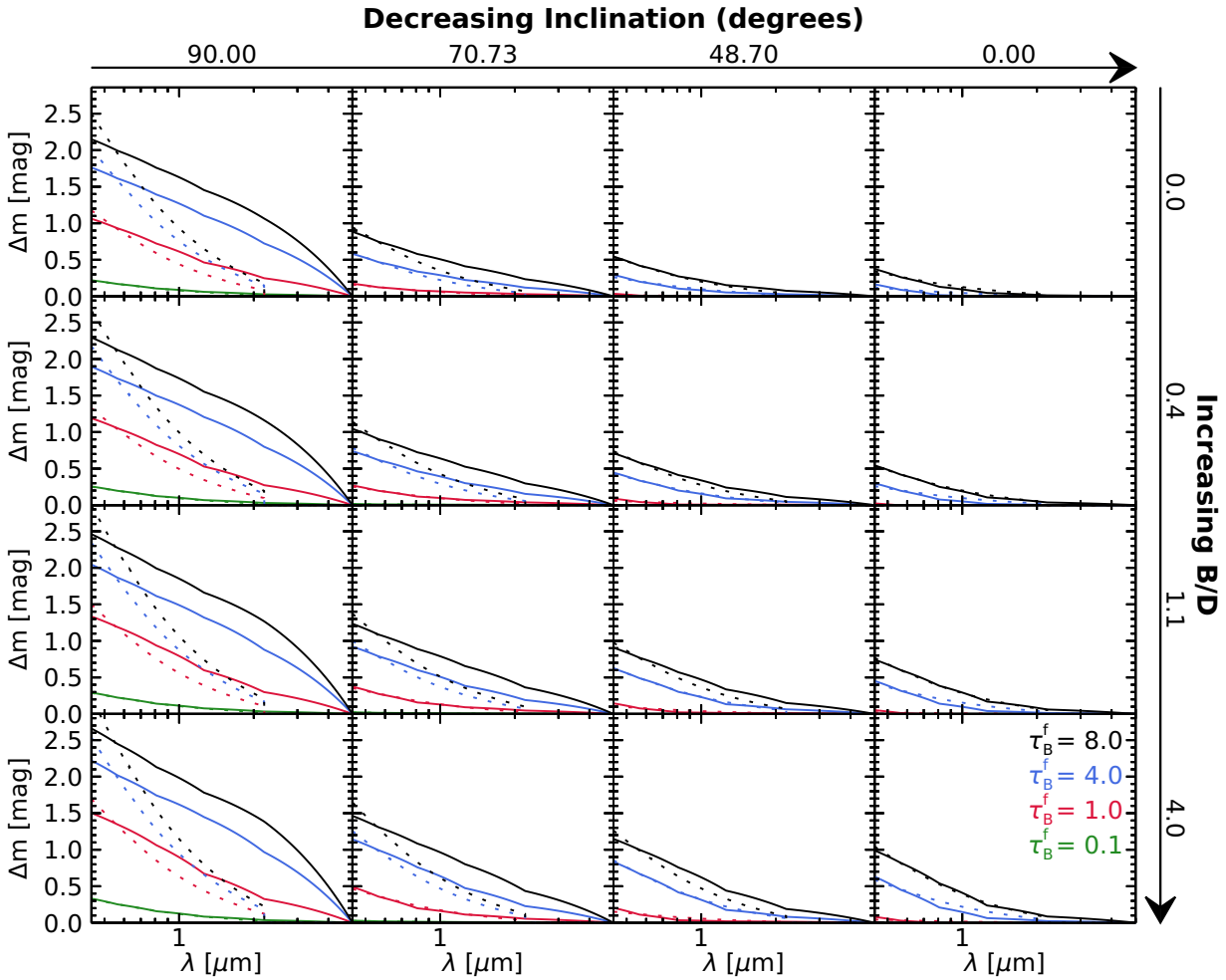

Figure 3.8: Each panel shows the attenuation as a function of the wavelength at four values of τ_B^f, the central face-on optical depth in the B-band (*solid* colored lines). Each curve has $r^{0,\mathrm{old}} = 1$ and $F = 0$, which are the fraction of intrinsic flux densities from the old components compared to the total intrinsic flux density of the galaxy and the clumpiness factor. The panels from left to right show how the attenuation is affected by decreasing inclination, with the inclination values being equally spaced in $\cos i$ space. The panels from top to bottom show how attenuation is affected by increasing the B/D ratio, with the B/D values being equally spaced in the bulge-to-total B/T space ($B/D = B/T/(1-B/T)$). The truncation of the attenuation curves at 0.443 μm is due to the assumption by Tuffs et al. (2004) that the old stellar population does not emit light at wavelengths shorter than 0.443 μm and therefore does not have attenuation. The *dotted* lines show the Calzetti et al. (2000) attenuation curve normalized to the same A_V (0.55 μm) as the corresponding *solid* colored line for comparison.

for the line-of-sight variation of the attenuated emission and aid in determining the total bolometric power.

When applying any of the attenuation modules to the stellar emission, `Lightning` can require energy balance/conservation between the dust emission and attenuated stellar emission. We model this independently for each SFH time step by requiring the total integrated IR luminosity ($L_{\rm TIR}$) from dust emission to be equal to the total integrated absorbed stellar luminosity ($L_{\star}^{\rm abs}$). Assuming azimuthal symmetry, this is given by

$$L_{\rm TIR} = L_{\star}^{\rm abs} = 2\pi {d_L}^2 \int_0^{\pi} \int_0^{\infty} \left({F_\nu}^{\rm unatt} - {F_\nu}^{\rm att} \right) \sin\theta \, d\nu \, d\theta, \tag{3.7}$$

where ${F_\nu}^{\rm unatt}$ and ${F_\nu}^{\rm att}$ are, respectively, the unattenuated and attenuated fluxes from the stellar emission. For an inclination-independent attenuation curve, this simplifies to the energy balance assumption:

$$L_{\rm TIR} = L_{\star}^{\rm abs} = L_{\rm bol}^{\rm unatt} - L_{\rm bol}^{\rm att}, \tag{3.8}$$

where $L_{\rm bol}^{\rm unatt}$ is the bolometric luminosity of the stellar population without attenuation being applied, and $L_{\rm bol}^{\rm att}$ is the bolometric luminosity after attenuation is applied assuming the line-of-sight emission is isotropic.

However, when using our inclination-dependent attenuation curves that assume anisotropic emission, Equation 3.7 does not simplify as easily, since ${F_\nu}^{\rm att}$ is a function of inclination (or θ). To compute $L_{\star}^{\rm abs}$, the polar angle θ in Equation 3.7 can be replaced with inclination and simplified to

$$L_{\rm TIR} = L_{\star}^{\rm abs} = L_{\rm bol}^{\rm unatt} - \int_0^{\pi/2} \tilde{L}_{\rm bol}^{\rm att}(i) \sin i \, di, \tag{3.9}$$

where $\tilde{L}_{\rm bol}^{\rm att}(i) \equiv 4\pi {d_L}^2 \int_0^{\infty} {F_\nu}^{\rm att}(i) \, d\nu$ and

$$L_{\rm bol}^{\rm att} = \int_0^{\pi/2} \tilde{L}_{\rm bol}^{\rm att}(i) \sin i \, di. \tag{3.10}$$

Therefore, Equation 3.10 must be integrated over inclination to generate $L_{\rm bol}^{\rm att}$ so that the $L_{\star}^{\rm abs}$ can

be calculated for the inclination-dependent model.

To calculate $L_\star^{\rm abs}$, we numerically integrated Equation 3.10 using the trapezoidal method for a grid of inclination angles spanning 0 to $\pi/2$. Due to $\tilde{L}_{\rm bol}^{\rm esc}$ being determined from the inclination-dependent attenuation curve, the attenuation had to be computed for this grid of inclination angles along with the input inclination. Rather than computing this integral and attenuation multiple times for each galaxy in our sample while fitting an SED, we precomputed an array of $L_\star^{\rm abs}$ for each SFH time step once from Equation 3.9 using a fine grid of the inclination-dependent attenuation parameters in Equation 3.4 (i.e., i, τ_B^f, F, $r^{0,\rm disk}$, and $r^{0,\rm bulge}$). This fine grid consisted of 51 equally spaced grid points for each attenuation parameter, except inclination. We used 70 inclination angles to ensure an accurate calculation of the integral. We also added 10 additional finely spaced grid points to τ_B^f between 0 and 0.1 (i.e., 0.01–0.1 in steps of 0.01) to ensure the accuracy of the $L_\star^{\rm abs}$ array, due to these values not being in the original Tuffs et al. (2004) tabulations. The $L_\star^{\rm abs}$ of the last two SFH time steps had to be computed for a grid of redshifts, since the age range of the step varied with the redshift, as described in Section 3.4.1. The redshift grid was computed in steps of 0.01, since this was the accuracy used for our spectroscopic redshifts. We then linearly interpolated between the fine attenuation parameter grid points to determine $L_\star^{\rm abs}$ for any possible combination of attenuation parameters at a given redshift. Comparing the interpolated $L_\star^{\rm abs}$ values from the precomputed arrays to $L_\star^{\rm abs}$ values computed from the exact attenuation parameters and 70 inclination grid points using Equation 3.9 showed that the interpolated values were always within 0.5% of the exact calculations of $L_\star^{\rm abs}$.

We recommend that if a precomputed array of $L_\star^{\rm abs}$ is not used, a grid of inclinations should be used that minimizes the computational time and maximizes the accuracy of the integral. We have allowed for this possibility in `Lightning` and provided the optimal grid, if one is not supplied. To

determine the optimal grid, we computed the integral for grids of 3 to 70 equally spaced inclination angles for various combinations of attenuation curve input parameters. We found that using $\gtrsim 13$ grid points for the integral resulted in $\lesssim 0.5\%$ difference in $L_\star^{\rm abs}$ compared to the grid with 70 points. Using more points minimally changed this difference, and fewer points rapidly increased the difference. Therefore, when computing the integral in Equation 3.10 without a specified grid of inclinations, we required 13 equally spaced inclinations besides the input inclination. We recommend using a precomputed array of model $L_\star^{\rm abs}$ rather than calculating it with the optimal grid for each new combination of attenuation parameters. Excluding the time required to make the precomputed array, using it is approximately 10 times faster computationally per calculation of $L_\star^{\rm abs}$ than using the optimal grid.

3.5 SED Fitting Results

3.5.1 Inclination-independent Comparison Fits

To test the efficacy of the inclination-dependent attenuation prescription, we derived SFHs using the inclination-independent Calzetti et al. (2000) attenuation curve in its original form for comparison. We used this attenuation curve within our adaptive MCMC procedure along with energy balance and our Draine & Li (2007) dust model. The Calzetti et al. (2000) attenuation curve was chosen due to its widespread use in SED fitting of deep-field galaxies (e.g., Daddi et al., 2005; Ilbert et al., 2010; Skelton et al., 2014; Mobasher et al., 2015).

In order to reduce potential degeneracies in the dust model, we set the parameters $U_{\rm max} = 3 \times 10^5$ and $\alpha = 2$ as discussed in Section 3.4.2. We also limit the dust models to be of MW composition with uniform priors spanning $0.4\% \leq q_{\rm PAH} \leq 4.6\%$ and $0.7 \leq U_{\rm min} \leq 25$. This range

and set of fixed parameters is the "restricted" dust model recommended by Draine et al. (2007) when submillimeter data are unavailable. The range of $q_{\rm PAH}$ spans the full range of values for the MW composition; however, the lower limit of $U_{\rm min}$ has been chosen to be 0.7 instead of 0.1. This is because small values of $U_{\rm min}$ correspond to cold dust temperatures, which require rest-frame submillimeter data ($\lambda_{\rm rest} > 500$ μm) to be properly constrained.

Besides the degeneracies in the dust model, the other main degeneracy in our fits is the well-established age-reddening-metallicity degeneracy. To help minimize this, we fixed the metallicity to the solar value for all of our age bins. We note that this ignores the underlying metallicity evolution and could cause systematic variation in our SFHs and stellar mass estimates. As metallicity decreases, the intrinsic UV-optical emission for our models increases for a fixed SFR. This can lead to slightly decreased SFRs for the younger populations of the SFH, assuming fixed attenuation, due to the younger populations dominating the UV-optical emission. However, the stellar mass estimates would be relatively unaffected due to the older populations, which mainly emit at wavelengths in the NIR and minimally contribute to the UV-optical emission, most strongly affecting the mass estimates. Further, fixing the metallicity still leaves some age-reddening degeneracy, but this is reduced by our energy balance assumption (see Section 3.4.4). Therefore, we do not expect any material impact on our results by ignoring metallicity evolution.

With our adopted priors on the dust model, we ran the adaptive MCMC algorithm for 10^5 iterations for an initial fit on each galaxy's SED with arbitrarily chosen starting values. To test for convergence to a single best solution, we ran 10 parallel chains at random starting values between 0 and 10 $M_\odot$ yr^{-1} for the five SFH bins and random starting values within the attenuation and dust parameter ranges. We chose the starting range for the SFH bins based off of the initial fits' SFH distributions, of which 75% had values less than 10 $M_\odot$ yr^{-1}. A larger starting range could

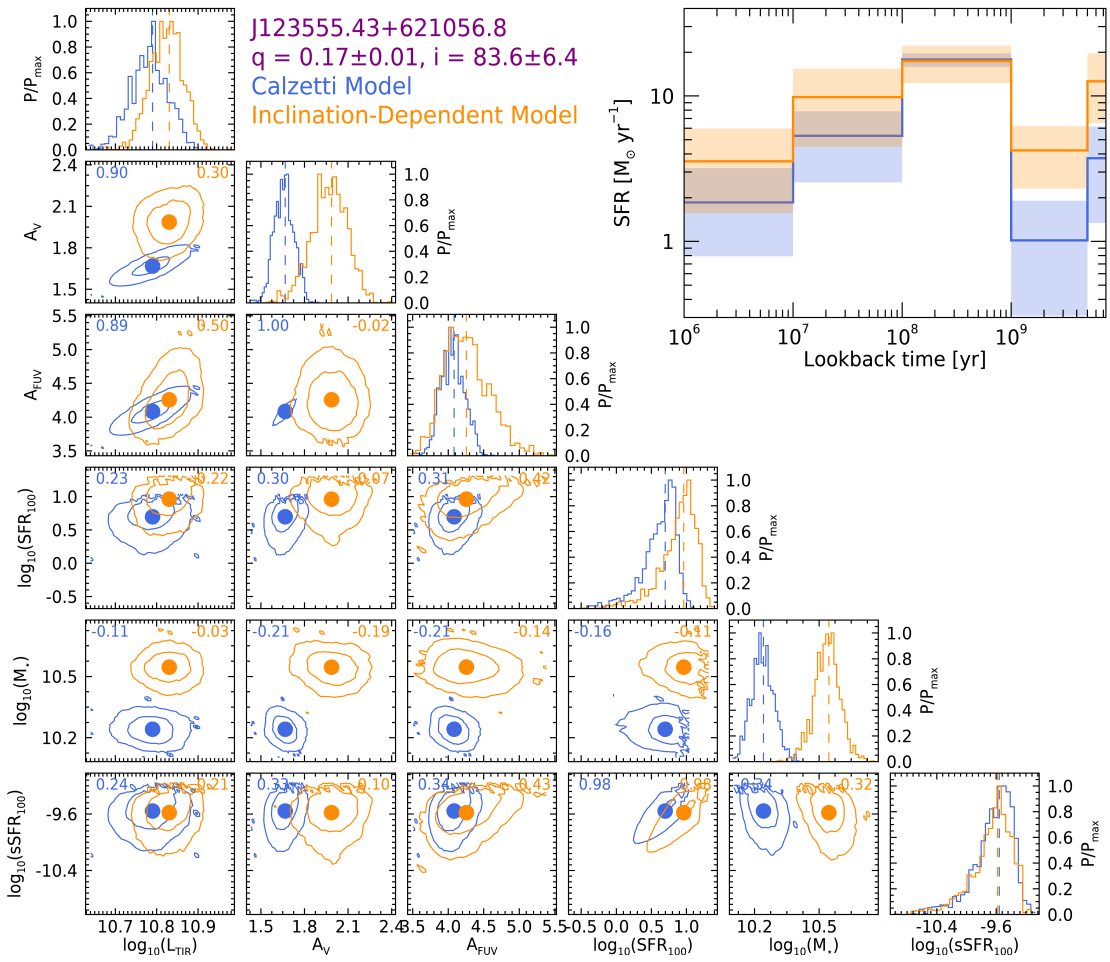

Figure 3.9: (*Lower left triangle plot*): Probability distribution functions in terms of $P/P_{\rm max}$ (diagonal elements) and the 68% and 95% confidence contours for $L_{\rm TIR}$ [$L_\odot$] , A_V [mag], $A_{\rm FUV}$ [mag], $\rm SFR_{100}$ [$\rm M_\odot\ yr^{-1}$], $M_\star$ [$M_\odot$], and $\rm sSFR_{100}$ [$\rm yr^{-1}$] parameter pairs (off-diagonal elements) for our most inclined example galaxy, J123555.43+621056.8. This galaxy is the galaxy with a purple outline in Figure 3.2. The vertical dashed lines in the histograms and solid colored circles in the contour plots indicate the median values of each parameter. The Pearson correlation coefficients for each set of parameters are shown in the upper corners of each contour plot. Blue represents the results from the Calzetti et al. (2000) fits, and orange represents the results from the inclination-dependent fits with the image-based inclination prior. (*Upper right corner*): The resulting median SFH and 16%–84% uncertainty range for J123555.43+621056.8 with the same color scheme. The youngest age bin lower bound has been truncated to 10^6 yr for plotting purposes, but truly extends to 0 yr.

result in a drastically increased burn-in phase if a starting value was much larger than the solution.

To confirm the convergence of the parallel chains, we performed the Gelman-Rubin test (Gelman & Rubin, 1992; Brooks & Gelman, 1998) on the last 5000 iterations of the chains. This test

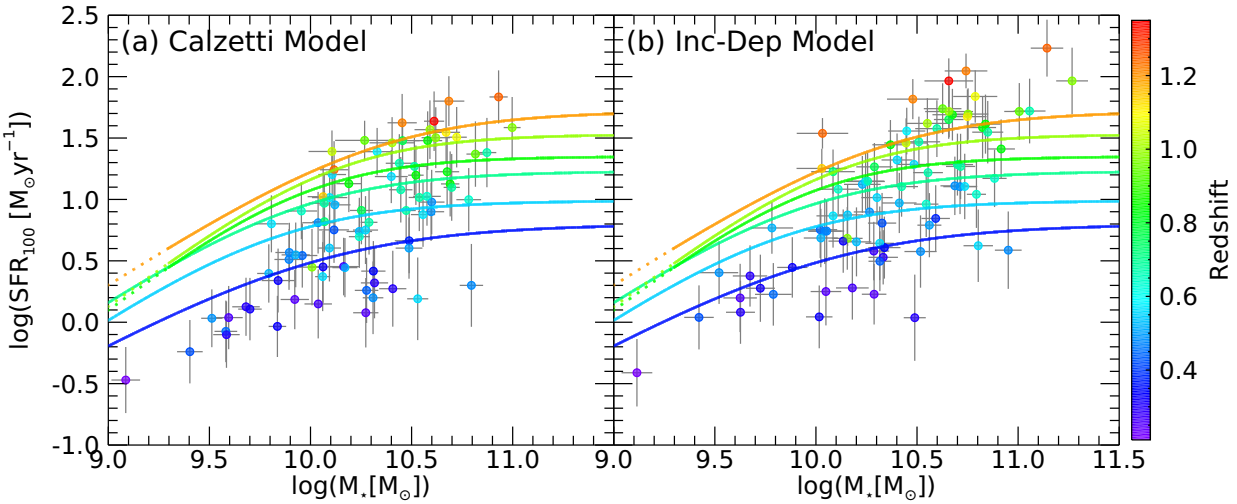

Figure 3.10: SFR_{100} vs. $M_\star$ for the 82 galaxies in our final sample colored by redshift. The colored curves show the location of the star-forming galaxy MS as derived by Lee et al. (2015) at their median redshifts given by the corresponding color in the color bar. The dotted sections of the higher redshift curves show the extrapolated region of the curves beyond the lower stellar mass limits. Panel (*a*) shows the SFR_{100} and stellar masses derived from the Calzetti et al. (2000) model, and panel (*b*) shows the values derived from the inclination-dependent model with the image-based inclination prior. Both panels show that most galaxies in the final sample tend to follow the star-forming MS at low redshifts ($z < 0.7$). As for higher redshift galaxies ($z > 0.7$), the inclination-dependent model shows that galaxies tend to be above the MS, while the Calzetti et al. (2000) model shows that they tend to follow the MS.

indicated that all chains for each galaxy converged to the same solution by the final 5000 iterations (i.e., $\sqrt{\hat{R}} \approx 1$). Therefore, we used the last 5000 iterations of the parallel chain that produced the minimum median χ^2 for our parameter distributions and subsequent analysis. To test the quality of fits to the SEDs, we performed a χ^2 goodness of fit test using the minimum χ^2 of each galaxy's chain. The resulting distribution of $P_{\rm null}$ from this test showed a relatively flat distribution (i.e., expected distribution of χ^2). Therefore, we conclude that the Calzetti et al. (2000) model can acceptably model the SEDs.

An example of the distributions for the parameters of interest, which are $L_{\rm TIR}$, V-band attenuation (A_V), FUV-band attenuation ($A_{\rm FUV}$), recent average SFR of the last 100 Myr (SFR_{100}), total stellar mass ($M_\star$), and specific SFR of the last 100 Myr ($sSFR_{100}$), are shown in Figure 3.9 as

the blue lines for our most inclined example galaxy, J123555.43+621056.8. The resulting median SFH and its 16%–84% uncertainty range is also shown in the upper right corner. In Figure 3.10(a), we show how the derived $M_\star$ and SFR_{100} from these fits compare to the star forming galaxy main sequence (MS) from Lee et al. (2015). The results from these fits tend to follow the MS at their respective redshift. Additional diagnostic plots showing the free parameter distributions and the global trends for all galaxies in the sample can be found in Appendix 3.B.

3.5.2 Inclination-dependent Fits

For our inclination-dependent fits, we used our adaptive MCMC procedure with energy conservation, the "restricted" Draine & Li (2007) dust model, and the inclination-dependent attenuation curves. For the inclination-dependent attenuation curves, we fix $r^{0,\mathrm{old}} = 0$ for the first three age bins of our SFHs and $r^{0,\mathrm{old}} = 1$ for the older two age bins, as to define them as the young and old populations, respectively, as discussed in Section 3.4.3. The third age bin (0.1–1 Gyr) is considered a "young" age bin due to the requirement that all age bins that contain ages < 500 Myr must be considered part of the young population as to have their nonnegligible UV emission attenuated.[7] Further, as stated in Section 3.2.2, we only analyzed SEDs of disk-dominated galaxies, rather than disk galaxies in general. Since we selected disk-dominated galaxies with approximately no bulge, we set $B/D = 0$ to reduce the number of free parameters and potential degeneracies. As stated by Tuffs et al. (2004) and noted in Section 3.4.3, increasing B/D with τ_B^f constant can have the same effect on the attenuation curve as increasing τ_B^f for a "pure" disk (i.e., $B/D = 0$). We therefore remove this degeneracy by selecting our sample to be disk-dominated, or as close to being a "pure" disk as possible. We note, however, that the presence of a small bulge has the effect of

[7] We tested how the choice of this third age bin upper limit affects our results and found that changing the upper limit to 500 Myr or 1.5 Gyr had no statistical impact on the results (see Section 3.6 and Figure 3.15).

systematically increasing the derived values of τ_B^f. In addition to this model degeneracy, there is another possible degeneracy between inclination and τ_B^f. As discussed in Section 3.4.3, increasing the inclination or τ_B^f has the effect of steepening the attenuation curve. We discuss how this degeneracy affects the derived inclinations in Section 3.5.3.

Beyond these degeneracies, we note that certain parameters could theoretically be linked together to make an even more physically motivated model. For example, the attenuation from the clumpy birth cloud component, F, could be linked to the fraction of the total dust luminosity that is radiated by dust grains in regions where $U > 10^2$, or $f_{\rm PDR}(U_{\rm min}, U_{\rm max}, \gamma_{\rm dust})$ (given by Equation 29 in Draine & Li 2007), which is typically associated with photodissociation regions (PDRs) near newly born luminous stars (Draine & Li, 2007). Not considering this linkage could result in nonphysical results where F is high and $f_{\rm PDR}$ is low. However, implementing potential linkages between parameters like this is beyond the scope of this paper, but is something that could be explored in future work.

For these fits, we ran the adaptive MCMC algorithm for 2×10^5 iterations. A larger number of iterations here compared with the Calzetti et al. (2000) fits in Section 3.5.1 was required due to the larger parameter space so that the best solution could be reached. We again tested for convergence of the chains to a single best solution by running 10 parallel chains at random starting values between 0 and 10 $M_\odot$ yr^{-1} for the five SFH bins and random starting values within the attenuation and dust parameter ranges. The Gelman-Rubin test was then performed on the last 5000 iterations of the parallel chains, which indicated that convergence to the same solution had been achieved by the final 5000 iterations. Therefore, like the Calzetti et al. (2000) fits, we used the last 5000 iterations of the parallel chain that had the minimum median χ^2 for our parameter distributions.

We tested the quality of these fits by performing a χ^2 goodness of fit test using the minimum

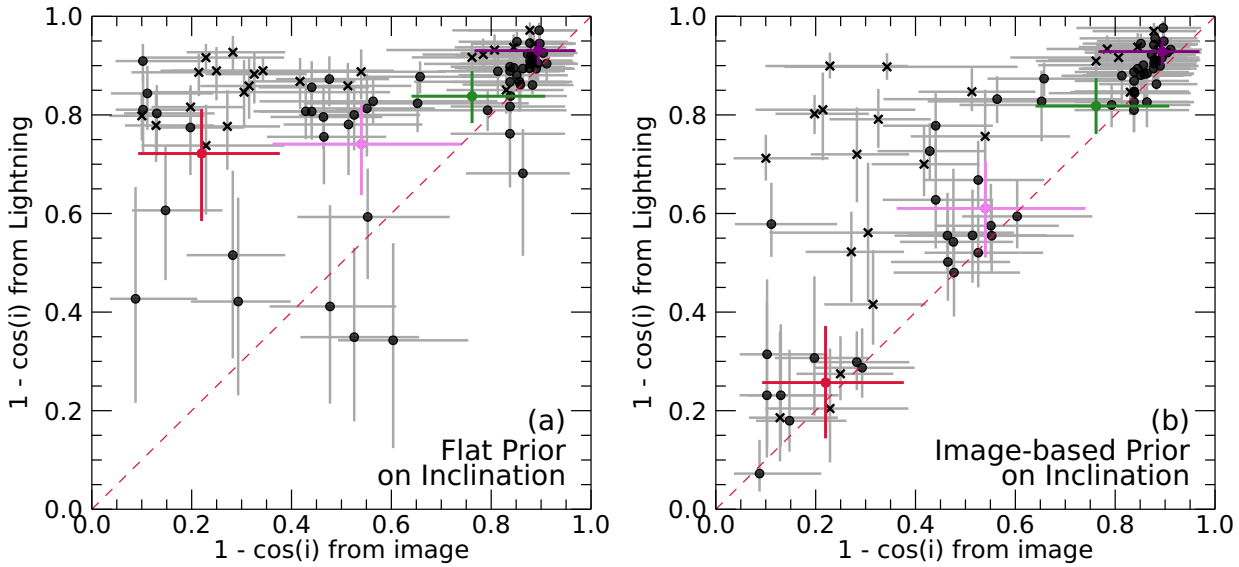

Figure 3.11: (*a*) Inclination ($1-\cos i$) derived from `Lightning` with flat inclination prior. (*b*) Inclination derived from `Lightning` with image-based inclination prior. Both are vs. the inclination derived from the image-based Monte Carlo simulation. The error bars span the 16th and 84th percentiles rather than 1σ due to the asymmetry of the image-based inclination distributions. The colored points are the inclination estimates of the four example galaxies shown in Figure 3.2 using the same color as the outline of the corresponding postage stamp. Red, pink, green, and purple represent J123626.62+621252.1, J123654.99+621658.5, J033231.18-274017.5, J123555.43+621056.8, respectively. Using the image-based priors aligns more galaxies to the unity line. Galaxies that still remain off of the line tend to have higher $L_{\rm TIR}$ and $z \geq 0.7$. In both panels, galaxies with $z < 0.7$ are indicated by the circles, and those with $z \geq 0.7$ are indicated by the X marks.

χ^2 of each galaxy's chain. This test showed that the resulting distribution of $P_{\rm null}$ had a relatively flat distribution (i.e., expected distribution of χ^2). Therefore, we concluded that our inclination-dependent model can also acceptably model these SEDs.

3.5.3 SED Inclination Estimates

After fitting the SEDs with the inclination-dependent model, we compared the derived inclination PDFs from the fits to the inclination PDFs from the image-based Monte Carlo simulation described in Section 3.3. This was done to determine the predictive power of the inclination-dependent model for inclination with the presence of the inclination-τ_B^f degeneracy. Figure 3.11(a)

shows this comparison as the median values from each distribution and the 16th and 84th percentile error ranges. This shows that `Lightning` tends to favor solutions at high inclinations, with a median value never falling below $1-\cos i \approx 0.3$, while the image-based method has inclinations down to $1-\cos i \approx 0.1$. To test the consistency of the fits' inclination PDFs with the image-based inclination PDFs, we computed R, which we define as the ratio of the intersection area to the union area of the two distributions, for each galaxy. This method would result in $R = 1$ if the two distributions were identical and $R = 0$ if they had no overlap. Using these ratios, we chose to set a value of $R_{\rm cutoff} = 0.05$ as the cutoff at which we define R values lower than this cutoff to have inclinations that are in disagreement between methods. For these fits, 60 out of the 82 PDFs ($\approx$73%) had $R > R_{\rm cutoff}$ with a median of $R = 0.29$.

Due to this relatively large disagreement ($\approx$27%) in inclination estimates and the apparent bias of the fit inclinations to higher values, we decided to refit the SEDs using the image-based PDFs of inclination as priors to minimize the inclination-τ_B^f degeneracy and to force the predicted inclinations to be more consistent with the image-based estimates. The method for refitting these SEDs and testing for convergence of the Markov chains was exactly the same as in Section 3.5.2, except for the introduction of the new prior on inclination. All other parameters were still fit using flat priors. Convergence of these chains to a single solution was achieved by the final 5000 iterations. We then used the last 5000 iterations selected using the same method described above to make our final parameter distributions. Testing the quality of these fits with a χ^2 goodness of fit test showed again that the resulting distribution of $P_{\rm null}$ had a relatively flat distribution (i.e., expected distribution of χ^2). Therefore, we concluded that adding the image-based inclination priors had no effect on the acceptability of the model, and we adopted these fits as our inclination-dependent fits for all further analyses.

Example distributions for the parameters of interest for our example galaxy, J123555.43+621056.8, from the inclination-dependent fits using the image-based prior are shown in Figure 3.9 as the orange lines. Comparing these distributions to the distributions from the Calzetti et al. (2000) fits shows that most parameters are highly consistent between models with the exception of A_V and $M_\star$. These inconsistencies and how they vary with inclination will be discussed in Section 3.6. As for the SFH in the upper right corner, the inclination-dependent model predicts higher median SFR at all but the third age bin. However, these values are consistent between models when considering the uncertainty. In Figure 3.10(b), we show how the derived $M_\star$ and SFR_{100} from these inclination-dependent fits compare to the star forming galaxy MS from Lee et al. (2015). The results from these fits tend to follow the MS for galaxies with $z \lesssim 0.8$. However, galaxies with $z \gtrsim 0.8$ tend to fall above the MS, and we discuss the potential causes for this below.

We then compared our inclinations from the updated fits with inclination priors to the image-based inclinations to determine the statistical impact of the prior. Figure 3.11(b) shows that indeed the inclinations for many of the galaxies were influenced by the use of the prior. To quantitatively test this impact, we again computed R for each galaxy for the updated fits and image-based PDFs. For these fits, 72 out of the 82 PDFs ($\approx$88%) had $R > R_{\mathrm{cutoff}}$ with a median of $R = 0.39$, which is an increase in the number of galaxies by 15% and median R by 0.10. This increase in agreement and median R showed that the inclination priors were informative for several galaxies and that adding the image-based priors allowed for more consistent inclination distributions between methods.

Examples of the prior and resulting posterior probability distributions from these updated fits can be seen in Figure 3.12 for the four example galaxies as the blue and gray lines, respectively. The black dashed lines show the posteriors from the fits with the flat inclination prior. In some cases, the image-based priors are informative (e.g., J123626.62+621252.1 and

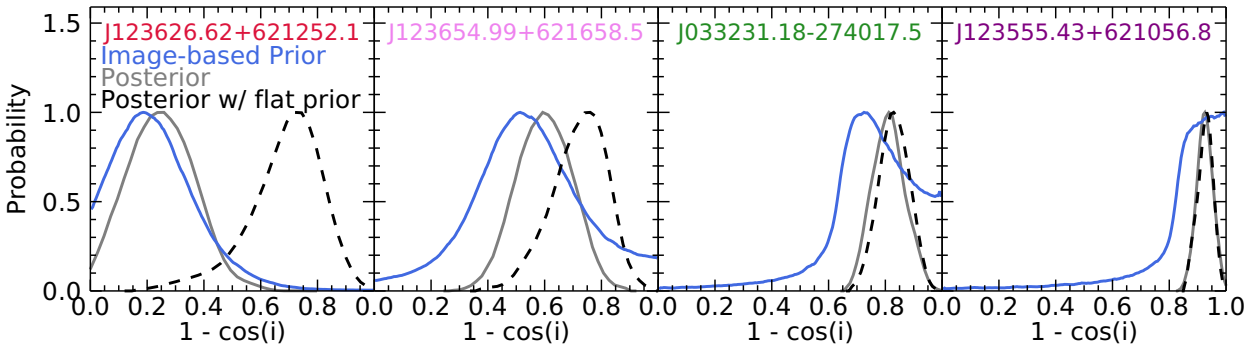

Figure 3.12: Image-based prior and resulting posterior probability distributions of the inclination ($1-\cos i$) as the blue and gray lines, respectively, as well as the resulting posterior assuming a flat prior as the black dashed line for the four example galaxies. Each distribution is normalized to 1 for comparison purposes. The names of the galaxies are colored using the same color as the outline of the corresponding postage stamp in Figure 3.2. For low-inclination galaxies like J123626.62+621252.1 and J123654.99+621658.5, the image-based priors are often informative, while for high-inclination galaxies like J033231.18-274017.5 and J123555.43+621056.8, inclination is primarily constrained by the likelihood.

J123654.99+621658.5), while in other cases they are not (e.g., J033231.18−274017.5).

As for the galaxies still with $R < R_{\rm cutoff}$, adding the image-based priors only had a slight effect, with the median R increasing from $R = 0.01$ to $R = 0.02$. Due to this inconsistency, even after adding the image-based priors, we further inspected these galaxies to determine the potential source of this inconsistency. We initially checked for visual morphological differences in the sample, and the galaxies that had $R < R_{\rm cutoff}$ tended to have bright, blue, off-center star forming clumps. To quantify this observed difference for each galaxy, we measured the concentration (C), asymmetry (A), and clumpiness (S) morphology parameters following the methods of Lotz et al. (2004) for the HST/ACS F435W postage stamp images. However, S was deemed to be an unreliable metric, due to the large range in redshift of our sample, which causes a large range in the physical resolution of each galaxy's postage stamp as well as decreasing signal-to-noise ratio. Therefore, we measured the second-order moment of the brightest 20% of the galaxy's flux (M_{20}) as defined in Lotz et al. (2004), which also measures the clumpiness of a galaxy. This metric is in-

fluenced less by the variation in the signal-to-noise ratio compared to S (see Figure 5 in Lotz et al. 2004), and would therefore be a more reliable metric with this variation in redshift. Comparing these parameters for the galaxies with $R > R_{\rm cutoff}$ to those with $R < R_{\rm cutoff}$, we found slightly lower values of C and higher values of A and M_{20} for the galaxies with $R < R_{\rm cutoff}$, which implies off-center clumps could be present more often in these objects. However, a two-sided KS test showed that these differences are not statistically significant (p-value > 0.5), and therefore, we could not confidently conclude that morphological differences are the driving factor for this disagreement in inclination.

Another possibility, in addition to morphology, that could be responsible for the disagreement in inclinations is limitations in the SED fitting techniques. As seen in Figure 3.11(b), if `Lightning` does not predict an inclination in agreement with the prior image-based inclination, it typically predicts an inclination value higher than the peak of this prior distribution. This is driven by the data requiring a relatively high attenuation made available by high inclinations models (and higher τ_B^f). This high attenuation requirement comes from an elevated $L_{\rm TIR}$ and the energy conservation requirement. Comparing $L_{\rm TIR}$ of the galaxies with $R > R_{\rm cutoff}$ and $R < R_{\rm cutoff}$, the galaxies with $R < R_{\rm cutoff}$ had a larger median $L_{\rm TIR}$ by a factor of $\approx$6 over the galaxies with $R > R_{\rm cutoff}$. A 2D KS test showed that this difference was highly significant (p-value $< 10^{-5}$), and likely a driving factor for this disagreement in inclination. This disparity in $L_{\rm TIR}$, which is also present in the Calzetti et al. (2000) fits, could arise because either the dust emission is actually elevated, or the dust emission is poorly constrained for these galaxies. If the dust emission is truly elevated, it could be that these galaxies are low-luminosity or obscured AGNs that made it though our removal of AGNs in the sample selection process, since AGNs are known to have increased $L_{\rm TIR}$ compared to star forming galaxies (Kirkpatrick et al., 2012). However, testing to see if the dust emission is truly

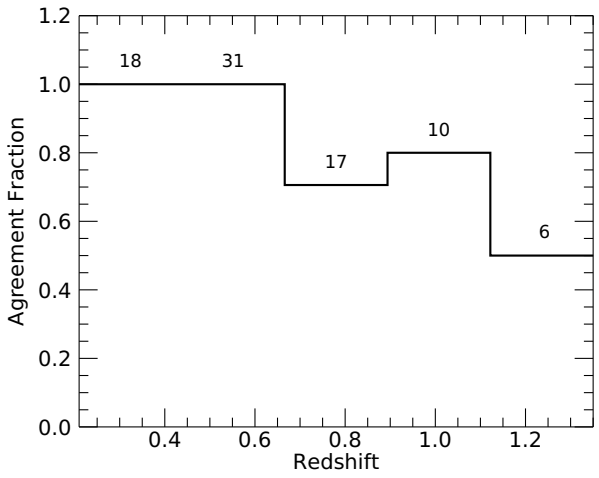

Figure 3.13: The fraction of galaxies with inclinations agreeing between the image-based and SED-based (with the image-based inclination as a prior) inclinations vs. redshift. Agreement was defined as $R > R_{\rm cutoff}$ where $R_{\rm cutoff} = 0.05$. The numbers of galaxies that are contained within each redshift bin are shown above that respective bin.

elevated would require additional IR data to fully constrain the dust emission of these galaxies.

To further check for limitations of the SED fitting techniques, we compared the redshifts of the galaxies with $R > R_{\rm cutoff}$ to those with $R < R_{\rm cutoff}$. The agreement fraction versus the redshift is displayed in Figure 3.13, with the total number of galaxies within each redshift bin labeled above the respective bin. The agreement fraction is defined as the number of galaxies with $R > R_{\rm cutoff}$ divided by the total number of galaxies within the respective redshift bin. From this, it can be seen that as the redshift increases the agreement fraction decreases, with a drop-off in the level of agreement above $z \approx 0.7$. A 2D KS test showed that this redshift variation was highly significant with p-value $< 10^{-3}$. It is possible that this variation and drop-off at $z \approx 0.7$ is due to the Tuffs et al. (2004) attenuation curves potentially not being physically appropriate to model these galaxies. The curves were made from the known thin and thick disk structure of local galaxies. However, it has been shown that galaxies with $z \gtrsim 1$ tend to be significantly thicker and dynamically hotter than galaxies in the local universe (e.g., Bird et al., 2013; van der Wel et al., 2014; Elmegreen et al.,

2017; Pillepich et al., 2019; Zhang et al., 2019). This would explain the drop-off in agreement at $z \sim 1$, the elevated $L_{\rm TIR}$ for the galaxies with $R < R_{\rm cutoff}$ due to the dynamically hotter environment, and would tie into potential morphological differences. However, to confirm this, we would need more sources at these higher redshifts in order to have better statistics.

3.6 Discussion

In Section 3.5, we were able to acceptably fit the SEDs of our sample galaxies with `Lightning` using both the Calzetti et al. (2000) and inclination-dependent attenuation models. Since the fits are independent of each other and the only difference in the models is the attenuation curves, we were able to directly compare these fits to determine the effect of incorporating inclination on their derived SFHs. However, as discussed in Section 3.5.3, the inclination-dependent model has a decreasing agreement between the image-based and SED-based inclination estimates with the redshift, suggesting some redshift evolution effects influence these higher redshift fits. Therefore, we chose to limit our comparisons in this section to the 58 galaxies that have $z < 0.7$ to mitigate any redshift evolution effects present in the inclination-dependent fits.

We first compared the values of $L_{\rm TIR}$ between fits to ensure the estimated global dust-absorbed radiative power was comparable between models. Due to the dust model being of the same form (i.e., Draine & Li, 2007) for both fits, $L_{\rm TIR}$ should, in principle, be similar between the Calzetti et al. (2000) and inclination-dependent fits. If significant differences in $L_{\rm TIR}$ occurred, then reliable comparisons between stellar properties would not be meaningful. This is due to the energy balance/conservation requirement, which tied the total amount of attenuation to $L_{\rm TIR}$ as discussed in Section 3.4.4. Therefore, differences in $L_{\rm TIR}$ between fits would result in differences in the total

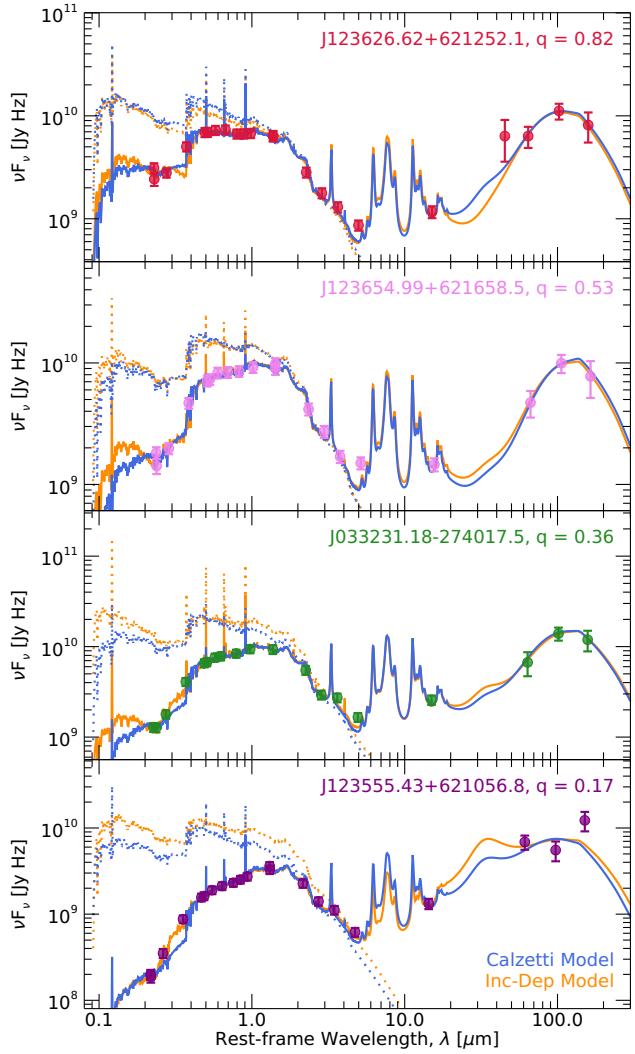

Figure 3.14: The best-fit models to the broadband SEDs from the Calzetti et al. (2000) fits and inclination-dependent fits with the image-based inclination prior for the four example galaxies shown in Figure 3.2 as the blue and orange lines, respectively. The solid lines are the combined dust and attenuated stellar models, and the dotted lines are the unattenuated stellar models. The broadband SEDs and the names of the galaxies are colored using the same color as the outline of the corresponding postage stamp in Figure 3.2. The galaxies are arranged from top to bottom from the least inclined to the most inclined.

attenuation between fits. These differences would boost the values of the intrinsic stellar properties for the fit with an elevated total attenuation, and potentially obscure any differences in stellar properties between fits that reveal trends with the inclination.

The dust emission model fits to the SEDs, from which $L_{\rm TIR}$ is derived, for the four exam-

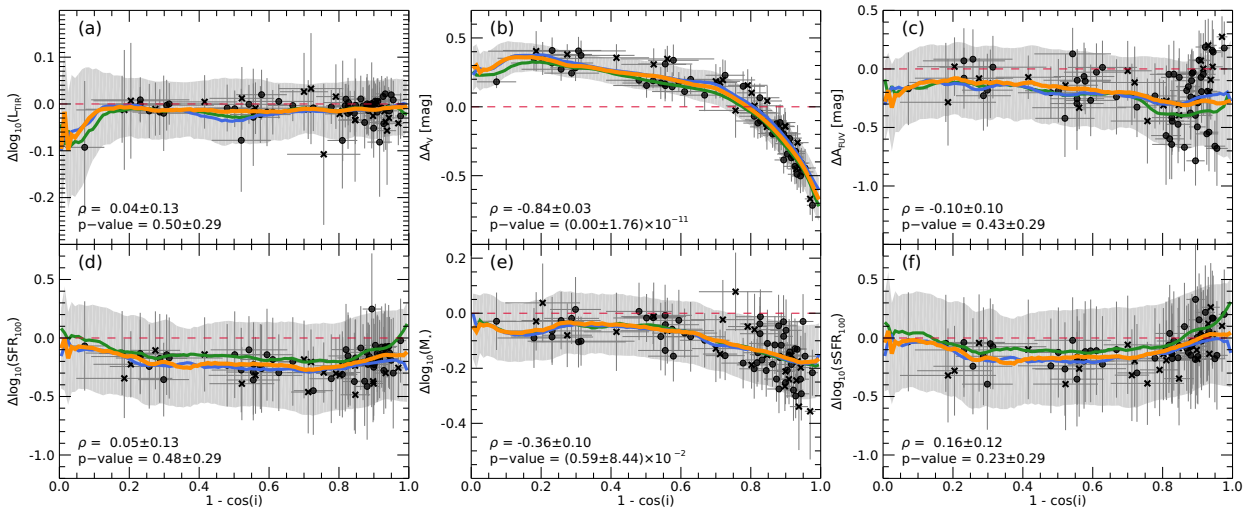

Figure 3.15: The panels show the median and 1σ dispersion of the logarithmic difference ($\log_{10}(\text{property}_{\text{Calz}}) - \log_{10}(\text{property}_{\text{Dep}})$; panels (a), (d), (e), and (f)) and difference ($\text{property}_{\text{Calz}} - \text{property}_{\text{Dep}}$; panels (b) and (c)) between the Calzetti et al. (2000) and inclination-dependent fits for the parameters of interest vs. the inclination ($1 - \cos i$) derived from the SED fittings. The solid circles represent the galaxies with $z < 0.7$, and the X's represent the galaxies with $z \geq 0.7$, which are not used in deriving the trend lines or correlations. The orange line and light gray 1σ dispersion range are the mean and standard deviation of $\Delta\cos i = 0.01$ bins calculated by using all 5000 elements within the respective distributions of each property as data points. The green and blue lines are the mean of $\Delta\cos i = 0.01$ bins for fits where the third age bin upper bound is adjusted to 500 Myr and 1.5 Gyr, respectively. These fits show no significant differences from the upper bound choice of 1 Gyr. The median and 1σ dispersion of ρ and p-value for the Monte Carlo Spearman's rank correlation are also shown in the bottom left of each panel.

ple galaxies can be seen in Figure 3.14. The solid blue (Calzetti et al. 2000 fits) and orange (inclination-dependent fits) lines represent the best-fit (minimum χ^2) models, with the dust emission dominating beyond $\lambda_{\text{rest}} > 5\mu$m. It can be seen that these four galaxies, as well as most other galaxies in the sample, have relatively well-constrained peaks of the dust emission. This is due to the sample requirement of at least one FIR data point being beyond rest frame 100 μm. However, while it appears from these examples that the dust emission in the MIR and L_{TIR} may vary in agreement between models, that is only for the best-fit values. Since `Lightning` produces probability distributions for these properties, a better comparison would be of these distributions.

A comparison of the L_{TIR} distributions is displayed in Figure 3.15(a), which shows the median

and 1σ difference of the logarithm between the Calzetti et al. (2000) and inclination-dependent estimates (i.e., logarithm of the ratio) of $L_{\rm TIR}$ versus the inclination derived from the SED fittings. The orange line and corresponding light gray 1σ dispersion range are the mean and standard deviation of $\Delta\cos i = 0.01$ bins calculated by using all 5000 elements within the MCMC chains of each property as data points (i.e., 58 galaxies $\times$ 5000 chain elements $= 290,000$ data points). From the binned average and data points, it can be seen that the $L_{\rm TIR}$ estimates between models are in excellent agreement for most galaxies, with the average and 1σ dispersion being consistent with zero at all inclinations. To illustrate the impact of SFH binning, we show in Figure 3.15 the cases where the upper bound on the third age bin is adjusted to 500 Myr (green lines) and 1.5 Gyr (blue lines) from its original 1 Gy (orange lines). We also computed the Spearman's rank correlation using a Monte Carlo method to check for the presence of any trends between fits. To do this, we selected a random value from the distribution of inclination and $\Delta\log_{10}(L_{\rm TIR})$ for each galaxy and computed Spearman's rank test for the ensemble. This was repeated 5000 times to build up a distribution of ρ and p-value, from which to determine the median and 1σ values; these are annotated in the bottom left of the panel. For $L_{\rm TIR}$, this shows that we are confident there is no monotonic relation with inclination, and that both fits have similar $L_{\rm TIR}$. Therefore, we concluded that $L_{\rm TIR}$ is comparable between fits for most galaxies and further comparisons between derived properties and their dependence on inclination are meaningful.

Examining the stellar models, the best-fit unattenuated stellar model spectra for both the Calzetti et al. (2000) and inclination-dependent fits are shown for the four example galaxies as the dotted lines in Figure 3.14. It can be seen that the nearly face-on galaxy (i.e., upper most panel) has similar unattenuated spectra. However, for the more inclined galaxies, the unattenuated spectra can vary greatly from the UV to the NIR. This difference is expected due to the significant differences

between the attenuation curves at high inclinations, as shown in Figures 3.7 and 3.8 (i.e., left most panels). This variation in edge-on galaxies is what drives observed differences in some stellar properties between fits with inclination, as shown in Figure 3.15.

It was expected that the Calzetti et al. (2000) fits would predict relatively high stellar emission attenuation at low inclinations and relatively low attenuation at high inclinations compared to the inclination-dependent fits. This is because the observed UV-optical flux will vary based on the viewing angle of the galaxy due to inclination-based attenuation, but the dust emission will be nearly unaffected by the viewing angle. Assuming a cylindrical geometry for the disk, we would expect to observe more rest-frame UV-optical flux from a nearly face-on view of a galaxy compared to the average view if it were randomly oriented (i.e., moderately inclined), but would predict similar levels of absorption due to $L_{\rm TIR}$ being unaffected by inclination. As for the edge-on view, we would expect to observe less rest-frame UV-optical flux than the average view, while still predicting similar levels of absorption. Therefore, since an inclination-independent model like the Calzetti et al. (2000) model should be most applicable to the average galaxy, it would overestimate the line-of-sight attenuation for more face-on galaxies and underestimate the line-of-sight attenuation for edge-on galaxies; contrarily the inclination-dependent model should properly account for inclination-dependent line-of-sight attenuation.

This effect can indeed be clearly seen in Figure 3.15(b), which shows the difference in A_V of the two fits versus inclination. From the Spearman's rank correlation, it can be seen that this trend is very strong and highly significant with a median p-value $< 10^{-11}$. For face-on to moderately inclined galaxies (i.e., $1-\cos i \lesssim 0.4$) in our $z < 0.7$ sample (9 galaxies), not accounting for inclination-based attenuation results in A_V being higher by 0.31 ± 0.04 magnitudes on average, whereas for edge-on galaxies (i.e., $1-\cos i = 0.9$–1.0, 14 galaxies) this results in A_V being lower

by 0.28–0.67 magnitudes.

However, this expected variation in attenuation with inclination is not seen in the FUV attenuation. Figure 3.15(c) shows the difference in A_{FUV} with inclination, which has the inclination-dependent model predicting $A_{\mathrm{FUV}} \approx 0.19$ magnitudes higher on average at all inclinations compared to the Calzetti et al. (2000) model. The lack of a trend with inclination for our sample could be due to either (1) the inclination-dependent model incorrectly predicting A_{FUV} or (2) the Calzetti et al. (2000) attenuation model is properly accounting for the inclination-based attenuation at FUV wavelengths at our current levels of uncertainty. To check which occurs, we compared each fit individually with the inclination and found that both fits had a strong increase in A_{FUV} with increasing inclination, which is expected to occur due to inclination-based attenuation. The increase in A_{FUV} with inclination and the expected trend being seen in the difference of A_V led us to conclude that explanation (2) was correct.

The lower average A_{FUV} of the Calzetti et al. (2000) model for galaxies in our sample leads to a similar lower average of 0.19 dex in SFR_{100} compared to the inclination-dependent model for all inclinations, as seen in Figure 3.15(d). This is due to SFR_{100} being correlated with A_{FUV} by the young UV emitting stellar population. Like A_{FUV}, there is practically no trend with inclination, and because of this relative lack of trend, we conclude that the Calzetti et al. (2000) attenuation curve can model inclination-based attenuation like the inclination-dependent model at FUV wavelengths and recover the resulting recent SFRs for the disk galaxies in our sample at all inclinations.

The reason for the Calzetti et al. (2000) model being able to account for the inclination-based attenuation at FUV wavelengths, while also having the expected trend in the V-band wavelengths with inclination, can be found in the results from the SED fits. Looking at the correlation between parameters, A_{FUV} for both fits is moderately to strongly correlated with L_{TIR}, with Pearson correla-

tion coefficients for a given fit averaged for all galaxies of $\rho = 0.40 \pm 0.13$ and $\rho = 0.79 \pm 0.12$ for the inclination-dependent and Calzetti et al. (2000) models, respectively. Therefore, since $A_{\rm FUV}$ and $L_{\rm TIR}$ are relatively correlated for a given fit with both models, and $L_{\rm TIR}$ is consistent between models, it results in $A_{\rm FUV}$ being relatively consistent as well. Comparing this to the correlations between A_V and $L_{\rm TIR}$, the inclination-dependent model has a weaker correlation of $\rho = 0.32 \pm 0.16$, while the Calzetti et al. (2000) model still has a strong correlation of $\rho = 0.79 \pm 0.12$. The strong correlation for both $A_{\rm FUV}$ and A_V with $L_{\rm TIR}$ for the Calzetti et al. (2000) model is due to the use of a single normalized attenuation curve, which causes a correlation of 1 between $A_{\rm FUV}$ and A_V. However, A_V has practically no correlation with $A_{\rm FUV}$ ($\rho = 0.01 \pm 0.24$) for a given fit with the inclination-dependent model, which allows for the expected trend with inclination and the difference between models. Thus, $A_{\rm FUV}$ and A_V are controlled by $L_{\rm TIR}$ for the Calzetti et al. (2000) model, whereas only $A_{\rm FUV}$ is controlled by $L_{\rm TIR}$ for the inclination-dependent model, and A_V can be a variety of values for a given $A_{\rm FUV}$.

This trend in the difference of A_V with inclination is also seen in the stellar mass logarithmic differences, due to the intrinsic optical emission, which A_V represents, dominating the stellar masses estimates. The logarithmic difference in $M_\star$ with inclination can be seen in Figure 3.15(e), which shows a moderate, statistically significant trend with a median p-value $< 10^{-2}$. From the panel for stellar mass, it can be seen that the mass is relatively consistent on average between fits with the Calzetti et al. (2000) fits producing a slightly lower estimate of $M_\star$ compared to the inclination-dependent fits by a factor of -0.05 ± 0.03 dex over $1 - \cos i = 0$–0.6 (19 galaxies). However, at $1 - \cos i \gtrsim 0.7$ (36 galaxies), the Calzetti et al. (2000) fits produce lower estimates of $M_\star$ compared to the inclination-dependent fits. Not including inclination-based attenuation can lead to lower $M_\star$ values by a factor of 0.12 ± 0.12 dex at $1 - \cos i \approx 0.75$ up to 0.17 ± 0.15

dex at $\approx 90^\circ$ for galaxies in our $z < 0.7$ sample. This result is consistent with the findings from Driver et al. (2007) and Wolf et al. (2018) who found stellar mass estimates (from inclination corrected mass-to-light ratios) to be inclination-independent for $i \lesssim 70^\circ$. However, above that angle, they found that stellar masses may be underestimated by a factor of ≈0.3 dex for an inclination-independent model.

Finally, Figure 3.15(f) shows the logarithmic difference in sSFR_{100} with inclination. Since sSFR_{100} is computed as SFR_{100} divided by the $M_\star$, the trend seen with inclination is a combination of the trend seen in SFR_{100} and the reflected trend seen in the stellar mass. This trend is not nearly as strong or statistically significant compared to the stellar mass due to the large dispersion and uncertainties introduced by SFR_{100}. Overall, sSFR_{100} is somewhat lower for the Calzetti et al. (2000) fits by a factor of 0.14 dex from $1 - \cos i = 0$–0.8 transitioning to becoming larger by a factor of 0.05 dex at 90°.

3.7 Summary

We developed and tested an inclination-dependent attenuation module for the SED fitting code `Lightning`, in order to test the effects of inclination-based attenuation on derived SFHs. The module utilizes the inclination-dependent attenuation curve from Tuffs et al. (2004) as updated by Popescu et al. (2011). We tested the module using 82 disk-dominated galaxies, as determined by their Sérsic index ($n < 1.2$) and subsequent visual inspection, that had UV to FIR data from the GOODS North and South fields.

Using the measured axis ratio q of each galaxy from van der Wel et al. (2012), we derived PDFs of inclination from a Monte Carlo method that incorporates the distributions of the intrinsic

thickness and asymmetry of spiral galaxies from Rodríguez & Padilla (2013). We found that these PDFs give median inclinations that are in excellent agreement with inclinations that are derived from Equation 3.1 with commonly used fixed values of γ if $i \gtrsim 30^{\circ}$. However, the inclination uncertainties derived from Equation 3.1 for all inclinations are generally underestimated by a factor of $\approx$7.5 compared to our inclination PDFs.

We then fitted the SEDs of our sample galaxies twice, first with the inclination-independent Calzetti et al. (2000) attenuation curve, and second with an inclination-dependent attenuation model. In order to accurately model the SEDs with the inclination-dependent model, we found that prior distributions on the inclination were required. With the priors, most inclinations ($\approx$88%) derived from the SED fits when compared to the inclination PDFs derived from the measured q had intersection-area-to-union-area ratios > 0.05, which we considered in agreement. Those that did not tended to have elevated $L_{\rm TIR}$ and higher redshifts ($z \gtrsim 0.7$). It is possible that this is due to the Tuffs et al. (2004) attenuation curves not being physically appropriate to model most galaxies above this redshift, because galaxies with $z \gtrsim 1$ tend to be significantly thicker and dynamically hotter than galaxies with $z < 1$ (e.g., Bird et al., 2013; van der Wel et al., 2014; Elmegreen et al., 2017; Pillepich et al., 2019; Zhang et al., 2019).

Limiting the 82 galaxy sample to only include the 58 galaxies with $z < 0.7$ as to mitigate any redshift evolution effects, we compared the inclination-dependent and Calzetti et al. (2000) fits for this $z < 0.7$ sample. We found that both fits recover the expected trend with inclination for $A_{\rm FUV}$ and average SFRs of the last 100 Myr at all inclinations. By contrast, not accounting for inclination-based attenuation in our sample of galaxies resulted in an average A_V being elevated by 0.31 ± 0.04 magnitudes for face-on to moderately inclined galaxies and underestimated by 0.28–0.67 magnitude for edge-on galaxies. Stellar masses were in good agreement between fits for

$1 - \cos i = 0$–0.6 with a minor scatter of $\approx$0.1 dex. For $1 - \cos i \gtrsim 0.75$, stellar masses could be underestimated up to a factor of 0.17 dex at 90° by the Calzetti et al. (2000) model compared to the inclination-dependent model. These results indicated for our sample of galaxies that the Calzetti et al. (2000) attenuation curve is able to correctly model the inclination-dependent attenuation of FUV emission, which dictates the recent SFRs, at all inclinations; but fails for the optical-NIR emission, which dominates the stellar masses estimates, at higher inclinations.

This work introduces and shows the impact of inclination-dependent attenuation on SFHs, and subsequently stellar masses and recent SFRs, derived from SED fitting. Incorporating inclination-dependent attenuation when fitting SEDs can help give better insight into the physical properties of highly inclined galaxies. In an upcoming paper, we use this inclination-dependent model to determine how inclination affects $A_{\rm FUV}$ calibrations that are used to compute SFRs and compare the results with previously published works. Beyond this, we intend to apply the inclination-dependent attenuation module to galaxies that have sizable bulge components, and a more complete sample of galaxies to test whether our results hold for the broader disk-galaxy population.

References

Aihara, H., Allende Prieto, C., An, D., et al. 2011, ApJS, 195, 26

Andrieu, C., & Thoms, J. 2008, Statistics and Computing, 18, 30

Balestra, I., Mainieri, V., Popesso, P., et al. 2010, A&A, 512, A12

Barger, A. J., Cowie, L. L., & Wang, W. H. 2008, ApJ, 689, 687

Barro, G., Pérez-González, P. G., Cava, A., et al. 2019, ApJS, 243, 22

Battisti, A. J., Calzetti, D., & Chary, R. R. 2017, ApJ, 851, 90

Bertin, E., & Arnouts, S. 1996, A&AS, 117, 393

Bird, J. C., Kazantzidis, S., Weinberg, D. H., et al. 2013, ApJ, 773, 43

Boquien, M., Burgarella, D., Roehlly, Y., et al. 2019, A&A, 622, A103

Boquien, M., Kennicutt, R., Calzetti, D., et al. 2016, A&A, 591, A6

Brooks, S. P., & Gelman, A. 1998, Journal of Computational and Graphical Statistics, 7, 434

Buat, V., Ciesla, L., Boquien, M., Małek, K., & Burgarella, D. 2019, A&A, 632, A79

Calzetti, D., Armus, L., Bohlin, R. C., et al. 2000, ApJ, 533, 682

Calzetti, D., Kennicutt, R. C., Engelbracht, C. W., et al. 2007, ApJ, 666, 870

Chevallard, J., & Charlot, S. 2016, MNRAS, 462, 1415

Chevallard, J., Charlot, S., Wandelt, B., & Wild, V. 2013, MNRAS, 432, 2061

Conroy, C. 2013, ARA&A, 51, 393

Cooper, M. C., Yan, R., Dickinson, M., et al. 2012, MNRAS, 425, 2116

da Cunha, E., Charlot, S., & Elbaz, D. 2008, MNRAS, 388, 1595

Daddi, E., Renzini, A., Pirzkal, N., et al. 2005, ApJ, 626, 680

Dahlen, T., Mobasher, B., Faber, S. M., et al. 2013, ApJ, 775, 93

Dalcanton, J. J., & Bernstein, R. A. 2002, AJ, 124, 1328

Devour, B. M., & Bell, E. F. 2016, MNRAS, 459, 2054

—. 2017, MNRAS, 468, L31

Donley, J. L., Koekemoer, A. M., Brusa, M., et al. 2012, ApJ, 748, 142

Draine, B. T. 2003, ARA&A, 41, 241

—. 2011, Physics of the Interstellar and Intergalactic Medium

Draine, B. T., & Li, A. 2007, ApJ, 657, 810

Draine, B. T., Dale, D. A., Bendo, G., et al. 2007, ApJ, 663, 866

Driver, S. P., Popescu, C. C., Tuffs, R. J., et al. 2007, MNRAS, 379, 1022

Elbaz, D., Dickinson, M., Hwang, H. S., et al. 2011, A&A, 533, A119

Elmegreen, B. G., Elmegreen, D. M., Tompkins, B., & Jenks, L. G. 2017, ApJ, 847, 14

Eufrasio, R. T., Lehmer, B. D., Zezas, A., et al. 2017, ApJ, 851, 10

Fadda, D., Yan, L., Lagache, G., et al. 2010, ApJ, 719, 425

Faisst, A. L., Fudamoto, Y., Oesch, P. A., et al. 2020, MNRAS, 498, 4192

Fioc, M., & Rocca-Volmerange, B. 1997, A&A, 500, 507

Fitzpatrick, E. L. 1999, PASP, 111, 63

Galametz, A., Grazian, A., Fontana, A., et al. 2013, ApJS, 206, 10

Gelman, A., Roberts, G., & Gilks, W. 1996, Bayesian Statistics, 5, 599

Gelman, A., & Rubin, D. B. 1992, Statistical Science, 7, 457

Giavalisco, M., Ferguson, H. C., Koekemoer, A. M., et al. 2004, ApJ, 600, L93

Giovanelli, R., Haynes, M. P., Salzer, J. J., et al. 1994, AJ, 107, 2036

Gordon, K. D., Misselt, K. A., Witt, A. N., & Clayton, G. C. 2001, ApJ, 551, 269

Graham, A. W., & Worley, C. C. 2008, MNRAS, 388, 1708

Grogin, N. A., Kocevski, D. D., Faber, S. M., et al. 2011, ApJS, 197, 35

Guo, Y., Ferguson, H. C., Giavalisco, M., et al. 2013, ApJS, 207, 24

Han, Y., & Han, Z. 2019, ApJS, 240, 3

Hao, C.-N., Kennicutt, R. C., Johnson, B. D., et al. 2011, ApJ, 741, 124

Hastings, W. K. 1970, Biometrika, 57, 12

Hubble, E. P. 1926, ApJ, 64, 321

Ilbert, O., Salvato, M., Le Floc'h, E., et al. 2010, ApJ, 709, 644

Kacharov, N., Neumayer, N., Seth, A. C., et al. 2018, MNRAS, 480, 1973

Kennicutt, Robert C., J. 1998, ARA&A, 36, 189

Kennicutt, Robert C., J., Armus, L., Bendo, G., et al. 2003, PASP, 115, 928

Kirkpatrick, A., Pope, A., Alexander, D. M., et al. 2012, ApJ, 759, 139

Kirkpatrick, A., Pope, A., Charmandaris, V., et al. 2013, ApJ, 763, 123

Koekemoer, A. M., Faber, S. M., Ferguson, H. C., et al. 2011, ApJS, 197, 36

Kriek, M., Shapley, A. E., Reddy, N. A., et al. 2015, ApJS, 218, 15

Kroupa, P. 2001, MNRAS, 322, 231

Kylafis, N. D., & Bahcall, J. N. 1987, ApJ, 317, 637

Laidler, V. G., Papovich, C., Grogin, N. A., et al. 2007, PASP, 119, 1325

Laor, A., & Draine, B. T. 1993, ApJ, 402, 441

Lee, N., Sanders, D. B., Casey, C. M., et al. 2015, ApJ, 801, 80

Leja, J., Carnall, A. C., Johnson, B. D., Conroy, C., & Speagle, J. S. 2019, ApJ, 876, 3

Leja, J., Johnson, B. D., Conroy, C., van Dokkum, P. G., & Byler, N. 2017, ApJ, 837, 170

Leslie, S. K., Schinnerer, E., Groves, B., et al. 2018a, A&A, 616, A157

Leslie, S. K., Sargent, M. T., Schinnerer, E., et al. 2018b, A&A, 615, A7

Lintott, C., Schawinski, K., Bamford, S., et al. 2011, MNRAS, 410, 166

Liu, D., Daddi, E., Dickinson, M., et al. 2018, ApJ, 853, 172

Lotz, J. M., Primack, J., & Madau, P. 2004, AJ, 128, 163

Luo, B., Brandt, W. N., Xue, Y. Q., et al. 2017, ApJS, 228, 2

Lutz, D., Poglitsch, A., Altieri, B., et al. 2011, A&A, 532, A90

Magnelli, B., Popesso, P., Berta, S., et al. 2013, A&A, 553, A132

Maller, A. H., Berlind, A. A., Blanton, M. R., & Hogg, D. W. 2009, ApJ, 691, 394

Masters, K. L., Nichol, R., Bamford, S., et al. 2010, MNRAS, 404, 792

Mathis, J. S., Mezger, P. G., & Panagia, N. 1983, A&A, 500, 259

Metropolis, N., Rosenbluth, A. W., Rosenbluth, M. N., Teller, A. H., & Teller, E. 1953, The Journal of Chemical Physics, 21, 1087

Mignoli, M., Cimatti, A., Zamorani, G., et al. 2005, A&A, 437, 883

Mobasher, B., Dahlen, T., Ferguson, H. C., et al. 2015, ApJ, 808, 101

Möllenhoff, C., Popescu, C. C., & Tuffs, R. J. 2006, A&A, 456, 941

Noll, S., Burgarella, D., Giovannoli, E., et al. 2009, A&A, 507, 1793

Oliver, S. J., Bock, J., Altieri, B., et al. 2012, MNRAS, 424, 1614

Padilla, N. D., & Strauss, M. A. 2008, MNRAS, 388, 1321

Peng, C. Y., Ho, L. C., Impey, C. D., & Rix, H.-W. 2002, AJ, 124, 266

Pérez-González, P. G., Rieke, G. H., Egami, E., et al. 2005, ApJ, 630, 82

Pérez-González, P. G., Rieke, G. H., Villar, V., et al. 2008, ApJ, 675, 234

Pérez-González, P. G., Egami, E., Rex, M., et al. 2010, A&A, 518, L15

Pillepich, A., Nelson, D., Springel, V., et al. 2019, MNRAS, 490, 3196

Popescu, C. C., Tuffs, R. J., Dopita, M. A., et al. 2011, A&A, 527, A109

Popesso, P., Dickinson, M., Nonino, M., et al. 2009, A&A, 494, 443

Ravikumar, C. D., Puech, M., Flores, H., et al. 2007, A&A, 465, 1099

Reddy, N. A., Steidel, C. C., Erb, D. K., Shapley, A. E., & Pettini, M. 2006, ApJ, 653, 1004

Rodríguez, S., & Padilla, N. D. 2013, MNRAS, 434, 2153

Roebuck, E., Sajina, A., Hayward, C. C., et al. 2019, ApJ, 881, 18

Ryden, B. S. 2006, ApJ, 641, 773

Salim, S., Boquien, M., & Lee, J. C. 2018, ApJ, 859, 11

Santini, P., Ferguson, H. C., Fontana, A., et al. 2015, ApJ, 801, 97

Sargent, M. T., Carollo, C. M., Lilly, S. J., et al. 2007, ApJS, 172, 434

Sargent, M. T., Carollo, C. M., Kampczyk, P., et al. 2010, ApJ, 714, L113

Schlafly, E. F., & Finkbeiner, D. P. 2011, ApJ, 737, 103

Schlegel, D. J., Finkbeiner, D. P., & Davis, M. 1998, ApJ, 500, 525

Sérsic, J. L. 1963, Boletin de la Asociacion Argentina de Astronomia La Plata Argentina, 6, 41

Skelton, R. E., Whitaker, K. E., Momcheva, I. G., et al. 2014, ApJS, 214, 24

Szokoly, G. P., Bergeron, J., Hasinger, G., et al. 2004, ApJS, 155, 271

Teplitz, H. I., Chary, R., Elbaz, D., et al. 2011, AJ, 141, 1

Tuffs, R. J., Popescu, C. C., Völk, H. J., Kylafis, N. D., & Dopita, M. A. 2004, A&A, 419, 821

Unterborn, C. T., & Ryden, B. S. 2008, ApJ, 687, 976

van der Wel, A., Bell, E. F., Häussler, B., et al. 2012, ApJS, 203, 24

van der Wel, A., Chang, Y.-Y., Bell, E. F., et al. 2014, ApJ, 792, L6

Vanzella, E., Cristiani, S., Dickinson, M., et al. 2008, A&A, 478, 83

Wang, W., Kassin, S. A., Pacifici, C., et al. 2018, ApJ, 869, 161

Weingartner, J. C., & Draine, B. T. 2001, ApJ, 548, 296

Wild, V., Charlot, S., Brinchmann, J., et al. 2011, MNRAS, 417, 1760

Wirth, G. D., Willmer, C. N. A., Amico, P., et al. 2004, AJ, 127, 3121

Wolf, C., Weinzirl, T., Aragón-Salamanca, A., et al. 2018, MNRAS, 480, 3788

Xue, Y. Q., Luo, B., Brandt, W. N., et al. 2016, ApJS, 224, 15

Zhang, H., Primack, J. R., Faber, S. M., et al. 2019, MNRAS, 484, 5170

Zubko, V., Dwek, E., & Arendt, R. G. 2004, ApJS, 152, 211

Appendix

3.A Mid-to-Far IR Photometry Assessment

Given the relatively large Herschel FIR PSFs, we tested the potential impact of blending and/or background fluctuations (Elbaz et al., 2011; Magnelli et al., 2013) that may be present in our final sample. As noted by Barro et al. (2019), there should be minimal confusion of source identifications due to their procedure of using the higher resolution MIPS 24 μm source locations as positional priors when determining the PACS and SPIRE counterparts. However, photometric issues could potentially arise due to nearby IR-bright sources.

We first visually inspected the PACS and SPIRE images for any obvious PSF blending, at the locations of our MIPS 24 μm sources that could impact the FIR photometry. We found negligible bright-source PSF overlap for all PACS bands and the SPIRE 250 μm band. However, the SPIRE 350 and 500 μm sources showed nonnegligible PSF overlap, and we therefore chose to exclude photometry based on these two bands when fitting the SEDs.

We further assessed whether the remaining FIR photometry was reliable, and did not suffer from important photometric blending from multiple bright sources within the PSFs. Using the MIPS 24 μm counterpart flags in Table 18 of Barro et al. (2019), we determined the number of MIPS 24 μm counterparts within each of the PACS and SPIRE 250 μm band PSFs and the contributions of the primary source counterpart to the full 24 μm flux within the PSFs. Using a PSF with a FWHM of $7''$, $11.2''$, and $18''$ for the PACS 100 μm, 160 μm, and SPIRE 250 μm, respectively, we found 5%, 18%, and 45% of our final sample that had the respective band contained more than one 24 μm detected source within the FWHM diameters. This indicated that the 160 μm and 250 μm bands may have some nonnegligible source confusion. However, for the 160 μm and

250 μm bands, 93% and 62% of the respective sources with more than one 24 μm counterpart had 24 μm fluxes dominated by the primary counterpart. This implies that the majority of the 160 μm and 250 μm sources with potentially blended counterparts would have fluxes elevated by $< 100\%$, with a median elevation of 41% and 39%, respectively, if all counterpart sources are blended. This minimal level of blending was expected, since Barro et al. (2019) found their mid-to-far IR photometry in the GOODS-N was in excellent agreement with the superdeblended photometry in Liu et al. (2018).

In addition to source blending, low signal-to-noise ratio FIR photometry may be impacted by fluctuations in local backgrounds. Elbaz et al. (2011) and Magnelli et al. (2013) used Monte Carlo simulations and showed that, at the 3σ limit adopted for our sample selection, the photometric accuracy is better than 33% for at least 68% of sources. This accuracy improves with increasing signal-to-noise ratio. Given that all FIR sources in our sample have signal-to-noise ratios > 3 and the majority of PACS sources (72% and 93% for PACS 100 μm and 160 μm, respectively) have signal-to-noise ratios > 5, we expect minimal photometric issues from background fluctuations in the PACS bands and expect the photometry to be highly accurate. We find that 37% of SPIRE 250 μm sources have signal-to-noise ratios > 5, so it is possible that the SPIRE 250 μm photometry may suffer from lower accuracy due to this confusion.

Since a sizable fraction of the SPIRE 250 μm sources in our sample could have nonnegligible blending and background fluctuations, we investigated the effects of including the SPIRE 250 μm photometry on the SED fits by refitting the 67 galaxies in the final sample that had the SPIRE 250 μm band without the SPIRE 250 μm band. We found that sources that had PACS 160 μm to constrain the peak of the dust emission had bolometric luminosities for the dust emission models always within 19% of the luminosities including the SPIRE 250 μm band, with a median and

scatter of $\log(L_{\rm IR}^{\rm with}/L_{\rm IR}^{\rm without}) = 0.00 \pm 0.03$ for the sample, where $L_{\rm IR}^{\rm with}$ and $L_{\rm IR}^{\rm without}$ are the bolometric luminosities from the fits with and without the SPIRE 250 μm band, respectively. However, sources that did not have the PACS 160 μm to constrain the peak of the dust emission could have bolometric luminosities that vary up to 45% from the luminosities including the SPIRE 250 μm band, with $\log(L_{\rm IR}^{\rm with}/L_{\rm IR}^{\rm without}) = 0.03 \pm 0.07$. Therefore, we utilize the the SPIRE 250 μm band in our fits due to it having minimal adverse effects on these fits and the beneficial effect of helping constrain the peak of dust emission.

3.B Diagnostic Figures

To show any degeneracies between parameters and their location in parameter space, diagnostic plots showing free parameter distributions and the global trends for all galaxies are provided. Figure 3.B.1 shows the distributions for the free parameters in the Calzetti et al. (2000) fit and inclination-dependent fit with an image-based inclination prior for our most inclined example galaxy, J123555.43+621056.8, in the upper right and lower left, respectively. Figures 3.B.2–3.B.4 show scatter plots of the median of each galaxies' free parameter pairs to display the global trends for these parameters for the Calzetti et al. (2000) fits, inclination-dependent fits with a flat inclination prior, and inclination-dependent fits with an image-based inclination prior, respectively. Figures 3.B.5–3.B.7 also show median parameter scatter plots, but for the parameters of interest and additionally redshift and axis ratio.

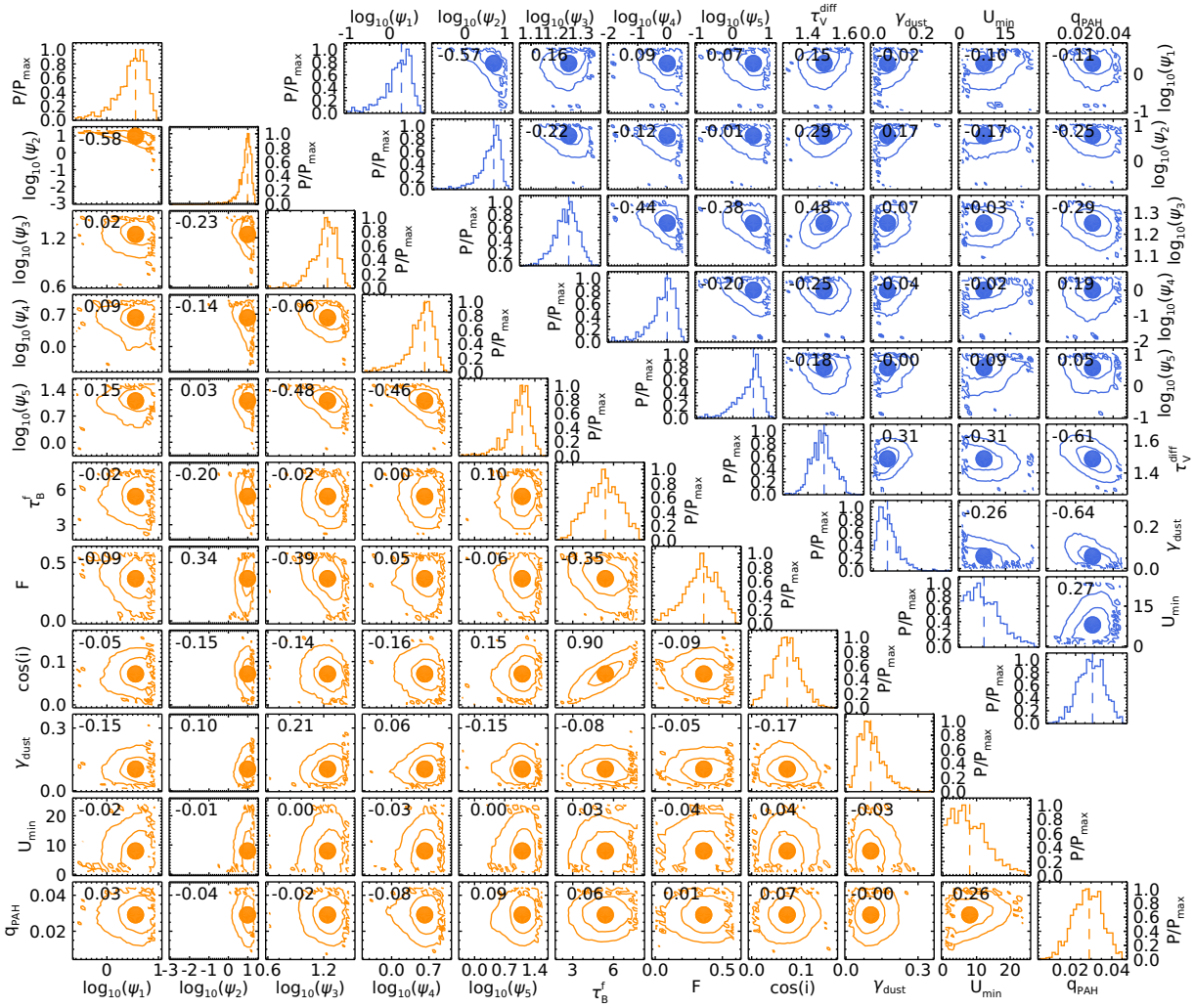

Figure 3.B.1: (*Lower left triangle plot*): Probability distribution functions in terms of $P/P_{\rm max}$ (diagonal elements) and the 68% and 95% confidence contours for the free parameter pairs (off-diagonal elements) in our inclination-dependent fits with the image-based inclination prior for our most inclined example galaxy, J123555.43+621056.8. This galaxy is the galaxy with a purple outline in Figure 3.2. The vertical dashed lines in the histograms and solid colored circles in the contour plots indicate the median values of each parameter. The Pearson correlation coefficients for each set of parameters are shown in the upper left corners of each contour plot. (*Upper right triangle plot*): Same as the lower left, except for the free parameters in the Calzetti et al. (2000) fits (see Table 3.2 for a list of parameters and units).

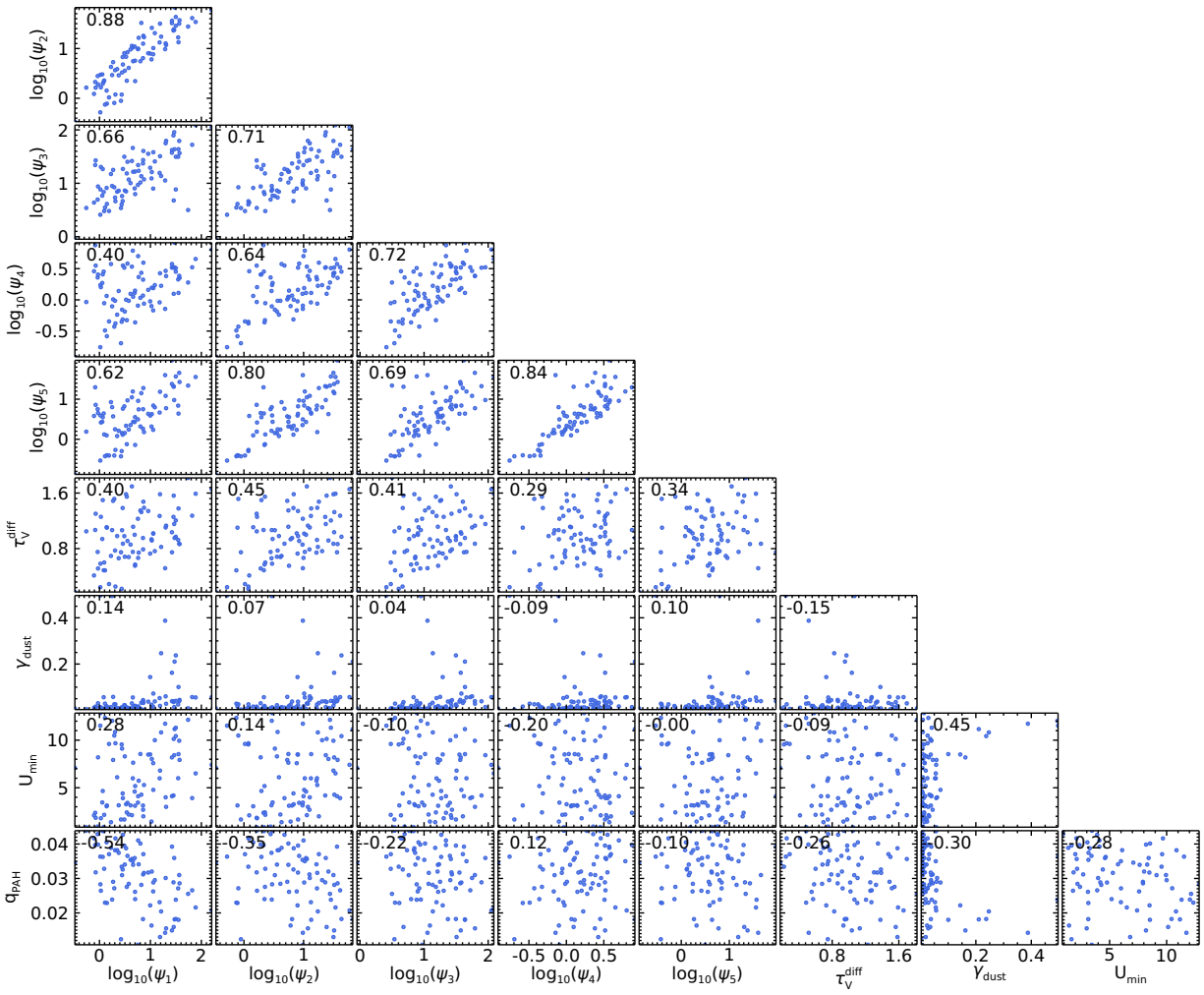

Figure 3.B.2: Scatter plots for the free parameter pairs in our Calzetti et al. (2000) fits. Each point represents the median value of that parameter for a galaxy in our sample. The Pearson correlation coefficients for each set of parameters are shown in the upper-left corners of each scatter plot. These coefficients show the global trends in the data. Most correlations seen were expected, such as that between ψ_i and $\tau_V^{\rm diff}$, and ψ_i and ψ_j, where i and j are different age bins. These strong correlations between ψ_i and $\tau_V^{\rm diff}$ are due to the increased attenuation allowing for larger SFRs (See Table 3.2 for list of parameters and units).

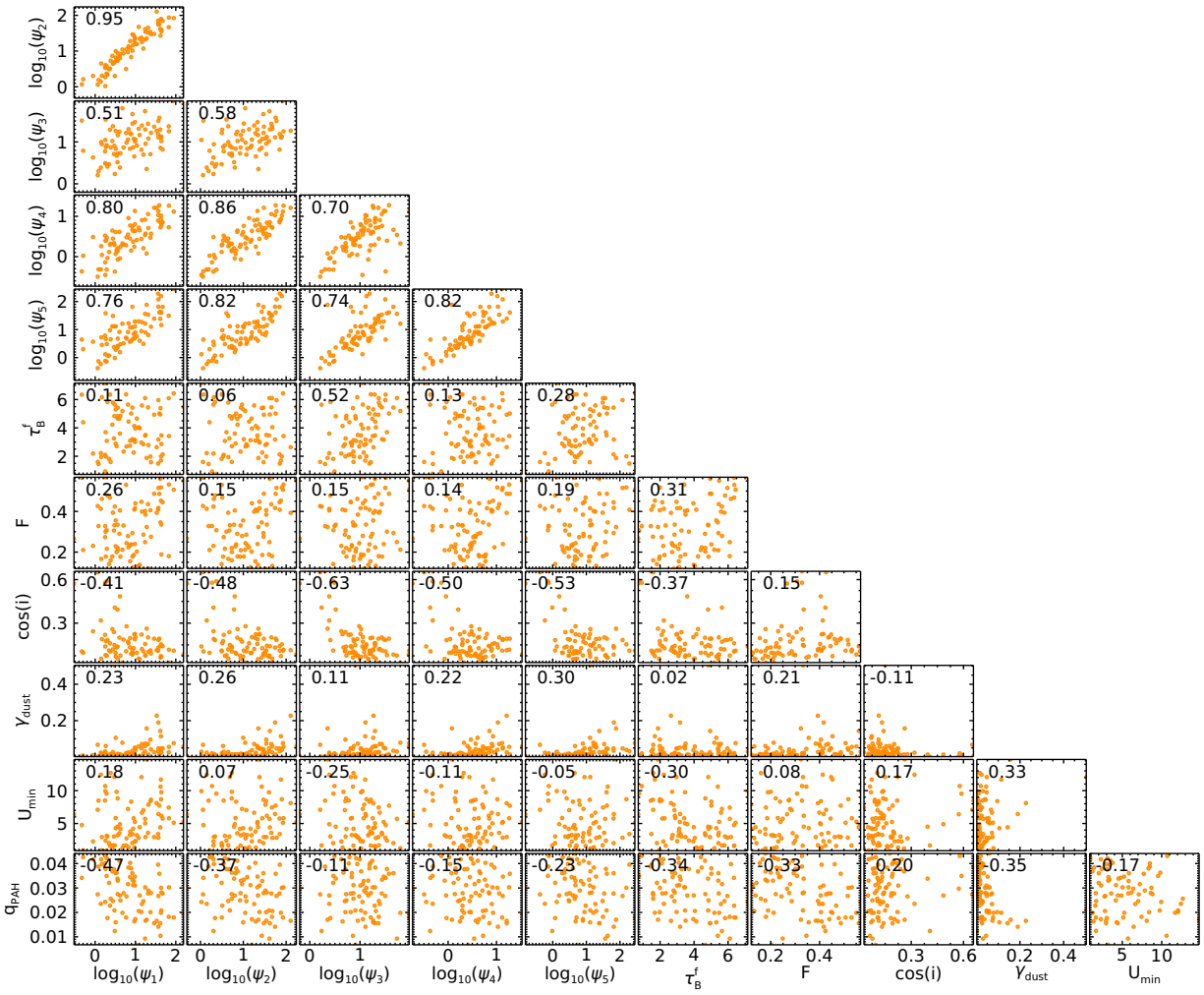

Figure 3.B.3: Same as Figure 3.B.2 except for the inclination-dependent fits with a flat inclination prior.

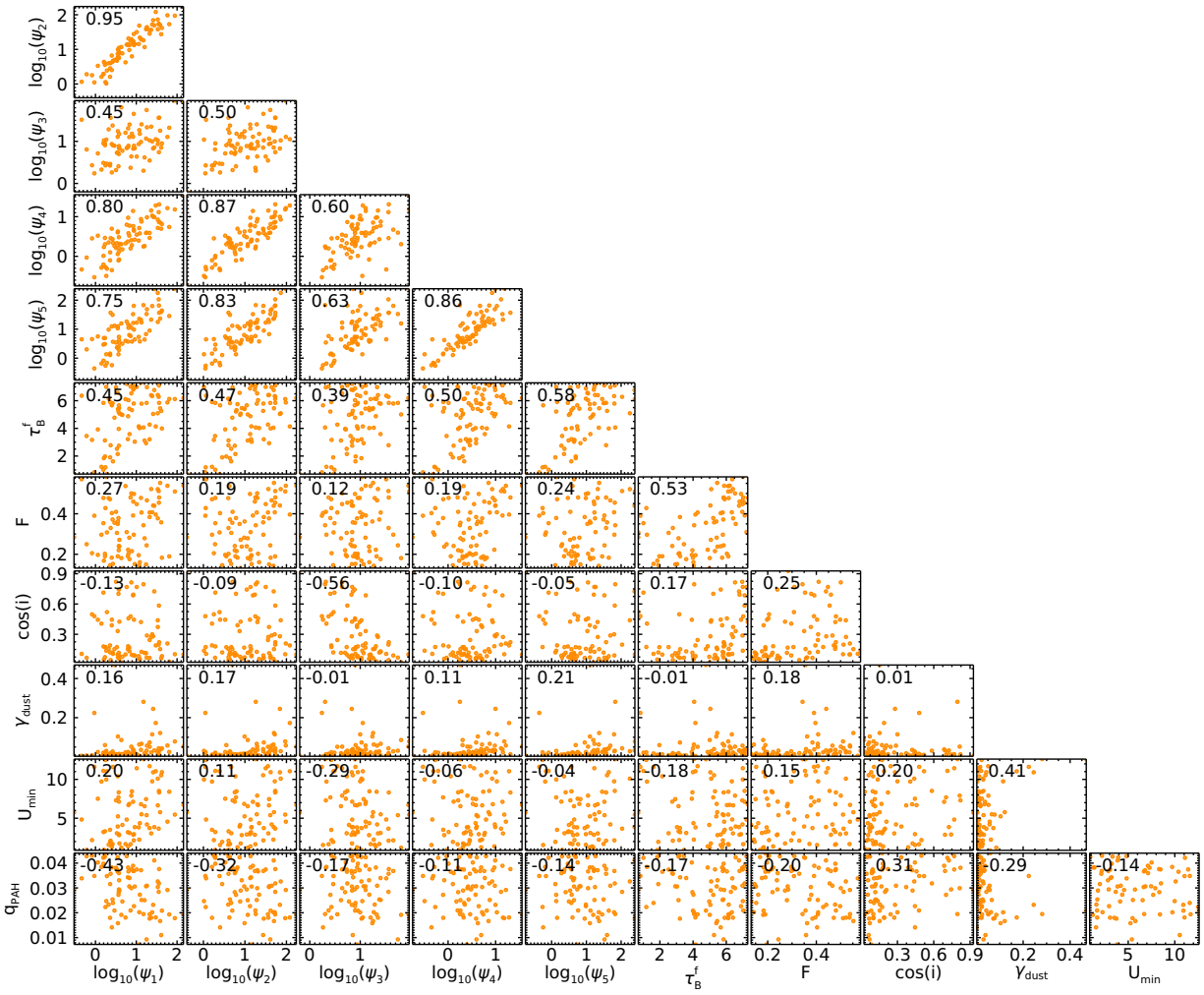

Figure 3.B.4: Same as Figure 3.B.2 except for the inclination-dependent fits with the image-based inclination prior. Like the Calzetti et al. (2000) fits, we see the expected correlations between τ_B^f and ψ_i, and ψ_i and ψ_j, where i and j are different age bins. One other notable feature is the effect of using the image-based inclination prior on the inclination-τ_B^f degeneracy. As seen in Figure 3.B.3, $\cos i$ and τ_B^f have a slight correlation. However, this correlation is minimized after implementing the image-based prior, implying that using this prior helps mitigate the inclination-τ_B^f degeneracy.

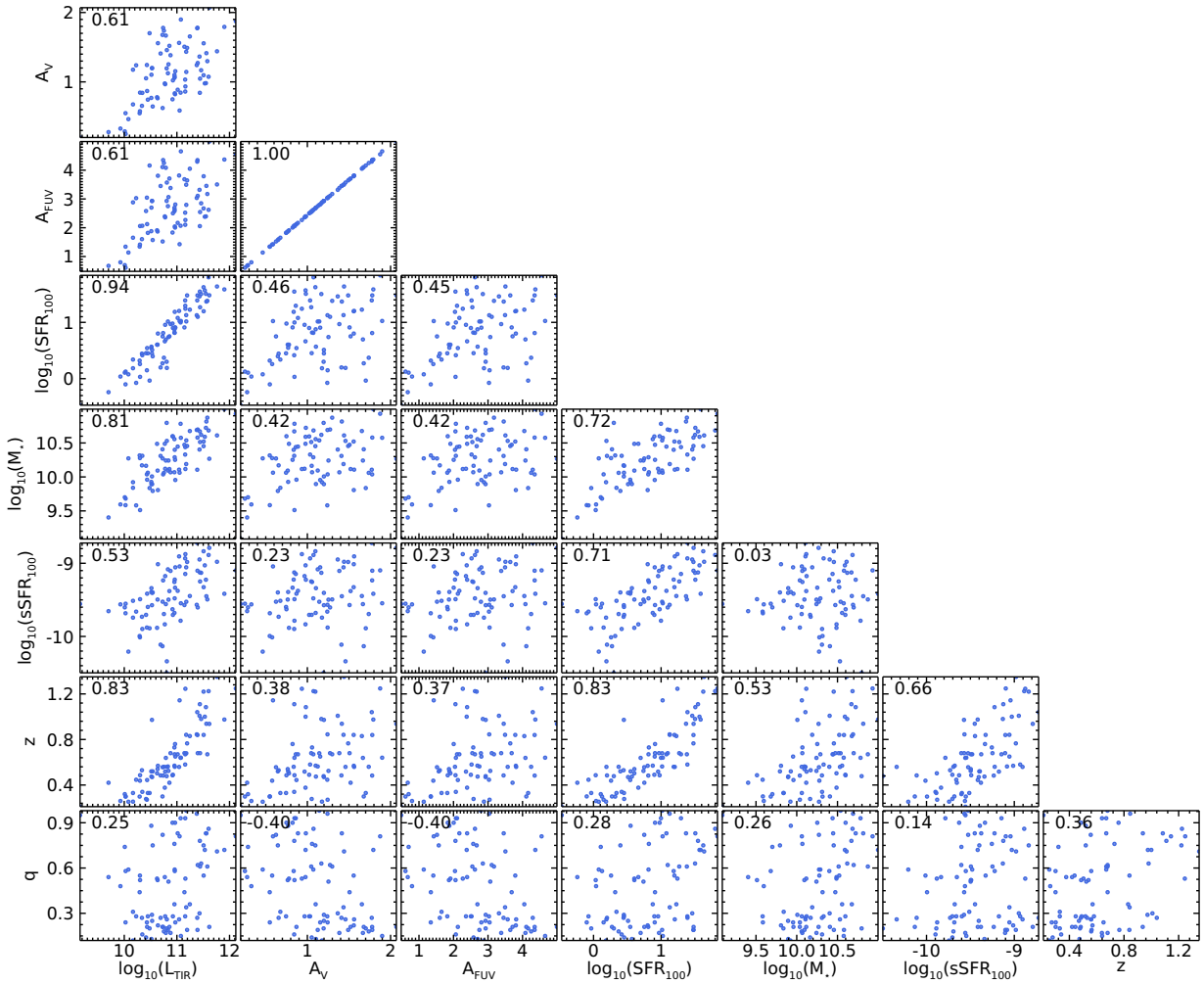

Figure 3.B.5: Scatter plots for the parameter of interest ($L_{\rm TIR}$ [$L_\odot$] , A_V [mag], A_{FUV} [mag], $\rm SFR_{100}$ [$\rm M_\odot$ $\rm yr^{-1}$], $M_\star$ [$M_\odot$], and $\rm sSFR_{100}$ [$\rm yr^{-1}$]) of our Calzetti et al. (2000) fits, along with redshift z and axis ratio q. Each point represents the median or given value of that parameter for a galaxy in our sample. The Pearson correlation coefficients for each set of parameters are shown in the upper-left corners of each scatter plot and give the global trends in the data. It is important to stress that these correlations are for the global trends and not the average of the individual fits as in Section 3.6. Most correlations seen were expected, such as that between $L_{\rm TIR}$ and all other properties besides q. These positive correlations with $L_{\rm TIR}$ are due to the energy balance assumption which requires larger attenuation and SFRs with increasing $L_{\rm TIR}$. As for z and $L_{\rm TIR}$, this correlation is a direct result of our selection process, which would require brighter IR emission at higher redshifts in order for the galaxy to be detected. It is also important to note that all parameters, besides A_V and A_{FUV}, are relatively independent of q, which confirms that selection effects are not significantly biasing our sample such that our results in Section 3.6 would be influenced by this bias.

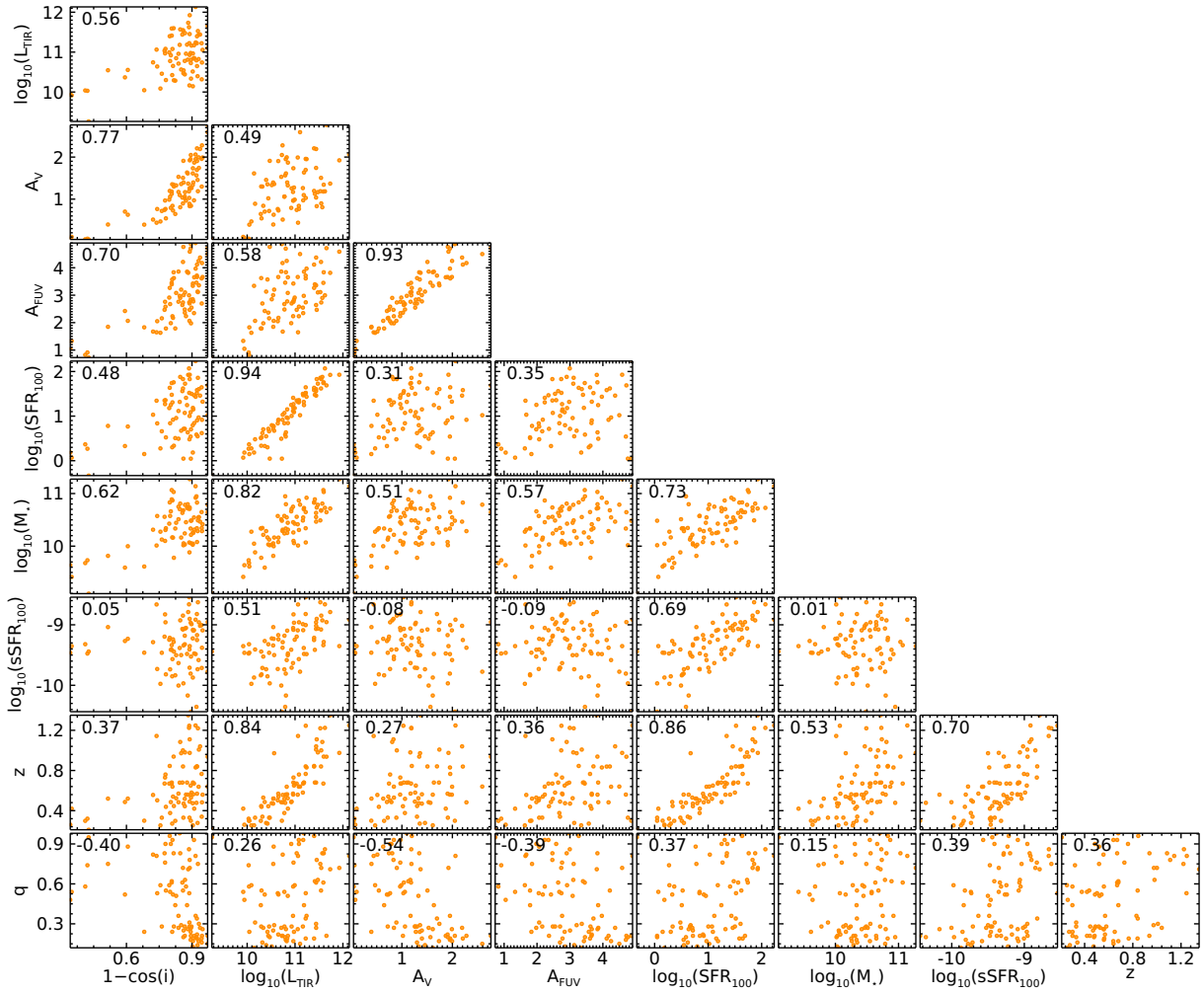

Figure 3.B.6: Same as Figure 3.B.5 except for the inclination-dependent fits with a flat inclination prior and the addition of the inclination parameter $(1 - \cos i)$.

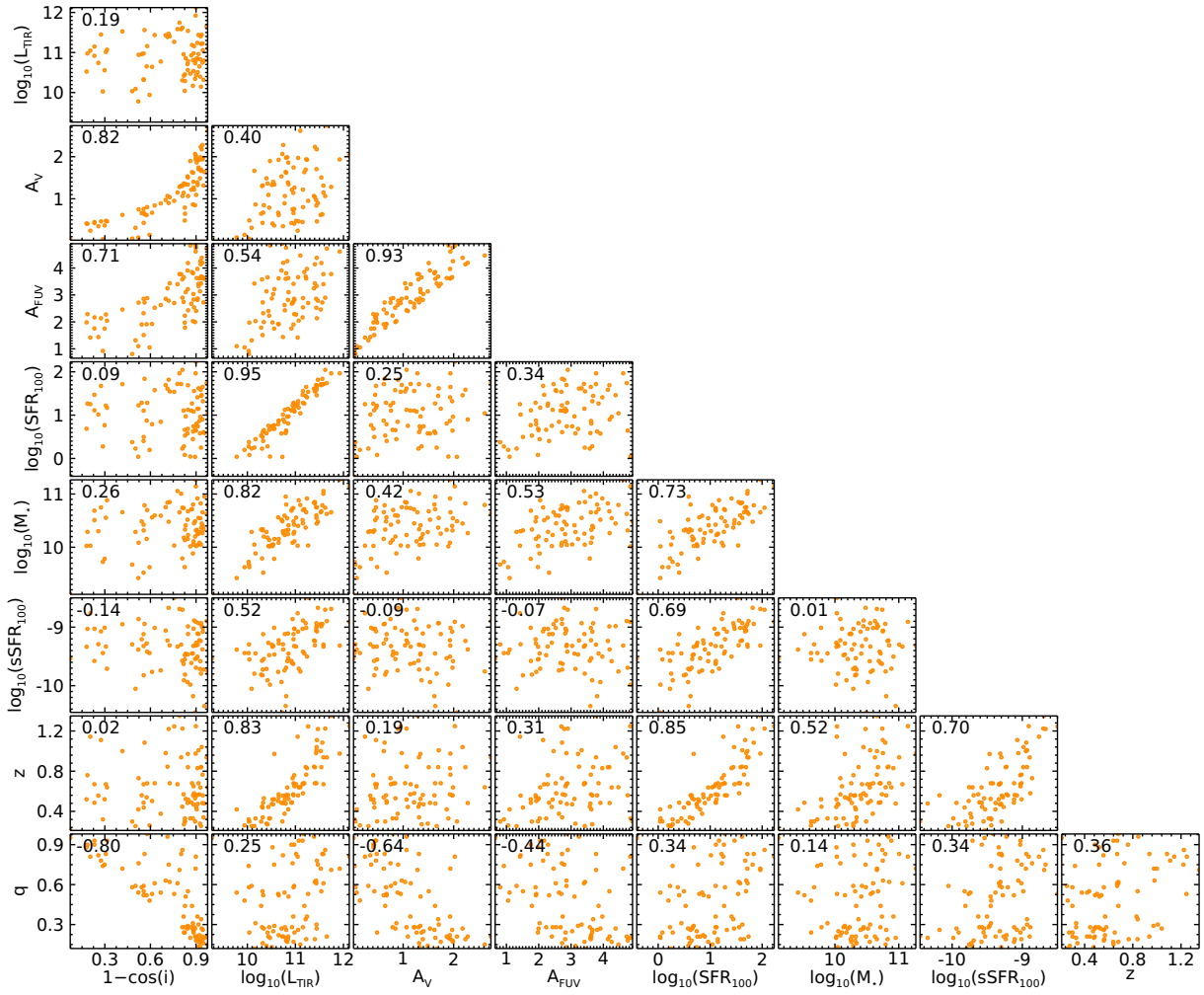

Figure 3.B.7: Same as Figure 3.B.5 except for the inclination-dependent fits with the image-based inclination prior and the addition of the inclination parameter ($1 - \cos i$). Like the Calzetti et al. (2000) fits, we see the expected correlations between $L_{\rm TIR}$ and the other parameters besides q and inclination. Again, minimal correlations can be seen between parameters (excluding A_V and $A_{\rm FUV}$) and q, which further implies that selection effects are not significantly biasing our sample. One other notable feature is the correlation between inclination and q with attenuation, which shows that more inclined galaxies tend to have increased attenuation.

Chapter 4

The Impact of Inclination-dependent Attenuation on Ultraviolet Star Formation Rate Tracers

Keith Doore, Rafael T. Eufrasio, Bret D. Lehmer, Erik B. Monson, Antara Basu-Zych, Kristen Garofali

The following chapter was originally published in The Astrophysical Journal, Volume 931, Issue 1, as article 53, with the same title.

Abstract

We examine and quantify how hybrid (e.g., UV+IR) star formation rate (SFR) estimators and the $A_{\rm FUV}$–β relation depend on inclination for disk-dominated galaxies using spectral energy distribution modeling that utilizes the inclination-dependent attenuation curves described in Doore et al. We perform this analysis on a sample of 133 disk-dominated galaxies from the CANDELS fields and 18 disk galaxies from the Spitzer Infrared Nearby Galaxies Survey and Key Insights on Nearby Galaxies: A Far-Infrared Survey with Herschel samples. We find that both the hybrid SFR estimators and the $A_{\rm FUV}$–β relation present clear dependencies on inclination. To quantify this dependence in the hybrid SFR estimators, we derive an inclination and a far-UV-near-IR color-dependent parametric relation for converting observed UV and IR luminosities into SFRs. For the $A_{\rm FUV}$–β relation, we introduce an inclination-dependent component that accounts for the majority of the inclination dependence with the scatter of the relation increasing with inclination. We then compare both of these inclination-dependent relations to similar inclination-independent relations found in the literature. From this comparison, we find that the UV+IR correction factor and $A_{\rm FUV}$

for our hybrid and $A_{\rm FUV}$–β relations, respectively, result in a reduction in the residual scatter of our sample by approximately a factor of 2. Therefore, we demonstrate that inclination must be considered in hybrid SFR estimators and the $A_{\rm FUV}$–β relation to produce more accurate SFR estimates in disk-dominated galaxies.

4.1 Introduction

Stars are one of the basic building blocks of galaxies, and measurements of their formation rates are critical for understanding how galaxies assembled and evolved. On extragalactic scales, star formation rates (SFRs) are typically determined for subgalactic star forming regions (e.g., Bigiel et al., 2008; Leroy et al., 2012; Eufrasio et al., 2014,0; Thorp et al., 2019) or, more commonly, entire integrated galaxies (e.g., Kennicutt, 1983; Gao & Solomon, 2004; Salim et al., 2007; Arnouts et al., 2013; Barro et al., 2019). At these scales, SFRs are typically determined from basic parametric descriptions (e.g. hybrid estimators, Meurer et al. 1999 relation, etc.), rather than physically based characterizations of the galaxy or each star forming region (see Kennicutt & Evans, 2012, for a review). Therefore, to improve estimates of SFRs, these parametric descriptions can be expanded to include dependencies on physical properties relevant to the SFR calculation.

Generally, parameterizations of SFRs use intrinsic (i.e., unattenuated) ultraviolet (UV) emission, which is almost exclusively produced by emission from young ($\leqslant$a few hundred Myr), massive stars,

$$\left(\frac{\rm SFR}{M_\odot\ {\rm yr}^{-1}}\right) = k_{\rm UV}\left(\frac{L_{\rm UV}^{\rm intr}}{L_\odot}\right), \tag{4.1}$$

where $k_{\rm UV}$ is the conversion from the intrinsic monochromatic luminosity in the UV ($L_{\rm UV}^{\rm intr}$, calculated as νL_ν) to the average SFR over the past 100 Myr (Kennicutt, 1998; Murphy et al., 2011;

Kennicutt & Evans, 2012). The conversion factor $k_{\rm UV}$ is typically determined from stellar population synthesis and depends upon the chosen UV bandpass filter, initial mass function (IMF), metallicity, and assumed star formation history (SFH, the SFR as a function of time).

Unlike $k_{\rm UV}$, which can be determined theoretically with basic assumptions, $L_{\rm UV}^{\rm intr}$ is more difficult to determine, since the true intrinsic luminosity cannot be measured directly due to attenuation by dust. Instead, $L_{\rm UV}^{\rm intr}$ must be estimated by modeling the attenuation of the observed emission in the rest-frame UV. There are two common methods for doing this, depending on the availability of quality infrared (IR) data. If quality IR data are available, hybrid SFR estimators are often chosen (e.g., Leroy et al., 2008; Zhu et al., 2008; Hao et al., 2011; Eufrasio et al., 2014; Catalán-Torrecilla et al., 2015; Boquien et al., 2016; Eufrasio et al., 2017). These tracers correct the observed UV luminosity to an intrinsic UV luminosity by assuming that some fraction of the attenuated UV light is absorbed by dust and reradiated in the IR, or

$$L_{\rm UV}^{\rm intr} = L_{\rm UV}^{\rm obs} + a_{\rm corr} \times L_{\rm IR}^{\rm obs}, \tag{4.2}$$

where $L_{\rm UV}^{\rm obs}$ is the observed rest-frame UV luminosity assuming isotropy, $a_{\rm corr}$ is the UV+IR correction factor that accounts for some fraction of the reradiated IR emission being from the attenuated UV light, and $L_{\rm IR}^{\rm obs}$ is the observed emission in a rest-frame IR bandpass, or the total integrated IR (TIR) luminosity. Many values of $a_{\rm corr}$ exist in the literature that have been empirically derived depending upon the chosen UV and IR bandpasses, as well as the choice of attenuation curve.

Another commonly used method for modeling the attenuation of the UV emission when IR data are not available is the $A_{\rm UV}$–β relation, which is also referred to as the Meurer et al. (1999) relation due to its initial derivation in Meurer et al. (1999). This relation links the slope of the observed UV emission (β; $F_\lambda \propto \lambda^\beta$) to the UV attenuation ($A_{\rm UV}$). Following the notation of Boquien et al.

(2012), a generalized version of the $A_{\rm UV}$–β relation is given by

$$A_{\rm UV} = a_\beta(\beta - \beta_0), \tag{4.3}$$

where β_0 is the slope of the unattenuated UV emission given by the galaxy's intrinsic properties (i.e., SFH, IMF, and metallicity), and a_β is defined by the shape of the chosen attenuation curve. This relation is commonly calibrated using a sample of galaxies that have IR measurements to use their "IR excess" (IRX) as a proxy for $A_{\rm UV}$ (Calzetti et al., 1994; Meurer et al., 1999; Gordon et al., 2000; Kong et al., 2004; Hao et al., 2011; Boquien et al., 2012; Buat et al., 2012). This leads to the so-called IRX–β relation, given by

$$\mathrm{IRX} \equiv \log_{10}\left(\frac{L_{\rm IR}^{\rm obs}}{L_{\rm UV}^{\rm obs}}\right) = \log_{10}\left[\left(10^{0.4a_\beta(\beta-\beta_0)} - 1\right)/a_{\rm corr}\right], \tag{4.4}$$

where $a_{\rm corr}$ is defined in Equation 4.2. Once a_β, β_0, and $a_{\rm corr}$ have been calibrated, the $A_{\rm UV}$–β relation can be used to determine the deattenuated, intrinsic UV luminosity for galaxies lacking IR data.

However, both of these methods have a common caveat. As stated above, the parameters $a_{\rm corr}$ and a_β strongly depend upon the choice of attenuation curve. Therefore, a simplified or inappropriate choice of attenuation curve can lead to various biases in these values. This is of particular importance when trying to determine the intrinsic UV emission of disk galaxies, as the inclination of the disk has been shown to significantly influence attenuation, with edge-on galaxies (i.e., $i \approx 90^\circ$) having increased attenuation compared to face-on galaxies (i.e., $i \approx 0^\circ$; Giovanelli et al., 1994; Driver et al., 2007; Unterborn & Ryden, 2008; Conroy et al., 2010; Masters et al., 2010; Wild et al., 2011; Devour & Bell, 2016; Battisti et al., 2017; Salim et al., 2018).

As an example, if a disk galaxy could be viewed from multiple inclinations, it would be ob-

served that the UV emission would decrease with increasing inclination, whereas the IR emission would be relatively unchanged due to minimal attenuation at these wavelengths. With the intrinsic UV emission being independent of inclination, Equation 4.2 indicates that $a_{\rm corr}$ must be dependent upon inclination to compensate for the inclination dependence of the observed UV emission. Therefore, in order to account for this effect and obtain accurate SFR estimators, it is critical to characterize how inclination affects the attenuation and scaling relations of disk galaxies.

Recent works by Conroy et al. (2010), Leslie et al. (2018b,0), Wang et al. (2018), and Wolf et al. (2018) have investigated how inclination affects the SFRs derived using UV emission. Specifically, Leslie et al. (2018b,0) and Wolf et al. (2018) showed that inclination-based attenuation alone can cause the uncorrected, observed UV emission to yield underestimated SFRs (by factors of 2.5–4) for edge-on galaxies compared to face-on galaxies. Conroy et al. (2010) and Wang et al. (2018) showed that the IRX–β relation is highly dependent upon inclination, with nearly edge-on galaxies having larger IRX values by factors of 1.2–1.5 compared to nearly face-on galaxies with the same β. However, Leslie et al. (2018a) showed that hybrid SFR estimators, when assuming a constant $a_{\rm corr}$, are relatively inclination-independent when compared to the galaxy main sequence (galaxy SFR–stellar mass relation). Yet this is not in contradiction with the theoretical stance that hybrid SFR estimators, when assuming a constant $a_{\rm corr}$, should be dependent upon inclination. This is due to the comparison with the galaxy main sequence, which was derived using these same hybrid SFR estimators. Therefore, it is expected that any trends with inclination are masked by using this comparison.

In this paper, we examine and quantify how both hybrid SFR estimators and the $A_{\rm UV}$–β relation depend on inclination using spectral energy distribution (SED) modeling that incorporates the inclination-dependent attenuation curves described in Doore et al. (2021), which are based on the

Tuffs et al. (2004) inclination-dependent attenuation curves. When examining this dependence, we specifically focus on the commonly used Galaxy Evolution Explorer (GALEX) far-UV (FUV) bandpass and TIR luminosity ($L_{\rm TIR}$). We quantify this inclination dependence using a sample of 133 galaxies from the Cosmic Assembly Near-infrared Deep Extragalactic Legacy Survey (CANDELS) fields (Grogin et al., 2011; Koekemoer et al., 2011) along with 18 disk galaxies from the Spitzer Infrared Nearby Galaxies Survey (SINGS; Kennicutt et al., 2003; Dale et al., 2005,0) and Key Insights on Nearby Galaxies: A Far-Infrared Survey with Herschel (KINGFISH; Kennicutt et al., 2011; Dale et al., 2012) samples. We discuss how we selected these galaxies and their photometry in Section 4.2. In Section 4.3, we derive the physical properties needed for our analysis using SED modeling. In Section 4.4, we examine, quantify, and present how both the hybrid SFR estimators and the $A_{\rm FUV}$–β relation depend on inclination and discuss how this inclination dependence compares with results from past studies. Finally, we summarize our results in Section 4.5.

In this work, we assume a Kroupa (2001) IMF with solar metallicity ($Z = Z_{\odot}$) and a flat ΛCDM cosmology where $\Omega_M = 0.30$ and $\Omega_\Lambda = 0.70$ with a Hubble constant of $H_0 = 70$ km s^{-1} Mpc^{-1}. Additionally, all quoted magnitudes are in AB magnitudes.

4.2 Data and Sample Selection

4.2.1 CANDELS sample

Since UV star formation tracers are commonly used to determine the SFRs of galaxies at intermediate redshifts, we utilized a sample of 133 disk-dominated galaxies that are contained within the CANDELS fields, spanning a redshift range of $z = 0.09$–0.98. Of these galaxies, 38 and 42 galaxies are contained within the Great Observatories Origins Deep Survey North (GOODS-N)

and South (GOODS-S) fields (Giavalisco et al., 2004), respectively; 23 are contained within the Extended Groth Strip (EGS; Davis et al., 2007); 25 are contained within the Cosmic Evolution Survey (COSMOS) field (Scoville et al., 2007); and five are contained within the UKIDSS Ultra-Deep Survey (UDS) field (Cirasuolo et al., 2007; Lawrence et al., 2007). To generate this sample of galaxies, we used a similar selection method as presented in Doore et al. (2021), which was shown to have minimal to no selection biases due to inclination.

We briefly summarize this method here. We first selected galaxies to have reliable spectroscopic redshifts from our compiled spectroscopic redshift catalog, which is described in Appendix 4.A. We then required each galaxy to have at least six photometric measurements in the mid-to-far IR (3–1000 μm), one of which was required to be greater than 100 μm rest frame to constrain the peak of the dust emission. Next, we considered any galaxy cross-matched within $1''$ of an X-ray-detected source in the Chandra X-ray catalogs (Nandra et al., 2015; Civano et al., 2016; Xue et al., 2016; Luo et al., 2017; Kocevski et al., 2018) as potentially harboring an active galactic nucleus (AGN). These potential AGNs were then removed to prevent any AGN-dominated galaxies from being in the sample. We also removed potentially obscured mid-IR AGNs using the Donley et al. (2012) IRAC selection criteria and Kirkpatrick et al. (2013) Spitzer/Herschel color-color criteria. We then reduced the sample to only disk-dominated galaxies (i.e., an approximate bulge-to-disk ratio of zero) via their Sérsic index n ($n < 1.2$; Sérsic, 1963) as measured by van der Wel et al. (2012)[1] in the Hubble Space Telescope (HST) WFC3/F125W band. We additionally required the Sérsic indices to be from "good fits" (i.e., flag of 0). Finally, a visual inspection of HST postage stamps was performed, and we removed any irregular or potentially merging galaxies that survived the Sérsic index cut.

[1] https://users.ugent.be/~avdrwel/research.html#candels

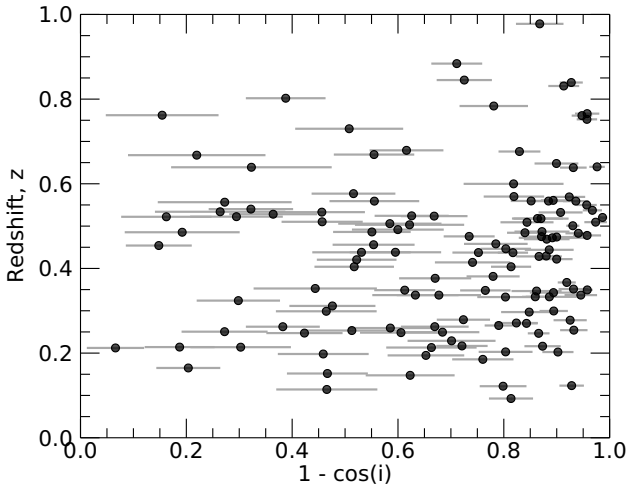

Figure 4.1: Inclinations derived from `Lightning` in terms of $1-\cos i$ vs. the spectroscopic redshift of each galaxy in the CANDELS sample. While the sample does contain more inclined galaxies compared to less inclined galaxies, there is no distinguishable trend in inclination with redshift.

To confirm that minimal to no selection biases due to inclination are present in our sample, we show the inclination of each galaxy as derived from our SED fittings (see Section 4.3.1) versus spectroscopic redshift in Figure 4.1. While there are more highly inclined galaxies compared to low-inclination galaxies, no distinguishable trend in inclination with redshift is present. Trends between inclination and redshift are possible, as edge-on galaxies can be preferentially selected at higher redshifts compared to face-on galaxies due to their higher surface brightness (Graham & Worley, 2008; Sargent et al., 2010; Devour & Bell, 2016). We quantitatively confirmed this lack of trend between inclination and redshift by splitting the sample into two groups along the median redshift of 0.45 and performing a Kolmogorov–Smirnov test. The test showed minimal differences in inclination distributions for the high- and low-redshift groups with a p-value > 0.1.

The UV–to–mid-IR photometry for the 133 galaxies was taken from the CANDELS multiband photometric catalogs[2], which are presented in Barro et al. (2019), Guo et al. (2013), Stefanon et al.

[2]https://archive.stsci.edu/prepds/candels/

(2017), Nayyeri et al. (2017), and Galametz et al. (2013) for the GOODS-N, GOODS-S, EGS, COSMOS, and UDS fields, respectively. We also utilized the far-IR photometry produced by Barro et al. (2019) for all five of the CANDELS fields. We corrected the photometry for Galactic extinction using the Schlafly & Finkbeiner (2011) recalibration of the Schlegel et al. (1998) dust maps and a Fitzpatrick (1999) reddening law with $R_V = 3.1$. The extinction was determined for the center of each field, and no variation across each field is considered, due to small overall extinction corrections and minimal variation across each field. We also added fractional calibration uncertainties to the catalog flux uncertainties to account for any additional sources of uncertainty and potential systematic variations in the photometry. These fractional calibration uncertainties are 2–15% of the measured flux as described in each instrument's user handbook and listed in Table 4.1 along with the mean wavelength, Galactic extinction, and corresponding filters used in each field.

To estimate the inclinations of each galaxy (see Section 4.3.1), we required an axis ratio q with uncertainty. Therefore, we utilized the WFC3/F125W measured axis ratios from the fits for the Sérsic index by van der Wel et al. (2012). We note that measurements of q have been shown to vary with rest-frame wavelength and redshift (Dalcanton & Bernstein, 2002). However, van der Wel et al. (2014) showed that this variation with redshift in the van der Wel et al. (2012) axis ratios is generally smaller than the uncertainty within our redshift range.

4.2.2 SINGS/KINGFISH sample

We supplemented our CANDELS sample with an additional 18 local disk-dominated galaxies from the combined SINGS and KINGFISH sample given in Dale et al. (2017), since UV star formation tracers are also commonly used in local galaxies. We first selected galaxies to be star-

Table 4.1: CANDELS Multiwavelength Coverage

Field	Telescope/Band	$\lambda_{\rm mean}$[a] (μm)	$A_\lambda^{\rm Gal}$[b] (mag)	$\sigma_{\rm C}^{\rm cal}$[c]	Field	Telescope/Band	$\lambda_{\rm mean}$[a] (μm)	$A_\lambda^{\rm Gal}$[b] (mag)	$\sigma_{\rm C}^{\rm cal}$[c]
GOODS-N	KPNO 4m/Mosaic U	0.3561	0.052	0.05	EGS	CFHT/MegaCam u^*	0.3799	0.032	0.05
	LBT/LBC U	0.3576	0.052	0.10		CFHT/MegaCam g'	0.4806	0.026	0.05
	HST/ACS F435W	0.4296	0.044	0.02		HST/ACS F606W	0.5804	0.020	0.02
	HST/ACS F606W	0.5804	0.031	0.02		CFHT/MegaCam r'	0.6189	0.018	0.05
	HST/ACS F775W	0.7656	0.020	0.02		CFHT/MegaCam i'	0.7571	0.013	0.05
	HST/ACS F814W	0.7979	0.019	0.02		HST/ACS F814W	0.7979	0.012	0.02
	HST/ACS F850LP	0.8990	0.015	0.02		CFHT/MegaCam z'	0.8782	0.011	0.05
	HST/WFC3 F105W	1.0449	0.012	0.02		Mayall/NEWFIRM J_1	1.0432	0.008	0.10
	HST/WFC3 F125W	1.2396	0.009	0.02		Mayall/NEWFIRM J_2	1.1922	0.006	0.10
	HST/WFC3 F140W	1.3784	0.007	0.02		HST/WFC3 F125W	1.2396	0.006	0.02
	HST/WFC3 F160W	1.5302	0.006	0.02		CFHT/WIRCam J	1.2513	0.006	0.05
	CFHT/WIRCam K_s	2.1413	0.004	0.05		Mayall/NEWFIRM J_3	1.2757	0.006	0.10
	Subaru/MOIRCS K_s	2.1442	0.004	0.05		HST/WFC3 F140W	1.3784	0.005	0.02
	Spitzer/IRAC1	3.5314	0.002	0.05		HST/WFC3 F160W	1.5302	0.004	0.02
	Spitzer/IRAC2	4.4690	0.000	0.05		Mayall/NEWFIRM H_1	1.5578	0.004	0.10
	Spitzer/IRAC3	5.6820	0.000	0.05		CFHT/WIRCam H	1.6217	0.004	0.05
	Spitzer/IRAC4	7.7546	0.000	0.05		Mayall/NEWFIRM H_2	1.7041	0.004	0.10
	Spitzer/MIPS 24 μm	23.513	0.000	0.05		CFHT/WIRCam K_s	2.1413	0.002	0.05
	Spitzer/MIPS 70 μm	70.389	0.000	0.10		Mayall/NEWFIRM K	2.1639	0.002	0.10
	Herschel/PACS 100 μm	100.05	0.000	0.05		Spitzer/IRAC1	3.5314	0.001	0.05
	Herschel/PACS 160 μm	159.31	0.000	0.05		Spitzer/IRAC2	4.4690	0.000	0.05
	Herschel/SPIRE 250 μm	247.21	0.000	0.15		Spitzer/IRAC3	5.6820	0.000	0.05
GOODS-S	Blanco/MOSAIC II U	0.3567	0.034	0.05		Spitzer/IRAC4	7.7546	0.000	0.05
	VLT/VIMOS U	0.3709	0.033	0.05		Spitzer/MIPS 24 μm	23.513	0.000	0.05
	HST/ACS F435W	0.4296	0.029	0.02		Spitzer/MIPS 70 μm	70.389	0.000	0.10
	HST/ACS F606W	0.5804	0.020	0.02		Herschel/PACS 100 μm	100.05	0.000	0.05
	HST/ACS F775W	0.7656	0.013	0.02		Herschel/PACS 160 μm	159.31	0.000	0.05
	HST/ACS F814W	0.7979	0.012	0.02		Herschel/SPIRE 250 μm	247.21	0.000	0.15
	HST/ACS F850LP	0.8990	0.010	0.02	COSMOS	CFHT/MegaCam u^*	0.3799	0.074	0.05
	HST/WFC3 F098M	0.9826	0.008	0.02		Subaru/Suprime-Cam B	0.4323	0.066	0.05
	HST/WFC3 F105W	1.0449	0.008	0.02		Subaru/Suprime-Cam g'	0.4634	0.062	0.05
	HST/WFC3 F125W	1.2396	0.006	0.02		CFHT/MegaCam g'	0.4806	0.059	0.05
	HST/WFC3 F160W	1.5302	0.004	0.02		Subaru/Suprime-Cam V	0.5416	0.051	0.05
	VLT/HAWK-I K_s	2.1403	0.002	0.05		HST/ACS F606W	0.5804	0.046	0.02
	VLT/ISAAC K_s	2.1541	0.002	0.05		CFHT/MegaCam r'	0.6189	0.041	0.05
	Spitzer/IRAC1	3.5314	0.001	0.05		Subaru/Suprime-Cam r'	0.6197	0.041	0.05
	Spitzer/IRAC2	4.4690	0.000	0.05		CFHT/MegaCam i'	0.7571	0.030	0.05
	Spitzer/IRAC3	5.6820	0.000	0.05		Subaru/Suprime-Cam i'	0.7622	0.030	0.05
	Spitzer/IRAC4	7.7546	0.000	0.05		HST/ACS F814W	0.7979	0.028	0.02
	Spitzer/MIPS 24 μm	23.513	0.000	0.05		CFHT/MegaCam z'	0.8782	0.024	0.05
	Spitzer/MIPS 70 μm	70.389	0.000	0.10		Subaru/Suprime-Cam z'	0.9154	0.023	0.05
	Herschel/PACS 100 μm	100.05	0.000	0.05		VISTA/VIRCAM Y	1.0194	0.018	0.05
	Herschel/PACS 160 μm	159.31	0.000	0.05		Mayall/NEWFIRM J_1	1.0432	0.018	0.10
	Herschel/SPIRE 250 μm	247.21	0.000	0.15		Mayall/NEWFIRM J_2	1.1922	0.014	0.10
UDS	CFHT/MegaCam u^*	0.3799	0.091	0.05		HST/WFC3 F125W	1.2396	0.013	0.02
	Subaru/Suprime-Cam B	0.4323	0.081	0.05		VISTA/VIRCAM J	1.2497	0.013	0.05
	Subaru/Suprime-Cam V	0.5416	0.063	0.05		Mayall/NEWFIRM J_3	1.2757	0.013	0.10
	HST/ACS F606W	0.5804	0.056	0.02		HST/WFC3 F160W	1.5302	0.009	0.02
	Subaru/Suprime-Cam R_c	0.6471	0.048	0.05		Mayall/NEWFIRM H_1	1.5578	0.009	0.10
	Subaru/Suprime-Cam i'	0.7622	0.037	0.05		VISTA/VIRCAM H	1.6374	0.008	0.05
	HST/ACS F814W	0.7979	0.034	0.02		Mayall/NEWFIRM H_2	1.7041	0.008	0.10
	Subaru/Suprime-Cam z'	0.9154	0.028	0.05		VISTA/VIRCAM K_s	2.1408	0.006	0.05
	VLT/HAWK-I Y	1.0187	0.023	0.05		Mayall/NEWFIRM K	2.1639	0.006	0.10
	HST/WFC3 F125W	1.2396	0.016	0.02		Spitzer/IRAC1	3.5314	0.003	0.05
	UKIRT/WFCAM J	1.2521	0.016	0.05		Spitzer/IRAC2	4.4690	0.000	0.05
	HST/WFC3 F160W	1.5302	0.011	0.02		Spitzer/IRAC3	5.6820	0.000	0.05
	UKIRT/WFCAM H	1.6406	0.010	0.05		Spitzer/IRAC4	7.7546	0.000	0.05
	VLT/HAWK-I K_s	2.1403	0.007	0.05		Spitzer/MIPS 24 μm	23.513	0.000	0.05
	UKIRT/WFCAM K	2.2261	0.007	0.05		Spitzer/MIPS 70 μm	70.389	0.000	0.10
	Spitzer/IRAC1	3.5314	0.004	0.05		Herschel/PACS 100 μm	100.05	0.000	0.05

Table 4.1: (Cont.)

Field	Telescope/Band	$\lambda_{\rm mean}$[a] (μm)	$A_\lambda^{\rm Gal}$[b] (mag)	$\sigma_{\rm C}^{\rm cal}$[c]	Field	Telescope/Band	$\lambda_{\rm mean}$[a] (μm)	$A_\lambda^{\rm Gal}$[b] (mag)	$\sigma_{\rm C}^{\rm cal}$[c]
UDS	Spitzer/IRAC2	4.4690	0.000	0.05	COSMOS	Herschel/PACS 160 μm	159.31	0.000	0.05
	Spitzer/IRAC3	5.6820	0.000	0.05		Herschel/SPIRE 250 μm	247.21	0.000	0.15
	Spitzer/IRAC4	7.7546	0.000	0.05					
	Spitzer/MIPS 24 μm	23.513	0.000	0.05					
	Spitzer/MIPS 70 μm	70.389	0.000	0.10					
	Herschel/PACS 100 μm	100.05	0.000	0.05					
	Herschel/PACS 160 μm	159.31	0.000	0.05					
	Herschel/SPIRE 250 μm	247.21	0.000	0.15					

[a]Mean wavelength of the filter calculated as $\lambda_{\rm mean} = \frac{\int \lambda T(\lambda) d\lambda}{\int T(\lambda) d\lambda}$, where $T(\lambda)$ is the filter transmission function.
[b]Galactic extinction for the center of the field.
[c]Calibration uncertainties as given by the corresponding instrument user handbook.

forming spiral galaxies (Sa and later types) as given by their optical morphologies in Dale et al. (2017). They were also selected to not be AGN-dominated (i.e., Seyfert galaxies) to limit any contamination of the photometry by AGNs, using the nuclear type given in Kennicutt et al. (2003). Further, we excluded galaxies with low Galactic latitude (absolute latitude $< 15^\circ$), as the large number of foreground stars can result in nonnegligible contamination of the observed fluxes. We also excluded any galaxies that are known to be or have companion galaxies (e.g., NGC 1097 and NGC 5457), as the interaction between companions could impact disk morphology, resulting in distorted inclination estimates. Finally, we visually inspected images of the remaining galaxies and excluded any that are irregularly shaped or contain bright or dominant bulges. With these criteria, our SINGS/KINGFISH sample includes the following 18 galaxies: NGC 24, NGC 337, NGC 628, NGC 925, NGC 2403, NGC 2976, NGC 3049, NGC 3184, NGC 3198, NGC 3938, NGC 4236, NGC 4254, NGC 4536, NGC 4559, NGC 4631, NGC 5055, NGC 7331, and NGC 7793.

The photometry that we used for the SINGS/KINGFISH sample was derived by Dale et al. (2017) and is given in their Table 2. We corrected this photometry for Galactic extinction using the

$E(B-V)$ values quoted in Dale et al. (2017) along with their A_V-normalized extinction values by bandpass. These extinction values were derived from the Schlafly & Finkbeiner (2011) recalibration of the Schlegel et al. (1998) dust maps and assuming a Li & Draine (2001) reddening curve with $R_V = 3.1$. Unlike the CANDELS sample, we do not add any additional fractional calibration uncertainties to these flux uncertainties, as fractional calibration uncertainties are already included in the uncertainties given by Dale et al. (2017).

The axis ratios for the SINGS/KINGFISH sample were gathered for each galaxy from the HyperLeda database[3] (Makarov et al., 2014). We do not use the major and minor axis values quoted in Dale et al. (2017) for our axis ratios, as they were chosen to encapsulate practically all of the fluxes at all measured wavelengths. Instead, the HyperLeda axis ratios and their uncertainties are derived from 25 mag/arcsec^2 B-band isophotes, which is more consistent with the axis ratio derivation of the CANDELS sample.

4.3 Derivation of Physical Properties

4.3.1 Lightning SED Modeling

We fitted the corrected photometry (as discussed in Section 4.2) of each galaxy using the SED fitting code `Lightning`[4] (Eufrasio et al., 2017; Doore et al., 2021), assuming a 10% model uncertainty for each band. For the fits, we assumed the same model as Doore et al. (2021) when fitting using the inclination-dependent model with an image-based inclination prior. This model consists of an SFH that has five constant SFR age bins, the inclination-dependent attenuation curves described in Doore et al. (2021), and the dust emission of Draine & Li (2007). A full description

[3] http://leda.univ-lyon1.fr/

[4] Version 2.0: https://github.com/rafaeleufrasio/lightning

of the model, a list of all free parameters and their corresponding prior distributions, and a description of the inclination-dependent attenuation curves can be found in Section 5, Table 2, and Section 4.3 of Doore et al. (2021), respectively. The only change to the model occurred for the SINGS/KINGFISH sample, where the lower limit of $U_{\rm min}$ (the minimum value of the radiation field intensity U for the dust emission) was changed from 0.7 to 0.1, since the SINGS/KINGFISH sample has rest-frame submillimeter data. For the image-based inclination prior distributions, we derived probability distributions of inclination given our axis ratios via the Monte Carlo method presented in Section 3 of Doore et al. (2021). The method creates a distribution of inclination for a given galaxy that accounts for variation in the measured axis ratio due to galaxy intrinsic thickness and asymmetry.

Using this model, we fitted the SED of each galaxy using the adaptive Markov Chain Monte Carlo (MCMC) procedure in `Lightning`. We ran each MCMC fit for 2×10^5 iterations and tested for convergence of the chains to a best solution using 10 parallel chains, each started at random starting locations within the parameter ranges. Convergence was tested using the Gelman–Rubin test (Gelman & Rubin, 1992; Brooks & Gelman, 1998) on the last 5000 iterations of the parallel chains, which indicated that the set of parallel chains for all galaxies converged to the same solution (i.e., $\sqrt{\hat{R}} \approx 1$). For each galaxy, we then used the last 5000 iterations of the parallel chain with the minimum χ^2 for our output parameter distributions. Finally, using the minimum χ^2 of each galaxy, we tested how well our model described the data by performing a χ^2 goodness-of-fit test. The results of this test showed a relatively flat $P_{\rm null}$ distribution, which indicates that the model has acceptably fit the SEDs.

4.3.2 Derived Physical Properties

From the output parameter distributions of the SED fitting, we derived the various properties needed for our analysis (e.g., inclination, $L_{\rm FUV}$, $A_{\rm FUV}$, $L_{\rm TIR}$, etc.). All of these properties for our sample are given in Table 4.2. For the bandpass luminosities (calculated as L_ν), they were derived by convolving the corresponding filter transmission function with the attenuated rest-frame model spectrum to avoid any redshift dependencies. Additionally, isotropy was assumed when calculating these luminosities from the model spectra, since isotropy is typically assumed when converting observed fluxes to luminosities. We note that for the remainder of the paper, when we refer to any attenuated (or unattenuated) bandpass luminosity or color, we are implicitly referring to these rest-frame model luminosities as given in Table 4.2. From the properties given in Table 4.2, we derived four additional properties needed for our analysis, specifically, $a_{\rm corr}$, β, β_0, and a_β (see Equations 4.2 and 4.3). A detailed description of how we calculated these properties is given below.

To first asses the accuracy of our derived inclinations, we compared these inclinations to the image-based inclination priors derived from the axis ratios. We show this comparison in Figure 4.2, where the vast majority of galaxies fall along the one-to-one line. However, the small number of galaxies that deviate significantly from the one-to-one line are all from the CANDELS sample. Doore et al. (2021) discussed that the galaxies far from the one-to-one line may have disks that are significantly thicker and dynamically hotter than the galaxies in the local universe, on which the inclination-dependent model was based. Therefore, the inclination-dependent model may not be physically appropriate for these galaxies. However, we continued to use our inclinations derived from `Lightning` as our inclination estimates and did not remove those four to five galaxies from

Table 4.2: Galaxy Sample and Properties.

Name	R.A. (deg)	Decl. (deg)	D (Mpc)	z	q	$1-\cos i$	$L_{\rm FUV}$ ($L_\odot$ Hz^{-1})	
(1)	(2)	(3)	(4)	(5)	(6)	(7)	(8)	
J123624.82+620719.2	189.1034	62.1220	···	0.11	0.591 ± 0.001	0.465 ± 0.096	$(1.471 \pm 0.381) \times 10^{-6}$	···
J123723.47+621448.3	189.3478	62.2468	···	0.25	0.595 ± 0.034	0.513 ± 0.094	$(1.252 \pm 0.294) \times 10^{-6}$	···
J123654.64+621127.1	189.2277	62.1909	···	0.25	0.118 ± 0.001	0.932 ± 0.026	$(2.106 \pm 0.585) \times 10^{-7}$	···
J123733.50+621941.0	189.3896	62.3281	···	0.27	0.243 ± 0.236	0.824 ± 0.041	$(2.591 \pm 0.800) \times 10^{-7}$	···
J123809.19+621638.1	189.5383	62.2772	···	0.28	0.136 ± 0.052	0.925 ± 0.031	$(5.536 \pm 1.342) \times 10^{-7}$	···
J123711.77+621514.9	189.2990	62.2541	···	0.30	0.583 ± 0.037	0.464 ± 0.095	$(3.351 \pm 0.651) \times 10^{-6}$	···
J123745.89+621435.0	189.4412	62.2430	···	0.30	0.211 ± 0.057	0.894 ± 0.027	$(1.204 \pm 0.241) \times 10^{-7}$	···
J123615.96+621008.2	189.0665	62.1689	···	0.34	0.500 ± 0.002	0.633 ± 0.081	$(1.883 \pm 0.446) \times 10^{-6}$	···
J123654.12+621737.8	189.2255	62.2938	···	0.38	0.537 ± 0.024	0.670 ± 0.068	$(1.691 \pm 0.383) \times 10^{-6}$	···
J123701.67+621814.4	189.2570	62.3040	···	0.44	0.472 ± 0.069	0.752 ± 0.049	$(1.025 \pm 0.234) \times 10^{-6}$	···
J123726.54+621826.3	189.3606	62.3073	···	0.44	0.555 ± 0.048	0.531 ± 0.093	$(1.803 \pm 0.293) \times 10^{-6}$	···
J123630.86+621433.5	189.1286	62.2426	···	0.44	0.497 ± 0.045	0.595 ± 0.086	$(1.239 \pm 0.214) \times 10^{-6}$	···
J123743.50+621631.7	189.4312	62.2755	···	0.44	0.212 ± 0.137	0.886 ± 0.046	$(1.635 \pm 0.238) \times 10^{-6}$	···
J123654.16+620821.4	189.2257	62.1393	···	0.45	0.282 ± 0.005	0.804 ± 0.048	$(2.716 \pm 0.731) \times 10^{-7}$	···
J123653.60+622111.6	189.2233	62.3532	···	0.47	0.231 ± 0.095	0.892 ± 0.063	$(2.570 \pm 0.378) \times 10^{-6}$	···
···	···	···	···	···	···	···	···	···
NGC 0024	2.4829	−24.9653	8.20	···	0.389 ± 0.025	0.670 ± 0.090	$(1.686 \pm 0.207) \times 10^{-7}$	···
NGC 0337	14.9613	−7.5789	19.30	···	0.647 ± 0.057	0.378 ± 0.096	$(1.088 \pm 0.084) \times 10^{-6}$	···
NGC 0628	24.1767	15.7864	7.20	···	0.944 ± 0.085	0.123 ± 0.080	$(1.170 \pm 0.117) \times 10^{-6}$	···
NGC 0925	36.8067	33.5844	9.12	···	0.537 ± 0.038	0.498 ± 0.085	$(1.196 \pm 0.113) \times 10^{-6}$	···
NGC 2403	114.2296	65.5928	3.50	···	0.505 ± 0.042	0.542 ± 0.079	$(8.678 \pm 0.928) \times 10^{-7}$	···
···	···	···	···	···	···	···	···	···

Notes – The full version of this table contains 20 columns of information for all galaxies in our CANDELS and SINGS/KINGFISH samples. An abbreviated version of the table is displayed here to illustrate its form and content. Col.(1): Adopted galaxy designation. Col.(2): Right ascension in J2000. Col.(3): Declination in J2000. Col.(4): Adopted distance (only for SINGS/KINGFISH sample). Col.(5): Adopted spectroscopic redshift (only for CANDELS sample). Col.(6): Measured axis ratio. Col.(7): Inclination derived from `Lightning`. Col.(8): Attenuated model rest-frame FUV-band luminosity in terms of L_ν. Col.(9): FUV-band attenuation. Col.(10): Attenuated model rest-frame NUV-band luminosity in terms of L_ν. Col.(11): NUV-band attenuation. Col.(12): Attenuated model rest-frame WFC3/F275W-band luminosity in terms of L_ν. Col.(13): WFC3/F275W-band attenuation. Col.(14-17): Attenuated model rest-frame J, H, K, and 3.6-band luminosities in terms of L_ν, respectively. Col.(18): Total integrated infrared luminosity. Col.(19): Total stellar mass. Col.(20): Recent star formation rate of last 100 Myr. (This table is available in its entirety in machine-readable form.)

our sample, as they had a statistically insignificant impact on our results.

To derive $a_{\rm corr}$ (see Equation 4.2), we utilized the attenuated and unattenuated rest-frame model FUV luminosities along with the model $L_{\rm TIR}$. After converting the FUV luminosities to monochromatic luminosities (i.e., νL_ν), $a_{\rm corr}$ was calculated following Equation 4.2. Figure 4.3 shows how $a_{\rm corr}$ varies with inclination. Typically, as inclination increases from face-on to edge-on, the value

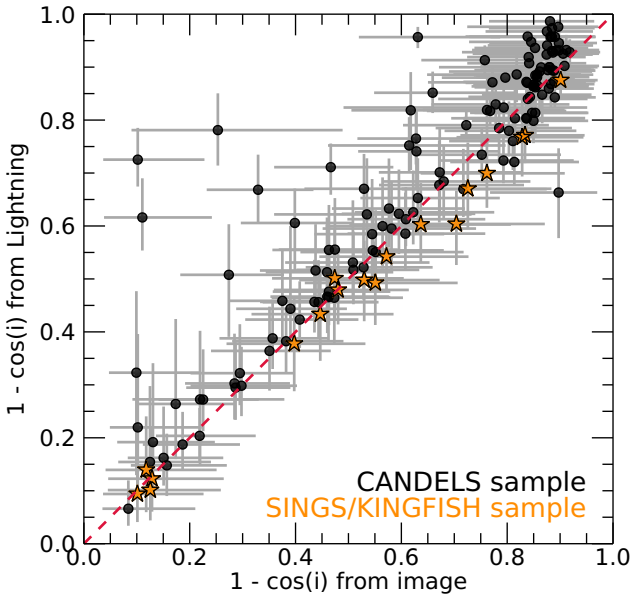

Figure 4.2: Inclinations derived from `Lightning` vs. the image-based inclinations derived from the axis ratio using the Monte Carlo method of Doore et al. (2021). The black circles are the inclination estimates for the CANDELS sample of galaxies, and the orange stars are the inclination estimates for the local SINGS/KINGFISH sample of galaxies. All of the SINGS/KINGFISH inclinations and the vast majority of CANDELS inclinations fall along the one-to-one line, indicating that the image-based inclination priors are informative.

of $a_{\rm corr}$ increases as expected. However, edge-on galaxies have a broad range of $a_{\rm corr}$ values, with some having lower $a_{\rm corr}$ values compared to face-on galaxies. As will be discussed in Section 4.4.1, this variation at high inclinations is correlated to the variation in each galaxy's physical properties, specifically the specific SFR (sSFR; defined as the SFR divided by stellar mass).

Following the procedures of past studies, where observations in only two UV bands are typically available, we derive the UV slope β from

$$\beta = \frac{\log_{10}(L_{\nu,1}/L_{\nu,2})}{\log_{10}(\lambda_1/\lambda_2)} - 2, \tag{4.5}$$

where L_ν is the attenuated rest-frame model luminosities for two UV bandpasses[5], and λ is the corresponding central wavelength of the bandpasses. To calculate β_0, the attenuated rest-frame

[5]For observations, the fluxes (F_ν) can simply be swapped for the luminosities, since isotropic luminosities have the property of $L_\nu \propto F_\nu$.

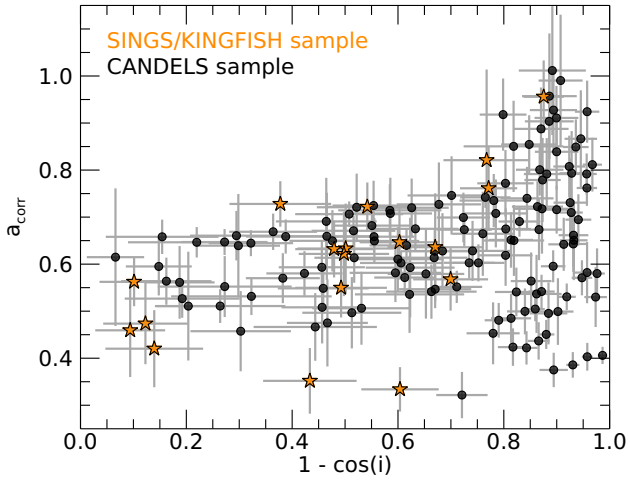

Figure 4.3: Inclinations derived from `Lightning` vs. $a_{\rm corr}$. The black circles represent the CANDELS sample of galaxies, and the orange stars represent the local SINGS/KINGFISH sample of galaxies. As inclination increases from face-on to edge-on, the value of $a_{\rm corr}$ tends to increase as expected. However, edge-on galaxies have a wider variation compared to face-on galaxies due to the variation in each galaxy's physical properties.

model luminosities in Equation 4.5 can simply be swapped for the unattenuated rest-frame model luminosities, since β_0 is an intrinsic, dust-free property.

To derive a_β, we substituted Equation 4.5 for both β and β_0 into Equation 4.3 along with $A_\lambda = -2.5\log_{10}(L_\nu/L_{\nu,0})$. For the FUV-band attenuation ($A_{\rm FUV}$), this gives

$$a_\beta = \frac{A_{\rm FUV}\log_{10}(\lambda_1/\lambda_2)}{0.4(A_{\lambda,2}-A_{\lambda,1})}, \tag{4.6}$$

where $A_{\lambda,i}$ is the attenuation for the ith UV bandpass at λ_i in Equation 4.5. From Equation 4.6, a_β can be seen to depend primarily on the attenuation curve, but it additionally depends on the choice of UV bandpasses. This same UV bandpass dependence is also present in Equation 4.5 for β (and similarly β_0), and it can have a significant impact on the derived values of both β and a_β. For example, if one of the selected UV bandpasses contains the rest-frame 2175 Å bump feature, which is present in our attenuation curves, then the measurements of β will be biased to smaller,

more negative values (Burgarella et al., 2005; Boquien et al., 2009; Conroy et al., 2010; Wild et al., 2011; Kriek & Conroy, 2013; Battisti et al., 2017; Popping et al., 2017; Tress et al., 2018) and a_β to larger values.

Since rest-frame observations that avoid the UV bump are not always available, we calculated two sets of values for β, β_0, and a_β via Equations 4.5 and 4.6. The first set includes the rest-frame model GALEX FUV ($\lambda = 1530$ Å) and near-UV (NUV; $\lambda = 2260$ Å) bandpasses, with the NUV bandpass overlapping with the UV bump. This set and subsequent relations derived in Section 4.4.2 will be more applicable to galaxies that have observational bands that contain the rest-frame UV bump feature (~ 2175 Å). As for the second set, we used the rest-frame model GALEX FUV and HST WFC3/F275W ($\lambda = 2690$ Å) bandpasses, both of which avoid the bump feature. The choice of the WFC3/F275W band is motivated by Popping et al. (2017), who showed that the WFC3/F275W band has minimal overlap with the UV bump, and, when used in combination with the GALEX FUV, calculated values of β are minimally impacted by the UV bump feature. Therefore, this set will be applicable to galaxies whose observations are relatively free of any bump feature contamination.

Figure 4.4 shows $A_{\rm FUV}$ (derived from the SED fits) versus both sets of β for the galaxies in our sample, with each galaxy being colored by its inclination derived from `Lightning`. The values of β in the left panel, which were derived from Equation 4.5 using the FUV and NUV bands, can be seen to be more negative than those in the right panel, which were derived with the FUV and F275W bands. Additionally, a clear inclination dependence can be seen in $A_{\rm FUV}$ for a fixed value of β. This variation with inclination is caused by a_β, the shape of the attenuation curve, being inclination-dependent.

Figure 4.5 shows how the two sets of a_β vary with inclination. The orange circles and stars rep-

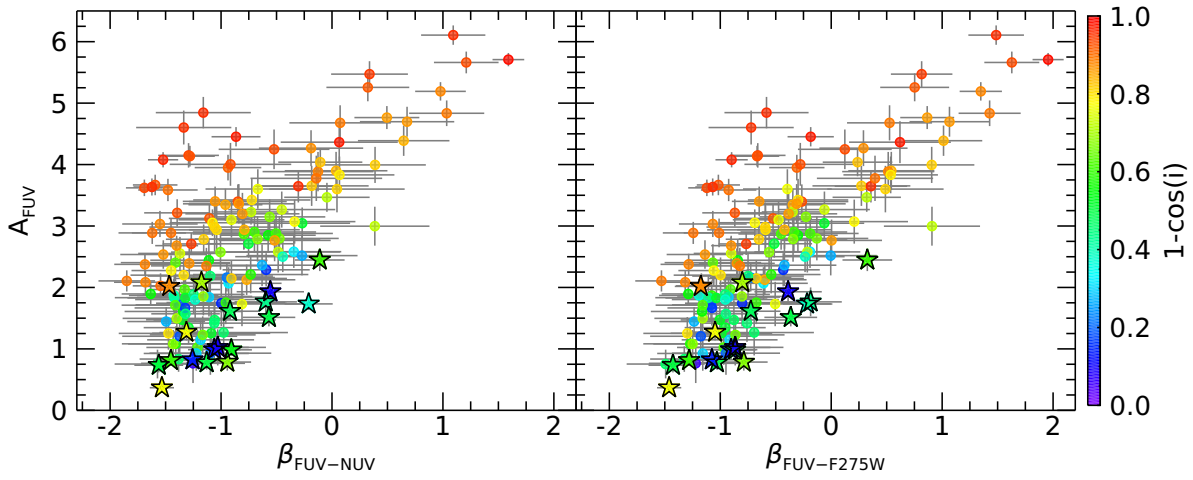

Figure 4.4: Shown is $A_{\rm FUV}$ vs. β for the galaxies in our sample, with the right panel β being calculated using the rest-frame model FUV and NUV bands ($\beta_{\rm FUV-NUV}$), and the left panel β being calculated using the rest-frame model FUV and F275W bands ($\beta_{\rm FUV-F275W}$). The circles are the galaxies in the CANDELS sample, and the stars are the galaxies in the SINGS/KINGFISH sample. Both are colored based on their inclination as derived by `Lightning`. A clear transition can be seen in $A_{\rm FUV}$ as inclination increases for a fixed value of β.

resent the CANDELS and SINGS/KINGFISH sample of galaxies, respectively, whose a_β values were derived using the FUV and NUV bands. The blue circles and stars represent the CANDELS and SINGS/KINGFISH sample of galaxies, respectively, whose a_β values were derived using the FUV and F275W bands. Both sets show an expected trend of increasing with inclination, but the values of a_β derived using the NUV band can clearly be seen to have larger values compared to those using the F275W band. These larger values of a_β are due to the UV bump, the presence of which causes an increase in attenuation in the NUV. The scatter that is present in both sets of a_β values is due to other attenuation parameters (i.e., the face-on optical depth in the B band, τ_B^f, and the galaxy clumpiness factor, F) influencing the value of a_β. The value of τ_B^f can also affect the strength of the UV bump, which causes larger scatter by approximately a factor of 2 at all inclinations in the values of a_β derived using the NUV band compared to those using the F275W band.

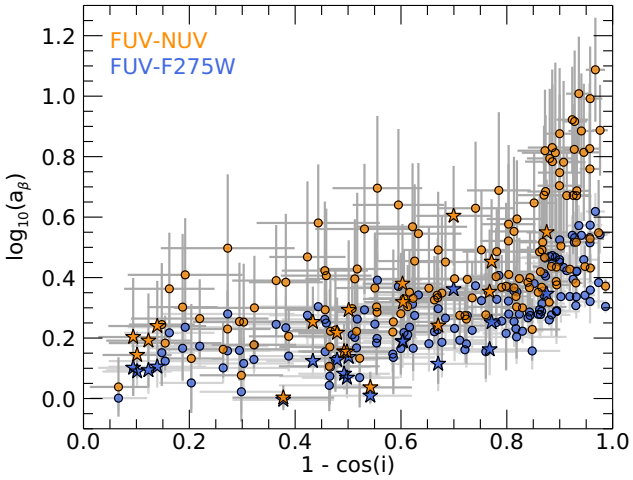

Figure 4.5: Inclinations derived from `Lightning` vs. a_β. The orange circles and stars represent the CANDELS and SINGS/KINGFISH samples of galaxies, respectively, whose a_β values were derived using the rest-frame model FUV and NUV bands. The blue circles and stars represent the CANDELS and SINGS/KINGFISH samples of galaxies, respectively, whose a_β values were derived using the rest-frame model FUV and F275W bands. The difference between sets of a_β values is due to the NUV band being contaminated by the 2175 Å bump feature, which biases a_β to higher values. The scatter that is present in both sets of a_β values is due to other attenuation parameters besides inclination influencing the value of a_β.

4.3.3 Simulated Data

As can be inferred from Figures 4.1, 4.2, 4.3, and 4.5, our sample of galaxies does not have an expected randomly selected distribution in inclination (uniform in $1-\cos i$ space), instead having more highly inclined galaxies compared to nearly face-on galaxies. This bias is due to the visual inspection process in our sample selection, since edge-on galaxies are less likely to be confused for irregular galaxies compared to face-on spirals. To more fully sample inclination space and better quantify inclination-dependent trends in $a_{\rm corr}$ and the $A_{\rm FUV}$–β relation in Sections 4.4.1.2 and 4.4.2.2, respectively, we simulated how all galaxies in our sample would appear if observed over a full range of possible inclinations. To achieve this, we used our solutions for the SFHs of our galaxies, along with our inclination-dependent attenuation curves, to construct emergent rest-

frame SEDs of our galaxies across a grid of inclinations. Thus, these simulated models allow for our sample's variety of SFHs to be available at all inclinations, rather than the SFHs being limited to the corresponding measured inclination of each galaxy.

To generate the simulated data for a given galaxy, we utilized the output parameter distributions (i.e., the resulting 5000 element Markov chain of each parameter) of the SED fitting. For a given element in the chain, all parameters excluding inclination were fixed, and attenuated rest-frame models were generated for a grid of inclinations (0–1 in steps of 0.01 in $\cos i$ space). From these attenuated models, the necessary physical properties for our study (e.g., $L_{\rm FUV}$, $A_{\rm FUV}$, $a_{\rm corr}$, β, etc.) were derived and recorded. This process was performed for all 5000 elements in the chain and, subsequently, each galaxy in the sample. Therefore, the simulated data set for a given physical property consists of a unique distribution for each galaxy in our sample at each inclination grid point. We note that, since inclination only affects attenuation, the unattenuated stellar models did not need to be simulated, as they would be the same at all inclinations.

An example of the simulated data for the randomly selected SINGS/KINGFISH galaxy NGC 3184 is displayed in Figure 4.6. For both panels, the background rainbow image is the averaged inclination of the simulated data points contained within each pixel. These images show how the distribution of each parameter changes as inclination is varied from face-on to edge-on, with the solid (dashed) black lines showing the median (1σ spread) of each parameter distribution for each inclination grid point. The left panel shows a clear transition to larger values of $a_{\rm corr}$ and rest-frame FUV–H color (the reason for using color is discussed in Section 4.4.1.1) as inclination increases. As for the right panel, which shows $A_{\rm FUV}$ versus β, $A_{\rm FUV}$ transitions to large values with inclination as expected. While β, calculated from the rest-frame FUV and NUV bands, does increase in value with inclination, this transition is minor compared to its spread.

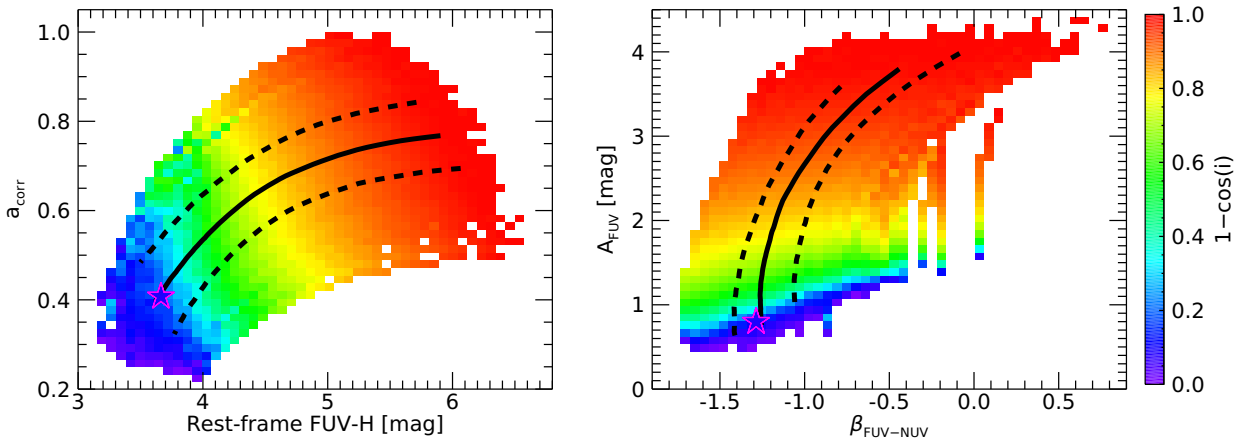

Figure 4.6: (Left) $a_{\rm corr}$ vs. rest-frame model FUV–H color. (Right) $A_{\rm FUV}$ vs. β calculated using the rest-frame model FUV and NUV bands ($\beta_{\rm FUV-NUV}$). Each panel shows the simulated data for NGC 3184. The rainbow background image in each panel is the averaged inclination of the simulated data points contained within each pixel. The solid (dashed) black lines show the median (1σ spread) of each parameter distribution for each inclination grid point, and the magenta star is the best-fit data point from the original parameter distribution chains. In each panel, the rainbow transition indicates how each parameter changes in parameter space with inclination.

4.4 Analysis and Discussion

4.4.1 Inclination Dependence of $a_{\rm corr}$ in Hybrid SFR Estimators

4.4.1.1 Influence of Inclination and SFH

Besides being dependent on inclination and other attenuation properties, the value of $a_{\rm corr}$ for a given galaxy is also dependent on the underlying stellar population or SFH (Leja et al., 2021). While the FUV emission primarily samples young massive stars with stellar lifetimes < 100 Myr, the $L_{\rm TIR}$ samples the entire radiation field that is absorbed by dust, which is generated by stars of all stellar ages. Therefore, based on Equation 4.2, if we were to fix the attenuation and the luminosity of the young population (the FUV emission) while increasing the luminosity of the old population (the optical–to–near-IR, NIR, emission), we would expect $a_{\rm corr}$ to decrease in response, since $L_{\rm TIR}$ can be significantly impacted by the old stellar population (Kennicutt et al., 2009). Alternatively,

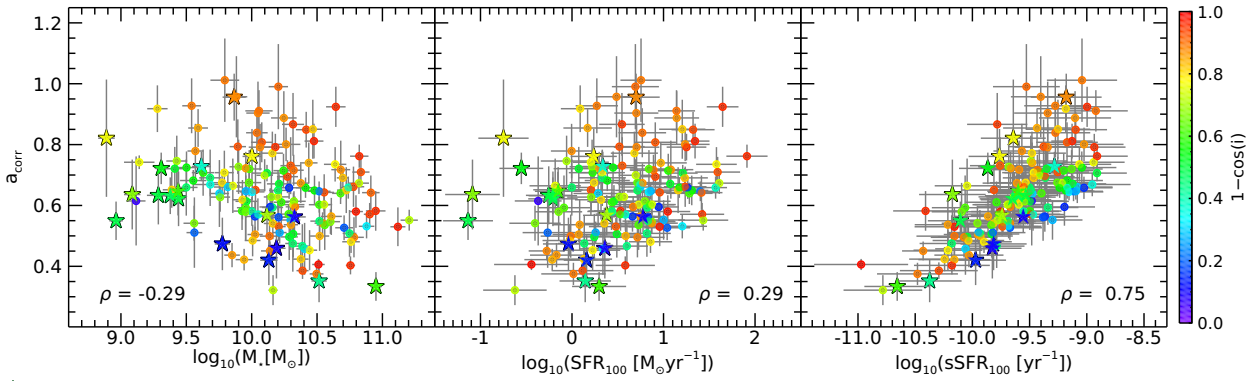

Figure 4.7: Each panel shows $a_{\rm corr}$ vs. a different physical property for the galaxies in our sample. Each galaxy is colored based on its median inclination as derived by `Lightning`. The circles are the CANDELS sample of galaxies, while the stars are the SINGS/KINGFISH sample. The Spearman correlation coefficient of each property vs. $a_{\rm corr}$ is shown in a lower corner of each panel. (Left) $a_{\rm corr}$ vs. total stellar mass ($M_\star$). The slight negative trend indicates that larger galaxies, which may have larger older populations, tend to have smaller values of $a_{\rm corr}$, with no clear trend with inclination. (Middle) $a_{\rm corr}$ vs. SFR averaged over the last 100 Myr (SFR$_{100}$). The slight positive trend indicates that galaxies with younger populations tend to have larger values of $a_{\rm corr}$, with no clear trend with inclination. (Right) $a_{\rm corr}$ vs. sSFR averaged over the last 100 Myr (sSFR$_{100}$). For a fixed sSFR$_{100}$, galaxies that are more inclined typically have larger values of $a_{\rm corr}$.

if the $L_{\rm TIR}$ was fixed instead, we would expect $a_{\rm corr}$ to increase with an increase in the young FUV emitting population.

These trends with $a_{\rm corr}$ for our sample of galaxies can be seen in Figure 4.7, which shows $a_{\rm corr}$ versus the total stellar mass ($M_\star$), the SFR averaged over the last 100 Myr (SFR$_{100}$), and the sSFR averaged over the last 100 Myr (sSFR$_{100} \equiv$ SFR$_{100}/M_\star$). The total stellar mass is typically dominated by old stars, and $a_{\rm corr}$ can be seen to generally decrease with increasing $M_\star$, with a Spearman correlation coefficient of $\rho = -0.29$. As for SFR$_{100}$, which is dominated by the young population, $a_{\rm corr}$ can be seen to generally increase with increasing SFR$_{100}$ ($\rho = 0.29$). However, these trends are both relatively weak, since $M_\star$ and SFR$_{100}$ are usually highly correlated. A better measure of the underlying stellar population, besides the SFH itself, would be the sSFR$_{100}$. Its trend with $a_{\rm corr}$ can be seen to be strong ($\rho = 0.75$) and highly significant (p-value $< 10^{-25}$).

This same trend between $a_{\rm corr}$ and $\rm sSFR_{100}$, ignoring inclination, was also found in several previous studies (e.g., Eufrasio et al., 2014,0; Boquien et al., 2016; Leja et al., 2021). Notably, Boquien et al. (2016) found a similarly strong trend in their sample of eight galaxies from KINGFISH. However, their sample was selected to exclude highly inclined galaxies ($1-\cos i < 0.5$), which minimizes the inclination-dependent attenuation effects on $a_{\rm corr}$ seen in Figure 4.3. As can be seen in the right panel of Figure 4.7, $a_{\rm corr}$ typically takes on a larger value as inclination increases for a fixed $\rm sSFR_{100}$. Therefore, any parameterization of $a_{\rm corr}$ must depend on both inclination and the $\rm sSFR_{100}$.

As noted in Boquien et al. (2016), a parameterization of $a_{\rm corr}$ with $\rm sSFR_{100}$ would not be a practical solution, as $\rm sSFR_{100}$ is a derived physical property rather than an observed quantity. Therefore, we utilized rest-frame FUV–NIR colors as in Boquien et al. (2016) instead of $\rm sSFR_{100}$, since FUV–NIR colors are observable quantities and have been shown to be good tracers of $\rm sSFR_{100}$ (Salim et al., 2005; Boquien et al., 2016). Figure 4.8 shows $a_{\rm corr}$ versus the rest-frame model FUV–J, FUV–K, FUV–H, and FUV–3.6 μm colors for the galaxies in our sample, where J, H, and K are the 2MASS J, H, and Ks bandpasses, and 3.6 μm is the Spitzer/IRAC 3.6 μm bandpass. In each panel of the figure, a clear stratification can be seen in the $a_{\rm corr}$–color space, where high-inclination galaxies ($1-\cos i \gtrsim 0.6$) populate regions of higher $a_{\rm corr}$ and FUV–NIR color compared to low-inclination galaxies ($1-\cos i \lesssim 0.6$). This striking trend can also be seen clearly in the simulated data in the left panel of Figure 4.6. In both the simulated data and Figure 4.8, the stratification of $a_{\rm corr}$ and FUV–NIR color with inclination is more pronounced at higher inclinations compared to lower inclinations due to the attenuation effects of inclination becoming more significant for inclinations of $1-\cos i \gtrsim 0.6$ (Chevallard et al., 2013; Doore et al., 2021; Zuckerman et al., 2021).

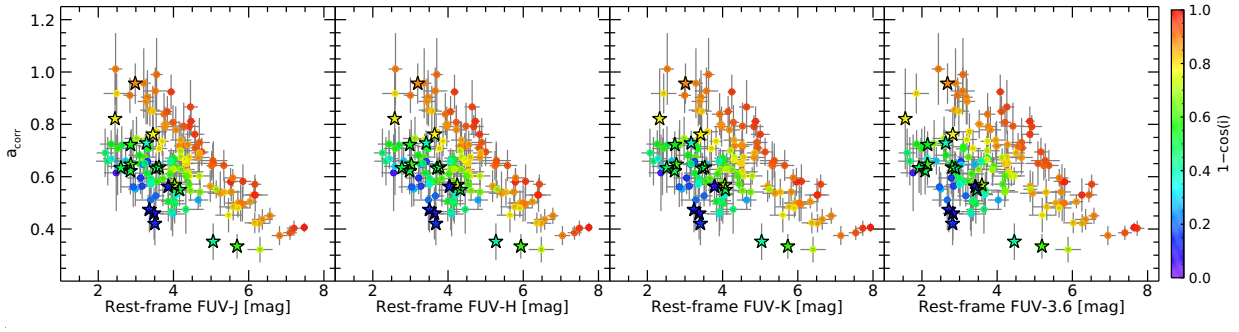

Figure 4.8: Each panel shows $a_{\rm corr}$ vs. a rest-frame model FUV–NIR color (FUV–J, FUV–H, FUV–K, FUV–3.6 μm from left to right) for the galaxies in our sample. Each galaxy is colored based on its median inclination as derived by `Lightning`. The circles are the CANDELS sample of galaxies, while the stars are the SINGS/KINGFISH sample. In all panels, a clear stratification can be seen in $a_{\rm corr}$–color space for galaxies of different inclinations.

4.4.1.2 Relation between $a_{\rm corr}$ and Inclination

Following the observed trends in Figure 4.8, we parameterized $a_{\rm corr}$ as a linear function of rest-frame FUV–NIR color for a given inclination using the functional form of

$$a_{\rm corr} = b + m \times ({\rm FUV} - {\rm NIR}), \tag{4.7}$$

where the linear coefficients b and m are both functions of inclination and unique to each FUV–NIR color. To derive these coefficients, we utilized our simulated data distributions described in Section 4.3.3, since using the data shown in Figure 4.8 would result in a sparse population of inclination–$a_{\rm corr}$–color space. The simulated data increased the amount of data at each inclination, since each galaxy was simulated for a grid of viewing angles.

For each inclination grid point of the simulated data, we used the median of the distributions of $a_{\rm corr}$ and FUV–NIR color of each galaxy (e.g., the solid black line in the left panel of Figure 4.6) as data points and fitted the linear relationship of Equation 4.7 to these median values. The corresponding standard deviations of the $a_{\rm corr}$ and FUV–NIR color distributions were included as uncertainties during the fitting process. The fitting was repeated for each inclination grid point,

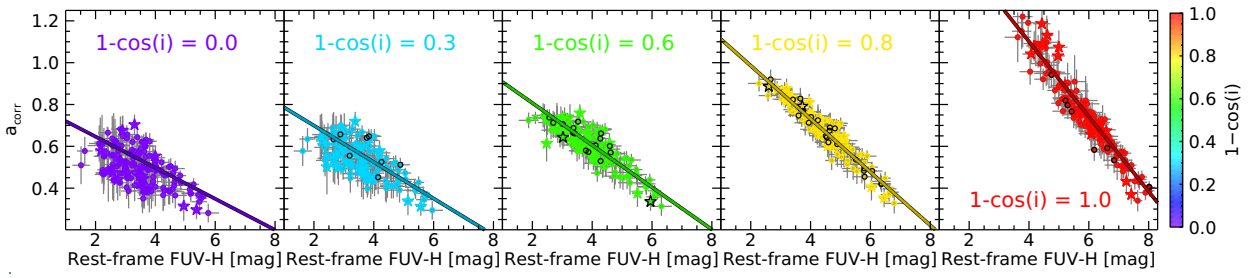

Figure 4.9: Each panel shows $a_{\rm corr}$ vs. rest-frame FUV–H color for our simulated data for a span of inclination grid points, with the data in each panel being colored based on their inclination grid value ($1-\cos i = [0.0, 0.3, 0.6, 0.8, 1.0]$, from left to right). The circles are the CANDELS sample of galaxies, while the stars are the SINGS/KINGFISH sample. Points outlined in black indicate galaxies whose measured inclinations, in terms of $1-\cos i$, are within ± 0.05 of the grid value. Each panel can be considered how the sample would appear if all galaxies were viewed from the respective inclination. The best-fit linear relation to the simulated data is shown in each panel. As inclination is increased from face-on to edge-on, the slope and intercept of the best-fit linear relations can be seen to decrease and increase, respectively.

resulting in derived b and m values with corresponding uncertainties at each of the inclination grid points. An example of this process can be seen in Figure 4.9, which shows the simulated data and best-fit $a_{\rm corr}$ versus FUV–NIR color relation at various inclination grid points. From the figure, the slope and intercept of the linear relation can be seen to decrease and increase with inclination, respectively. These resulting trends in b and m versus inclination can be more clearly seen in Figure 4.10 for each FUV–NIR color. For each color, the linear coefficients show very similar trends, with more rapid changes in value occurring at high inclinations ($1-\cos i > 0.7$), where the attenuation effects of inclination become more significant.

To account for the variation in b and m with inclination, we fitted polynomials to the derived b and m values utilizing their corresponding uncertainties. The degree of the polynomial was selected by minimizing the Akaike information criterion (AIC). For all FUV–NIR colors, this resulted in fourth- and third-order polynomials being chosen for the b and m parameters, respectively.

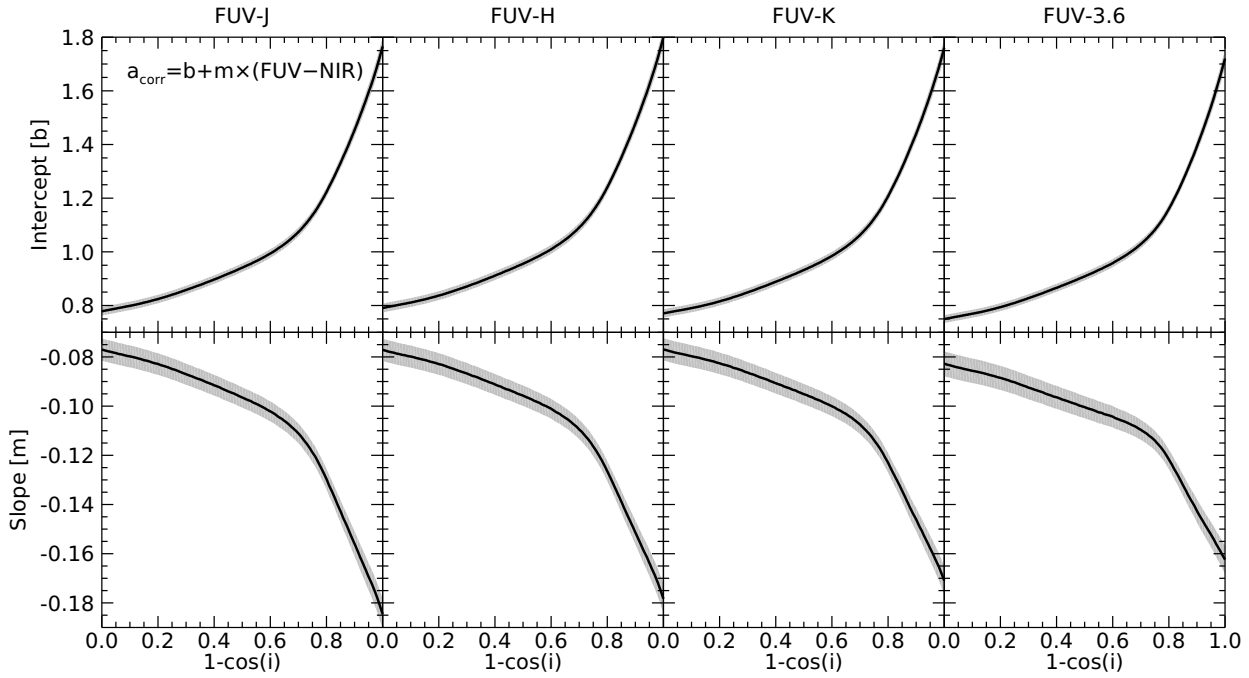

Figure 4.10: Linear coefficients for Equation 4.7 vs. inclination for the four rest-frame FUV–NIR colors. The black line shows the derived values at each inclination, with the gray shaded region giving the derived uncertainties.

Incorporating this inclination dependence on b and m, Equation 4.7 can be rewritten as

$$a_{\rm corr} = \sum_{n=0}^{4} b_n (1-\cos i)^n + \sum_{n=0}^{3} m_n (1-\cos i)^n \times ({\rm FUV}-{\rm NIR}), \tag{4.8}$$

where b_n and m_n are the polynomial coefficients of b and m, which can be found in Table 4.3 along with their corresponding uncertainty for each FUV–NIR color. Therefore, Equation 4.8 gives a parametric estimation of $a_{\rm corr}$ that only depends on the observable quantities of FUV–NIR color and inclination, allowing for an easy-to-use inclination-dependent hybrid SFR estimator.

Table 4.3: Polynomial Coefficients to estimate $a_{\rm corr}$ as a function of inclination and rest-frame FUV–NIR color via Equation 4.8.

	Polynomial Coefficients for Intercept b				
Color	b_0	b_1	b_2	b_3	b_4
FUV–J	0.7820 ± 0.0075	0.0298 ± 0.1090	1.4679 ± 0.4645	-3.1348 ± 0.7284	2.6395 ± 0.3762
FUV–H	0.7950 ± 0.0078	0.0081 ± 0.1137	1.6177 ± 0.4840	-3.4210 ± 0.7578	2.8188 ± 0.3908
FUV–K	0.7759 ± 0.0073	-0.0248 ± 0.1065	1.7531 ± 0.4544	-3.6430 ± 0.7130	2.9165 ± 0.3684
FUV–3.6	0.7579 ± 0.0070	-0.1099 ± 0.1022	2.2370 ± 0.4365	-4.5584 ± 0.6857	3.4086 ± 0.3548
	Polynomial Coefficients for Slope m				
Color	m_0	m_1	m_2	m_3	
FUV–J	-0.0741 ± 0.0017	-0.0819 ± 0.0149	0.1931 ± 0.0351	-0.2230 ± 0.0235	
FUV–H	-0.0743 ± 0.0017	-0.0797 ± 0.0149	0.1865 ± 0.0349	-0.2118 ± 0.0232	
FUV–K	-0.0742 ± 0.0017	-0.0774 ± 0.0148	0.1770 ± 0.0345	-0.1974 ± 0.0229	
FUV–3.6	-0.0797 ± 0.0019	-0.0832 ± 0.0161	0.1835 ± 0.0371	-0.1847 ± 0.0244	

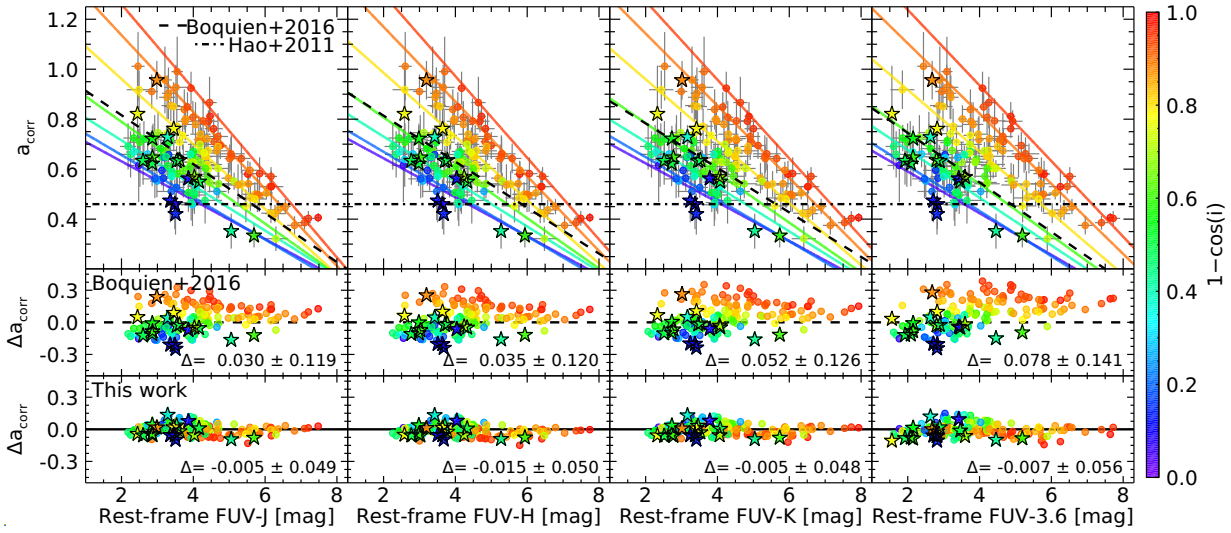

Figure 4.11: In all panels, the circles are the CANDELS sample of galaxies, while the stars are the SINGS/KINGFISH sample. Each galaxy is colored based on its median inclination as derived by `Lightning`. (Upper row) Each panel shows $a_{\rm corr}$ vs. a rest-frame model FUV–NIR color (FUV–J, FUV–H, FUV–K, FUV–3.6 μm from left to right) for the galaxies in our sample. The parametric estimation of $a_{\rm corr}$ from this study is shown as the solid colored lines, with the color indicating the inclination used in the calculation ($1-\cos i = [0.05, 0.2, 0.4, 0.6, 0.8, 0.9, 0.95]$). The dashed-dotted and dashed lines are the $a_{\rm corr}$ value from Hao et al. (2011) and $a_{\rm corr}$–color relation from Boquien et al. (2016), respectively, for the FUV and $L_{\rm TIR}$. (Middle row) Difference between $a_{\rm corr}$ derived from `Lightning` and $a_{\rm corr}$ derived from the Boquien et al. (2016) relation vs. an FUV–NIR color. The delta in the lower right corner is the mean and standard deviation of $\Delta a_{\rm corr}$ (i.e., the mean and scatter of the residuals). (Lower row) The difference between $a_{\rm corr}$ derived from `Lightning` and $a_{\rm corr}$ derived from the parametric relation in this work vs. an FUV–NIR color. The delta in the lower right corner is the mean and standard deviation of $\Delta a_{\rm corr}$.

4.4.1.3 Comparison with Past Studies

The parametric estimation of $a_{\rm corr}$ as a function of inclination and rest-frame FUV–NIR color can be seen in the upper row of Figure 4.11. This upper row is the same as Figure 4.8, but it now includes the parametric estimation of $a_{\rm corr}$ from Equation 4.8 as the solid colored lines, with the color indicating the inclination used in the calculation. Additionally, the corresponding $a_{\rm corr}$ value from Hao et al. (2011) and $a_{\rm corr}$–color relation from Boquien et al. (2016) for the FUV and $L_{\rm TIR}$ are shown as the dashed-dotted and dashed lines, respectively. From this upper row, it can be seen that the value of $a_{\rm corr}$ from Hao et al. (2011) is much lower than the derived $a_{\rm corr}$ values for the vast majority of our galaxies. This discrepancy is caused by the differences in the utilized galaxy samples. Hao et al. (2011) used a sample of galaxies including both late- and early-type galaxies, where we selected only late-type, star-forming galaxies. Therefore, our sample will, on average, have galaxies with higher sSFR, which will correspondingly result in larger values of $a_{\rm corr}$.

As for the Boquien et al. (2016) $a_{\rm corr}$–color relation, the upper row of panels shows near agreement with our parameterization for $1-\cos i \approx 0.6$ ($i \approx 66^\circ$). This coinciding inclination supports our methodology, since the majority of the Boquien et al. (2016) galaxy sample had $i = 50^\circ$–60°. In the bottom two rows of Figure 4.11, we show residuals of $a_{\rm corr}$ ($\Delta a_{\rm corr}$; the difference between $a_{\rm corr}$ derived from `Lightning` and $a_{\rm corr}$ derived from the Boquien et al. 2016 relation or the parametric relation in this work) versus FUV–NIR color. From these panels, it can be seen that the Boquien et al. (2016) relation, on average, is consistent with our data but results in large scatter that has a clear inclination dependence, with more face-on galaxies typically having their $a_{\rm corr}$ overestimated and more edge-on galaxies having their $a_{\rm corr}$ underestimated. However, the parameterization in this work results in residuals that have a scatter that is less than half that from the Boquien et al.

(2016) relation and no inclination dependence, implying that the effects of inclination are being properly accounted for in our relation. Therefore, our parameterization is the first, to our knowledge, that accounts for both the effects of SFH and inclination that are expected to be present when determining $a_{\rm corr}$. We note, however, that the $a_{\rm corr}$ relation presented above has a specific range of applicability and a few caveats, which are discussed in Section 4.4.3.

4.4.2 Inclination Dependence of the $A_{\rm FUV}$–β Relation

4.4.2.1 Influence of Inclination and SFH

Based on the definition of the $A_{\rm FUV}$–β relation used in Equation 4.3, the calibrated parameter a_β should solely depend on the choice of attenuation curve, and β_0 should only depend on the SFH of the galaxy, since we assumed a fixed metallicity and IMF. In our study, we chose to use inclination-dependent attenuation curves, which depend on three free parameters: τ_B^f (the face-on optical depth in the B band), F (the galaxy clumpiness factor), and inclination. While inclination is a quantity that can be readily determined from basic observations, τ_B^f and F are intrinsic properties that can only be derived from modeling. Therefore, our parameterization of a_β can only be a function of inclination, since it is the only observable property, and any scatter in the parameterization will be due to the variation in other attenuation parameters at a given inclination.

As for β_0, in theory, its value will be unique for each galaxy, since it is dependent on the SFH. However, in application, a fixed value of β_0 for a sample of galaxies is generally utilized (e.g., Meurer et al., 1999; Overzier et al., 2011; Boquien et al., 2012; Wang et al., 2018), since the SFH of a galaxy is not an observable property. While the SFH could be approximated using a rest-frame FUV–NIR or a comparable color, the $A_{\rm FUV}$–β relation is typically helpful when minimal UV

observational data are available, preventing use of an SFH proxy. Therefore, we do not include any color dependence in our $A_{\rm FUV}$–β relation and note that additional scatter and potential systematic effects will be present in the relation due to not incorporating any SFH dependence on β_0.

Finally, as discussed in Section 4.3.2, a_β and β_0 will depend on the choice of UV bandpasses utilized in the calculation. While β_0 will have minimal variation from the choice of UV bandpasses due to it being a dust-free property, a_β can be biased to larger values if a chosen UV bandpass is contaminated by the 2175 Å bump feature. Therefore, in the next section, we derive two inclination-dependent $A_{\rm FUV}$–β relations using the combination of bandpasses discussed in Section 4.3.2. The first uses the combination of the GALEX FUV and NUV bands, which will suffer from UV bump contamination. The second uses the combination of the GALEX FUV and HST WFC3/F275W bands, neither of which overlap the bump feature region.

4.4.2.2 Inclination-dependent $A_{\rm FUV}$–β Relation

Since the relation between $A_{\rm FUV}$ and β given in Equation 4.3 is linear, we followed the same method as in Section 4.4.1.2 when deriving a_β and β_0 for the $A_{\rm FUV}$–β relations. This method again relied on our simulated data distributions at each inclination. For each inclination grid point of the simulated data, we utilized the median of the distributions of $A_{\rm FUV}$ and β of each galaxy (e.g., the solid black line in the right panel of Figure 4.6) as data points and fitted the linear relationship of Equation 4.3 to these data. The corresponding standard deviations of the $A_{\rm FUV}$ and β distributions were included as uncertainties during the fitting process. The fitting was repeated for each inclination grid point, resulting in derived a_β and β_0 values with corresponding uncertainties at each of the inclination grid points. An example of the process can be seen in Figure 4.12, which shows the simulated data and best-fit relation at various inclination grid points.

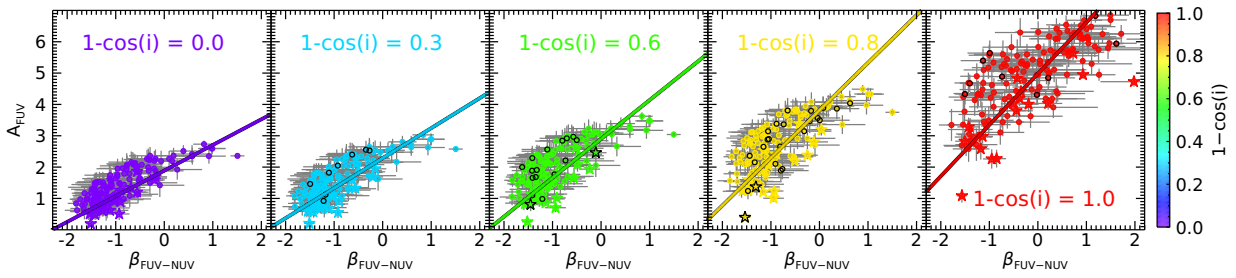

Figure 4.12: Each panel shows $A_{\rm FUV}$ vs. β, calculated from the rest-frame model FUV and NUV bands ($\beta_{\rm FUV-NUV}$), for our simulated data for a span of inclination grid points, with the data in each panel being colored based on their inclination grid value ($1-\cos i = [0.0, 0.3, 0.6, 0.8, 1.0]$, from left to right). The circles are the CANDELS sample of galaxies, while the stars are the SINGS/KINGFISH sample. Points outlined in black indicate galaxies whose measured inclinations, in terms of $1-\cos i$, are within ± 0.05 of the grid value. Each panel can be considered how the sample would appear if all galaxies were viewed from the respective inclination. The best-fit linear relation to the simulated data is shown in each panel. As inclination is increased from face-on to edge-on, the slope of the best-fit linear relation can also be seen to increase, while the β-intercept only decreases at the largest inclinations.

The resulting trends in a_β and β_0 versus inclination are shown in Figure 4.13 for the two sets of UV bandpasses used when calculating β. For both sets of bandpasses, a_β and β_0 show similar trends. As expected, a_β increases in value as inclination increases from face-on to edge-on. However, above $1-\cos i \approx 0.9$, a_β begins to decrease with increasing inclination. This decrease is correlated to the unexpected result of β_0 decreasing at $1-\cos i > 0.75$. Theoretically, β_0 is expected to be inclination-independent, since it is a dust-free property. Therefore, it should be constant as a function of inclination, and the observed decrease at high inclinations could be due to our various simplifying assumptions. For example, the SFH dependence of β_0 could be disguised as an inclination dependence at these high inclinations. Additionally, the assumption in the $A_{\rm FUV}-\beta$ relation that the UV slope is linearly related to UV attenuation could be too simplified for high-inclination galaxies.

Rather than attempting to correct for these simplifying assumptions (i.e., adding an SFH dependence, changing from a linear relation, etc.), we only add an inclination dependence to a_β and

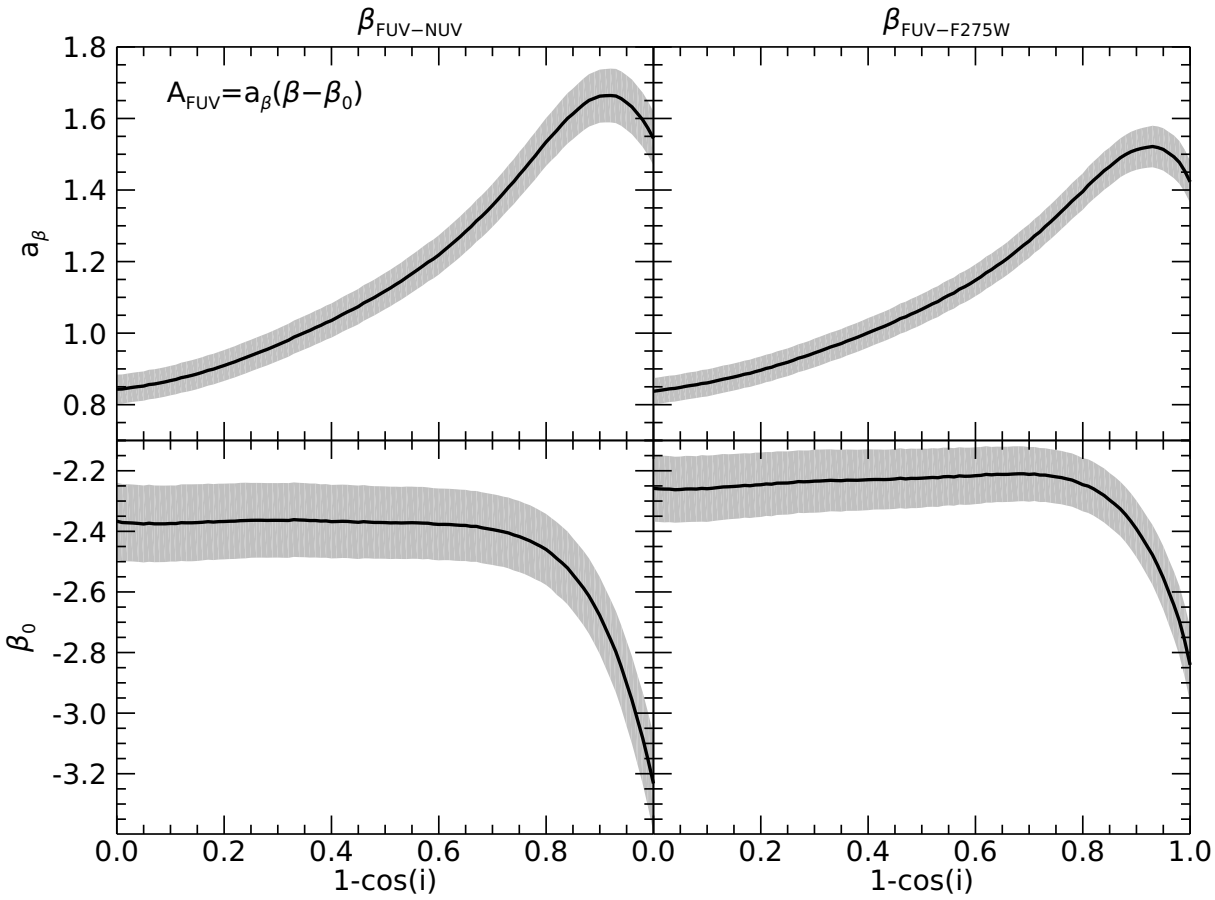

Figure 4.13: Linear coefficients, a_β and β_0, for Equation 4.3 vs. inclination for the two combinations of UV bandpasses. The black line shows the derived values at each inclination, with the gray shaded region giving the derived uncertainties.

β_0 to maintain the $A_{\rm FUV}$–β relation's simplistic format. To account for the variation in a_β and β_0 with inclination for both sets of UV bandpasses, we fitted polynomials to the corresponding a_β and β_0 values in Figure 4.13 utilizing their derived uncertainties. We selected the degree of the polynomials by minimizing the AIC. For both sets of bandpasses, this resulted in fifth- and fourth-order polynomials being chosen for a_β and β_0, respectively. Incorporating this inclination dependence

Table 4.4: Polynomial Coefficients to Estimate $A_{\rm FUV}$ as a Function of β and Inclination via Equation 4.9.

Coefficients	UV Bump FUV–NUV	No UV Bump FUV–F275W
$a_{\beta,0}$	0.8564 ± 0.0230	0.8507 ± 0.0206
$a_{\beta,1}$	-0.4759 ± 0.5065	-0.3892 ± 0.4447
$a_{\beta,2}$	7.0243 ± 3.3703	5.8447 ± 2.9072
$a_{\beta,3}$	-21.4069 ± 9.0246	-17.6998 ± 7.6714
$a_{\beta,4}$	29.5716 ± 10.3862	24.0990 ± 8.7243
$a_{\beta,5}$	-14.0028 ± 4.2785	-11.2503 ± 3.5597
$\beta_{0,0}$	-2.4084 ± 0.0596	-2.2972 ± 0.0508
$\beta_{0,1}$	0.9974 ± 0.8306	0.9985 ± 0.6937
$\beta_{0,2}$	-5.7388 ± 3.4059	-5.2784 ± 2.7990
$\beta_{0,3}$	11.5513 ± 5.1544	10.4165 ± 4.1830
$\beta_{0,4}$	-7.5682 ± 2.5757	-6.6026 ± 2.0700

on a_β and β_0, Equation 4.3 can be rewritten as

$$A_{\rm FUV} = \sum_{n=0}^{5} a_{\beta,n}(1-\cos i)^n \times \left(\beta - \sum_{n=0}^{4} \beta_{0,n}(1-\cos i)^n\right) \tag{4.9}$$

where $a_{\beta,n}$ and $\beta_{0,n}$ are the polynomial coefficients of a_β and β_0, which can be found in Table 4.4 along with their corresponding uncertainty for each set of UV bandpasses.

4.4.2.3 Comparison with Past Studies

The inclination-dependent $A_{\rm FUV}$–β relations for each set of UV bandpasses are shown in the upper row of Figure 4.14. This upper row is the same as Figure 4.3 but includes these inclination-dependent relations as the solid colored lines, with the color indicating the inclination used in the calculation. Additionally, we show different $A_{\rm FUV}$–β relations derived in past studies.

In the left column, we compare our results with the two relations derived in Overzier et al. (2011): one from their sample of Lyman break analogs (LBAs) and the other from the same sample of galaxies in Meurer et al. (1999). These relations were calibrated using the IRX–β relation,

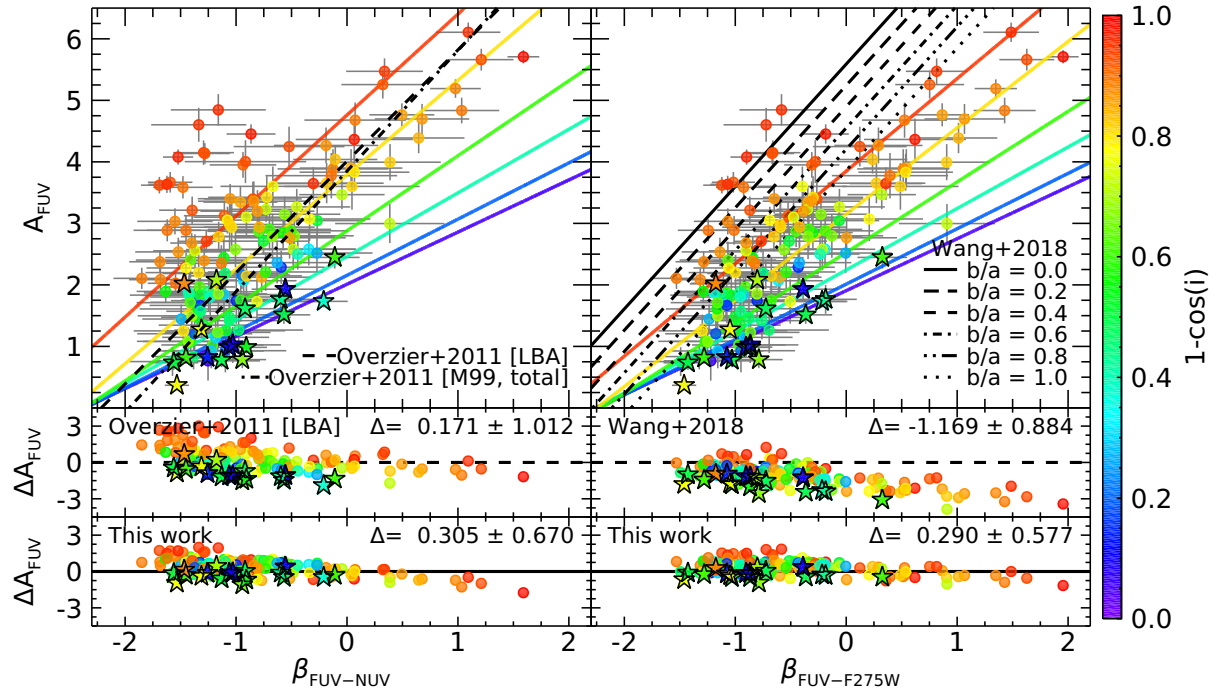

Figure 4.14: In all panels, the circles are the CANDELS sample of galaxies, while the stars are the SINGS/KINGFISH sample. Each galaxy is colored based on its median inclination as derived by `Lightning`. (Upper row) Each panel shows $A_{\rm FUV}$ vs. β calculated using the rest-frame model FUV and NUV bands ($\beta_{\rm FUV-NUV}$) and FUV and F275W bands ($\beta_{\rm FUV-F275W}$) in the left and right panels, respectively. The corresponding inclination-dependent $A_{\rm FUV}$–β relations from this study are shown as the solid colored lines, with the color indicating the inclination used in the calculation ($1-\cos i = [0.05, 0.2, 0.4, 0.6, 0.75]$). The dashed and dashed-dotted lines in the left panel are the relations from Overzier et al. (2011) for their LBA sample and the Meurer et al. (1999) sample, respectively. The black lines of changing line style in the right panel are the inclination-dependent Wang et al. (2018) relation, where each line style represents a different value of axis ratio. (Middle row) Difference between $A_{\rm FUV}$ derived from `Lightning` and $A_{\rm FUV}$ derived from the Overzier et al. (2011) LBA relation and the Wang et al. (2018) relation utilizing each galaxies' measured axis ratio on the left and right, respectively. The delta in the upper right corner is the mean and standard deviation of $\Delta A_{\rm FUV}$ (i.e., the mean and scatter of the residuals). (Lower row) Difference between $A_{\rm FUV}$ derived from `Lightning` and $A_{\rm FUV}$ derived from the inclination-dependent $A_{\rm FUV}$–β relations in this work. The delta in the upper right corner is the mean and standard deviation of $\Delta A_{\rm FUV}$.

where the β values were calculated using the GALEX FUV and NUV bands, which will share the same bias as our inclination-dependent relation calculated using these bands. We find that the LBA sample relation has a similar β_0 value ($\beta_0 = -2.22$) as that of our relation at low-to-moderate inclinations ($\beta_0 \approx -2.35$), while the Meurer et al. (1999) sample relation is significantly

higher ($\beta_0 = -1.96$). Therefore, in the middle panel of the left column, we show residuals of $A_{\rm FUV}$ ($\Delta A_{\rm FUV}$; the difference between $A_{\rm FUV}$ derived from `Lightning` and $A_{\rm FUV}$ derived from the LBA relation) versus β for the LBA relation. From this panel, it can be seen that the LBA relation from Overzier et al. (2011) has a clear inclination dependence in the residuals, with low-inclination galaxies typically having their $A_{\rm FUV}$ overestimated and high-inclination galaxies typically having theirs underestimated. However, the relation in our work results in residuals (lower left panel of Figure 4.14) with minimal inclination dependence. Also, the scatter in the residuals of our relation is smaller than the residuals of the LBA relation by a factor of $\approx$1.5, indicating that its inclination dependence is accounting for some additional variation present in the $A_{\rm FUV}$–β relation.

In the right column of Figure 4.14, we compare our results to the inclination-dependent $A_{\rm FUV}$–β relation from Wang et al. (2018), which utilized axis ratio ($q = b/a$; $q = 0$ is edge-on and $q = 1$ is face-on) rather than inclination. To briefly explain the derivation of this relation, its inclination dependence was derived by first assuming the hybrid SFR estimators are inclination-independent, and then using this assumption to correct the $A_{\rm FUV}$–β relation for inclination. This inclination correction was then added to the β_0 term, while a_β was fixed to a constant value. Also, the β values used in the derivation were calculated by fitting a power law to three observed UV photometric data points, all of which were selected to avoid the UV bump feature. Therefore, we compared this relation to our relation calculated using the FUV and F275W bands, since both relations should avoid the bias introduced by the presence of the UV bump.

The upper right panel of Figure 4.14 shows the inclination-dependent Wang et al. (2018) relation as the black lines of changing line style, where each line style represents a different value of axis ratio. From this panel, it can be seen that the Wang et al. (2018) relation overestimates $A_{\rm FUV}$ for practically all of the galaxies in our sample. This is clearly seen in the residuals for the

Wang et al. (2018) relation shown in the middle panel, where the $A_{\rm FUV}$ values from the Wang et al. (2018) relation were calculated utilizing the axis ratios of our galaxies as described in Section 4.2. The reason for this overestimation by the Wang et al. (2018) relation for our sample comes from their critical assumption that hybrid SFR estimators are inclination-independent, which this paper has shown to not be the case. Ignoring this inclination dependence in their calculation is causing overestimates of $A_{\rm FUV}$, especially at low inclinations, where the hybrid SFR estimator is likely overestimating the SFR.

4.4.3 Range of Applicability and Caveats

It is important to stress that the relations for unattenuating the FUV luminosity presented in this paper were derived from a specific sample of disk-dominated galaxies (see Section 4.2). Therefore, their use should be limited to galaxies whose physical properties fall within the range of our sample. Extrapolating their use to galaxies outside this range could result in unrealistic unattenuated luminosities. For the inclination- and color-dependent hybrid SFR estimator, the rest-frame FUV–NIR colors should be within the following ranges:

$2.18 <$ FUV–$J <$ 7.48 mag,

$2.26 <$ FUV–$H <$ 7.74 mag,

$2.07 <$ FUV–$K <$ 7.93 mag, and

$1.56 <$ FUV–3.6 $<$ 7.72 mag.

As for the inclination-dependent $A_{\rm FUV}$–β relation, β values should fall within

$-1.85 < \beta_{\rm bump} < 1.59$ and

$$-1.53 < \beta_{\text{no bump}} < 1.96$$

for galaxies that have and do not have UV bump-contaminated observations, respectively. Additionally, galaxies, as per Section 4.2, should be star-forming disk galaxies with a minimal bulge component and reside at redshifts of $z < 1$. The morphology can be determined from either visual inspection or meeting the sample selection requirement of a Seŕsic index of $n < 1.2$. Finally, the relations should not be applied to galaxies classified as having AGNs, as the AGNs could contaminate observations from the FUV to IR (Ciesla et al., 2015).

Additionally, the inclination estimates used in this study rely on the various assumptions made in Doore et al. (2021) to convert axis ratio to inclination. If alternative methods and assumptions are used, they have been shown to typically result in comparable inclination estimates. However, they tend to underestimate the uncertainty on inclination when simply propagating the axis ratio uncertainty (see Section 3 of Doore et al. 2021 for details). Therefore, the relations presented in this study will be applicable even if the inclinations are estimated from an axis ratio via a different method.

While the relations presented in this paper derive an unattenuated FUV luminosity, the actual quantity of interest is the SFR. To determine the SFR from the unattenuated FUV luminosity, a conversion factor k_{UV} (specifically, k_{FUV}) for use in Equation 4.1 must be selected. A variety of values can be theoretically determined depending on the assumed IMF, metallicity, and SFH, with a constant SFH over the last 100 Myr typically being assumed (e.g., Kennicutt, 1998; Murphy et al., 2011; Kennicutt & Evans, 2012). For our assumed IMF and metallicity, this constant SFH results in $k_{\text{FUV}} = 1.6 \times 10^{-10}$. However, while the galaxies in our sample assume the same IMF and metallicity, they each have a unique SFH, which will result in each galaxy having a unique

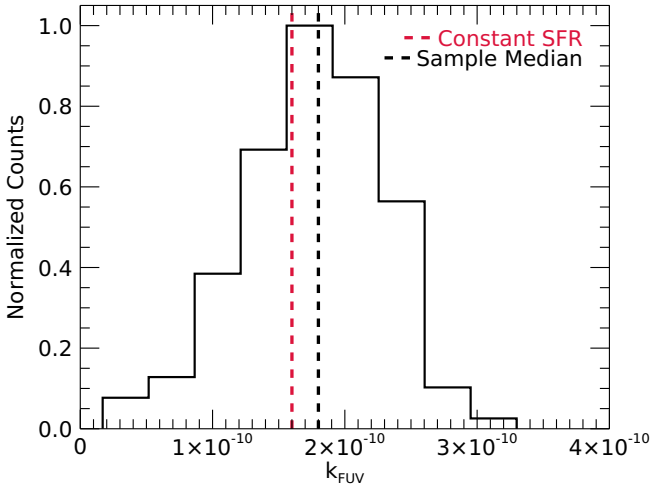

Figure 4.15: Histogram of $k_{\rm FUV}$ for the CANDELS and SINGS/KINGFISH samples. The dashed red line gives the value of $k_{\rm FUV}$ assuming a constant SFR over the last 100 Myr ($k_{\rm FUV} = 1.6 \times 10^{-10}$), and the dashed black line gives the sample median.

value of $k_{\rm FUV}$. In Figure 4.15, we show how these unique $k_{\rm FUV}$ values compare to the constant value of $k_{\rm FUV}$ assuming a constant SFH, which is shown as the dashed red line. On average, the galaxies in our sample have a higher $k_{\rm FUV}$ than this constant value but are consistent when considering the relatively large uncertainty with a sample median and standard deviation of $k_{\rm FUV} = (1.80 \pm 0.54) \times 10^{-10}$. Since $k_{\rm FUV}$ is dependent on the SFH, we investigated parameterizing $k_{\rm FUV}$ as function of FUV–NIR color. However, we found that any parameterization of $k_{\rm FUV}$ with color yielded results consistent with those for a constant value of $k_{\rm FUV}$. Therefore, we recommend using the theoretical constant value of $k_{\rm FUV} = 1.6 \times 10^{-10}$ with a propagated uncertainty of 0.54×10^{-10} when using our relations to convert FUV luminosity to SFR.

4.5 Summary

We analyzed how both hybrid SFR estimators and the $A_{\rm FUV}$–β relation depend on inclination and derived new relations to account for this inclination dependence. This analysis utilized the

inclination-dependent attenuation module in the SED fitting code `Lightning`, which was applied to a sample of 133 galaxies from the CANDELS fields along with 18 local galaxies from the SINGS/KINGFISH sample in Dale et al. (2017). All galaxies were selected to be disk-dominated via their Seŕsic index and/or a visual inspection.

For the hybrid SFR estimators, we found that the UV+IR correction factor $a_{\rm corr}$ was found to be highly dependent on the inclination of a galaxy in addition to its sSFR. Since the sSFR is not an observable quantity, a rest-frame FUV–NIR color was used as a proxy along with inclination to derive the parametric relation for $a_{\rm corr}$ given in Equation 4.8. The relation was a simple linear fit of FUV–NIR color to $a_{\rm corr}$, with the linear coefficients being polynomials of inclination. These polynomial coefficients were presented in Table 4.3 for four different FUV–NIR colors. These relations were shown to predict values of $a_{\rm corr}$ that were highly consistent with the data and properly account for any inclination dependence.

As for the $A_{\rm FUV}$–β relation, we derived two different sets of β to account for the potential contamination of observations by the rest-frame UV bump feature. The first set includes the rest-frame GALEX FUV and NUV bandpasses, with the NUV bandpass overlapping with the UV bump. The second set includes the rest-frame GALEX FUV and HST WFC3/F275W bandpasses, both of which avoid the bump feature. For both sets of β, we found that there is a definite inclination dependence with edge-on galaxies having a higher $A_{\rm FUV}$ by 1-2 mag for a given value of β compared to more face-on galaxies. To derive our inclination-dependent $A_{\rm FUV}$–β relation for each set, we fit the relation given in Equation 4.3 to our data. These fits resulted in the expected trends of an increase in a_β and a constant β_0 with inclination for $1 - \cos i \leq 0.75$. However, at higher inclinations, a_β and β_0 deviated from these expected trends, with both decreasing with increasing inclination. We attributed these deviations to various simplifying assumptions within the $A_{\rm FUV}$–β

relation. Regardless, we fitted polynomials for the full range of inclination to a_β and β_0, whose coefficients were presented in Table 4.4, and noted that the linearity of the $A_{\rm FUV}$–β relation is likely too simplified for highly inclined galaxies.

The results of this work illustrate that inclination can significantly affect the derived SFR in disk-dominated galaxies when using UV SFR tracers. We find that including an inclination dependence in these tracers is critical for more accurate SFR estimates. In future work, we plan to apply the inclination-dependent attenuation module in `Lightning` to a more complete sample of galaxies that have sizable bulge components, rather than a purely disk-dominated sample. We intend to see how the bulge component of a galaxy affects the inclination dependence of our results and check if similar relations apply to the broader disk galaxy population.

References

Arnouts, S., Le Floc'h, E., Chevallard, J., et al. 2013, A&A, 558, A67

Barro, G., Pérez-González, P. G., Cava, A., et al. 2019, ApJS, 243, 22

Battisti, A. J., Calzetti, D., & Chary, R. R. 2017, ApJ, 851, 90

Bigiel, F., Leroy, A., Walter, F., et al. 2008, AJ, 136, 2846

Boquien, M., Calzetti, D., Kennicutt, R., et al. 2009, ApJ, 706, 553

Boquien, M., Buat, V., Boselli, A., et al. 2012, A&A, 539, A145

Boquien, M., Kennicutt, R., Calzetti, D., et al. 2016, A&A, 591, A6

Bradshaw, E. J., Almaini, O., Hartley, W. G., et al. 2013, MNRAS, 433, 194

Brooks, S. P., & Gelman, A. 1998, Journal of Computational and Graphical Statistics, 7, 434

Buat, V., Noll, S., Burgarella, D., et al. 2012, A&A, 545, A141

Burgarella, D., Buat, V., & Iglesias-Páramo, J. 2005, MNRAS, 360, 1413

Calzetti, D., Kinney, A. L., & Storchi-Bergmann, T. 1994, ApJ, 429, 582

Catalán-Torrecilla, C., Gil de Paz, A., Castillo-Morales, A., et al. 2015, A&A, 584, A87

Chevallard, J., Charlot, S., Wandelt, B., & Wild, V. 2013, MNRAS, 432, 2061

Ciesla, L., Charmandaris, V., Georgakakis, A., et al. 2015, A&A, 576, A10

Cirasuolo, M., McLure, R. J., Dunlop, J. S., et al. 2007, MNRAS, 380, 585

Civano, F., Marchesi, S., Comastri, A., et al. 2016, ApJ, 819, 62

Coil, A. L., Davis, M., Madgwick, D. S., et al. 2004, ApJ, 609, 525

Conroy, C., Schiminovich, D., & Blanton, M. R. 2010, ApJ, 718, 184

Cooper, M. C., Aird, J. A., Coil, A. L., et al. 2011, ApJS, 193, 14

Cooper, M. C., Yan, R., Dickinson, M., et al. 2012a, MNRAS, 425, 2116

Cooper, M. C., Griffith, R. L., Newman, J. A., et al. 2012b, MNRAS, 419, 3018

Dalcanton, J. J., & Bernstein, R. A. 2002, AJ, 124, 1328

Dale, D. A., Bendo, G. J., Engelbracht, C. W., et al. 2005, ApJ, 633, 857

Dale, D. A., Gil de Paz, A., Gordon, K. D., et al. 2007, ApJ, 655, 863

Dale, D. A., Aniano, G., Engelbracht, C. W., et al. 2012, ApJ, 745, 95

Dale, D. A., Cook, D. O., Roussel, H., et al. 2017, ApJ, 837, 90

Damjanov, I., Zahid, H. J., Geller, M. J., Fabricant, D. G., & Hwang, H. S. 2018, ApJS, 234, 21

Davis, M., Guhathakurta, P., Konidaris, N. P., et al. 2007, ApJ, 660, L1

Devour, B. M., & Bell, E. F. 2016, MNRAS, 459, 2054

Donley, J. L., Koekemoer, A. M., Brusa, M., et al. 2012, ApJ, 748, 142

Doore, K., Eufrasio, R. T., Lehmer, B. D., et al. 2021, ApJ, 923, 26

Draine, B. T., & Li, A. 2007, ApJ, 657, 810

Driver, S. P., Popescu, C. C., Tuffs, R. J., et al. 2007, MNRAS, 379, 1022

Eufrasio, R. T., Dwek, E., Arendt, R. G., et al. 2014, ApJ, 795, 89

Eufrasio, R. T., Lehmer, B. D., Zezas, A., et al. 2017, ApJ, 851, 10

Fitzpatrick, E. L. 1999, PASP, 111, 63

Galametz, A., Grazian, A., Fontana, A., et al. 2013, ApJS, 206, 10

Gao, Y., & Solomon, P. M. 2004, ApJ, 606, 271

Garilli, B., McLure, R., Pentericci, L., et al. 2021, A&A, 647, A150

Gelman, A., & Rubin, D. B. 1992, Statistical Science, 7, 457

Giavalisco, M., Ferguson, H. C., Koekemoer, A. M., et al. 2004, ApJ, 600, L93

Giovanelli, R., Haynes, M. P., Salzer, J. J., et al. 1994, AJ, 107, 2036

Gordon, K. D., Clayton, G. C., Witt, A. N., & Misselt, K. A. 2000, ApJ, 533, 236

Graham, A. W., & Worley, C. C. 2008, MNRAS, 388, 1708

Grogin, N. A., Kocevski, D. D., Faber, S. M., et al. 2011, ApJS, 197, 35

Guo, Y., Ferguson, H. C., Giavalisco, M., et al. 2013, ApJS, 207, 24

Hao, C.-N., Kennicutt, R. C., Johnson, B. D., et al. 2011, ApJ, 741, 124

Hasinger, G., Capak, P., Salvato, M., et al. 2018, ApJ, 858, 77

Kennicutt, R. C., J. 1983, ApJ, 272, 54

Kennicutt, Robert C., J. 1998, ARA&A, 36, 189

Kennicutt, Robert C., J., Armus, L., Bendo, G., et al. 2003, PASP, 115, 928

Kennicutt, Robert C., J., Hao, C.-N., Calzetti, D., et al. 2009, ApJ, 703, 1672

Kennicutt, R. C., & Evans, N. J. 2012, ARA&A, 50, 531

Kennicutt, R. C., Calzetti, D., Aniano, G., et al. 2011, PASP, 123, 1347

Kirkpatrick, A., Pope, A., Charmandaris, V., et al. 2013, ApJ, 763, 123

Kocevski, D. D., Hasinger, G., Brightman, M., et al. 2018, ApJS, 236, 48

Koekemoer, A. M., Faber, S. M., Ferguson, H. C., et al. 2011, ApJS, 197, 36

Kong, X., Charlot, S., Brinchmann, J., & Fall, S. M. 2004, MNRAS, 349, 769

Kriek, M., & Conroy, C. 2013, ApJ, 775, L16

Kroupa, P. 2001, MNRAS, 322, 231

Lawrence, A., Warren, S. J., Almaini, O., et al. 2007, MNRAS, 379, 1599

Leja, J., Speagle, J. S., Ting, Y.-S., et al. 2021, arXiv e-prints, arXiv:2110.04314

Leroy, A. K., Walter, F., Brinks, E., et al. 2008, AJ, 136, 2782

Leroy, A. K., Bigiel, F., de Blok, W. J. G., et al. 2012, AJ, 144, 3

Leslie, S. K., Schinnerer, E., Groves, B., et al. 2018a, A&A, 616, A157

Leslie, S. K., Sargent, M. T., Schinnerer, E., et al. 2018b, A&A, 615, A7

Li, A., & Draine, B. T. 2001, ApJ, 554, 778

Lilly, S. J., Le Brun, V., Maier, C., et al. 2009, ApJS, 184, 218

Luo, B., Brandt, W. N., Xue, Y. Q., et al. 2017, ApJS, 228, 2

Makarov, D., Prugniel, P., Terekhova, N., Courtois, H., & Vauglin, I. 2014, A&A, 570, A13

Masters, D. C., Stern, D. K., Cohen, J. G., et al. 2019, ApJ, 877, 81

Masters, K. L., Nichol, R., Bamford, S., et al. 2010, MNRAS, 404, 792

McLure, R. J., Pearce, H. J., Dunlop, J. S., et al. 2013, MNRAS, 428, 1088

Meurer, G. R., Heckman, T. M., & Calzetti, D. 1999, ApJ, 521, 64

Murphy, E. J., Condon, J. J., Schinnerer, E., et al. 2011, ApJ, 737, 67

Nandra, K., Laird, E. S., Aird, J. A., et al. 2015, ApJS, 220, 10

Nayyeri, H., Hemmati, S., Mobasher, B., et al. 2017, ApJS, 228, 7

Newman, J. A., Cooper, M. C., Davis, M., et al. 2013, ApJS, 208, 5

Overzier, R. A., Heckman, T. M., Wang, J., et al. 2011, ApJ, 726, L7

Popping, G., Puglisi, A., & Norman, C. A. 2017, MNRAS, 472, 2315

Salim, S., Boquien, M., & Lee, J. C. 2018, ApJ, 859, 11

Salim, S., Charlot, S., Rich, R. M., et al. 2005, ApJ, 619, L39

Salim, S., Rich, R. M., Charlot, S., et al. 2007, ApJS, 173, 267

Santini, P., Ferguson, H. C., Fontana, A., et al. 2015, ApJ, 801, 97

Sargent, M. T., Carollo, C. M., Kampczyk, P., et al. 2010, ApJ, 714, L113

Schlafly, E. F., & Finkbeiner, D. P. 2011, ApJ, 737, 103

Schlegel, D. J., Finkbeiner, D. P., & Davis, M. 1998, ApJ, 500, 525

Scoville, N., Aussel, H., Brusa, M., et al. 2007, ApJS, 172, 1

Sérsic, J. L. 1963, Boletin de la Asociacion Argentina de Astronomia La Plata Argentina, 6, 41

Silverman, J. D., Kashino, D., Sanders, D., et al. 2015, ApJS, 220, 12

Stefanon, M., Yan, H., Mobasher, B., et al. 2017, ApJS, 229, 32

Thorp, M. D., Ellison, S. L., Simard, L., Sánchez, S. F., & Antonio, B. 2019, MNRAS, 482, L55

Tress, M., Mármol-Queraltó, E., Ferreras, I., et al. 2018, MNRAS, 475, 2363

Trump, J. R., Impey, C. D., Elvis, M., et al. 2009, ApJ, 696, 1195

Tuffs, R. J., Popescu, C. C., Völk, H. J., Kylafis, N. D., & Dopita, M. A. 2004, A&A, 419, 821

Unterborn, C. T., & Ryden, B. S. 2008, ApJ, 687, 976

van der Wel, A., Bell, E. F., Häussler, B., et al. 2012, ApJS, 203, 24

van der Wel, A., Chang, Y.-Y., Bell, E. F., et al. 2014, ApJ, 792, L6

van der Wel, A., Noeske, K., Bezanson, R., et al. 2016, ApJS, 223, 29

Wang, W., Kassin, S. A., Pacifici, C., et al. 2018, ApJ, 869, 161

Wild, V., Charlot, S., Brinchmann, J., et al. 2011, MNRAS, 417, 1760

Willner, S. P., Coil, A. L., Goss, W. M., et al. 2006, AJ, 132, 2159

Wolf, C., Weinzirl, T., Aragón-Salamanca, A., et al. 2018, MNRAS, 480, 3788

Xue, Y. Q., Luo, B., Brandt, W. N., et al. 2016, ApJS, 224, 15

Zhu, Y.-N., Wu, H., Cao, C., & Li, H.-N. 2008, ApJ, 686, 155

Zuckerman, L. D., Belli, S., Leja, J., & Tacchella, S. 2021, ApJ, 922, L32

Appendix

4.A Spectroscopic Redshift Catalog

The spectroscopic redshifts assigned to sources in the CANDELS fields were compiled from various sources. For the GOODS-N, we used the relatively comprehensive CANDELS redshift catalog from Barro et al. (2019). For the GOODS-S, we compiled spectroscopic redshifts from the Chandra Deep Field-South "master spectroscopic catalog,"[6] ACES (Cooper et al., 2012a), and VANDELS spectroscopic surveys (Garilli et al., 2021) that were not already included in the GOODS-S CANDELS redshift and mass catalog (Santini et al., 2015). These sources were then cross-matched to the nearest CANDELS source within $0.5''$. If a source in the master catalog, ACES, or VANDELS had a higher reliability flag than what was in the CANDELS catalog, we replaced the CANDELS spectroscopic redshift with the more reliable measurement. For the EGS, we cross-matched spectroscopic redshift sources from the DEEP2+3 survey data release 4 (Coil et al., 2004; Willner et al., 2006; Cooper et al., 2011,0; Newman et al., 2013)[7] to the nearest source within $0.5''$ in the CANDELS EGS multiband catalog. For the COSMOS field, we cross-matched spectroscopic redshift sources from IMACS (Trump et al., 2009), zCOSMOS data release 3 (DR3; Lilly et al., 2009)[8], FMOS (Silverman et al., 2015), LEGA-C DR3 (van der Wel et al., 2016)[9], hCOSMOS (Damjanov et al., 2018), DEIMOS (Hasinger et al., 2018), and C3R2 (Masters et al., 2019) to the nearest source within $0.5''$ in the CANDELS COSMOS multiband catalog. If a galaxy had redshifts from multiple surveys, the most reliable redshift was used. For the UDS field, we included any spectroscopic redshifts from the UDSz spectroscopic catalog (Bradshaw et al., 2013;

[6] https://www.eso.org/sci/activities/garching/projects/goods/MasterSpectroscopy.html
[7] https://deep.ps.uci.edu
[8] https://www.eso.org/qi/catalog/show/65
[9] https://www.eso.org/qi/catalog/show/379

McLure et al., 2013)[10], VANDELS spectroscopic survey, and C3R2 that were not already included in the UDS CANDELS redshift and mass catalog (Santini et al., 2015) by cross-matching them to the nearest source within $0.5''$. If a source in UDSz, VANDELS, or C3R2 had a higher reliability flag than what was in the CANDELS catalog, we replaced the CANDELS spectroscopic redshift with the more reliable measurement.

[10]https://www.nottingham.ac.uk/astronomy/UDS/UDSz/

Chapter 5

Conclusion

In this dissertation, we developed and implemented an inclination-dependent attenuation module within our updated SED fitting code `Lightning`. The module utilizes the inclination-dependent attenuation curves from Tuffs et al. (2004) as updated by Popescu et al. (2011), which we reformatted to take advantage of the non-parametric SFH implementation within `Lightning`. By utilizing this inclination-dependent attenuation module, we were able to test and better understand the impact inclination-dependent attenuation has on the derived SFHs, and subsequently, evolution of disk galaxies. A brief review of each of the submitted or published articles contained in Chapters 2, 3, and 4 is as follows:

- In Chapter 2, we presented the most recent version of our SED fitting code `Lightning`. The models and algorithms in this new version of `Lightning` can be used to model emission from any combination of stellar, dust, and AGN sources in an observed X-ray to submillimeter SED, while accounting for either basic inclination-independent dust attenuation or our physically-motivated, inclination-dependent attenuation module. Using a variety of combinations of these models, we presented different example applications of `Lightning` to demonstrate its capabilities and some of its potential uses.

- In Chapter 3, we tested our inclination-dependent attenuation module utilizing 82 disk-dominated galaxies, with UV-to-FIR photometry from the GOODS North and South fields. We also presented a Monte Carlo method for deriving inclination probability distributions utilizing the measured axis ratio of a galaxy. Using these inclination probability distributions as priors, we fit the SEDs of our galaxy sample using `Lightning` with its inclination-

dependent attenuation module, in addition to fitting a second time with the basic inclination-independent dust attenuation model. By comparing the two fits with the different attenuation models, we found that not accounting for inclination-based attenuation resulted in an average A_V overestimation of 0.31 ± 0.04 magnitudes for face-on to moderately inclined galaxies and an underestimation of 0.28–0.67 magnitudes for edge-on galaxies. Additionally, stellar masses were underestimated up to a factor of 0.17 dex at 90° by the inclination-independent model compared to the inclination-dependent model. Therefore, this chapter showed how SED fitting assuming inclination-independent attenuation potentially underestimates the optical attenuation and stellar masses in highly inclined disk galaxies.

- In Chapter 4, we further implemented our inclination-dependent attenuation module to analyze the inclination dependence of both hybrid UV+IR SFR estimators and the $A_{\rm FUV}$–β relation, which are commonly used when SED fitting is not feasible. Using this module in `Lightning`, we fit the SEDs of 133 CANDELS field galaxies along with 18 local galaxies from SINGS and KINGFISH, all of which were selected to be disk-dominated. From the analysis of this sample, we found that the UV+IR correction factor $a_{\rm corr}$ in hybrid SFR estimators and a_β in the $A_{\rm FUV}$–β relation were highly dependent on the inclination of a galaxy. To account for this variation with inclination, we derived updated parametric relations for both estimators that make $a_{\rm corr}$ and a_β polynomials of inclination. Finally, we compared these new relations with inclination-independent relations in the literature and found that adding an inclination dependence can reduce the residual scatter in the estimated SFRs of our sample by up to a factor of two.

Overall, this dissertation developed the crucial first steps needed to evaluate the impact of

inclination-dependent attenuation on the physical properties (e.g., SFHs and stellar masses) derived from SED fitting. By incorporating a physically-motivated inclination-dependent attenuation model in our SED fitting, we have shown that more accurate estimates of these physical properties can be derived for disk galaxies at any inclination, thereby improving our understanding of disk galaxy evolution. However, we note that our analyses and results were limited to disk-dominated galaxies. Future work that expands on these results could apply the inclination-dependent attenuation module in `Lightning` to a more complete sample of galaxies that have a variety of bulge component sizes, rather than a purely disk-dominated sample. An analysis such as this would be able to check how the bulge component of a disk galaxy affects the inclination dependence of our results and whether our results hold for the broader disk-galaxy population.

References

Popescu, C. C., Tuffs, R. J., Dopita, M. A., et al. 2011, A&A, 527, A109

Tuffs, R. J., Popescu, C. C., Völk, H. J., Kylafis, N. D., & Dopita, M. A. 2004, A&A, 419, 821